The biology and roles of lipid droplets in regulating pluripotent stem cell biology and metabolism

by Donja Karimlou

Thesis submitted towards fulfilment of the degree of

Doctor of Philosophy

Institute of Reproductive and Developmental Biology

Faculty of Medicine

Imperial College London

October 2018

Statement of Originality

All experiments included in this thesis were performed by the author unless otherwise stated below or in the text.

David Barneda generated the Cidea overexpressing embryonic stem cells (ESCs) used in this work, and was involved in the initial establishment of ESC clones harbouring different lipid droplet morphologies, and their further C^{12} glucose GC-MS characterisation together with James Ellis as described in Chapter 6. Michelle Percharde generated the Cidea knockdown ESCs used in this study, and was involved in the characterisation of Cidea as a direct target of the transcription factor *Esrrb* as described in Chapter 3. Christopher Royer generated the embryo images subsequently used to establish the tissue-specific dynamics of lipid droplets *in vivo* as described in chapter 4. King Hang (Tommy) Mau generated the Cidea knockout ESCs used in this work, and performed the 3D differentiation experiments described in Chapter 4. He also contributed to this project during the completion of this Master degrees under my joint supervision with Dr Véronique Azuara, performing embryoid body experiments described in Chapter 5. Mark Christian and Yi-Wah Chan supported the RNA sequencing data analysis described in Chapter 6. Austin Smith kindly provided the Esrrb knockout and control cells used in this work.

Copyright Declaration

The copyright of this thesis rests with the author and is made available under a Creative Commons Attribution Non-Commercial No Derivatives licence. Researchers are free to copy, distribute or transmit the thesis on the condition that they attribute it, that they do not use it for commercial purposes and that they do not alter, transform or build upon it. For any reuse or redistribution, researchers must make clear to others the licence terms of this work.

Acknowledgements

First and foremost, I would like to thank my supervisor Dr Véronique Azuara. She has supported me throughout with exciting discussions, and encouraging words on a professional and personal level, which eventually unfolded the full potential of this project. I would also like to thank all other scientists for their insightful discussions which notably supported the development of this project, in particular: Mark Christian for his guidance on the metabolic aspect of the project, Shankar Srinivas and Christopher Royer for their contribution to the *in vivo* part of the project, Hector Keun and James Ellis for supporting my GC-MS work, Alexandro Sardini and David Carling for supporting my Seahorse experiments, and Dirk Dorman for supporting my confocal work. I would like to thank Willem Voncken who introduced me to Véronique during my masters at Maastricht University, The Netherlands.

I am thankful to the following past laboratory members in particular: Rute Tomaz who kindly adopted me as a master student in the lab, David Barneda who introduced me to this project, and Emma Bell for introducing me to bioinformatics. A special thank you to my friend and colleague Tommy King Mau, with whom I had countless scientific and not-so-scientific discussion in tissue culture room 1011.

I am very grateful for having met so many wonderful people throughout these past few years in London; at uni, at the student accommodation and at the various sports societies. This has made my time in London unforgettable. However, without the unconditional support of my parents I would not have come this far.

This thesis is dedicated to my dad Fathali Karimlou, who passed away on April 11th 2017.

Abstract

Lipid droplets (LDs) are intracellular organelles, which have long been ignored as passive aggregates of lipids. However, recent research firmly established LDs as dynamic structures, actively regulating energy storage and generating signalling molecules. Concomitant with unfolding the regulatory mechanisms of LDs, including the identification of LD-associated proteins, their functional importance is increasingly being recognised in various pathologies such as metabolic diseases and cancer.

Early embryogenesis is a tightly orchestrated process, often investigated through *in vitro* models, such as pluripotent stem cells. Interestingly, dynamic LD enlargement and lipid storage was found to operate in *in vivo* and blastocyst-derived embryonic stem cells (ESCs). The overall objective of this PhD research project is to specifically investigate the biology and role(s) of LDs in regulating pluripotent stem cell biology and metabolism. Here, we demonstrate an essential role for LD-associated protein Cidea in promoting LD enlargement in ESCs using gain- and loss-of-function approaches. *In vivo*, we observe that *Cidea* expression peaks at the morula-blastocyst transition consistent with the formation of enlarged LDs throughout the embryo. Yet these are mobilised in the pluripotent (epiblast) compartment at the onset of implantation, pointing to enhanced, tissue-specific lipid usage during this key developmental step.

Using ESC models, we recognize a possible role for Cidea during the morphogenesis events accompanying epiblast maturation post-implantation. From a metabolic perspective, we find that enforced Cidea expression and LD enlargement correlate with enhanced oxygen consumption and TCA cycle activity with unchanged anaerobic glycolytic capacity. The functional significance of these alterations is further investigated using self-renewing, ESC clonal populations that harbour different LD morphologies, gene expression patterns and metabolic capacities. Integrating RNA-sequencing data, GC-MS and Seahorse-based experiments, we propose that ESCs might transiently enhance their oxidative status to sustain the energy-demanding process of lipid synthesis taking place at the exit of ESC pluripotency.

Contents

Statement of Originality . . . 2
Copyright Declaration . . . 3
Acknowledgements . . . 4
Abstract . . . 5
List of Figures . . . 11
List of Tables . . . 12
Abbreviations . . . 13

1 Introduction **16**

1.1 Animal Model: *mus musculus* . . . 17
1.2 Early mouse embryogenesis . . . 17
1.2.1 Pre-implantation development of the mouse embryo . . . 18
1.2.2 Post-implantation development of the mouse embryo . . . 19
1.3 From *in vivo* embryos to *in vitro* stem cell models . . . 20
1.3.1 Isolation and maintenance of stem cell populations from the early embryo . . . 20
1.3.1.1 Embryonic stem cell heterogeneity . . . 22
1.3.1.2 Naïve-to-primed stem cell pluripotency . . . 23
1.3.1.3 Cross-talk between pluripotency sustaining factors . . . 24
1.4 Pluripotent stem cell metabolism . . . 25
1.4.1 General cell metabolism . . . 26
1.4.2 Metabolism in naïve and primed pluripotency . . . 28
1.4.2.1 Cross-talk between metabolism and other regulatory mechanisms in controlling stem cell states. . . . 30
1.4.3 Metabolic switch: is there a role for lipid metabolism in the naïve-to-primed ESC transition? . . . 32
1.5 Lipid droplets . . . 32
1.5.1 Lipid droplet structure, composition and biogenesis . . . 32
1.5.2 Interactions of lipid droplets with other organelles . . . 34
1.5.3 Lipid droplet-associated proteins . . . 34
1.5.3.1 Lipid droplet-associated protein Cidea . . . 36
1.6 Hypothesis and Aims . . . 38

2 Materials and Methods **41**

2.1 Materials . . . 42
2.1.1 Antibodies . . . 42
2.1.2 Enzymes . . . 42
2.1.3 Kits . . . 43
2.1.4 Inhibitors . . . 43
2.1.5 Media supplements . . . 43
2.1.6 Reagents . . . 44
2.1.7 Solutions . . . 45
2.1.8 Media . . . 46
2.1.9 Cell lines . . . 46
2.2 Methods . . . 46
2.2.1 Cell culture . . . 46
2.2.1.1 Embryonic stem cell culture . . . 46
2.2.1.2 Derivation of knockdown, overexpression and knockout cells . . . 47
2.2.1.3 Clonal isolation and expansion . . . 47
2.2.1.4 Cryopreservation . . . 47
2.2.1.5 Production of leukaemia inhibitory factor . . . 48
2.2.2 Phenotypic characterization of embryonic stem cells . . . 48
2.2.2.1 Growth Curve . . . 48
2.2.2.2 Self-renewal assay . . . 48
2.2.2.3 Luciferase reporter assay . . . 48
2.2.2.4 Chromatin immunoprecipitation . . . 49
2.2.2.5 Lipid droplet staining and quantification . . . 49
2.2.2.6 RNA sequencing . . . 49
2.2.2.7 Motif analysis . . . 50
2.2.3 Metabolic characterization of embryonic stem cells . . . 50
2.2.3.1 Gas chromatography-mass spectrometry . . . 50
2.2.3.2 Nuclear magnetic resonance . . . 51
2.2.3.3 Determination of oxygen consumption rate and extracellular acidification rate . . . 51
2.2.4 Embryonic stem cell differentiation . . . 52
2.2.4.1 Embryoid body formation . . . 52
2.2.4.2 3D differentiation assay . . . 52
2.2.5 *In vivo* . . . 52
2.2.5.1 Embryo dissection . . . 52
2.2.5.2 Embryo staining and lipid droplet quantification . . . 52
2.2.6 Quantitative reverse transcriptase PCR . . . 53

2.2.6.1 RNA extraction . . . 53
2.2.6.2 cDNA synthesis . . . 53
2.2.6.3 Realtime quantitative PCR analysis . . . 53
2.2.6.4 Primer design and validation . . . 54
2.2.7 Protein analysis . . . 54
2.2.7.1 Immunofluorescent staining . . . 54
2.2.7.2 Western blot . . . 54

3 The uncovering of Cidea-mediated lipid droplet enlargement in embryonic stem cells 56
3.1 Introduction . . . 57
3.2 Results . . . 58
3.2.1 Embryonic stem cells dynamically form large lipid droplets upon KSR exposure . . 58
3.2.2 LD enlargement correlates with *Cidea* induction in KSR-treated embryonic stem cells . . . 60
3.2.3 The Albumax fraction of KSR is alone sufficient for inducing *Cidea* expression and LD enlargement . . . 62
3.2.4 Ectopically expressing Cidea in ESCs is sufficient to drive LD enlargement . . . 64
3.2.5 Cidea depletion in ESCs inhibits LD-LD fusion events . . . 66
3.2.6 *Cidea* expression is associated with an undifferentiated ESC state . . . 70
3.3 Summary and Conclusions . . . 73

4 Characterizing Cidea expression profile and lipid droplet dynamics in the developing embryo *in vivo* 74
4.1 Introduction . . . 75
4.2 Results . . . 76
4.2.1 Cidea and lipid metabolism genes show dynamic expression patterns during early development . . . 76
4.2.2 Cidea protein is coating lipid droplets in the *in vivo* early blastocyst . . . 77
4.2.3 Lipid droplet tissue-specificity and dynamics across peri-implantation *in vivo* . . . 79
4.2.4 ESC organoids in extracellular matrix recapitulate peri-implantation morphogenesis 81
4.3 Summary and Conclusions . . . 85

5 Assessing the impact of Cidea-modulation on embryonic stem cell biology 86
5.1 Introduction . . . 87
5.2 Results . . . 88
5.2.1 Modulating Cidea expression in ESCs does not impact on their self-renewing abilities 88
5.2.2 Cidea knockdown impacts on embryoid body morphology . . . 90
5.2.3 Characterising the impact of Cidea modulation on ESC metabolism . . . 94
5.2.4 Cidea modulation impacts on ESC oxidative status . . . 97
5.2.5 Analysing substrate utilisation in Cidea overexpressing cells . . . 101

5.3 Summary and Conclusions . . . 103

6 Investigating the functional importance of LDs and lipid metabolism at the onset of ESC differentiation and glycolytic switch 104

6.1 Introduction . . . 105

6.2 Results . . . 106

6.2.1 Isolation of ESC clones that stably harbour different LD morphologies under self-renewing conditions. . . . 106

6.2.2 Functional characterization of selected small and large LD embryonic stem cell clones 108

6.2.3 Clustering of small LD and large LD embryonic stem cell clones based on differential gene expression signatures . . . 111

6.2.4 Preliminary evidence for different lipid trafficking and usage in sLD and LLD embryonic stem cell clones . . . 113

6.2.5 Untargeted metabolic profiling of sLD and LLD embryonic stem cell clones. . . . 115

6.2.6 Glucose tracing in sLD and LLD embryonic stem cell clones. . . . 119

6.2.7 LLD and sLD embryonic stem cell clones display different oxidative status and glycolytic rate . . . 121

6.3 Summary and Conclusions . . . 123

7 Discussion 125

7.1 Investigating the molecular mechanism(s) underlying LD dynamics in ESCs and in the early embryo. . . . 126

7.1.1 Does Cidea expression control the formation of supersized LDs in ESCs? . . . 126

7.1.2 What regulates Cidea expression in pluripotent stem cells? . . . 127

7.1.3 Does Cidea-mediated LD enlargement operate in the developing embryo *in vivo*? . 128

7.1.4 What is the role of Cidea in ESC self-renewal and differentiation ability? . . . 130

7.1.5 Characterising the impact of Cidea expression modulation on ESC metabolism . . 132

7.2 Investigating the functional importance of LD biology and heterogeneity in ESCs. . . . 134

7.2.1 Lipid accumulation in an ESC differentiation trajectory. . . . 134

7.2.2 The lipid switch in self-renewing ESCs prior to the exit of the naïve pluripotent state. 136

7.2.3 What is the functional importance of the lipid switch for enabling differentiation in ESCs? . . . 140

8 Appendix 163

List of Figures

1.1 Pre-implantation development of the mouse embryo. 18
1.2 Early post-implantation development of the mouse embryo. 20
1.3 Timeline indicating key discoveries for establishing and maintaining ESC *in vitro*. 21
1.4 Embryonic stem cell heterogeneity *in vitro*. 22
1.5 Naïve and primed pluripotent stem cell properties. 24
1.6 Cross-talk between pluripotency regulatory mechanisms. 25
1.7 Schematic diagrams of key cellular metabolic pathways. 27
1.8 Metabolic changes occurring *in vivo* during early development, and *in vitro* in ESCs. . . . 29
1.9 Cross-talk between metabolism and other regulatory mechanisms in controlling stem cell states. 30
1.10 Lipid droplet structure, composition and biogenesis. 33
1.11 Lipid droplet associated organelles. 34
1.12 Examples of classes of LD-associated proteins. 35
1.13 Sequence homology between CIDE protein, and DNA fragmentation factor (DFF), and Perilipin. 37
1.14 Timeline indicating a selection of discoveries about Cidea. 38
1.15 Key discoveries regarding lipid droplets in the embryo. 39
1.16 Naïve-to-primed pluripotency, a focus on ESCs metabolic properties. 40

3.1 Lipid droplet enlargement in embryonic stem cells and mouse embryonic fibroblasts. . . . 59
3.2 Gene expression profiling in ESCs and MEFs cultured in routine (FBS/LIF) and lipid-rich media (KSR/LIF). 61
3.3 The Albumax fraction of KSR is alone sufficient to enforce LD enlargement. 63
3.4 Generation and characterisation of Cidea overexpressing ESCs. 65
3.5 Generation and characterisation of Cidea knockdown ESCs. 67
3.6 Generation and characterisation of Cidea knockout ESCs. 68
3.7 Lipid droplet morphology in Cidea knockout and rescue ESCs. 69
3.8 Cidea-mediated lipid droplet enlargement is partly regulated by key pluripotency transcription factors. 71

4.1 Lipid associated gene expression patterns in the early embryo. 77

4.2 *In vivo* analysis of functional Cidea expression. 78
4.3 *In vivo* analysis of lipid droplet size and distribution during early development. 80
4.4 Cidea knockout ESC organoids display aberrant lumen formation. 83

5.1 Cidea-modulated ESCs retain normal self-renewal ability. 89
5.2 Embryoid body (EB) formation in Cidea overexpressing and knockdown ESCs. 91
5.3 Cavity formation in embryoid bodies (EBs) from Cidea knockdown and knockout cells. . . 93
5.4 GC-MS analysis of Cidea-OE and Cidea-KD cells. 97
5.5 Seahorse analysis of Cidea-modulated cells and Esrrb-KO cells. 100
5.6 Analysis of increased oxygen consumption in Cidea-OE via Seahorse. 102

6.1 Generation of ESC clones with different LD morphologies. 107
6.2 Functional characterization of ESC clones with different LD morphologies. 110
6.3 RNA-sequencing data analysis of ESC clones with different LD morphology. 112
6.4 RT-qPCR validation of differential gene expression profiles in sLD and LLD clones. 114
6.5 GC-MS based, glycolysis and TCA cycle-focused, metabolic profiling in the three LD clone clusters. 116
6.6 GC-MS based protein-focused metabolic profiling in the three LD clone clusters. 118
6.7 GC-MS lipid-focused metabolic analysis of ^{13}C glucose tracing in the three LD clone clusters. 120
6.8 Seahorse-based analysis of the sLD and LLD clones. 122

7.1 Lipid droplet dynamics throughout peri-implantation development. 129
7.2 Lipid droplet dynamics throughout 3D ESC organoid differentiation. 131
7.3 Model of the lipid switch in a heterogeneous self-renewing ESC population. 139

List of Tables

8.1 Sequences of primers used for RT-qPCR. 164
8.2 Cidea promoter motif enrichment. 165
8.3 All metabolites reliably detected in untargetted GC-MS analysis of lipid droplet clones. . 166
8.4 Pathway enrichment analysis in large LD and small LD clones. 167
8.5 Pathway enrichment analysis in large LD (L_1LD only) and small LD clones. 168
8.6 Pathway enrichment analysis in large LD (L_2LD only) and small LD clones. 169
8.7 Pathway enrichment analysis in L_1LD and L_2LD clones. 173

Abbreviations

°C	Celsius
2-DG	2-deoxy-glucose
2i	2 inhibitors
3D	3 dimensional
AMDIS	Automated Mass Spectral Deconvolution and Identification System
AME	Analysis of Motif Enrichment
AP	Alkaline phosphatase
atRA	All trans retinoic acid
BSA	Bovine serum albumin
CAG	Chicken beta-actin
cDNA	Complementary DNA
ChIP	Chromatin
CPDB	ConsensusPathDB
CT	Cycle threshold
DAPI	4',6diamidino-2phenylindole
DE	Definitive endoderm
DMEM	Dulbecco's modified eagle medium
DMSO	Dimethyl sulfoxide
DNA	Deoxyribonucleic acid
dNTP	Deoxynucleoside triphosphate
DTT	Dithiothreitol
E	Embryonic day
EB	Embryoid body
ECAR	Extracellular acidification rate
ECL	Enhanced chemiluminescence
EDTA	Ethylenediaminetetraacetic

EPC	Ectoplacental cone
Epi	Epiblast
EpiSC	Epiblast stem cell
ERK	Extracellular signal-regulatedkinase
ESC	Embryonic stem cell
EtOH	Ethanol
ExE	Extra embryonic ectoderm
FA	Fatty acid
FAO	Fatty acid oxidation
FBS	Fetal bovine serum
FCCP	Carbonyl cyanide-4-(trifluoromethoxy)phenylhydrazone
FFA	Free fatty acid
Fgf	Fibroblast growth factor
Fig	Figure
GC-MS	Gas chromatography-mass spectrometry
GFP	Green fluorescent protein
GMEM	Glasgow modified eagle medium
GSK	Glycogen synthase kinase
h	hour
H3K27me3	Tri-methylation of lysine 27 of histone H3
HEPES	4(2hydroxyethyl)-1-piperazineethanesulfonic acid
HRP	Horseradish peroxidase
ICM	Inner cell mass
IF	Immunofluorescence
IgG	Immunoglobulin
iPSC	Induced pluripotent stem cell
KD	Knockout
kDa	Kilo Dalton
KO	Knockdown
KSR	KnockOut serum replacement
L_1LD	large lipid droplet clone with good self-renewal capacity
L_2LD	large lipid droplet clone with poor self-renewal capacity
LD	Lipid droplet
LIF	Leukemia inhibitory factor
LLD	Large lipid droplet clone
Luc	Luciferase
MAPK/MEK	Mitogen-activated protein kinase
MEF	Mouse embryonic fibroblast
MEME	Multiple Em for Motif Elicitation
mRNA	Messenger RNA

NMR	Nuclear magnetic resonance
OCR	Oxygen consumption rate
OE	Overexpressing
P	P-value
PBS	Phosphate buffered saline
PC	Pyruvate carboxylase
PCA	Principal component analysis
PCR	Polymerase chain reaction
PDH	Pyruvate dehydrogenase
PE	Parietal endoderm
PFA	Paraformaldehyde
PMSF	Phenylmethanesulfonylfluoride
PRC2	Polycomb repressive compelx 2
PrE	Primitive endoderm
Puro	Puromycin
PVDF	Polyvinylidene fluoride
qPCR	Quantitative PCR
RIPA	Radio Immuno Precipitation Assay
RNA	Ribonucleic acid
RNAi	RNA interference
rpm	Rounds per minute
RT	Room temperature
RT-PCR	Reverse transcription PCR
SDS	Sodium dodecyl sulfate
SDS-PAGE	Sodium dodecyl sulfate-polyacrylamide gel electrophoresis
SEM	Standard error fo the mean
shRNA	Small hairpin RNA
siRNA	Small interfering RNA
sLD	Small lipid droplet clone
STAT	Signal Transducer and Activator of Transcription
TBS-T	Tris-buffered saline with 0.10% Tween-20
TCA	Tricarboxylic acid
TE	Trophectoderm
TPM	Transcripts per million
UHPLC	Ultra-high-pressure liquid chromatography
USCS	University of California Santa Cruz
v/v	Volume/volume
VE	Visceral endoderm
w/v	Weight/volume

Chapter 1

Introduction

1.1 Animal Model: *mus musculus*

The question of how and when human life begins holds a powerful fascination. Indeed, stem cell research offers great promise for understanding basic mechanisms of human development and differentiation, as well as the hope for new treatments of diseases. Despite this potential, human embryonic stem cell research is ethically controversial because it involves the destruction of human embryos [1]. Besides these ethical barriers, additional technical barriers have caused the mouse to be recognized as a leading mammalian model system for the study of molecular and cellular processes relevant to human biology.

Despite having diverged some 75 million years ago, mice and humans share a remarkable degree of genomic, anatomical, and physiological similarity. Almost every gene found in humans so far has been found in a closely related form in mice, though divergences exist in the tissue-specific expression patterns of some genes. As mammals, mice facilitate the study of processes and pathologies that cannot be modelled in yeast, worms, or flies. Apart from its small size, the mouse has, compared with other mammals, a short generation time and is relatively fecund. This makes it feasible to carry out studies that necessarily involve significant numbers of animals and considerable breeding efforts.

The isolation and propagation of pluripotent mouse embryonic stem cells (ESCs) in the early 1980s has triggered a major advance in mouse genetics with the emergence of gene targeting technology [2, 3]. Researchers have utilized an array of innovative genetic technologies to produce custom-made mouse models for a wide array of specific diseases, as well as to study the function of targeted genes. One of the most important advances has been the ability to create transgenic mice, in which a new gene is inserted into the animal's germline. Even more powerful approaches, dependent on homologous recombination, have permitted the development of tools to "knock out" genes, which involves replacing existing genes with altered versions; or to "knock in" genes, which involves altering a mouse gene in its natural location. Evidently, mouse models have significantly contributed to our understanding of human biology, and allowed us to develop a considerable understanding of mammalian development.

1.2 Early mouse embryogenesis

Early mouse embryogenesis and derived stem cells are central concepts in this PhD research, and will therefore be described in depth in this section. In this setting "early" refers to the time period before and just after implantation, a critical natural selection checkpoint in early embryo development, also referred to as peri-implantation. Specifically, this process is roughly denoted as pre-implantation (up to embryonic day (E) 4.5) and post-implantation (beyond E4.5).

1.2.1 Pre-implantation development of the mouse embryo

Fertilization occurs between two haploid gametes (the egg and sperm cell) to form a diploid zygote. This totipotent cell contains the paternal and maternal genetic information, and holds the ability to give rise to all cells of the developing organism. Up until the implantation in the uterine wall, the zygote will follow a series of sequential cell divisions into progressively smaller cells, or blastomeres, over the first four and a half days of life (E4.5), forming a hollow ball of cells, the blastocyst (Fig 1.1). The blastocyst comprises three distinct cell populations: the trophectoderm (TE) that will contribute to the placenta formation, the primitive endoderm (PrE) that will give rise to the yolk sac, and the primitive ectoderm, or epiblast (Epi), comprising pluripotent progenitors that will generate the proper embryo (Fig 1.1) [4]. But how are these distinct blastocyst lineages accomplished? First, two rounds of asymmetric cell divisions occur between 8 to 16-cell stage (E2.5), and 16 to 32-cell stage (E3.0) (Fig 1.1). This leads to the segregation of two distinct populations in morula-stage embryos, depending on their location. Polar cells located on the outside will go on to form the TE, whereas inner apolar cells will form the inner cell mass (ICM) [5]. This process is highly dependent on cell polarity, position and cell-cell signalling, also influenced by molecular heterogeneity between individual blastomeres [4]. By the 32-cell stage the embryo cavitates with full specification of the TE, the orientation of which will define the embryonic-abembryonic axis of the embryo. The second event of cell fate decision occurs at the 32 to 64-cell transition where the ICM further segregates into the PrE and the epiblast by E4.5. Cell lineage tracing techniques have unveiled that before this segregation, ICM blastomeres are already engaged into either PrE or Epi. This bias occurs in a heterogeneous "salt and pepper" manner, concomitant with acquisition of exclusive expression of PrE and Epi-specific markers *Gata6* and *Nanog*, respectively [6, 7].

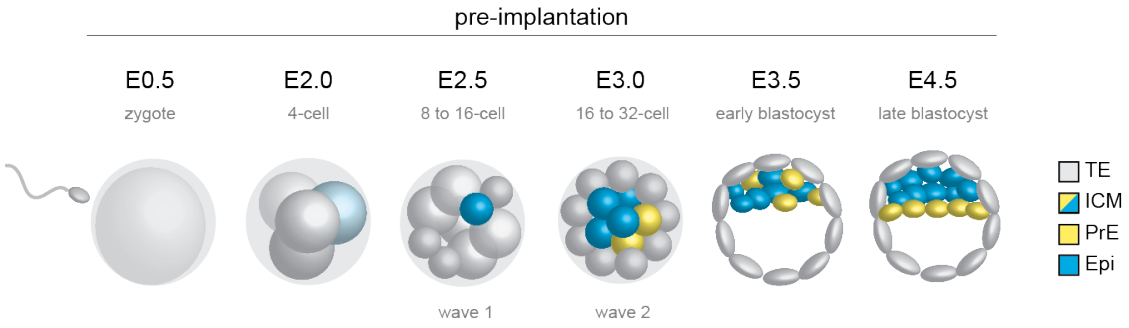


Figure 1.1: Pre-implantation development of the mouse embryo.

After fertilization, the zygote forms and divides through the early cleavage stages of mammalian development up to the morula (E3.0). Embryonic and extra-embryonic lineages cells are specified by two cell fate decisions. The first waves of cell divisions segregate inside (blue) and outside (grey) layers of (E2.5) cells with outside cells later giving rise to extra-embryonic trophectoderm (TE), while inside cells tend to preferentially form the pluripotent inner cell mass (ICM). Secondly, at the early blastocyst stage (E3.5) the ICM segregated into the extra-embryonic primitive endoderm (PrE; yellow) and the epiblast (Epi; blue) progenitors, with further maturation and compartmentalization of these lineages at the late-blastocyst stage (E4.5), just before implantation. Adapted from Bedzhov et al. [4].

1.2.2 Post-implantation development of the mouse embryo

When all three pre-implantation cell lineages have been segregated, the blastocyst attaches to the maternal uterine wall, upon hatching of the zona pellucida (the glycoprotein layer surrounding the plasma membrane of mammalian oocytes). This process is a natural selection checkpoint as it permits the developmental progress only of embryos that are able to hatch. The mural TE cells make the first contact with maternal tissues, merging the blastocyst to the maternal uterine wall, to form the ectoplacental cone (EPC). Local vasculature remodelling and angiogenesis are induced at the implantation site to mediate nutrient, waste and gas exchange between the growing embryo and the mother. Following implantation, the epiblast undergoes a major rearrangement with the emergence of a single layered epithelium that forms an organized rosette-like cylinder, enclosing a pro-amniotic cavity, in a manner highly influenced by polarization (Fig 1.2) [4]. Cavity formation was initially thought to be highly apoptosis driven [8, 9], however it has now indeed become clear that it is mainly based on tissue self-organisation ability [4]. The TE-derived extra-embryonic ectoderm (ExE) and the Epi become surrounded by PrE-derived parietal endoderm (PE) and visceral endoderm (VE) layer (Fig 1.2). The VE has a crucial role in anterior-posterior patterning of the embryo. In particular, a sub-population emerging at the tip of the egg cylinder migrates to the distal side of the embryo to form the anterior visceral endoderm (AVE), influencing the patterning of the newly formed primitive streak - the site of gastrulation, which emerges on its opposite side (Fig 1.2) [10, 11]. Correct formation and placement of the primitive streak is dependent on reciprocal signalling cues between Epi, ExE, and AVE, respectively [12]. Upon gastrulation (at E6.5), epiblast cells ingress into the primitive streak, where they develop the mesoderm layer and additionally are integrated into the surrounding VE layer as definitive endoderm (DE). Thus, prior to this point (at E5.5), epiblast cells transiently exist in a mesendoderm state, having the potential to become either mesoderm or endoderm. Cells that are retained in the epiblast anterior site give rise to the ectoderm, and later on the surface ectoderm, which includes the epidermis and the neural tissues [11]. Mesoderm cells are subsequently compartmentalised depending on the time and location of ingression within the strike. The earliest and most posterior compartment forms the extra-embryonic mesoderm (yolk sac vasculature and blood), followed by the lateral plate (circulatory system and gut wall), paraxial (somites) and cardiac mesoderm in the intermediate and anterior regions. Finally, at the anterior tip, the axial mesoderm (notochord) is formed as well as the DE (gut tube and organs).

The above descibed pre- and post-implantation embryonic patterning is dependent on the interplay between signalling pathways and transcriptional cascades [13]. There are 11 main classes of signaling pathways important in development: Notch, FGF, EGF, Wnt/Wingless (Wg), Hedgehog (Hh), transforming growth factor β (TGFβ)/BMPs, cytokine (nonreceptor tyrosine kinase JAK-STAT pathway), Hippo, Jun kinase (JNK), NF-κB, and retinoic acid receptor (RAR) [14, 15, 13]. These pathways involve either cell-to-cell contact via surface proteins, or secreted diffusible growth and differentiation factors. Downstream gene expression is diverse, and can be examplified by the previously mentioned transciption factors *Gata6* and *Nanog* which are also regulated by such signalling pathways [16].

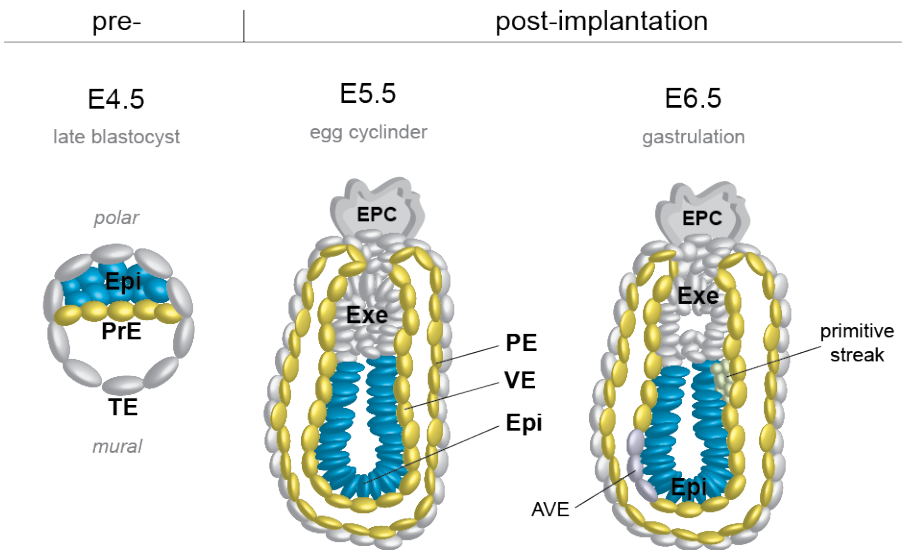


Figure 1.2: Early post-implantation development of the mouse embryo.

Before implantation (E4.5), three distinct lineages in the early embryo have been segregated: trophectoderm (TE, grey), primitive endoderm (PrE, yellow) and epiblast (Epi, blue). Upon implantation (E.5.5), the polar TE (side attached to the Epi), invades the maternal tissues forming an ectoplacental cone (EPC) and extra-embryonic ectoderm (ExE). The PrE colonizes the mural TE (opposite side of Epi) and segregates into parietal endoderm (PE) and visceral endoderm (VE), surrounding the epiblast and the pro-amniotic cavity. Upon gastrulation (E6.5), the anterior visceral endoderm (AVE, purple) is established, and epiblast cells are recruited to the posterior region (primitive streak, green), where they will form mesoderm and definitive endoderm (not indicated). Adapted from Bedzhov et al. and Tam and Loebel [4, 11]

1.3 From *in vivo* embryos to *in vitro* stem cell models

Studying embryonic stem cells (ESCs) *in vitro* offers several advantages over comparable approaches in the whole embryo and indeed provides a powerful model system for addressing questions related to stem cell biology and lineage commitment. First, the generation of specific lineages from ESCs in culture provides access to populations of early precursors that are difficult, if not impossible, to access *in vivo*. Second, the developmental potential of ESCs carrying targeted mutations of genes essential for embryonic development can be determined in culture. Analyses of these mutations *in vivo* are often complicated by early death or extensive compensatory mechanisms of the embryo in utero.

1.3.1 Isolation and maintenance of stem cell populations from the early embryo

A milestone in the developmental biology field has been the ability to isolate stem cell populations from the early blastocyst and stably culture these *in vitro*, while maintaining the developmental potency of their cognate lineages [17]. Interestingly, this discovery was preceded by decades of research on teratocarcinomas (Fig 1.3). This work revealed that the transplant ability of sporadically acquired teratocarcinomas in mice was attributed to the presence of embryonal carcinoma cells. This proliferative undifferentiated group of cells could regenerate all of the cell types forming teratocarcinomas, but also self-renew *in vitro*,

eventually leading to the isolation of numerous cell lines derived from teratocarcinomas, and the establishment of embryonal carcinomas in the early 1970s. The identification of culture conditions (serum and a feeder layer of mitotically inactivated fibroblasts) under which these populations could retain its pluripotency *in vitro* was critical for the later derivation of embryonic stem cells (ESCs) [18, 19]. In the early 1980s, two groups independently derived ESCs from pre-implantation blastocysts (Fig 1.3). These cells could be expanded indefinitely while retaining their ability to self-renew and to contribute to the germline in addition to forming all somatic cell types when re-introduced back into an embryo environment [2, 20]. Later on, their self-renewal requirements for serum and feeders were found to be substitutable by bone morphogenetic protein 4 (BMP4) and leukemia inhibitory factors (LIF), revealing these as key signalling pathways in promoting self-renewal and blocking differentiation cues (Fig 1.3) [21, 22]. These cells derived from the pre-implantation embryo, are considered to present a naïve state of pluripotency [23]. In addition to the traditional serum/LIF conditions, mouse ESCs can be cultured in the presence of two small molecule inhibitors targeting the differentiation-associated glycogen synthase kinase 3 (GSK3) and extracellular signal-regulated kinase (ERK) signalling pathways, termed 2i [24]. In contrast to serum/LIF media, 2i/LIF supports a so called ground-state of pluripotency, resembling E4.5 epiblast cells (although this is debatable), which robustly impedes differentiation triggers (Fig 1.3) [24, 25, 26]. Phenotypically, 2i/LIF culture conditions result in a much more homogeneous cell population in terms of epigenetic and transcriptional profile, while ESCs grown with serum/LIF are considered to present a more metastable state where sub-populations may be identified [27], as described later on.

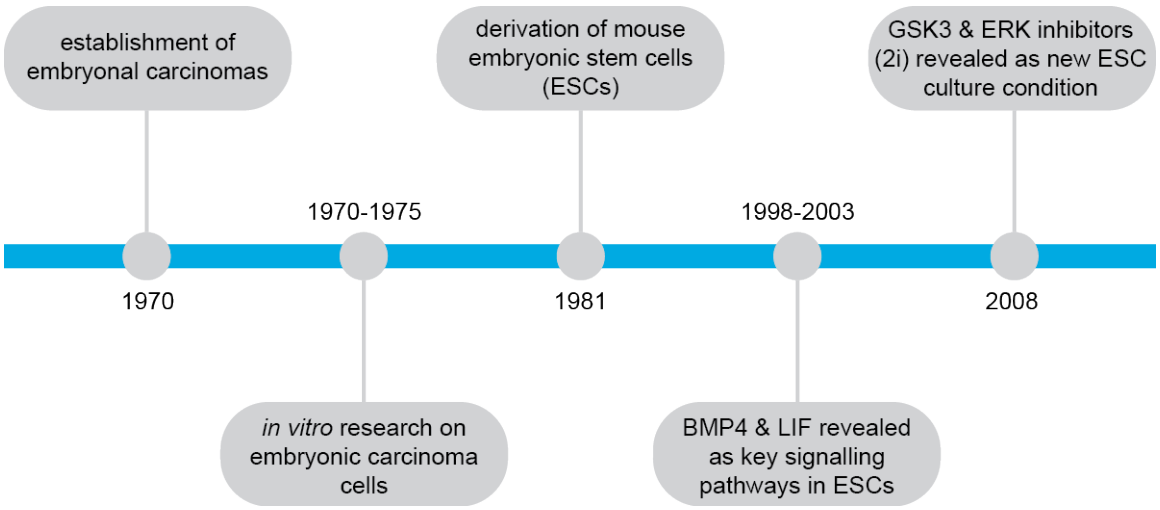


Figure 1.3: Timeline indicating key discoveries for establishing and maintaining ESC *in vitro*.

ESCs, Embryonic stem cells; BMP4, Bone morphogenetic protein 4; Leukemia inhibitory factors, LIF; GSK3, Glycogen synthase kinase 3; ERK, Extracellular signal-regulated kinases

1.3.1.1 Embryonic stem cell heterogeneity

Although ESCs are commonly derived from the ICM of early blastocysts, they have also been successfully established from any pre-implantation stage and even from single blastomeres [28, 29], acquiring very similar characteristics. This suggested that the derivation process allows cells to progress to a common developmental stage in which *in vitro* self-renewal can be achieved. Experiments investigating the naïve pluripotency marker *Rex1* exemplify these properties. Due to its high expression in ESCs and rapid downregulation upon differentiation [30], researchers often employ *Rex1* as a barometer of pluripotency state. Cultured ESCs in serum/LIF can be divided into *Rex1* high expressing (*Rex1*$^+$) and *Rex1* low expressing (*Rex1*$^-$) subpopulations where transcript expression of naïve pluripotency factors such as *Dppa3*, *Klf4*, and *Esrrb* correlates with the expression of *Rex1* [30]. Conversely, transcription of the early differentiation markers *Fgf5*, *Brachyury* and *Eomes* negatively correlates with *Rex1* expression. When isolated and seeded into culture both Rex1$^+$ and *Rex1*$^-$ cell populations can regenerate the other. *Rex1*$^+$ cells readily contribute to chimeric embryos, whereas *Rex1*$^-$ cells do not, implying that ESC pluripotency favours a *Rex1*$^+$ environment. Indeed, similar conclusions were drawn based on work using another reporter for *Nanog* [26]. ESCs cultured in 2i/LIF, although generally considered more homogeneous in terms of gene expression, also show heterogeneity. In 2i/LIF ESC cultures, the *Hex*-positive fraction is primed to differentiate into trophoblast and extra-embryonic endoderm, indicating the capability of ESCs to contributing to extra-embryonic lineages [31].

These experiments exemplify that ESCs maintain distinct cell sub-populations in culture, and freely convert between these sub-populations (Fig 1.4). Furthermore, these sub-populations exhibit different capacities for pluripotency.

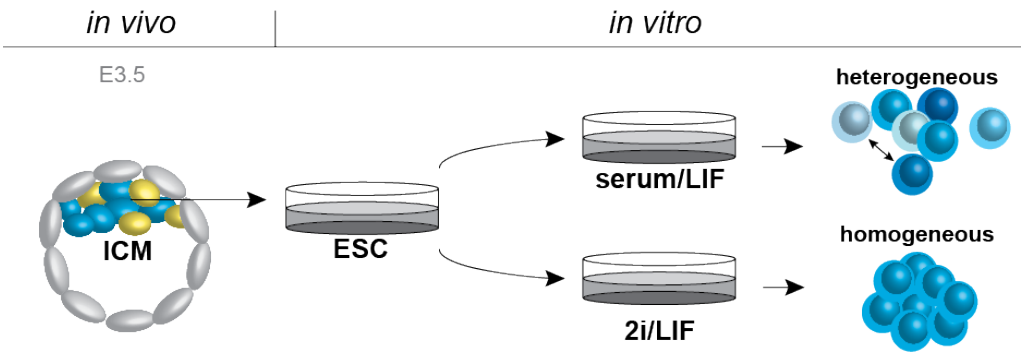


Figure 1.4: Embryonic stem cell heterogeneity *in vitro*.

Embryonic stem cells isolated from the embryo can be cultured under serum/LIf or 2i/LIF conditions, of which the latter generally results in a more homogeneous cell population in terms of epigenetic and transcriptional profile. ESCs grown with serum/LIF are considered to present a more metastable state where sub-populations may be identified, and freely convert between these sub-populations.

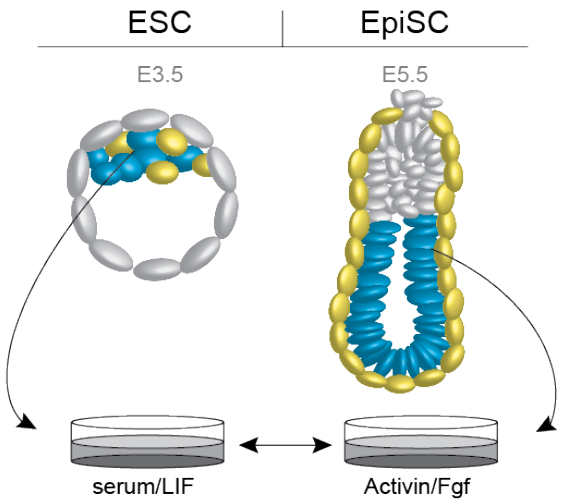
1.3.1.2 Naïve-to-primed stem cell pluripotency

More recently, the derivation of pluripotent stem cell lines from the epiblast of post-implantation stage embryos also proved to be possible [32, 33]. Although epiblast stem cells (EpiSC) are self-renewing and possess similar pluripotent properties of ESCs, they are unable to contribute to chimaeras when introduced into a host blastocyst [34], unless when implanted in the post-implantation stage [35]. Moreover, signalling pathway requirements for the maintenance of their self-renewal ability are different from ESCs, involving Activin/Nodal and fibroblast growth factor (Fgf) signalling as opposed to BMP4 and LIF signalling pathways [36]. Thus, it is considered that ESCs represent an immature or so-called naïve state of pluripotency, which resembles that of the pre-implantation epiblast and is characterized by the ability to give rise to all somatic cell types and germline competency. Conversely, EpiSCs are considered to represent a more advanced state of pluripotency, primed for differentiation (therefore sometimes also referred to as primed ESCs), as seen in the post-implantation epiblast lineage *in vivo*. Of note, in contrast to their *in vivo* counterparts EpiSCs have generally lost the ability of forming the germline [35, 37]. Similarly to ESCs, derivation of EpiSCs from post-implantation E5.5 to E8.5 allows cells to progress to a common self-renewing stage *in vitro* [38]. ESCs and EpiSCs maintain distinct yet overlapping transcriptomes, comprising rewiring of enhancer landscape rather than promoter inactivation (i.e. the same promoters are active however regulated by different distal regulatory regions) [39, 40, 41, 42]. Both cell types express *Oct4*, *Sox2* and *Nanog*, genes identified in ESCs as the foundation of pluripotency [32, 33]. However, key ESC-specific (naïve) genes lose expression in EpiSCs (e.g. *Esrrb*, *Dppa3*, *Klf4*, *Tbx3* and *Rex1*), while genes associated with primed pluripotency gain expression (e.g. *Fgf5*, *Nodal* and *Otx2*) [32, 33]. Additionally, ESCs and EpiSCs display a different epigenetic state, exemplified by a global wave of *de novo* DNA methylation in the epiblast, the occurrence of random X chromosome inactivation [43, 44], and metabolic differences which will be describe later on in the next section. Of note, while it is possible to efficiently differentiate ESCs to EpiSCs upon provision of typical culture conditions (Activin/Fgf) [34, 45], the reverse event, however, is rare, which is possibly due to the epigenetic barrier. EpiSCs can only efficiently convert into ESCs through reprogramming by ectopic expression of naïve factors such as *Klf4* and *Esrrb* [34, 46].

While distinct naïve and primed pluripotent states have been recognised (Fig 5), the progressive nature of development means that a broad continuum of pluripotency likely exists within the developing embryo. A 2D differentiation protocol has been described to investigate the transition from naïve-to-primed pluripotency *in vitro*, in which cells culture in 2i are differentiated upon 2i withdrawal [47]. These experiments illustrated the several remodelling events taking place upon transition from naïve-to-primed pluripotency *in vitro*, including transcriptional- and epigenetic remodelling as well as metabolic remodelling (see next section), leading to the identification of an intermediate pluripotent state named formative [47]. Cellular remodelling events are also taking place, which have been captured using a 3D differentiation assay [4]. This encompassed the formation of polarised rosette-structure and central lumen, closely resembling the epiblast epithelialization and pro-amniotic cavity formation *in vivo* [4]. Interestingly, more

recently, another state of intermittent pluripotency is described [48]. This state is said to emerge rapidly during the transition from naïve-to-primed ESCs *in vitro*, characterized by the high expression of most pluripotency factors, while the expression of other naïve pluripotency factors are already downregulated.

Of note, pluripotent stem cells can also be derived from the human embryo. Although the conventional human ESCs will be more closely related to the primed mouse EpiSC-stage, there is currently a lot of effort to capture the human ESCs in the naïve stage [49, 50].



Gene expression	Esrrb, Tbx3	Fgf5, Otx2
Global DNA hypomethylation	Yes	No
X chromosome inactivation	No	Yes
Capacity for colonization of host pre-implantation ICM and contribution to advanced embryonic chimeras	High	Low

Figure 1.5: Naïve and primed pluripotent stem cell properties.

Stem cells isolated from the pre-implantation inner cell mass (ICM) or the post-implantation epiblast (Epi), give rise to distinct cell lines *in vitro* (i.e. embryonic stem cells (ESCs) and epiblast stem cells (EpiSC) respectively), requiring distinct culture conditions. Several properties can be used to distinguish between these so called naïve (ESCs) and primed (EpiSCs) pluripotent cells, of which few are shown here [51].

1.3.1.3 Cross-talk between pluripotency sustaining factors

As described above, embryo-derived pluripotent stem cell lines are easily manipulated *in vitro* culture, providing an extraordinary tool to decipher the molecular mechanisms that govern self-renewal and the remarkable long-term maintenance of multi-lineage developmental potency. Over the past decades, accumulating evidence highlighted that not one, but multiple regulatory mechanisms cooperate to sustain the unique ESC and EpiSC identities. The general view has been that the integrated action of multiple signalling pathways with complex gene regulatory networks, reinforced by DNA and histone modifiers,

safeguards the self-renewing state while priming gene expression for efficient response to differentiation stimuli [52]. Interestingly, more recently it is increasingly recognized that together with core genetic and epigenetic factors [53, 54], the state of pluripotent stem cells is also influenced by their metabolic profiles (Fig 1.6). Indeed, stem cell metabolism has its role in affecting signalling pathways and epigenetic processes, apart from synthesizing precursors and generating energy for stem cell renewal [55] (Fig 1.6). Therefore, understanding the metabolism of pluripotent stem cells holds promise for understanding early development as well as for regenerative medicine [55]. This PhD further explores stem cell pluripotency from a metabolic viewpoint, therefore pluripotent stem cell metabolism will be described in full detail in the next section.

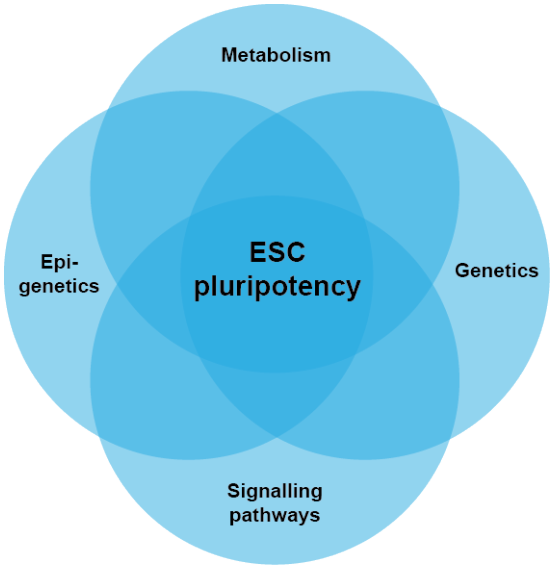


Figure 1.6: Cross-talk between pluripotency regulatory mechanisms.

Gene expression, epigenetics, metabolism and signalling pathways coordinately regulate the pluripotent state of ESCs.

1.4 Pluripotent stem cell metabolism

In its broadest sense, cellular metabolism is essentially a linked series of chemical reactions that begins with a particular molecule and converts it into some other molecule or molecules in a carefully defined fashion [56]. There are many such defined pathways in the cell (Fig 1.7), which are interdependent, and their activity is coordinated by exquisitely sensitive means of communication [56]. Metabolic pathways are divided into two broad classes: [a] those that convert energy into biologically useful forms (i.e. catabolism) and [b] those that require inputs of energy to proceed (i.e. anabolism). The importance of cell metabolism is straightforward in certain contexts, such as building biomass for cell proliferation. However, it might seem less obvious in the contexts of cell-state transitions linked to epigenetic remodelling, specific gene activation or suppression, and signalling pathways. In this section, an overview of the important metabolic processes that regulate pluripotent stem cells will be outlined, starting with an introduction on general cell metabolism.

1.4.1 General cell metabolism

Cellular metabolism involves complex sequences of controlled biochemical reactions, better known as metabolic pathways (Fig 1.7). One of the most conserved pathways to provide an organism with energy is anaerobic glycolysis [56] (Fig 1.7A). During anaerobic glycolysis one molecule of glucose is converted into pyruvate, rendering 2 molecules of ATP and 2 of NADH. Pyruvate is a key cellular metabolite synthesised by this pathway and is a substrate for other metabolic routes [56]. Cells that depend mainly on anaerobic glycolysis for ATP production further convert pyruvate to lactate, which is consequently secreted. This process does not require the availability of oxygen and is therefore preferred in anaerobic environments. Contrary, in an oxygen-rich environment cells may prefer oxidative phosphorylation (OXPHOS) for their ATP production, whereby 34 to 36 additional ATP molecules can be generated per glucose via oxidative conversion of pyruvate into acetyl-CoA, which then enters the mitochondrial tricarboxylic acid (TCA) cycle (Fig 1.7B) and electron transport chain (ETC) (Fig 1.7D). Metabolites derived from glucose and the TCA cycle can additionally be used to synthesize fatty acids or sterols from citrate in the cytoplasm, or to synthesize amino acids from oxaloacetate or α-ketoglutarate. Conversely, acetyl-CoA can also be produced through lipid breakdown and fatty acid β-oxidation (Fig 1.7C), in addition to amino acids which can enter and fuel the TCA cycle at various points. This merely exemplifies how the various metabolic pathways are interconnected, whereas the complete picture is far more complex.

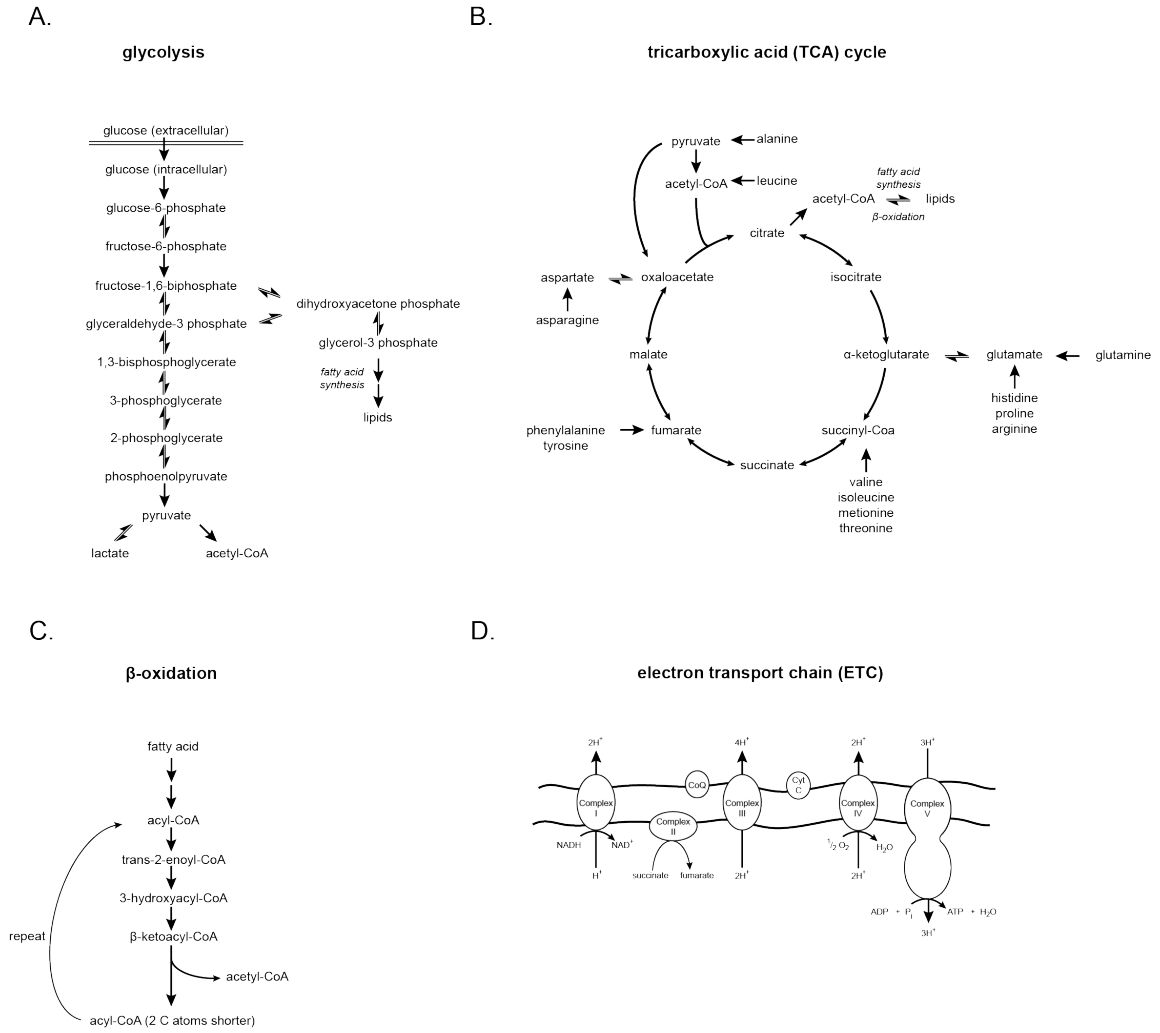


Figure 1.7: Schematic diagrams of key cellular metabolic pathways.

A Schematic diagram of the anaerobic glycolysis. **B** Schematic diagram of the tricarboxylic acid (TCA) cycle. **C** Schematic diagram of β-oxidation. **D** Schematic diagram of the electron transport chain (ETC), with enzymes depicted in circles. Note that in A-C the focus is put on the metabolites, rather then the enzymes (not depicted) which are involved in the transitions.

Pluripotent stem cells mainly produce their energy by the enzymatic conversion of glucose to lactate, in contrast to resting somatic cells that favour OXPHOS [57]. Despite a markedly lower ATP yield per glucose molecule, elevated anaerobic glycolysis in pluripotent stem cells has several key advantages [57]. Increased glycolytic flux fuels the biosynthesis of nucleotides and lipids to support rapid cell replication [57, 58]. Maintaining embryonic integrity requires the reduction of genomic and mitochondrial DNA damage, but also protein and lipid oxidation, from reactive oxygen species (ROS) produced by OXPHOS [57, 59, 60]. Note that upholding embryonic integrity also manifests as heightened apoptosis sensitivity in early embryos, germ cells, and pluripotent stem cells [61, 62]. Besides anaerobic glycolysis and OXPHOS, glutamine also supports pluripotent stem cell survival and expansion by fuelling mitochondrial energy metabolism and increasing antioxidant glutathione [63]. Additionally, robust lipid synthesis is required to replenish membranes and organelles [57].

1.4.2 Metabolism in naïve and primed pluripotency

Substrate usage throughout early development is subjected to crucial changes ensuring successful embryo propagation. Whereas pyruvate is the main source of energy from the zygote to the morula stage, glucose becomes the predominant substrate at the blastocyst stage (Fig 1.8A). Lack of pyruvate in the media of cultured mouse zygotes leads to a two-cell stage arrest [64, 65]. The importance of anaerobic glycolysis to blastocysts is evident *in vivo*, as mutations in four glycolytic enzymes - glucose-6-phosphate isomerase, glyceraldehyde-3-phosphate dehydrogenase, triosephosphate isomerase and lactate dehydrogenase A (LDHA) - result in early post-implantation lethality [66, 67, 68, 69]. Throughout early development OXPHOS rates also increase and oxygen consumption in blastocysts rises up until implantation (Fig 1.8A). Two studies examining single-cell RNA transcriptomes of mouse and human pre-implantation embryos showed the induction of genes controlling OXPHOS during the blastocyst stage of development [64, 70, 71]. These results agree with prior studies that showed blastocysts consuming high levels of oxygen, most likely through mitochondrial respiration [64, 72, 73]. Consequently, upon implantation, the oxidative capacity of the embryo decreases concomitant with the priming of the glycolytic system (Fig 1.8A). This may occur in anticipation of implantation into the hypoxic uterine wall, which stimulates the expression of glycolytic genes and represses those involved in oxidative phosphorylation in the maturing epiblast [74]. As glucose uptake is further accelerated following implantation, virtually all glucose is metabolised to lactate [75]. During later development, mitochondrial replication and maturation into tubular cristae-dense structures supports reinitiating of oxidative metabolism and progressive decline in anaerobic glycolysis. The chronology of metabolic regimes is underscored by embryonic phenotypes that reflect disrupted metabolic processes (see table in [76]). Glycolytic gene mutations precipitate early post-implantation lethality, while defects in oxidative processes, such as pyruvate dehydrogenase mutations or genetic disruption of the mitochondrial transcription factor TFAM, result in developmental delay and/or late onset lethality [76, 77]. These metabolic changes that occur *in vivo* are also reflected *in vitro* (Fig 1.8B).

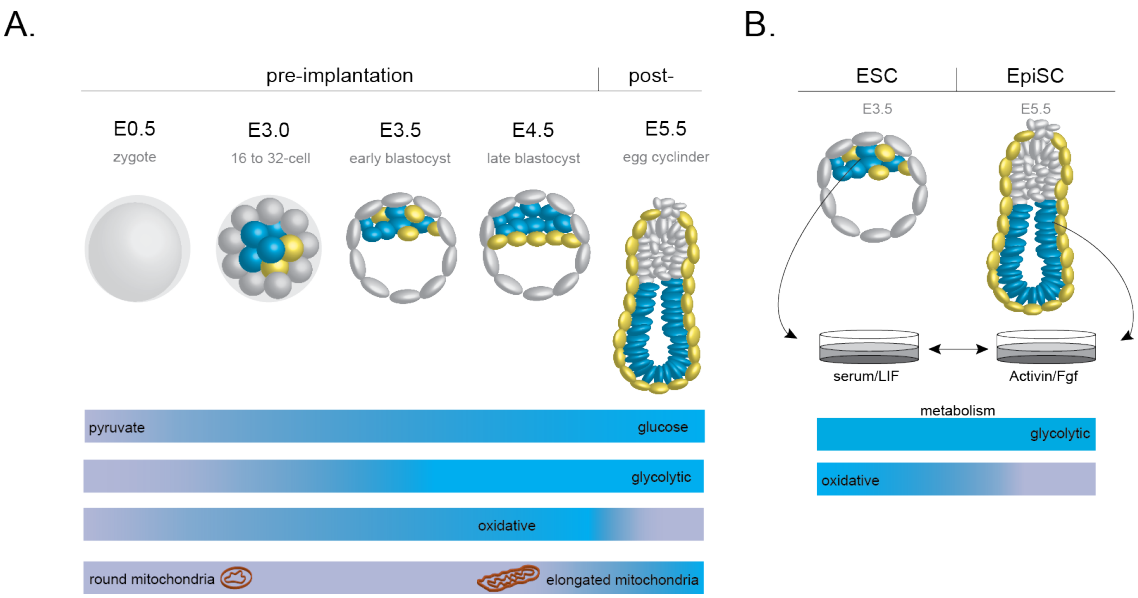


Figure 1.8: Metabolic changes occurring *in vivo* during early development, and *in vitro* ESCs.

A Remodelling of energy metabolism and mitochondria during early embryonic development. A shift from pyruvate as the main energy source from the zygote to the morula stage, to glucose at the blastocyst stage. Upon implantation the oxidative capacity of the embryo decreased and a switch to exclusive anaerobic glycolytic metabolism takes place, which is also reflecting *in vitro* (see **B**). Concomitantly, round mitochondria with low cristae density from the zygote until the blastocyst stage, elongate and mature their cristae organization upon implantation [75, 78].

How does the metabolic dynamics of the *in vivo* developing embryo then reflect that of *in vitro* pluripotent stem cells (Fig 1.8B)? Interestingly, and as seen *in vivo*, a dramatic switch from the capacity to switch from anaerobic glycolysis to mitochondrial respiration on demand, to exclusively anaerobic glycolytic metabolism is suggested to takes place between the two pluripotent stages reflective of the pre-implantation (naïve) ICM and post-implantation (primed) epiblast [74]. Naïve ESCs predominantly employ mitochondrial oxidative metabolism [74, 79, 80], and utilize more glucose and less glutamine. In contrast, EpiSC are mainly relying on anaerobic glycolysis for cellular ATP demand [74, 81], accompanied by glutaminolysis [82]. As highlighted before, ESCs can be cultured in either traditional serum/LIF conditions or chemically defined 2i/LIF media, of which the latter results in a much more homogeneous cell population. Indeed, differences in the metabolic state of serum/LIF and 2i/LIF cultured ESCs have also been described [83]. Here it was shown that differentially expressed proteins were involved in glycolytic metabolism, oxidation-reduction, and amino acid and lipid metabolism [83].

1.4.2.1 Cross-talk between metabolism and other regulatory mechanisms in controlling stem cell states.

It is clear that distinct patterns of metabolic activity associate with specific stages of the early embryo development. This might also potentially imply some level of integration between circuitries that control pluripotency, cell fate commitments and cellular metabolic states. Indeed, accumulating evidence from pluripotent stem cell studies supports the existence of cross-talk between metabolism and epigenetics, transcription programs, cellular signalling and redox homeostasis in the control of stem cell states (Fig 1.9). Each of these integrative examples are illustrated here after.

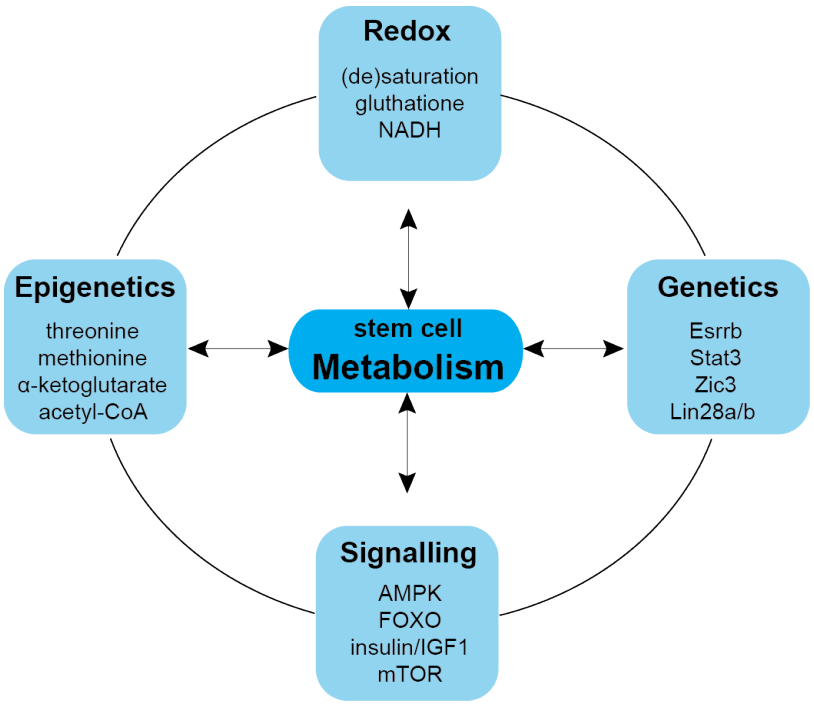


Figure 1.9: Cross-talk between metabolism and other regulatory mechanisms in controlling stem cell states.

Diagram illustrating the existence of cross-talk between metabolism and epigenetics, transcription programs, cellular signalling and redox homeostasis in the control of stem cell states, exemplified by various factors.

Naïve pluripotency is associated with global DNA hypomethylation, whereas primed pluripotency is associated with hypermethylation [84]. Epigenome-modifying enzymes (i.e. DNA methyltransferases) are reliant on metabolites that serve as co-factors. SAM acts as a methyl donor for histone methyltransferases (HMT) as well as DNA methyltransferases. A direct link between the pluripotency state and metabolite-regulated enzyme activity has however not been made. In contrast, glycolysis-mediated acetyl-CoA production is linked to the exit from naïve pluripotency [85]. Threonine and methionine metabolism are both required for S-adenosyl methionine (SAM) generation via the folate cycle in pluripotent stem cells [86, 87], whether this is directly linked to cell fate transitions remains to be investigated. Furthermore, α-ketoglutarate is an important cofactor for demethylation reactions that helps to maintain naïve pluripotent stem cells [88].

A cross-talk between transcriptional regulation and metabolism is just appearing in the field, with few examples supporting this. A transition from naïve-to-primed pluripotent states engages developmental transcription factors *Stat3*, *Esrrb*, *Zic3*, and *Lin28a/b* and provides a link between the metabolic network and transcription program circuitry in the regulation of pluripotency [89, 90, 91]. For naïve-state pluripotent stem cells, *Stat3* sustains the nucleus naïve gene expression profile and also interacts with the mitochondrial genome to activate genes promoting respiration [91]. *Esrrb* induces OXPHOS through an unknown mechanism during the primed-to-naïve-state transition, and it has a similar function during somatic cell reprogramming to pluripotency [89]. It was here reported that *Esrrb* and *Zic3* synergistically enhance anaerobic glycolysis during induced pluripotent stem cell generation, with direct binding of *Zic3* at glycolysis promoting genes where *Esrrb* is consequently recruited. Interestingly, *Zic3* in the absence of *Esrrb* can repress OXPHOS and activate glycolysis to help establish the primed state metabolic profile [89]. *Lin28a/b* regulates anaerobic glycolysis by repressing *let-7*, which targets *Pdk1* [92], and influences by other mechanism OXPHOS gene expression in mouse ESCs [90]. Additionally, to maintain or induce pluripotency, developmentally activated *c-Myc* directly activates glycolysis genes [93, 94]. The hexosamine biosynthetic pathway is a branch of glucose metabolism which produces UDP-GlcNAc, a substrate for addition of O-linked-N-acetylglucosamine (O-GlcNAc) to proteins [95]. This nutrient-sensitive posttranslational modification regulates the transcriptional activity of core pluripotency network members, including *Oct4* and *Sox2* [96]. Reducing this post-translational modification through inhibition of O-GlcNAc transferase or reducing glucose concentrations impairs ESC self-renewal and nuclear reprogramming. Conversely, increasing global O-GlcNAc levels inhibits differentiation, thus again linking metabolic status with fundamental stem cell function [96].

Other cross-talks between metabolism and stem cell regulatory mechanisms have also been established. Nutrient-sensitive signalling pathways that regulate lifespan and energy metabolism, such as those mediated by AMPK, FOXO, insulin/IGF1, and mTOR, impact on stem cell function [97, 98]. Stemness is maintained in *Drosophila* germline stem cell in response to signals of insulin and abundant amino acids, while signal reduction during starvation induces differentiation [99]. In addition, AMPK/mTOR pathway activity is required for post-implantation proliferation of embryonic and extra-embryonic cells *in vivo* [100].

Metabolomic comparison of ESCs and their differentiated progenies identified a global enrichment of unsaturated metabolites (mostly fatty acids) in the pluripotent state [101]. Metabolites with a high degree of structural unsaturation contain a number of carbon-carbon double and triple bonds, which renders them reactive and readily susceptible to oxidative reactions. The unsaturated metabolome may prime ESCs to differentiate in response to oxidative processes, as levels of these metabolites decrease upon differentiation. In support of this concept, inhibition of the eicosanoid pathway in ESCs, which maintains high levels of unsaturated fatty acids, preserves pluripotency, while addition of saturated metabolites (fatty acids and acyl-carnitines) to ESC media supports oxidative metabolism and accelerates lineage specification [101]. Additionally, during differentiation, the ratio of reduced to oxidized glutathione decreases as does the level of NADH, effectively increasing the overall cellular oxidation state [86, 101].

1.4.3 Metabolic switch: is there a role for lipid metabolism in the naïve-to-primed ESC transition?

The switch from flexible metabolism in naïve ESCs to an exclusively anaerobic glycolytic metabolism in primed ESCs (i.e. EpiSCs) is increasingly studied, linking glucose and amino acid metabolism with epigenetics, transcription programs, cellular signalling and redox homeostasis as discussed above. In contrast, lipid metabolism is relative unmentioned as a player in this metabolic remodelling, both *in vitro* and *in vivo*, although it holds great promise as a key contributor. Extensive work done in adult stem cells (i.e. HSC and NSC) shows that a switch to *de novo* lipid synthesis regulates quiescence (i.e. stem cell maintenance), and proliferation and differentiation [102, 103]. Recently, ESCs transition (mouse and human) from naïve to primed state has been characterized by a pronounced difference in stearic acid and cholesterol levels, indicating the occurrence of a major switch in lipid metabolism during this transition [104]. Additionally, the same group showed, in concordance with the significant increase in long carbon chain lipid content in primed (mouse and human) ESCs, an accumulation of lipid droplets in the primed state [104], although the functional significance need to be fully investigated. The role of lipid droplets in mouse embryonic stem cell pluripotency and metabolism will be extensively discussed in this PhD thesis, therefore, the next section will review lipid droplet structure, composition and biogenesis, including lipid droplet-associated proteins and the interaction of lipid droplets with other cellular organelles. Eventually, the current knowledge of lipid droplets in pluripotent stem cells will be reviewed.

1.5 Lipid droplets

What are lipid droplets? Lipid droplets are intracellular organelles that regulate the storage and release of fatty acid-derived esters (Fig 1.10). A multitude of different names have been used in the literature to refer to these cytosolic lipid assemblies. Depending on the biological organisms or cell types in which they were studied, LDs have been referred to as oil bodies (plant seeds), lipid particles (yeast), lipid bodies (animal cells), lipid droplets (animal cells), adiposomes (in mammalian adipocytes), lipid vacuoles (animal cells), and oleosomes (oil seeds) [105]. Currently, the most common term to describe these cytosolic lipid inclusions is “lipid droplets”, although “lipid body” is also frequently used.

1.5.1 Lipid droplet structure, composition and biogenesis

Lipid droplets (LDs) are composed of a neural lipid core (e.g. triacylglycerols (TAGs) and sterol esters (SE)) separated from the cytoplasm by a phospholipid monolayer that mainly consists of phosphatidylcholine (PC) and phosphatidylethanolamine (PE) [106, 107] (Fig 1.10B). While most white adipocytes contain a single LD (unilocular) with a diameter of up to 100 μm, non-adipocyte tissues might contain a much higher number of smaller LDs, generally with a diameter between 0.5 and 1 μm [108] (Fig 1.10A). Biochemical and ultrastructural studies have shown that LDs are formed in endoplasmic reticulum (ER) [109, 110], however a process of maturation is likely to happen whereas the composition of the lipid droplet membrane differs from the ER membrane in terms of lipid composition [111].

LD biogenesis and growth requires biosynthesis of neutral lipids including TAG and cholesteryl esters (Fig 1.10C-D) [112]. TAG synthesis plays an important role in many physiological processes including storage of excess fatty acids and protection against lipotoxicity [113, 114, 115]. There are two major biochemical pathways leading to TAG biosynthesis: the glycerol-3-phosphate (G-3-P) pathway and the monoacylglycerol (MAG) pathway [116]. Both pathways start with the acylation of G-3-P and MAG with fatty acyl-CoA by glycerol-3-phosphate acyltransferase (GPAT) and monoacylglycerol acyltransferase (MGAT), respectively. The two pathways share the final step in TAG synthesis where diacylglycerol (DAG) is converted to TAG in an acylation reaction catalysed by diacylglycerol acyltransferase (DGAT) (Fig 1.10C). The other neutral lipid in LDs, cholesteryl ester, is synthesized by cholesterol from acyl-coenzyme A: cholesterol acyltransferase (ACAT), an enzyme catalysing the esterification of cholesterol [117] (Fig 1.10D). In mammals, ACAT and DGAT exist in two isoforms and are localized to the ER membrane, the site of LD biogenesis. The other enzymes involved in TAG synthesis are also found in the ER membranes including MGAT, GPAT, 1-acylglycerol-3-phosphate acyltransferase (AGPAT) and phosphatidic acid phosphatase 1 (PAP) [118]. Once stored, FAs can be released for use via two distinct pathways, known as lipolysis and lipophagy [119, 120]. Specific lipases, primarily via adipose triglyceride lipase (ATGL) and hormone-sensitive Lipase (HSL), can free TAG-derived metabolites including fatty acids into the cytoplasm [121]. On the other hand, lipophagy refers to a LD-specific autophagy mechanism taking place in acidic lysosomes.

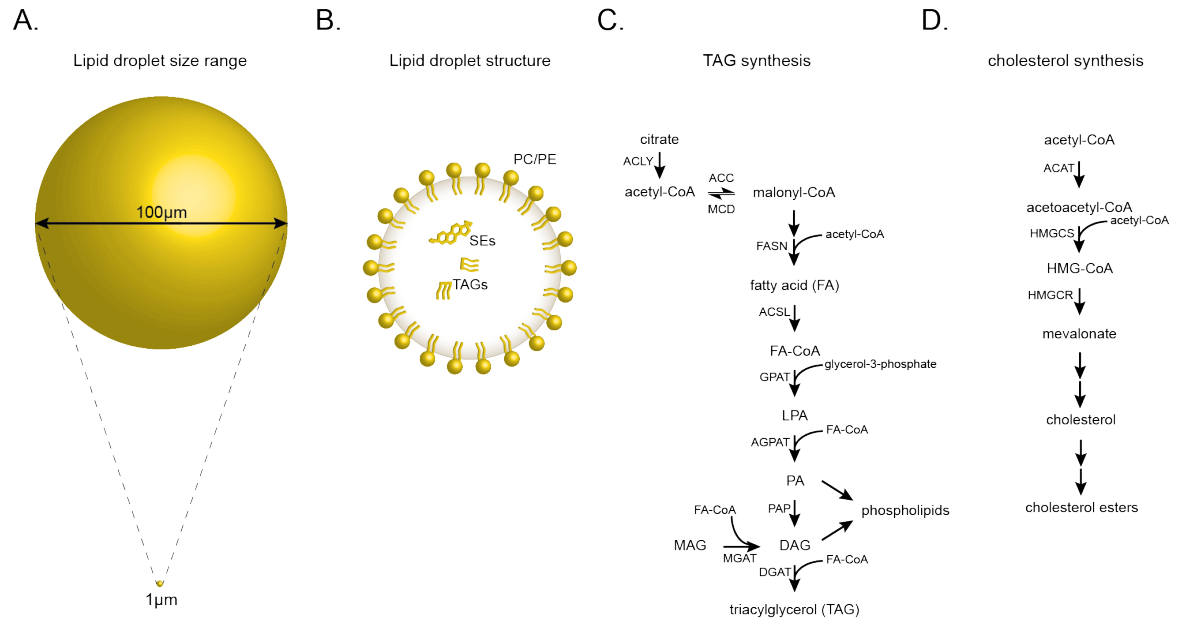


Figure 1.10: Lipid droplet structure, composition and biogenesis.

A Illustrating the droplet size range from a diameter of 100 μm to 1 μm. **B** Illustrating a lipid droplet, composed of a neural lipid core (e.g. triacylglycerols (TAGs) and sterol esters (SE)) separated from the cytoplasm by a phospholipid monolayer that mainly consists of phosphatidylcholine (PC) and phosphatidylethanolamine (PE). **C** Schematic diagram of TAG synthesis. **D** Schematic diagram of cholesterol synthesis.

1.5.2 Interactions of lipid droplets with other organelles

LDs have been reported to undergo heterotypic interactions with other cellular organelles and even homotypic interactions with other LDs [122] (Fig 1.11). These interactions are more prominent in non-adipocytes, since LDs are smaller and more mobile as compared to LDs in adipocytes. To date, LDs have been shown to interact with the ER, mitochondria, peroxisomes, lysosomes, autophagosomes and endosomes [122, 123]. Given that many of these organelles are involved in fatty acid metabolism, such interactions may play important functions in cellular lipid metabolism. For instance, close positioning of LDs with mitochondria facilitates the coupling of TAG hydrolysis to mitochondrial fatty acid oxidation [124]. Interplay between lipid metabolism and autophagy has also been discovered, showing that lipid droplets are engulfed by lipoautophagosomes and transported to lysosomes, where triacylglycerols and other lipids undergo acid lipolysis by lysosomal acid lipase (LAL) [123, 120] (as mentioned before, this is one of the mechanisms to release LD content). In this regard, lysosomes are implicated in LD degradation and recycling of LD lipids [125]. Interestingly, removal of the LD-associated proteins represents the preliminary step that opens up the lipid components of the LD core for degradation (in both lipophagy an lipolysis) [125]. These important LD-associated proteins will be further reviewed in the next section.

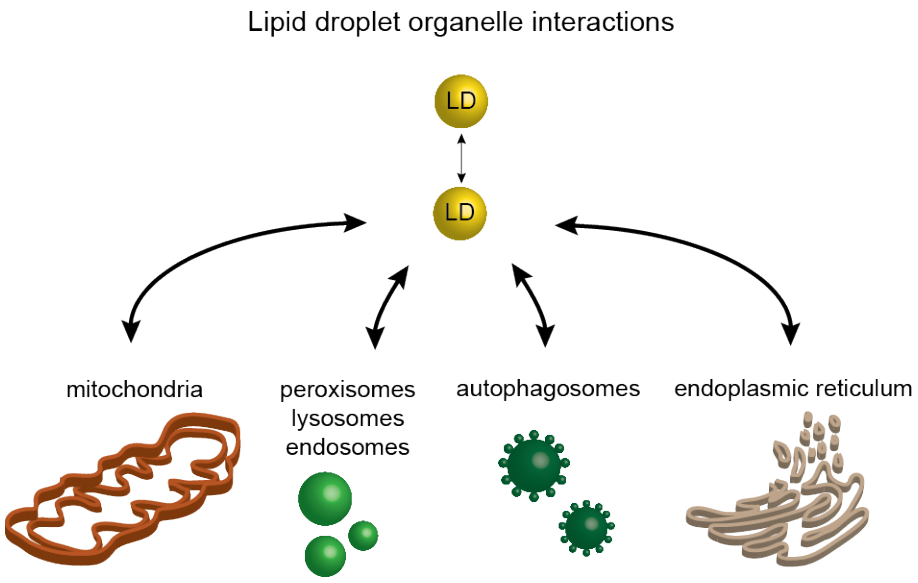


Figure 1.11: Lipid droplet associated organelles.

A schematic of the organelles that have been observed in association with lipid droplets (LDs), including other LDs.

1.5.3 Lipid droplet-associated proteins

LD associated proteins play essential roles in regulating TAG storage and mobilization, as well as interactions with other organelles or other LDs [126]. In this PhD research, we mainly focus on DNA fragmentation factor-alpha-like effector A (Cidea). In brown adipocytes, Cidea and Cidec are known to promote LD enlargement, and together with Cideb form the cell death inducing DNA fragmentation

factor 45 like effector (CIDE) family of LD-associated proteins [127, 128]. Before focussing on Cidea, an overview of prominent LD-associated proteins follows first. In general, proteins appear to access the LD surface either from the ER (e.g. ACSL, GPAT, DGAT, ATGL) the site of *de novo* lipid droplet synthesis, or from the cytosol [129] (Fig 1.12).

Lipid droplet-associated proteins

Class	Examples
ER derived	ACSL GPAT DGAT1 ATGL
PAT family	perilipin ADRP Tip47 S3-12 OXPAT
CIDE family	CIDEA CIDEB CIDEC

Figure 1.12: Examples of classes of LD-associated proteins.

The surface proteins of LDs play multiple roles including LD biogenesis, stabilization, trafficking and mobilisation. The existence of proteins on the surface of LDs was reported for the first time about three decades ago. In 1991, a protein associated with LDs which could be regulated by phosphorylation in response to lipolytic stimuli was identified, this protein was perilipin [130]. Consequently, adipose-differentiation related protein (ADRP) (also known as adipophilin), which shares extensive sequence similarity with perilipin in the amino terminus, became the second protein found to be associated with the surface of LDs [131]. Three additional LD-associated proteins with sequence similarity to perilipin and ADRP were identified hereafter, these proteins are tail-interacting protein 47 (Tip47), S3-12 and myocardial LD protein (MLDP)/OXPAT [132, 133, 134]. The amino acid sequence of Tip47 is 43% identical to ADRP and shows an even higher sequence identity in the amino terminus [132]. Hence, they were grouped as a family called the PAT protein family, named after the three members, perilipin, ADRP and Tip47 [135]. Two additional non-mammalian PAT proteins with conserved sequences in the N-terminus were identified in insects, lipid storage droplet-1 and -2 (LSD1 and LSD2) [136, 137].

Other proteins that are difficult to classify include those that use lipid modifications, such as palmitoylation, as lipid anchors to bind to the LD surface [129]. An example of such protein is Rab18. Interestingly, Rab18 localises to a distinct subpopulation of LDs [138, 139], and negatively correlates with the localisation of (ADRP) [138]. These data suggest that LDs have different protein components, possibly reflecting the functional state of individual droplets [122]. Currently, the full proteomics associated with LDs has been established in different tissues, providing further insights that LD-associated proteins vary between cell and tissue types and typically number in the tens to hundreds [140, 141, 142, 143, 144, 145, 146, 147]. Common among them in mammalian cells are perilipins [148, 149, 150, 151].

In a different context, cell death-inducing DNA fragmentation factor-alpha (DFFA)-like effector (CIDE) proteins including Cidea, Cideb and Cidec/fat specific protein 27 (Fsp27) were first identified by their sequence homology with the N-terminal domain of the DNA fragmentation factor (DFF) [152].

1.5.3.1 Lipid droplet-associated protein Cidea

Human Cidea and Cideb were first identified in 1998 by sequence homology with the N-terminal domain of DFF [152]. Before this report, in 1984, Fsp27/Cidec was cloned after identification as an up-regulated gene by a differential screening approach during adipogenesis of murine TA1 preadipocytes [153]. Subsequently, the human Cidec gene (originally named CIDE-3) was cloned as a homolog of murine Fsp27 and shown to translate into two proteins, a long form (CIDE-3, six exons) and a short form (CIDE-3 alpha, five exons) [154]. All three CIDE proteins possess an evolutionarily conserved CIDE-N domain (N-terminus) sharing homology to DFF and a CIDE-C domain (C-terminus) that is unique among CIDE proteins (Fig 1.13) [155]. The CIDE-N domain of Cidea, Cideb and Cidec possesses homology with DFF45 of 39, 29 and 38%, respectively. Furthermore, the CIDE-C domain of Cidea or Cideb possesses homology with that of Cidec of 54 and 53%, respectively. Mouse Cidea is exclusively expressed in brown adipose tissue (BAT) [156], Cideb is expressed in liver and kidney [153], and Fsp27 in BAT and white adipose tissue (WAT) [157, 158].
In various human cell lines, ectopic-expression of Cidea or Cideb induced apoptosis and DNA fragmentation [152]. It was further revealed that Cideb-induced apoptosis is dependent on caspase-3 activity and release of mitochondrial cytochrome c in COS cells [159]. A caspase-dependent mitochondrial-mediated mechanism is also reportedly involved in Cidea [160] and Fsp27 [161] induced cell death. However, gene targeting studies have now revealed that CIDE proteins are also involved in energy metabolism [156, 162, 157, 158].

Initially, ectopic expression of Cidea, Cideb or Cidec proteins was found to co-localize with mitochondria specific marker (mitotracker), suggesting these localize to the mitochondria. This localization pattern was likely due to the later stage of apoptosis, whereas more recent studies have demonstrated that CIDE proteins localize to LDs and the ER but not mitochondria. Mouse Cidea and Fsp27 share four homology domains with perilipin, the previously mentioned LD-associated protein. These domains include a short N-terminal sequence with shared homology to adipophilin, a segment with homology to a region of perilipin thought to shield LDs from lipases, and two regions thought to function in the targeting and binding of LDs (Fig 1.13) [163, 164]. It was consequently observed that overexpression of Cidea as well as Fsp27 increased the accumulation and size of LDs in 3T3-L1 adipocytes and COS cells [164]. As of now, Mark Christian and colleagues have unravelled in depth the mechanisms by which Cidea establishes this lipid droplet enlargement in adipocytes, which involves the targeting of LDs, the docking of LD pairs, and the transference of lipids between them [127] (Fig 1.14). This study elegantly demonstrated, by using an extensive collection of v5-tagged CIDE point and deletion mutants, the functional importance of the various Cidea protein domains during the LD enlargement process in adipocytes. This led to the observation of various phenotypes, amongst others a phenotype displaying small LDs which grouped in a few large clusters, indicating an abrogated lipid transfer process while LD-LD docking was still efficient. This study also revealed the mechanical importance of the functional domains. Whereas the N-term domain is mainly important in LD enlargement, the C-term domain regulates LD targeting

and localization. In addition, both the C-term and the N-term domain of Cidea can contribute to LD-LD docking, by forming complexes with its counterparts on the adjacent LD.

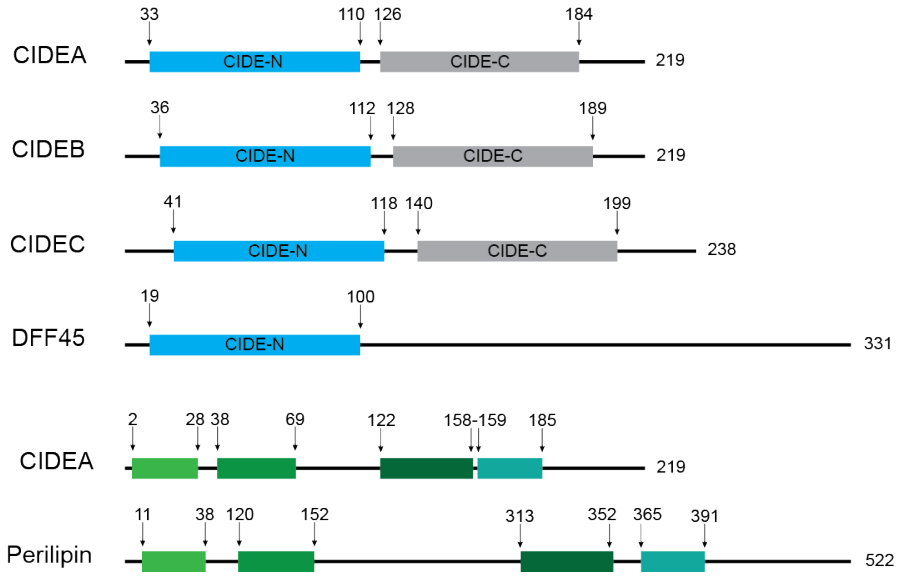


Figure 1.13: Lipid droplet associated organelles.

Cell death-inducing DNA fragmentation factor-alpha-like effector (CIDE) shows sequence homology with the N-terminal domain of DNA fragmentation factor (DFF). Furthermore, four conserved regions were identified between Cidea and Perilipin. From left to right; adipophilin-like sequence; TAG shielding region that plays a critical role for protecting stored TAG from cytosolic lipases, targeting and anchoring lipid droplet regions.

Ever since the discovery of Cidea in 1998, its functional importance has been extensively studied specifically in adipose tissue and liver (Fig 1.14). Cidea gained particular attention as a metabolic target gene after 2003, when the Cidea-null mice was born (Fig 1.14) [156]. The observation that Cidea-null mice were lean with enhanced glucose uptake from the blood by the peripheral tissues and resistance to high-fat diet-induced obesity and diabetes [156], was understandably of great interest for human weight management and metabolic syndromes. Indeed, Cidea (and Cidec) expression in white adipose tissue of obese human subjects was found to correlate positively with whole-body insulin sensitivity (Fig 1.14) [164]. Various studies in this context have confirmed an important role for the Cidea protein in the development of metabolic diseases such as obesity, metabolic syndrome, type 2 diabetes and their vascular complications, therefore Cidea gene and protein are now potential therapeutic targets in the case of these diseases [165]. Cidea is currently also increasingly studied in the context of cancer, either from a metabolic [166] or apoptotic [167] viewpoint (Fig 1.14). In brown adipose tissue (BAT), cold exposure was found to results in a profound increase in Cidea protein levels (independent of transcriptional regulation) [168]. The profound increase in Cidea was coincident with elevated lipolysis and *de novo* lipogenesis [169]. It is therefore likely that Cidea has a central role in coupling these processes to package newly synthesized TAG in LDs for subsequent lipolysis and fatty acid oxidation [127]. The concomitant activation of lipogenesis and fatty acid oxidation has been described in brown adipocytes as well as hepatocytes, linked to thermogenesis and protection against cytotoxic damage respectively [170, 171].

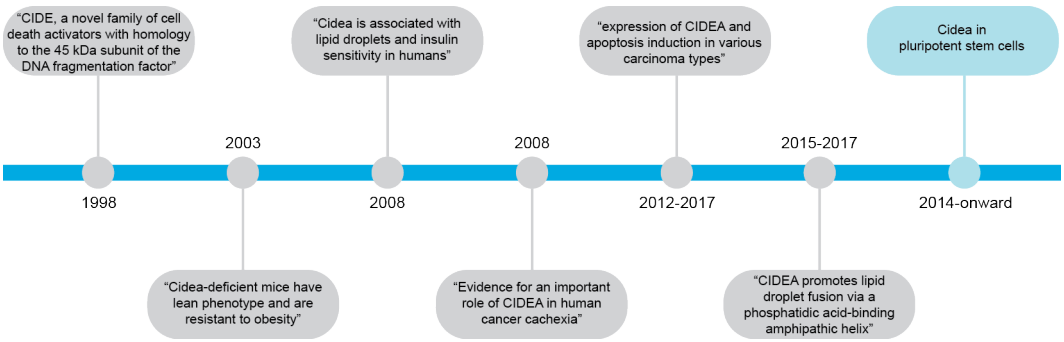


Figure 1.14: Timeline indicating a selection of discoveries about Cidea.

Timeline indicating a summarized overview of selected discoveries about Cidea as describd in full in the text. At the right side of the timeline, indicated in blue, this PhD thesis.

1.6 Hypothesis and Aims

What about lipid droplets in stem cells? A quick PubMed search on "lipid droplets" and "stem cells" retrieved a mere 18 articles, mostly published after 2007. In contrast, "lipid droplets" and "embryo" retrieved almost 300 studies, going all the way back to 1963. These studies revealed that lipid droplets have been observed in the eggs and oocytes of many animals, including insects, spiders, annelids, frogs, fish, marsupials, and placental mammals (Fig 1.15A) [172, 173, 174, 175, 176, 177, 178, 179, 180, 181]. Presumably, lipid droplets were to provide a critical, maternally generated energy source for the developing embryo not yet able to feed (Fig 1.14A). In addition to lipid storage, cleavage stage embryonic lipid droplets were also thought to store specific proteins to support embryogenesis in *Drosophila* (Fig 1.15A) [142, 182]. Another study revealed that *Drosophila* neural stem cell proliferation is reliant on reducing oxidative stress (Fig 1.15A) [183]. Here lipid droplets in the niche glia are indicated as a critical element of the protective mechanism [183]. Additionally, lipid droplet accumulation and profile are suggested to have an important role on tumorigenic properties of cancer stem cells, linking LDs with cancer stemness which is thought to advance tumour progression [184].

Interestingly, lipid droplets have also been detected in the mouse embryo, during the pre-implantation development (Fig 1.15A) [173]. Shankar and colleagues here found numerous small droplets at the morula stage, followed by an increase in size concomitant with a decrease in number during the blastocyst stage [173] (Fig 1.15B). However, the functional significance of lipid droplets as well as the mechanism(s) regulating their enlargement at the blastocyst stage remain to be fully investigated.

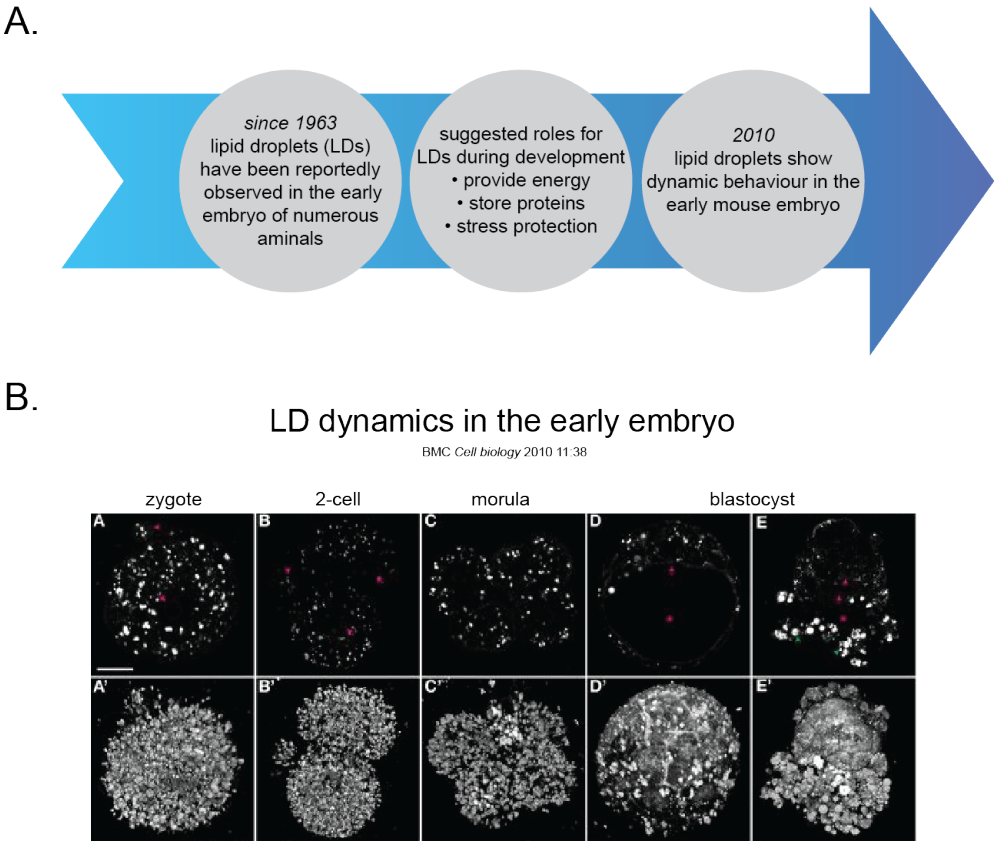


Figure 1.15: Key discoveries regarding lipid droplets in the embryo.

A A summarized overview of the current knowledge on lipid droplets (LDs) in the embryo, as described in the text. **B** LD dynamics in the early embryo, adapted from Shankar and colleagues [173]. Indicating numerous small droplets at the morula stage (C), followed by an increase in size concomitant with a decrease in number during the blastocyst stage (D and E). In white the third harmonic generation (THG) signal coming from LDs. (A - E) Optical sections. (A' - E') Opacity rendered 3D views.

Interestingly, independent evidence in our group suggested that ESCs might also share with brown adipocytes and the early embryo, the ability to dynamically enlarge lipid droplets upon stimulation. Notably, *Cidea* was identified as a potential target of the naïve pluripotency transcription factor *Esrrb* in ESCs [185], suggesting that this factor might be expressed in ESCs where it could potentially play a role in regulating lipid droplet biology and/or apoptosis events. In favour of the biology, it was furthermore revealed that mouse embryonic fibroblast (MEF)-derived induced pluripotent stem cells (iPSCs) established under lipid rich conditions unexpectedly contain a considerable number of large lipid droplets that could be readily detected using the neutral lipid dye BODIPY 493/503. Whether the presence of large lipid droplets was merely the effect of the culture conditions used and/or represented a unique novel hallmark of the pluripotent state remained to be investigated. However, in conjunction with the previous discovery of dynamic behaviour of lipid droplets in the early mouse embryo we were keen to further investigate this interesting observation.

Up until the beginning of this project in 2014, little was known about the biological relevance and mechanisms by which lipid droplets function is conferred in pluripotent stem cells. Thus, the overall aim of this project was to elucidate the role of the lipid droplet-associated protein Cidea in regulating embryonic stem cell metabolism and biology. Notably, we aim at determining if modulation of Cidea expression underlines the formation of enlarged LDs in ESCs and in the early embryo *in vivo*. We will investigate the functional importance of LDs in the context of metabolic remodelling and transition from naïve-to-primed pluripotency upon embryo implantation (Fig 1.16). Additionally, we will explore the existence of distinct metabolic states and lipid signatures underlying the priming of ESCs for differentiation.

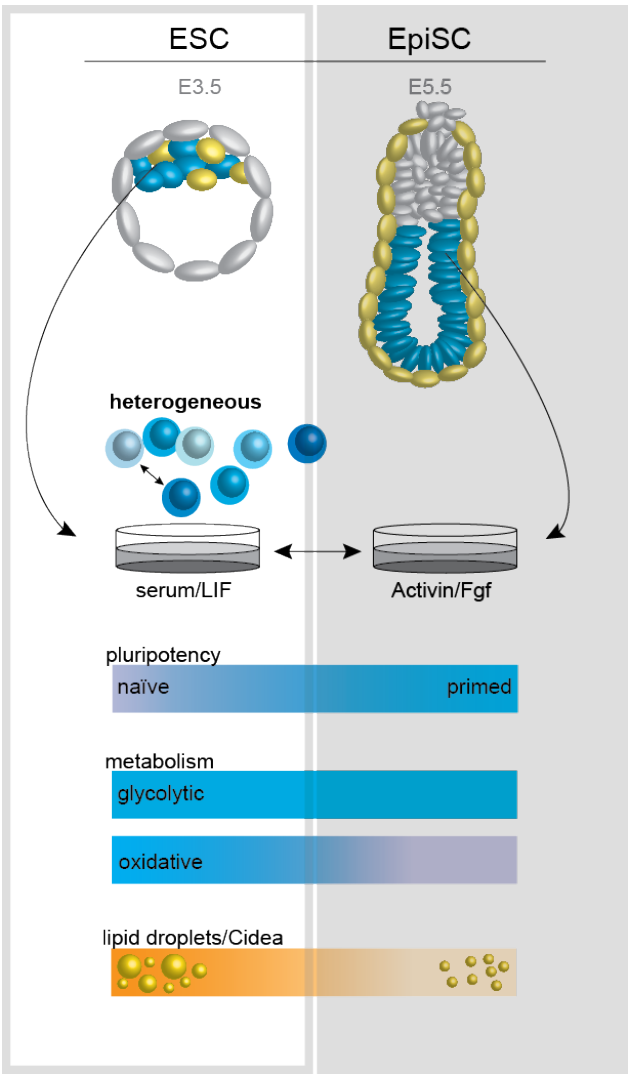


Figure 1.16: Naïve-to-primed pluripotency, a focus on ESCs metabolic properties.

Pluripotent stem cell remodelling from flexible metabolism in ESCs (i.e. being capable of both anaerobic glycolysis and oxidative metabolism to fulfil their energy demands), to anaerobic glycolytic metabolism in EpiSCs. Concomitant with ESCs being metabolically flexible, these cells display *in vivo* and *in vitro* dynamic lipid droplet (LD) enlargement mediated by LD-associated proteins (e.g. Cidea).

Chapter 2

Materials and Methods

2.1 Materials

2.1.1 Antibodies

Primary Antibody	Host species	Catalogue Number	Source	Western Blot	IF
Cidea	mouse	SAB1405623	Sigma	-	1:50
E-Cadherin	rat	U3254	Sigma	-	1:500
Esrrb	mouse	H6705	R&D Systems	1:1000	-
V5	mouse	46-0705	Invitrogen	1:2000	1:1000
Vinculin	mouse	V9264	Sigma-Aldrich	-	-
α-Tubulin	mouse	T6074	Sigma-Aldrich	1:20K	-

Secondary Antibody	Catalogue Number	Source	Western Blot	IF
Alexa488 Goat Anti-Mouse IgG	A11034	ThermoFisher	-	1:500
Alexa488 Goat Anti-Rat IgG	A11006	ThermoFisher	-	1:500
Alexa633 Goat Anti-Mouse IgG	A21052	ThermoFisher	-	1:500
Goat Anti-Mouse IgG-HRP	sc-2004	SantaCruz	1:2000	-
Donkey Anti-Goat IgG-HRP	sc-2020	SantaCruz	1:5000	-

2.1.2 Enzymes

Enzyme	Catalogue Number	Source
RNase Out	10777-019	Lifetechnologies
Superscript II Reverse Transcriptase	18064014	Lifetechnologies
Superscript III Reverse Transcriptase	18080044	Lifetechnologies
SYBR Green Taq Kicqstart Polymerase	KCQS02	Sigma-Aldrich

2.1.3 Kits

Kits	Catalogue Number	Source
Amersham ECL Prime Western Blotting Detection Reagent	25080060	GE Healthcare
Seahorse XF24 FluxPak mini	100867-100	Agilent Technologies
RNAeasy mini	74106	Qiagen
RNase-Free DNase Set (50)	79254	Qiagen

2.1.4 Inhibitors

Inhibitor	Working Dilution/ Concentration	Catalogue Number	Source
Phenylmethylsulfonyl fluoride (0.1M)	1:1000	93482	Sigma-Aldrich
Complete Protease inhibitor tablets (50x)	1:50	11697498001	Roche
Sodium Fluoride (NaF)	5mM	201154	Sigma
Sodium Orthovanadate (Na_3VO_4)	2mM	S6508	Sigma
Etomoxir	40mM	E1905	Sigma-Aldrich
2-DG	50mM	103020-100	Agilent Technologies
Oligomycin	1-2.5μM	103020-100	Agilent Technologies
Rotenone	2μM	103010-100	Agilent Technologies
Antimycin	2μM	103010-100	Agilent Technologies
FCCP	0.4uM	103010-100	Agilent Technologies

2.1.5 Media supplements

Supplement	Working Dilution/ Concentration	Catalogue Number	Source
AlbuMAX II Lipid-Rich BSA	0.2%, 1% or 5%	11021-029	Lifetechnologies
LIF	Batch-dependent	-	In house
D-(+)-Glucose	4.5g/l	G8270	Sigma-Aldrich
D-Glucose-13C6	4.5g/l	389374	Sigma-Aldrich

2.1.6 Reagents

Reagent	Source
Acetone	Fisher Scientific
Acrylamide/Bis Solution	Biorad
Ammonium Persulfate (APS)	Sigma-Aldrich
Bovine Serum Albumin (BSA)	PAA
DAPI	Sigma
Deoxynucleotide Triphosphate (dNTPs) 10mM	Lifetechnologies
DEPC-Treated Water	Ambion
Dimethyl Sulfoxide (DMSO)	Sigma-Aldrich
Ethanol	Fisher Scientific
Formaldehyde Solution, 37%	Sigma-Aldrich
Isopropanol	Fisher Scientific
Laemmli Sample Buffer	BioRad
LB	MP Biomedicals
Lipofectamine 2000 Transfection Reagent	Lifetechnologies
Magnesium Sulphate ($MgSO_2$)	Novagen
Methanol	Fisher Scientific
Normal Goat Serum	Sigma-Aldrich
Oligonucleotides	Lifetechnologies
Paraformaldehyde (PFA)	Sigma-Aldrich
Chloroform	Sigma-Aldrich
PVDF Membrane	GE Healthcare
Random Hexamers	Lifetechnologies
Seahorse XF Assay Medium	Agilent Technologies
SDS-PAGE Resolving Buffer	Biorad
SDS-PAGE Stacking Buffer	BioRad
Skimmed Milk Powder	Fluka
Sodium Azide (NaN3)	Sigma-Aldrich
Sodium Dodecyl Sulfate (SDS) Solution 10%	Fluka
Tetramethylethylenediamine (TEMED)	Sigma-Aldrich
Triton X-100	Sigma-Aldrich
Vectashield with DAPI	Vector Laboratories
β-Mercaptoethanol	Sigma-Aldrich

2.1.7 Solutions

Alkaline phosphatase staining	
AP fixation solution	25.5%(v/v) Citrate solution
	66.3%(v/v) Acetone
	8.2%(v/v) Formaldehyde 37%
AP staining solution	1.9%(v/v) Na-Nitrite
	1.9%(v/v) FRV-alkaline
	94.3%(v/v) dH_2O
	1.9%(v/v) Naphthol Alkaline
Immunofluorescent staining	
PFA 4%	4% (w/v) Paraformaldehyde in PBS
	2mM NaOH
Blocking Buffer	90%(v/v) PBS
	10%(v/v) serum (same species as the secondary antibody)
Permeabilization Buffer	0.4% TritonX-100
	in Blocking Buffer
Western blot	
RIPA Buffer	50mM Tris pH 8.0
(Total Protein Extraction)	1mM EDTA
	0.5mM EGTA
	1% (v/v) Triton X-100
	0.1% (w/v) Na-deoxycholate
	140mM NaCl
	Freshly supplemented with protease and phosphatase inhibitors.
10% Resolving gel	375mM Tris HCl pH 8.8
	10% (w/v) Acrylamide/Bis
	0.1% (w/v) SDS
	0.05% (w/v) Ammonium Persulfate
	0.005% (v/v) TEMED
4% Stacking gel	125mM Tris HCl pH 6.8
	4% (w/v) Acrylamide/Bis
	0.1% (w/v) SDS
	0.05% (w/v) Ammonium Persulfate
	0.01% (v/v) TEMED
SDS Running Buffer	25mM Tris base
	190mM Glycine
	0.1% (w/v) SDS
Transfer Buffer	25 mM Tris,
	192 mM glycine
	0.01% (w/v) SDS
	10% (v/v) methanol for proteins >50KDa
	or 20% (v/v) methanol for proteins <50KDa
TBS-T	130mM NaCl
	20mM Tris pH 7.6
	0.1% (v/v) Tween-20

2.1.8 Media

Cell line	Media Composition
ESC E14 media	GMEM- BHK21 supplemented with: 10% (v/v) Batch tested FBS 0.1mM β-Mercaptoethanol 0.24% (w/v) Sodium Bicarbonate 1mM Sodium Pyruvate 0.1mM Non-essential Amino Acids 2mM L-Glutamine 25U/mL Penicillin 25μg/mL Streptomycin Optimized dilution of LIF
MEF/COS-7 media	DMEM supplemented with: 10% (v/v) FBS 0.1mM 2-Mercaptoethanol 2mM L-Glutamine 25U/mL Penicillin 25μg/mL Streptomycin

2.1.9 Cell lines

Cell Line	Genetic Background	Information
E14Tg2A	129/Ola	Feeder-independent *Hprt*-deficient mouse ES cell line derived from Lesch-Nyhan embryos [186].
R1	129X1 x 129S1	Feeder-independent, germline-competent, wild type cell line derived from 129 sub-strain.
MEF	CF-1	Primary culture of mouse embryonic fibroblasts derived from CF-1 mice.
COS-7	CV-1	Derived from monkey kidney tissue cell line CV-1 by transformation with an origin defective mutant of SV40 which codes for wild type T antigen [187]

2.2 Methods

2.2.1 Cell culture

In this work, various embryonic stem cell lines were used harbouring the wild type (WT) backgrounds E14Tg2A (E14) or R1. Cells were culture in their respective media as described below at 37°C under 5% CO_2. ESCs were cultured feeder-free on plates coated with 0.1% gelatin and passaged 1:5-1:10 every other day. Media was replenished every day. In general, all stem cell lines were not used beyond 45 passages. Cells and media were manipulated in a laminar flow cabinet under aseptic conditions. All cell lines used in experiments were routinely tested negative for the presence of Mycoplasma infections.

2.2.1.1 Embryonic stem cell culture

Mouse E14Tg2A (E14) and R1 embryonic stem cells (ESCs) were grown and maintained in an undifferentiated state in either GMEM-BHK21 medium plus 10% fetal calf serum, or when indicated in serum free

conditions plus 15% Knockout Serum Replacement (KSR). GMEM-FBS and GMEM-KSR, also referred to as E14-FBS or E14-KSR, were both supplemented with Penicillin/Streptomycin (P/S), L-Glutamine, Leukaemia Inhibitory Factor (LIF), Nonessential Amino Acids (NEAA), Sodium Pyruvate, Sodium Bicarbonate and β-Mercapethanol (Section 2.1.8 Media). For passaging, ESCs were dissociated into single cells with Trypsin for 3 minutes at 37°C, after being washed with DPBS. Trypsin was inactivated by dilution and cells suspensions were collected and centrifuged for 5 minutes at 1000rpm.

2.2.1.2 Derivation of knockdown, overexpression and knockout cells

Transfection of ESCs was performed with Lipofectamine 2000 (Lifetechnologies) in accordance with the manufacturers protocols. Here we used pLKO.1-puro (Sigma) vector (containing an insert encoding for shRNA constructs specific for Cidea), as well as with the mCidea-v overexpression construct (cloned into pPy-CAG) [188]. For the generation of stable clones expressing the desired vectors, 400,000 E14 ESCs were seeded in a 100mm dish and incubated in E14-FBS media without antibiotics for 5h at 37°C prior to transfection. For each dish, 6.4μg pDNA and 20 μl Lipofectamine 2000 were diluted in 1.6ml OptiMEM and added to the culture media. 24h after transfection, cells were incubated in E14-FBS media with puromycin 1.0 μg/ml, and maintained in these selection conditions for 7 days. Selected colonies were picked and transferred into individual wells for clonal expansion. Knockdown and overexpression was confirmed by real-time qPCR and western blot respectively.
Cidea knockout was generated in R1 ESCs by means of the CRISPR/Cas9 technology. Therefore we used two plasmids, Px458 and Px459 (Fung Zheng), each containing one CRISPR guide RNA (gRNA), targetting the first intron and last exon of Cidea gene respectively. Electroporation was consequently used to transfect R1 ESCs, followed by the generation of single cell derived clonal cell lines and confirmation of the KO phenotype by PCR an RT-qPCR.

2.2.1.3 Clonal isolation and expansion

Large- and small lipid droplet (LD) clones were isolated from E14-ESC line. E14-ESCs were seeded at a low density (4,000 cells/well) on 0.2% gelatin-coated 100mm dishes, cultured in FBS medium and maintained under normal cell culture conditions. After 8 days, individual clones were isolated based on their LD content as visualized under phase contrast microscopy. All clones were expanded in FBS medium and frozen at early passages (p3-p4). Their differential LD content was confirmed using BODIPY 493/503 staining and confocal imaging.

2.2.1.4 Cryopreservation

All cell lines were routinely frozen in their respective media supplemented with 10% DMSO and 50% FBS and stored in cryogenic tubes which were transferred into a Mr Frosty Freezing Container and kept at -80°C for up to a month before moved indefinitely into N2 liquid. All cell lines were thaw by placing the cryogenic tube in a 37°C water bath for 2 minutes, and subsequent dilution of the cell suspension by 10 times with plain media. Cells were centrifuged for 5 minutes at 950rpm and seeded in their respective

conditions. Media was replenished the next morning to eliminate dead cells.

2.2.1.5 Production of leukaemia inhibitory factor

The leukaemia inhibitory factor (LIF), a key component of mouse ES cell media, was prepared in-house. The monkey kidney cell line COS-7 was used as a host for the production of this component. COS-7 cells were cultured in COS-7 media for one passage, after which cells were expanded in 20x10cm plates in 10ml of E14 media in the absence of LIF. When cells reached 70% confluency 24μg of LIF-expressing vector were delivered per plate following the procedures described in 2.3.3. After 24h the media of each plate was collected and replenished with fresh 10ml of E14 media (minus LIF) per plate. After 24h the media was again collected and the 2 batches mixed together, filtered, aliquoted and stored at -20°C. The optimal dilution of each batch produced was determined by titration and comparison with the previous batch and a commercially available batch of LIF. Cells plated at low density were cultured in the presence of the three batches of LIF and their undifferentiated state evaluated following alkaline phosphatase staining (Section 2.2.2.2 Self-Renewal Assay).

2.2.2 Phenotypic characterization of embryonic stem cells

Phenotypic characterization of manipulated and WT ESC was performed using various wet lab and computational methods.

2.2.2.1 Growth Curve

To access the growth rate of ESC lines, 300,000-500,000 cells (per well) were plated in FBS-containing medium supplemented with LIF, in a 6-well pre-coated with 0.1% gelatin. After 48h the cells were dissociated to single cell level with Trypsin and the total number of cells counted using a haemocytometer. Subsequently, the initial number of cells (300,000-500,000) was re-plated in a new well. The same procedure was repeated over 8 passages and the media replenished in between. The total number of cells at each passage was determined by multiplying by the previous passage.

2.2.2.2 Self-renewal assay

Cells were seeded at a low density (1,000 cells/ml) in 6-well plates coated with 0.1% gelatin. The medium was changed every day during the experiment. After 7-8 days, cells were stained for alkaline phosphatase (AP), which is a marker of undifferentiated cells, using the Alkaline Phosphatase Staining kit (86R-1KT, Sigma), following the manufacturers protocol. Stained colonies were counted and categorized as undifferentiated, mixed or differentiated based on AP staining intensity and colony morphology.

2.2.2.3 Luciferase reporter assay

ESCs were plated 5 hours prior to transfection at a density of $2x10^4$ cells per well in gelatin-coated 96-well plates. ESCs were transfected with Lipofectamine 2000, and 20ng/well luciferase vector, 10ng Renilla or GFP (used to normalize for transfection efficiency in each well) and 20-40ng expression vector. RNAi

constructs, where added, were at 30-40ng/well (shRNA) or 2.5-3pmol/well (siRNA). Transfection mix was removed from cells 16 hours post-transfection and exchanged for normal media, or media supplemented with ligand or inhibitors where indicated. Cells were harvested 48 hours post-transfection to assay for Firefly luciferase activity using the Steadylite Plus Kit (PerkinElmer), according to manufacturers guidelines. GFP fluorescence was read prior to lysis in Steadylite Buffer. GFP and luciferase were both read on a Wallac Victor microplate reader.

2.2.2.4 Chromatin immunoprecipitation

Chromatin immunoprecipitation was carried out with chromatin prepared from ESCs as previously described [185]. For all procedures, protease inhibitor cocktail, PMSF (1:1000), NaF (1:200) and Na $_3VO_4$ (1:50) were added to swelling and sonication buffers to prevent protein degradation. ESCs cultured in 175cm^2 flasks were first washed in PBS then fixed with 1% (v/v) formaldehyde at 37°C, 10 min. The reaction was quenched by addition of glycine to 1.25M final concentration and incubated at RT, 5 min. Fixed cells were washed three times in cold PBS then placed on ice with 5mL swelling buffer, 10 min. Cells were scraped, homogenized in a douce homogenizer and centrifuged to pellet cells and the pellet resuspended in 2mL sonication buffer. Sonication was carried out in a Bioruptor Sonicator at 4°C for 60 min total in pulses of 30 sec, generating DNA fragments of 400-1000bp. Sonicated DNA was centrifuged at 16000xg, 10 min to pellet insoluble material with the resultant supernatant then collected and used for immunoprecipitation (IP) or stored at -80°C for future use.

2.2.2.5 Lipid droplet staining and quantification

125,000 cells/well were seeded on 0.2% gelatin-coated glass coverslips in 24-well plates. Cells were either grown in one type of culture media for 48 hours, or grown in E14-FBS for 24 hours followed by a media swap for another 24 hours. Thereafter, cells were fixed with 4% paraformaldehyde in PBS (300μl/well) for 10 minutes at room temperature (RT). Then, cells were washed 3 times with PBS and LDs were stained by incubating cells for 15 minutes in a dark place at RT with BODIPY493/503 (1 μg/ml) in PBS. Hereafter, cells were washed 3 times with PBS and finally the coverslips were mounted on slides with Prolong Gold Antifade mounting medium with DAPI (Invitrogen) and examined under a Leica SP5 confocal microscope. For quantification of the LDs, slides where examined under a Nikon E400 Eclipse microscope. Consequently, for each condition, at least fifteen colonies where automated counted by CellProfiler 2.1.1 using an in-house script provided by Dirk Dorman.

2.2.2.6 RNA sequencing

RNA sequencing was performed in collaboration with Dr Mark Christian and Dr Yi-Wah Chan, Warwick University. Total RNA was extracted by the RNeasy protect mini kit (Qiagen) and RNase-free DNase (Qiagen) for digestion of residual DNA, according to the manufacturer's specifications. Two micrograms of total RNA was used for the library preparation of each sample. The libraries were clustered via Illumina paired-end RNA sequencing. Transcriptome alignments were generated by Source BioScience (Tophat

v.2.1.0) from first strand paired-end RNA-Seq sequence data using the University of California Santa Cruz (UCSC) mm10 2013 reference transcriptome (Illumina iGenomes resource) and an inner-mate distance of 100. Count data was obtained using HTSeq-0.6.1. Differentially expressed genes were detected using three different methods: Cuffdiff2 v.2.2.1 and the count-based methods DESeq2 v.1.12.3 and EdgeR v.3.14.0. Median gene lengths for mm10 were obtained using the getlength() function from goseq v1.24.0, which were subsequently used to calculate transcripts per million (TPM) expression values from the read count data. Spearman correlation analysis was performed using R to show reproducibility between biological replicates. Principal component analysis (PCA) was performed in R using prcomp() using the TPM data.

To identify differentially expressed pathways amongst the significantly differentially expressed genes, limmas [189] geneSetTest() function was used in conjunction with the meta-database ConsensusPathDB (CPDB, http://cpdb.molgen.mpg.de/MCPDB) was used. GeneSetTest was run with both the DESeq and CuffDiff differential expression t-statistics. The resulting P-values were corrected for multiple hypotheses testing using the Benjamini-Hochberg method. A summary P-value was generated using Fishers combined P-value [190].The presented P-values represent the probability of finding the specific subset of genes from a certain pathway in a random set of genes drawn from the complete gene list. Consequently, heat maps where generated from genes in selected pathways, comparing two groups as indicated.

2.2.2.7 Motif analysis

Motif enrichment was performed using AME in the MEME suite. Using an AME analysis of stored motifs from the JASPAR CORE VETEBRATE database we searched for transcription factor motifs that may be selectively enriched at the target site of interest. Running the peak sequences against a shuffled background we confirmed whether motifs were consistently enriched at the target site.

2.2.3 Metabolic characterization of embryonic stem cells

2.2.3.1 Gas chromatography-mass spectrometry

Metabolites were extracted from E14 and individual ESC clone cell pellets using a dual phase extraction as described elsewhere [191]. Sample preparation order was randomized, and 300 μl of chloroform/methanol (2:1) was added to each tube containing the frozen cell pellet. Samples were vortex mixed for 30 s, and 300μl of UHPLC-grade water added, before vortexing again for another 30 s. The samples were consequently centrifuged (14000 rpm, 10 min), and the aqueous and organic layers removed to separate sample tubes. The extraction was then repeated to maximize metabolite recovery, and the aqueous and organic layers were pooled with the samples obtained from the first extraction. All samples were dried for 12h in the fumehood to remove any organic solvent. The organic were stored (80°C) in this dried state, and the remaining solvent was removed from the aqueous samples by freeze-drying. The GC-MS analysis was performed on an Agilent Technology 7890A. Following the addition of 10μl of Myristic acid d27 as a standard solution to each sample vial, the samples were dried in a centrifugal evaporator. The aqueous fraction was supplemented with 20μl Methoxyamine (20 mg/ml) dissolved in anhydrous pyridine

(Merck AG) before incubated at 30°C for 90 minutes. Metabolite data was processed with MATLAB using an in-house script (GAVIN22) provided by Volker Behrens and Greg Tredwell. The identity of the metabolites was assigned with the Automated Mass Spectral Deconvolution and Identification System (AMDIS) based on in-house databases and FiehnLib.

2.2.3.2 Nuclear magnetic resonance

Culture medium samples were kept frozen in eppendorfs in -80°C freezers after sample harvesting, and samples were prepared into NMR tubes on the day of the spectroscopic analysis. After the samples were thawed, they were kept on ice. 550 μl of the medium sample was transferred into a new eppendorf, and 50 μl of internal standard DSA (4,4-Dimethyl-4-silapentane-1-ammonium trifluoroacetate) in D_2O (11.6mM) was added into the sample as a quantitation reference. The mixture was then pipetted into a standard 5mm NMR tube.

2.2.3.3 Determination of oxygen consumption rate and extracellular acidification rate

To determine the oxygen consumption rate (OCR) and the extracellular acidification rate (ECAR), 50,000 ESCs were seeded into each well of a Seahorse XFe24 cell culture plate, coated with 0.2% gelatin, cultured for 16h. The next day, the medium was changed to pre-warmed Seahorse Assay medium and OCR determined according to the manufacturers instructions using the Seahorse XF Cell Mito Stress Kit (Seahorse Bioscience, North Billerica, MA, USA). Basal respiration was measured in unstimulated cells during three cycles of measurement. Afterwards, Oligomycin (1μM) was added to quantify ATP production followed by carbonyl cyanide-4-(trifluoromethoxy)phenylhydrazone (FCCP; 0.4μM) injection to assess maximal cellular respiration (respiratory capacity). Finally, Antimycin A and Rotenone (2μM) treatment revealed the amount of non-mitochondrial respiration. Basal ECAR was measured in unstimulated cells initially starved of glucose as there is no glucose present in the Seahorse XF Base Medium, during three cycles of measurement. Afterwards, glucose (2.5mM) was added to determine the glycolytic flux, followed by Oligomycin (2.5μM) injection to assess the maximal glycolytic capacity. The final injection is 2-deoxy-glucose (2-DG) (50mM), a glucose analog, that inhibits glycolysis through competitive binding to glucose hexokinase, the first enzyme in the glycolytic pathway, revealing the non-glycolytic acidification rate.
For quantification, cells where fixed in the Seahorse plate and stained for DAPI. Seahorse plates were scanned on a fully automated Olympus IX70 microscope. Images of the individual wells were stitched together and total DAPI fluorescence was automatically measured in a large circular region in each well. In addition, to correct for difference in cell growth, the growth rate (Section 2.2.2.1 Growth Curve) of ESC lines was determined before any Seahorse experiments.

2.2.4 Embryonic stem cell differentiation

2.2.4.1 Embryoid body formation

ESCs growing in routine culture were mobilized with Trypsin and counted. After resuspended, 100,000 cells (each well) were seeded on 6-well ultra-low attachment plate (Corning, USA) in medium with 5% FBS and no LIF. EBs were pictured and collected at day 3, 6 and 9 after the seeding day, with half of the media being replenished every day. Collected EBs were lysed for RNA extraction.

2.2.4.2 3D differentiation assay

ESCs growing in routine culture were mobilized with Trypsin and pelleted by centrifugation for 5 min/1,200 rpm, washed with PBS, and repelleted. The pellet was resuspended in matrigel (BD, 356230) by pipetting to single cells. The cell suspension was plated on ibiTreat microscopy plastic μ-plates (Ibidi) or on 8-well glass chamber slides (Lab-Tek) and incubated for 23 min on 37°C until the matrigel solidified. The plate was then filled with prewarmed medium (E14-GMEM) supplemented with 15% FBS.

2.2.5 *In vivo*

2.2.5.1 Embryo dissection

Embryo dissection was done under the supervision of Christophe Royer in the lab of Shankar Srinivas (Oxford University). Mice were housed in a 12 hour dark, 12 hour light cycle. CD1 females were crossed with CD1 males to obtain stage specific embryos. Noon of the day of finding the mating plug was designated 0.5 dpc. Eight embryos were dissected in M2 medium (Sigma M7167). All experimental procedures complied with Home Office regulations and were approved by a local Ethical Review Committee.

2.2.5.2 Embryo staining and lipid droplet quantification

Dissected embryos were washed in PBS and fixed in 4% paraformaldehyde (PFA) for 15 minutes. Fixed cells were permeabilised with 0.1% Triton X-100 in blocking buffer (Section 2.1.7 Solutions), for 15 minutes at room temperature. After washing with PBS, the suspended embryos were incubated with primary antibody diluted in blocking buffer overnight at 4°C. Embryo suspension was washed in PBS and incubated with the fluorophore-conjugated secondary antibodies diluted in blocking buffer overnight at 4°C. Consequently, embryos were washed in PBS and individually mounted in Vectashield with 1μg/ml DAPI on a glass slide prepared with tape to create a small chamber in order for the embryo not to be crushed. Embryos were imaged using Zeiss LSM710 confocal microscope, at an axial step-size of 0.5-1.0μm. A minimum of 6 embryos were stained at each stage. Image analysis, 3D rendering, calculation of LD size and number were done using Volocity software.

2.2.6 Quantitative reverse transcriptase PCR

2.2.6.1 RNA extraction

RNA extraction was performed using RNeasy Mini kit following the manufacturers instructions. For RNA extraction of adherent cultures, 350μl of RLT buffer supplemented with 1% (v/v) 2-Mercaptoethanol, were added to each well of cells washed with DPBS and the lysates collected and frozen at -80°C until extraction. For RNA extraction of suspension cultures (EBs), cells were collected and pelleted by centrifugation, before the same procedure above was applied. In brief, compete lysis was achieved by pipetting and vortexing the cell suspension in RLT. The lysates were mixed with 1 volume of 70%(v/v) ethanol and transferred into a MinElute spin column. Columns were centrifuged at 10.000rpm for 1 minute and flow-through discarded. Columns were washed with 350μl of Buffer BW1 and contaminant DNA was removed by incubation with 10μl DNAse I diluted in 70μl of buffer RDD, at room temperature for 20 minutes. After a second wash with 350μl of Buffer BW1, columns were washed twice with 500μl Buffer RPE. RNA was eluted from the columns with 30μl RNase-free water. Concentration was measured in a NanoDrop 2000 spectrophotometer and RNA samples stored at -80°C.

2.2.6.2 cDNA synthesis

Between 0.5 and 1μg of total RNA were reverse transcribed using Superscript FirstStrand Synthesis kit. RNA was mixed with 1μl of 10 mM dNTP mix and 1 μl of oligo (dT)1218 and diluted in RNase-free water to a final volume of 13 μl and incubated at 65°C for 5 minutes. Subsequently, 2 μl of 0.1 M DTT, 4μl of 5X first strand buffer, and 1 μl of RnaseOUT were added and the mixture at 42°C. After 1 minute 1μl of 200U/μl Superscript II was added to each reaction and incubated at 42°C for 1hour and at 70°C for 15 min. Each newly synthesised cDNA sample was diluted 20 times with RNasefree and stored a -20°C.

2.2.6.3 Realtime quantitative PCR analysis

Quantitative realtime polymerase chain reactions (qPCR) were carried out in either a total volume of 20μl with 50% (v/v) Jumpstart SybrGreen PCR Mastermix and 1% ROX, or in a total volume of 10μl with 50% (v/v) KicQstart SybrGreen PCR Mastermix (incuding ROX). To each reaction 300nM of primers and 5% (v/v) of cDNA/DNA were added. A control reaction without cDNA/DNA was included to check for the formation of primer-dimers, and all reactions were performed in duplicate in the same plate. Cycling conditions were as follows: 95°C for 15 minutes (denaturation), 40 cycles of 94°C for 15seconds (denaturation) and 60°C for 30seconds (annealing), and finally 72°C for 30 seconds (extension). The quantification of the abundance of target sequences was determined by using the Δ CT and Δ Δ CT method [192, 193] in which the CT represents the number of cycles in the reaction necessary to achieve a defined level of fluorescence in the exponential phase of amplification. For gene expression analysis, this was either normalized to the CT average of 2 housekeeping genes (*S17* and *L19*) and represented as mRNA levels, or normalized to both the housekeeping genes and a control sample and represented as fold enrichment over control. For detection of protein binding by chromatin immunoprecipitation, the

CT of the target region was normalized to 1% of input DNA and to a background (typically intergenic) region and represented as fold enrichment over background.

2.2.6.4 Primer design and validation

Primers for RT-qPCR were design with the following criteria: amplicon size of 100200bp, primer GC content of 45-55%, primer melting temperature 57-63°C, low 3' stability (no more than 2 C'2 and/or G's in the last 5bp of the primer) and primer size of 1825bp. Moreover, for expression analysis primers were designed in different exons. Target sequences were obtained in the Ensembl and the UCSB genome browsers and the primers were aligned to the genome using the BLAT function of the NCBI. For each pair of primers designed, the efficiency in qRT-PCR was tested in 2-fold dilutions of DNA/cDNA [193]. Primers were considered efficient, and therefore suitable for the Δ Δ CT method, when yielding a good linear fit (R2<0.98) in CT vs. logarithm of the dilution factor plot and the efficiency calculated was between 1.8 and 2.2 (Efficiency=10(1/slope)). The full list of primers used can be found in Appendix.

2.2.7 Protein analysis

2.2.7.1 Immunofluorescent staining

Cells were cultured on 0.2% gelatin-coated glass coverslips or plastic 8-well chambers. When 80% confluent the cells were washed in PBS and fixed in 4% paraformaldehyde (PFA) for 10 minutes. Fixed cells were permeabilised with 0.4% Triton X-100 in blocking buffer (Section 2.1.7 Solutions), for 30 minutes at room temperature. After washing with PBS, the coverslips were incubated in blocking buffer for 30 minutes. Finally, samples were incubated with primary antibody diluted in blocking buffer overnight at 4°C in a humid chamber. Coverslips were washed in PBS and incubated with the fluorophore-conjugated secondary antibodies diluted in blocking buffer for 1 hour at room temperature. Coverslips were washed in PBS and mounted in Vectashield with 1μg/ml DAPI. Samples were visualised using a SP5 Leica laser-scanning confocal microscope or an inverted fluorescent/brightfield microscope with an attached Nikon camera. For whole mount and organoids staining, the permeabilization time was extended to hours dependant on the size of the sample and incubation time for blocking, primary and seconday antibodies were extended to overnight. Phalloidin was added with secondary antibody mix for incubation (1:50).

2.2.7.2 Western blot

Whole cell extracts were obtained by lysing the cells cultured in 6-well plates with cold RIPA buffer supplemented with protease and phosphatase inhibitors. Lysates were incubated for 20 minutes on a rotating wheel at 4°C, centrifuged at 14,000rpm for 20 minutes and the supernatant collected. The protein extracts were quantified by Bradford assay and stored at -20°C. The appropriate amount of protein lysates (5-30μg for whole extracts) was diluted 3:1 with Laemmli sample buffer (4x) with 5%(v/v) β-mercaptoethanol and incubated at 95°C for 5 minutes. Lysates were resolved on an 8% SDS polyacrylamide gel electrophoresis (SDS-PAGE) gel and subsequently transferred into a methanol-activated Polyvinylidene fluoride (PDVF) membrane using wet-transfer method at 90V for 1 hour at 4°C. Blots

were blocked with 5% skimmed milk in Tris-Buffered Saline with 0.5% Tween20 (TBS-T) for 1 hour at room temperature. After washing with TBS-T, the appropriate amount of primary antibody was diluted in 5% skimmed milk in TBS-T and incubated overnight at 4°C. Membranes were washed with TBS-T and then incubated with the appropriate HRP-conjugated secondary antibody diluted in 5% skimmed milk in TBS-T for 1 hour at room temperature. After washing with TBS-T, detection of the proteins was achieved by treating the blots with enhanced chemiluminescence (ECL) western blotting detection reagents and exposing in the ImagQuant LAS4000.

Chapter 3

The uncovering of Cidea-mediated lipid droplet enlargement in embryonic stem cells

3.1 Introduction

Embryonic stem cells can be maintained in self-renewing state under various culture conditions. Besides chemically defined media [24], fetal bovine serum (FBS) and KnockOut Serum Replacement (KSR) together with LIF are widely used, including in our lab. While we use FBS/LIF for routine ESC culture, we primarily use KSR/LIF for generating induced pluripotent stem cells (iPSCs) from mouse embryonic fibroblasts (MEFs) [185]; a condition recently shown to improve the efficiency of reprogramming [194]. Remarkably, Michelle Percharde and David Barneda in our group previously noticed that MEF-derived iPSC established under KSR conditions unexpectedly contain a considerable number of large lipid droplets that could be readily detected using the neutral lipid dye BODIPY 493/503 (unpublished). Whether the presence of large lipid droplets was merely the effect of the culture conditions used and/or represented a unique novel hallmark of the pluripotent state remained to be investigated.

In this chapter we first determine whether lipid droplets can also be detected in embryonic stem cells (ESCs), compared to MEFs, and under which culture conditions. The observed presence of lipid droplets in ESCs appears to be a highly dynamic process of which its regulation is consequently further investigated here. A particular focus in this context is the lipid-droplet associated protein Cidea, previously identified to promote LD enlargement in brown adipocytes. Whereas we observed that external factors like media composition can generally affect the interplay between Cidea and lipid droplet dynamics, the intrinsic role of Cidea is further investigated using Cidea-modulated (overexpressing, knockdown and knockout) cells. Cidea forms together with Cideb and Cidec the cell death inducing DNA fragmentation factor 45 like effector (CIDE) family of LD-associated proteins [195], and is extensively studied in adipocytes as a brown adipocyte-specific marker. In addition, its important roles in controlling LD growth and other aspects of lipid metabolism are observed in numerous different cell types. Interestingly, embryonic stem cells are not included in this extensive range of cell types studied, although the CIDE-domain is highly conserved among species [152, 155, 196]. Cidea has been mentioned in a handful of studies related to stem cells, however it was merely used as a brown-fat signature gene in the context of adipocyte differentiation. Here, a detailed characterization of the phenotype of Cidea-modulated cells reveals for the first time an interesting role for this protein in ESCs. In particular, using Cidea promoter analysis approaches in conjunction with parallel analysis of Cidea and pluripotency associated genes, we uncovered a link between Cidea expression and the undifferentiated ESC state.

3.2 Results

3.2.1 Embryonic stem cells dynamically form large lipid droplets upon KSR exposure

Interestingly, lipid droplet abundance has been used as a marker for reprogramming, additionally the same group determined that reprogramming is improved under KSR conditions [194]. Our lab observed that lipid droplet size is increased under these conditions, however it remains unclear whether these lipid droplet dynamics are the impact of the medium or the cell state. Therefore, we first addressed if the presence of large lipid droplets could also be detected in ESCs and whether this was inductive upon exposure to KSR (a serum replacement supplement that contain a large fraction of BSA-conjugated lipids). We stained ESCs with the fluorescent neutral lipid dye BODIPY 493/503 when either routinely grown under FBS/LIF or transferred into KSR-supplemented medium for 24 hours (KSR/LIF), DAPI was used to visualize nuclei (Fig 3.1A, upper panel). Multiple image sections were acquired and merged to reconstitute the presented three-dimensional images in Figure 3.1A. Interestingly, when analysing LDs present in ESCs grown in KSR, we observed the presence of numerous LDs of variable sizes with an obvious fraction of cells containing larger LDs compared to ESCs grown in FBS (Fig 3.1A; upper panels with zoom-in). In contrast, the ability to form enlarged lipid droplets under KSR/LIF conditions was not attributed to MEFs which were originally used to generate the iPSCs (Fig 3.1A; lower panels with zoom-in). Although this difference in LD phenotype between ESCs and MEFs was particularly evident upon KSR treatment, it was also observed in FBS culture conditions (Fig 3.1A; left panels). Therefore, we conclude that the ability to form enlarged lipid droplets under KSR conditions is inherent to ESCs, indeed reflecting (the acquisition of) the ESCs state rather than merely a medium effect.

LD size differences can operate through LD enlargement, which has previously been reported in adult tissues as a dynamic and highly regulated process [197]. In brown adipocytes LD enlargement is regulated by key molecules which reside at the surface of the LD [197]. In this LD fusion process, LD-associated proteins catalyse a fusion mechanism in which a donor LD transfers its content to a acceptor LD (Fig 3.1B)[127]. These LD-coating proteins are thought to stabilize LD pairs at the LD-LD contact site, where they facilitate the transport of neutral lipids through the LDs phospholipid monolayer (Fig 3.1B))[127]. To examine whether LD enlargement might also occur through a regulated process in ESCs, we performed live cell imaging on ESCs upon KSR exposure. LDs were identified based on BODIPY signal, and their dynamics was analysed in a one-dimensional microscopic section during time-lapse imaging 8 hours after changing FBS/LIF to KSR/LIF. We first identified two lipid droplets that seem to hold a LD-LD contact site, to consequently follow their fate over the course of 4 hours (Fig 3.1C). As described for adipocytes, we here similarly observed that a generally smaller donor LD transferred its content to the acceptor LD, leading to the progressive enlargement of the acceptor LD and shrinkage of the donor LD to eventually form one larger LD of about 2.5μm in diameter. From these observations, we concluded that LD enlargement in KSR-treated ESCs most likely operates via the fusion of pre-existing LDs as previously established in brown adipocytes by our collaborator Dr Mark Christian and others [195, 127]. Altogether,

our findings establish that ESCs have the capacity of dynamically forming enlarged lipid droplets upon KSR exposure in striking contrast to MEFs. Hence, our previous and unexpected detection of enlarged LDs in iPSCs might indeed both reflect the acquisition of an ESC state and the ability of these cells to respond to lipid rich medium by increasing cellular neutral lipid storage.

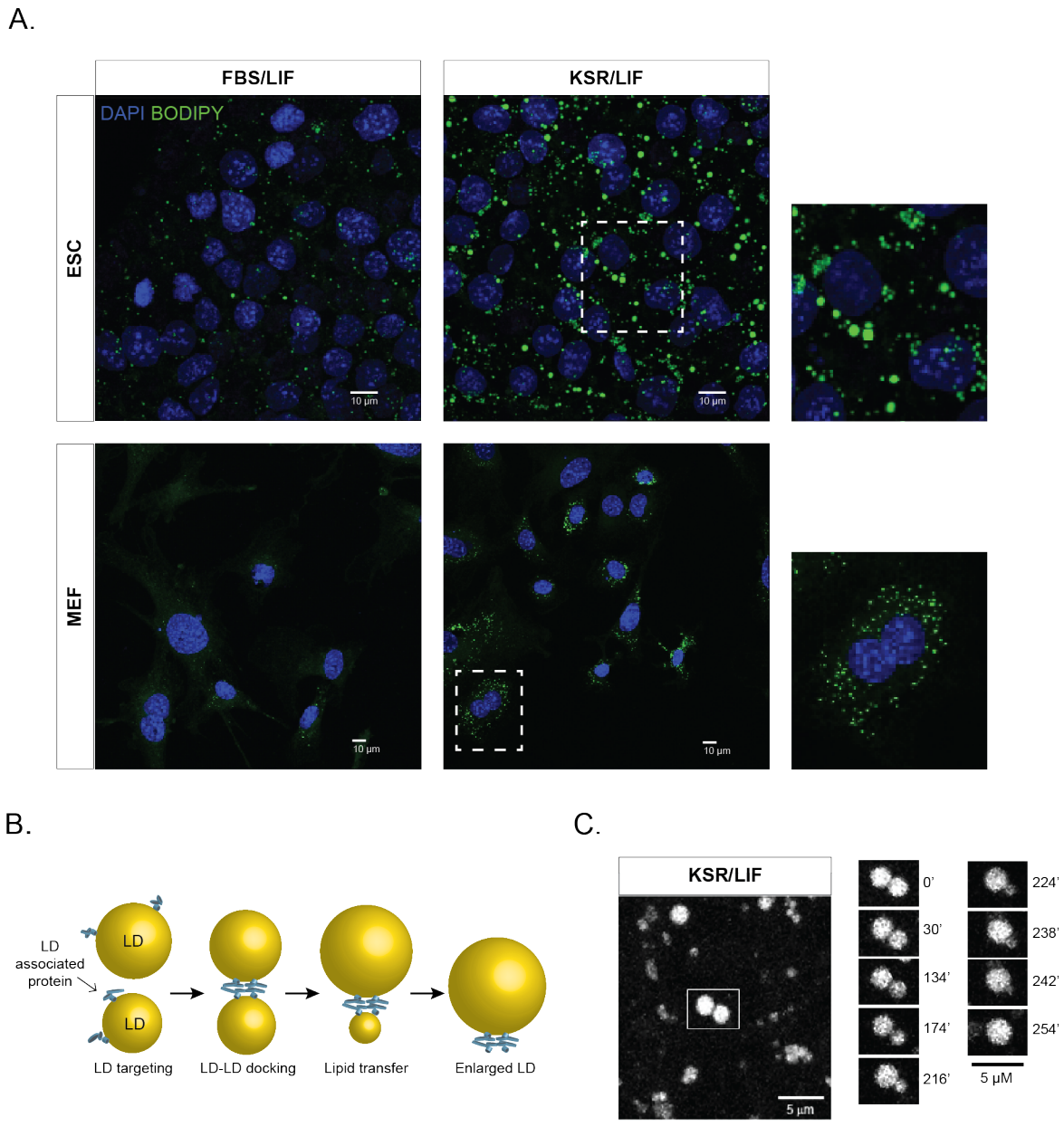


Figure 3.1: Lipid droplet enlargement in embryonic stem cells and mouse embryonic fibroblasts.

(A) Confocal imaging of lipid droplet (LD) staining with neutral lipid dye BODIPY 493/503 (green) in ESCs and MEFs cultured in routine media (FBS/LIF), or exposed to lipid-enriched media (KSR/LIF) for 24 hours. Each picture represents a three-dimensional image of merged Z-stack images. A zoom-in of the white dotted square is shown on the side. DAPI staining was used to visualise nuclei (blue). Bar, 10μm. Images are representative of three independent experiments. **(B)** A schematic diagram showing the proposed mechanism of LD enlargement in brown-adipocytes. LD-associated proteins target LDs and are diffused on the LD surface. By forming interactions with each other, within and between lipid droplets, the LD-LD contact site is formed, creating a local perturbation in the phospholipid barrier that increases its permeability

to lipid transfer from a donor LD to a acceptor LD, ultimately forming one enlarged LD (adapted from [127]). **(C)** Time lapse microscopy pictures showing the fusion of two LDs leading to the formation of one large droplet in KSR-treated ESCs. Lipid droplets are stained with neutral lipid dye BODIPY 493/503 (white). Images are consecutively acquired 8 hours after the exposure of cell cultures in routine media to lipid-rich KSR media. A zoom-in of the two LDs in the white square is shown on the side with a time-scale in minutes. Bar, 5μm

3.2.2 LD enlargement correlates with *Cidea* induction in KSR-treated embryonic stem cells

In an attempt to uncover which intrinsic factors regulate LD dynamics in ESCs but not in MEFs, we screened for adipocyte-expressed molecules with known roles in modulating LD size [195]. In particular, we compared by real-time quantitative PCR (RT-qPCR) the relative mRNA levels of *Perilipin* (*Plin1-5*) and *Cide* (*Cidea-c*) gene family members in ESCs and MEFs grown in FBS-containing media and upon treatment with KSR for 24 hours. Strikingly, we thus identified a selective induction of *Cidea* in ESCs (Fig 3.2A-B). In routine (FBS) conditions, *Cidea* is expressed at 44-fold higher levels in ESCs relative to MEFs (Fig 3.2A-B). Upon KSR induction of LD enlargement, *Cidea* expression further increased over 5-fold in ESCs, reaching a greater than 200-fold higher expression levels than in MEFs. In contrast, *Cidea* expression in MEF is increased 4-fold upon KSR treatment. Analysis of the other LD size-modulating proteins revealed that *Plin1* was barely expressed in ESCs and MEFs, and although *Plin2-5* were expressed in ESCs, their expression was either not induced upon KSR treatment or to similar extent as in MEFs (Fig 3.2A-B). *Cideb* and *Cidec* are both expressed in ESCs and MEFs and induced upon KSR treatment, however to a much lower extent compared to *Cidea* (Figure 3.2A-B). Therefore, it seems unlikely that any of the other genes examined besides *Cidea* could explain the observed difference in LD morphology between ESCs and MEFs.

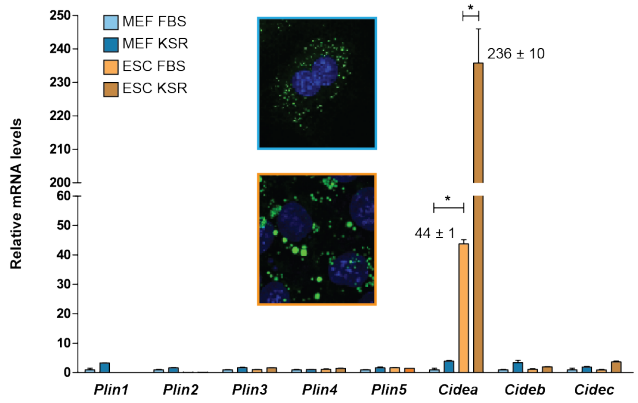
Parallel analysis of pluripotency-associated genes confirmed that ESCs under KSR conditions retained a self-renewing phenotype with steady *Oct4*, *Nanog*, *Klf4*, *Rex1* and *Tbx3* expression levels, and no induction of the early differentiation marker *Fgf5* in both FBS and KSR culture conditions (Fig 3.2C). As excepted and in contrast to ESC, pluripotency factors and *Fgf5* were expressed in low levels in differentiated MEFs (Fig 3.2C). Although KSR treatment did not change the ESC state, we were furthermore interested in its impact on the metabolic signature of the cells, as indicated by the expression levels of two key metabolic genes, *Pdk1* and *Cox7a1*. Concurrent expression of *Pdk1* which inhibits the formation of acetyl-CoA from pyruvate, and *Cox7a1* an oxidative-associated gene regulating mitochondrial activity, in FBS/LIF conditions highlights the flexible metabolic signature of ESCs. Here, we could not detect increased expression of either genes upon KSR treated ESCs (Fig 3.2C). In MEFs, both enzymes are expressed at low levels in FBS/LIF and KSR/LIF conditions. In comparison to ESCs the low *Pdk1* expression in MEFs confirms their more oxidative profile, whereas ESCs are more anaerobic glycolytic.

Furthermore, as expected both ESCs and MEFs have the capacity for *de novo* lipid synthesis as indicated by steady expression of *Fasn*, *Acc1*, *Dgat1* and *2* (Fig 3.2D). However, KSR-induced LD enlargement was not accompanied by the upregulation of these genes. Therefore, in this model, LD enlargement is

assigned to Cidea-mediated dynamic lipid storage capacity, rather than *de novo* lipid synthesis.

Taken together, these data demonstrate that culturing undifferentiated ESCs in lipid-enriched medium strongly and specifically induced expression of *Cidea*, a LD-associated factor that we know promotes LD enlargement in brown adipocytes via LD-LD fusion and transfer of stored lipid [127] (see also Fig 3.1B).

A.

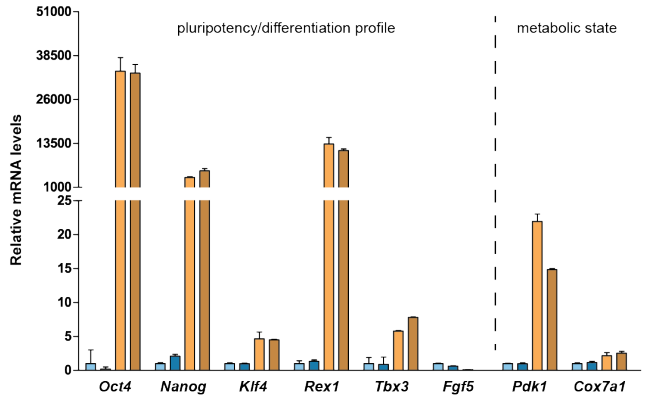


B.

mRNA levels ($2^{-\Delta CT} * 10^7$)

	MEF		ESC	
	FBS	KSR	FBS	KSR
Plin1	19.59	47.60	1.57	<LOD
Plin2	98403.77	161360.89	7995.69	14804.08
Plin3	24854.13	42172.56	25702.76	40600.42
Plin4	17911.87	19544.37	20461.76	25767.35
Plin5	287.68	473.75	483.62	419.14
Cidea	12.47	48.13	545.91	2941.00
Cideb	349.77	1184.78	386.88	688.74
Cidec	9.35	38.64	8.76	33.75

C.



D.

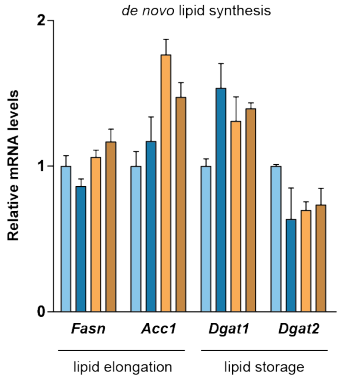


Figure 3.2: Gene expression profiling in ESCs and MEFs cultured in routine (FBS/LIF) and lipid-rich media (KSR/LIF).

Relative mRNA levels of **(A, B)** lipid-droplet associated gene family members *Perilipin* (*Plin1-5*) and *Cide* (*Cidea-c*) with known roles in modulating LD size, **(C)** key pluripotency-associated genes (*Oct4*, *Nanog*, *Klf4*, *Rex1* and *Tbx3*), early differentiation (*Fgf5*), and key metabolic processes (*Pdk1* and *Cox7a1*), and **(D)** genes involved in lipid synthesis (*Fasn*, *Acc1* and *Dgat1-2*) in ESCs and MEFs grown in FBS-containing media and upon treatment with KSR for 24 hours. Data were normalized to the housekeeping genes *S17* and *L19*, and expressed relative to MEFs cultured in FBS. Error bars represent SEM of three biological replicates. $P<0.05$ (*), Student's t test. Confocal images in (A) represent MEF in KSR (blue border) and ESC in KSR (orange border), from Fig 3.1A. Panel (B) shows mRNA levels of lipid-droplet associated genes from (A) not normalized to MEFs, indicated as $2^{-\Delta CT}$ (times 10^7 for better data presentation). <LOD, value smaller than limit of detection.

3.2.3 The Albumax fraction of KSR is alone sufficient for inducing *Cidea* expression and LD enlargement

Gene expression profiling of KSR treated ESCs and MEFs also revealed the induction of free fatty acid (FFAs) receptors (Fig 3.3A). The G-protein coupled FFA receptor family consists of four variants, activated by various exogenous free fatty acids. Whereas FFA2 and 3 are identified as receptors for (saturated) short-chain fatty acids, FFA1 and 4 are receptors for (saturated and unsaturated) medium- and long-chain fatty acids [198]. Notably, all *FFAs* were induced in ESCs upon KSR treatment compared to FBS, prompting us to closely examine the composition of KSR. Its full composition can be found in its published patent (Fig 3.3B)[199, 200], as a mixture of small organic molecules (amino acids, vitamins and antioxidants), trace elements and three proteins, namely insulin, transferrin and lipid-rich albumin. Of interest, lipid ligands of FFA receptors are typically found in the lipid-rich albumin fraction (or Albumax). Although we did not investigate a potential link between FFA receptor activation and LD enlargement, we here tested whether Albumax might be the active component of KSR responsible for the induction of *Cidea* expression in ESCs. For this, we compared the effect of 24 hours KSR treatment with Albumax treatment in a dose-dependent manner. Three different concentrations of Albumax were tested; 0.2%, 1% and 5%, where 1% Albumax corresponds to the equivalent Albumax concentration in the 15% KSR typically used in ESC culture medium. As a readout for this experiment, *Cidea* expression and LD enlargement were both assessed by RT-qPCR and confocal imaging, respectively. Here we observed that Albumax was able to induce *Cidea* transcript expression from the lowest concentration tested (0.2%) (Fig 3.3C). ESCs exposed to higher concentrations (1% and 5%) did not show any further induction reaching a plateau of *Cidea* expression. In contrast, no induction was observed upon treatment with the lipid-poor albumin (BSA fraction V), suggesting that *Cidea* induction is independent of the BSA protein component of Albumax and that the cells are very responsive to the lipid component alone. Under all Albumax concentrations, ESCs were verified to retain steady expression levels of pluripotency genes such as *Nanog* and *Oct4*, and did not induce differentiation marker *Fgf5* (Fig 3.3C), as previously examined upon KSR treatment (see Fig 3.2C). This also excludes that the differentiation status of the cells might be, at least partly, related to the observed *Cidea* induction. Consistent with this induction, we found that Albumax was able to mimic the LD phenotype of the KSR-treated cells, that is, the detection of numerous large LDs. Here, we qualitatively present in Fig 3.3D evidence for a dose-dependent increase in the number of large LDs formed upon Albumax treatment; an effect not observed in BSA protein-control cultures. Altogether, these data demonstrate that the lipid-rich fraction of KSR can alone recapitulate KSR-induced *Cidea* expression and LD enlargement in ESCs.

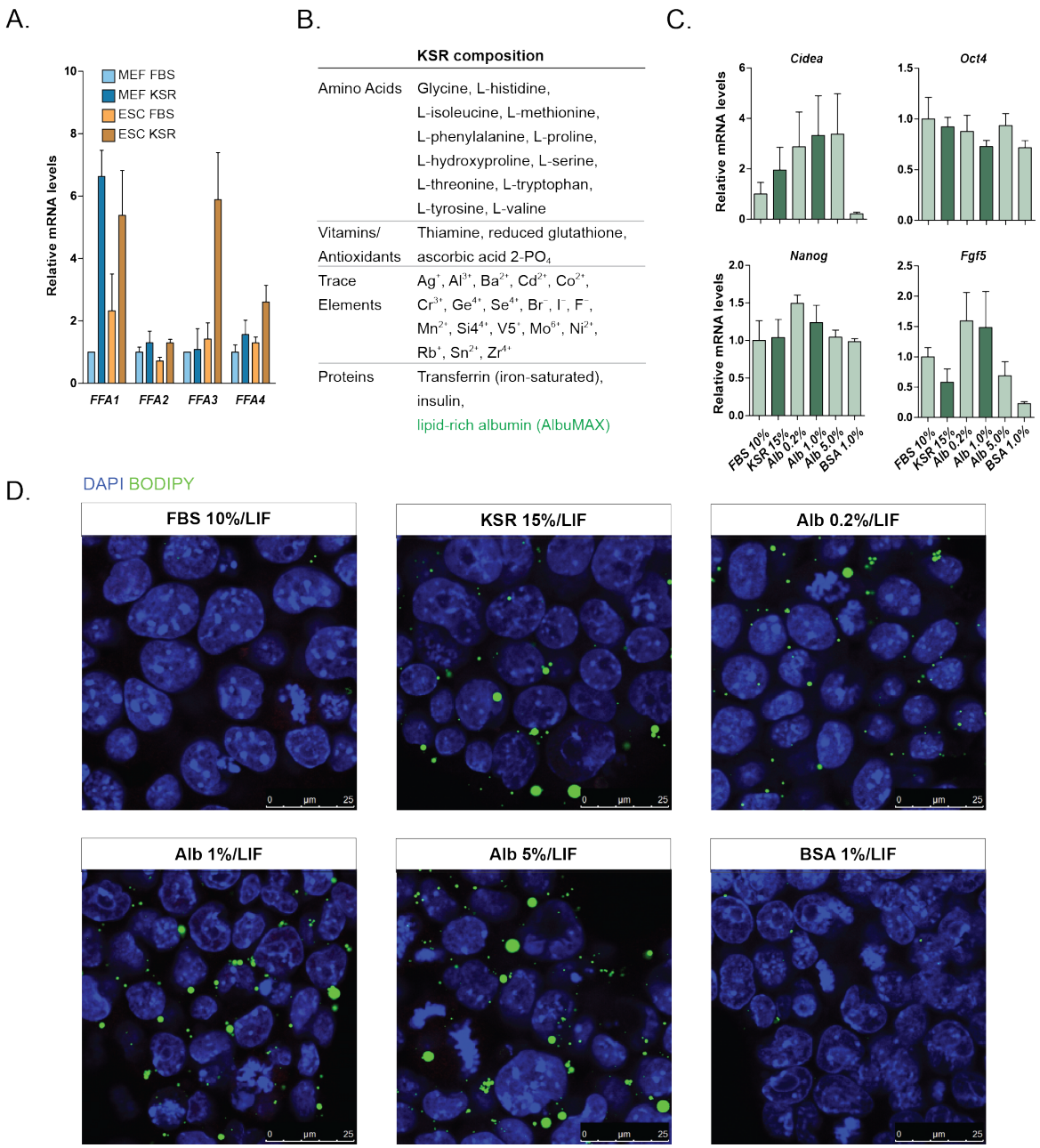


Figure 3.3: The Albumax fraction of KSR is alone sufficient to enforce LD enlargement.

(A) G-protein coupled free fatty acid (*FFA1-4*) receptor family gene expression in ESCs and MEFs in routine FBS media and upon 24 hour-KSR treatment. Data were normalized to the housekeeping genes *S17* and *L19*, and expressed relative to MEFs cultured in FBS. Error bars represent SEM of three biological replicates. **(B)** KnockOut Serum Replacement composition (KSR) [199, 200] **(C)** ESC expression profile of genes related to lipid droplets (*Cidea*), self-renewal (*Oct4* and *Nanog*), and early differentiation (*Fgf5*), when cultured in routine FBS media and upon 24 hour-exposure to KSR, and various concentrations (0.2%, 1% and 5%) of lipid-rich BSA fraction (Albumax) of KSR. Lipid-poor albumin (BSA fraction V) was used as a control. 1% Albumax corresponds to the equivalent Albumax concentration in the 15% KSR typically used in ESC culture medium, both indicated in dark green. Gene expression data were normalized to the housekeeping genes *S17* and *L19*, and expressed relative to ESCs cultured in FBS. Error bars represent SEM of three biological replicates. **(D)** Immunofluorescence of lipid droplets with neutral lipid dye BODIPY 493/503 (green) in ESCs cultured in routine FBS media and upon 24 hour-exposure to exogenous lipids as described in (C). DAPI staining was used to visualise nuclei. Bar, 25μm. Images are representative of three independent experiments.

3.2.4 Ectopically expressing Cidea in ESCs is sufficient to drive LD enlargement

To directly test whether Cidea induction mediates LD enlargement in ESCs, we next thought to ectopically express Cidea using previously developed V5-tagged Cidea construct [127]. For this PhD, the construct was sub-cloned into a CAG-vector allowing for stable expression in ESCs [201]. ESCs were consequently transfected with either an empty vector (control) or V5-Cidea vector, selected in the presence of puromycin, and examined as a pool of stably transfected cells (V5 pool) and derived clones. Here we selected the clone with the highest *Cidea* expression values, namely clone 3 (V5 C3) for subsequent analyses. Validation of Cidea over-expression in the pool of transfected cells (V5 pool) and derived V5 C3 clone along with control cells (CAG empty) was performed by RT-qPCR and western blot analyses as shown in Fig 3.4A and 3.4B. For this, we designed a series of primer pairs that selectively amplify genomic and/or plasmid *Cidea*. The results indicated that endogenous (genomic) *Cidea* expression was not significantly affected in V5-Cidea transfected cells compared to control cells in FBS conditions, while *Cidea* ectopic (plasmid) expression was only detected in V5 pool and V5 C3 populations (Fig 3.4A). As expected, KSR treatment induced endogenous *Cidea* transcript expression; an effect not conveyed on plasmid *Cidea* expression. Western blot analysis confirmed that the pool of transfected cells and derived V5 C3 clone successfully expressed the V5-tagged Cidea protein; however, as expected, sub-cloning enhanced V5-tagged Cidea total protein levels (Figure 3.4B). When culturing the cells in KSR, we unexpectedly observed that the level of ectopic Cidea protein expression was further increased without any noticeable change at the transcriptional level. This suggested that Cidea protein might be stabilized under these lipid-rich conditions, possibly involving post-transcriptional modifications, as previously mentioned but never fully investigated in brown adipocytes [127].

To validate the functional capacity of the V5-tagged Cidea protein, its cellular distribution was verified by confocal imaging in stably expressing V5 C3 cells. As expected, Cidea protein localized at the surface of enlarged LDs as visualized by co-staining with anti-V5 (red) antibody and BODIPY (green) (Fig 3.4C). To examine whether ectopically expressing Cidea alone is enough to enforce lipid droplet enlargement regardless of tissue culture conditions, we then compared the LD morphology of V5-Cidea and empty transfected cells in FBS and KSR. By confocal imaging we confirmed the detection of larger lipid droplets in V5-Cidea transfected cells compared to control cells in FBS conditions; an effect reinforced in the presence of KSR (Fig 3.4D). To quantify the effect of ectopic Cidea expression we precisely investigated the number and size of the LDs across the four populations - i.e. CAG empty and V5 C3 in FBS and KSR. In order to do so, we used automatic quantification of LDs in acquired microscopy images. For each condition, LDs in at least fifteen colonies were automated counted by CellProfiler 2.1.1 using an in-house script provided by Dirk Dorman. The nuclei were identified based on DAPI staining, followed by the automatic determination of the putative cell boundary. Consequently, the lipid droplets were scored based on BODIPY staining, with additional settings of threshold parameters and methods to distinguish "clumped objects" (i.e. clustering lipid droplets). Besides the determination of the size and number of the lipid droplets on each image, each droplet was assigned to a cell, using the previously established cell

boundary. Here, we observed a 2-fold increase in the average size of LDs formed in the V5 C3 ESC clone relative to control cells in routine (FBS) conditions. This relative difference was however maintained upon KSR treatment (Fig 3.4E). The number of droplets was relatively the same between Cidea overexpressing and control cells when cultured in routine conditions, interestingly upon KSR treatment, the control cells greatly increased (7-fold) the number of droplets per cells, more so than the Cidea overexpressing cells (4-fold) (Fig 3.4E). Overall, this indicates the availability of many small LDs and relatively less LDs of bigger size in control cells compared to Cidea overexpressing cells, which is consistent with the role of Cidea in LD-LD fusion events and evident in confocal imaging (Fig D3.4). Taken together, these findings establish that Cidea expression alone is sufficient to promote LD enlargement in the absence of KSR induction.

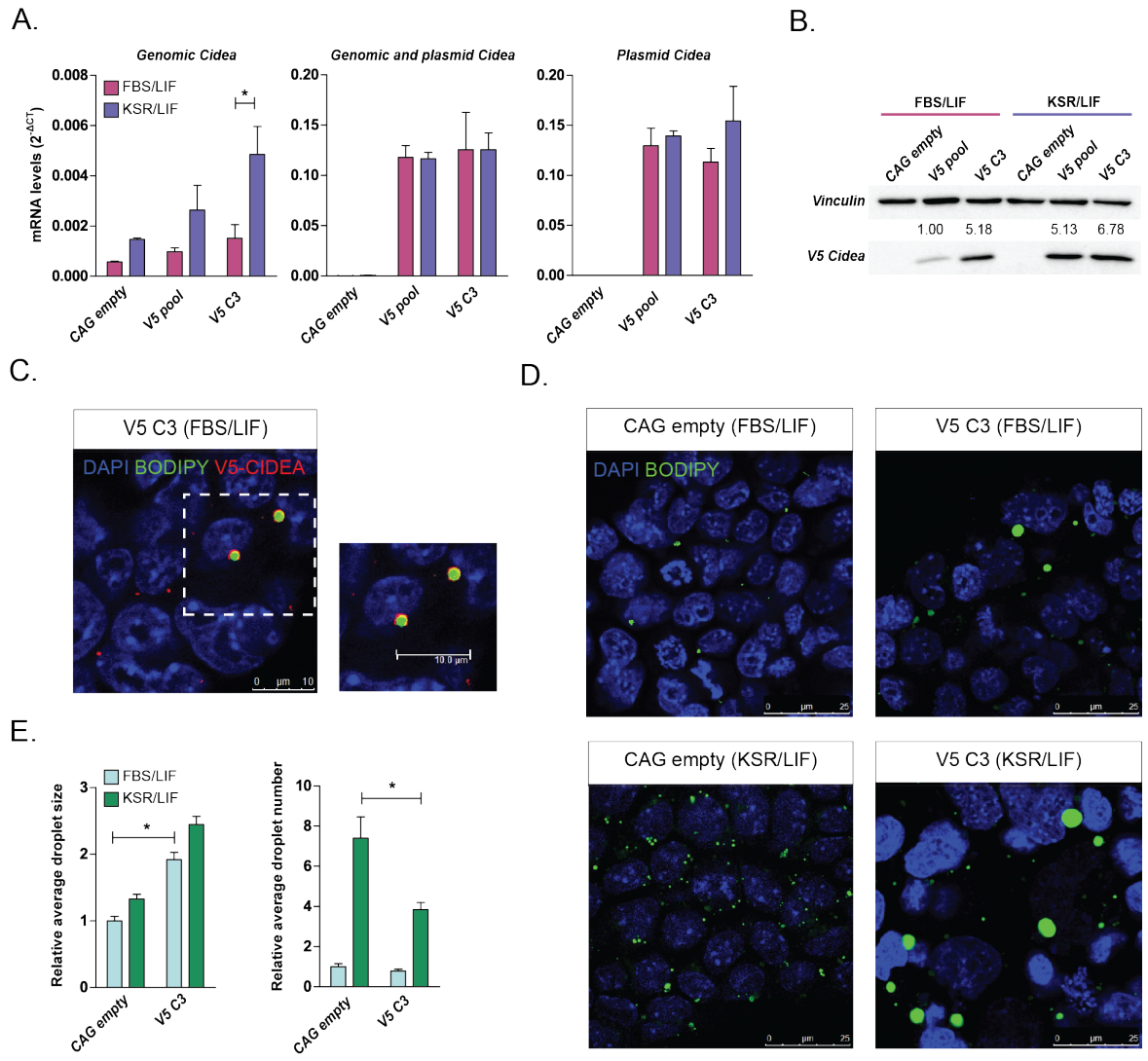


Figure 3.4: Generation and characterisation of Cidea overexpressing ESCs.

(A) Validation of Cidea over-expression in a pool of transfected ESCs (V5 pool) with V5-tagged Cidea encoding CAG vector and derived V5 C3 clone along with cells transfected with an empty vector (control; CAG empty) by RT-qPCR using various primer pairs to detect genomic and/or plasmid *Cidea* expression in routine culture conditions (FBS/LIF) and upon 24 hour-KSR treatment (KSR/LIF). RT-qPCR data were normalized to the housekeeping genes *S17* and *L19*. Error bars represent SEM of three biological replicates. P<0.05 (*), Student's t test. **(B)** Anti-V5 Western blot for V5-tagged

Cidea protein in whole cell lysates from cells described in (A) under similar culture conditions. Vinculin was used as a loading control. **(C)** Cidea protein localized at the surface of enlarged LDs as visualized by co-staining with anti-V5 (red) antibody and neutral lipid dye BODIPY 493/503 (green), in stably Cidea overexpressing (V5 C3) ESCs. DAPI staining was used to visualise nuclei. Bar, 10μm. Image is representative of three independent experiments. **(D)** Confocal imaging of Cidea overexpressing ESCs (V5 C3) and control cells (CAG empty), stained for neutral lipid dye BODIPY 493/503 (green), in routine culture conditions (FBS/LIF) and upon 24 hour-KSR treatment (KSR/LIF). DAPI staining was used to visualise nuclei. Bar, 25μm. Images are representative of three independent experiments. **(E)** Quantification of the average number and size of droplets per nuclei of images described in (D). For the automatic quantification of LD size and number, microscopy images were acquired using a Nikon E400 Eclipse microscope. For each condition, at least fifteen colonies where automated counted by CellProfiler 2.1.1 using an in-house script provided by Dirk Dorman. Data was normalized to control cells (CAG empty). $P<0.05$ (*), Student's t test.

3.2.5 Cidea depletion in ESCs inhibits LD-LD fusion events

To further determine whether Cidea expression is strictly required for LD enlargement in ESCs, we next knocked down Cidea using a previously validated puromycin-selectable shRNA vector (by Michelle Percharde in our lab). ESCs were transfected with either Cidea-specific (shCidea) or control (shMir39) shRNA vectors followed by 6 days of puromycin selection. *C. Elegans* Mir39 was selected as a control shRNA due to its lack of sequence homology to mouse RNA. This resulted in destabilization of shCidea-transfected cells apparent by the increased amount of differentiated colonies compared to control cells, as measured by a decreased alkaline phosphatase staining 6 days post-transfection in the pool of shCidea-transfected cells (Fig 3.5A). However, the extent of Cidea knockdown was specific and substantial with a reduction of over 60% in *Cidea* mRNA levels and no significant alteration in *Cideb* and *Cidec* expression profiles as verified by RT-qPCR on a pool of shCidea-transfected cells (Fig 3.5B). From this pool, we were consequently able to derive three stable Cidea-KD ESC clones (shCidea1, 3 and 4), showing a range of knockdown level from 50 to 70% relative to control cells (Fig 3.5C). Although *Cidea* expression was not fully depleted in these clones, the full impact of the depletion was revealed upon KSR treatment. Under these conditions, we observed a lack of *Cidea* transcript induction after 24 hours KSR treatment, in contrast to control cells, which showed the expected *Cidea* induction (Fig 3.5D). Consistent with a role for Cidea in promoting LD enlargement in ESCs, we interestingly found that all three clones failed to show evidence of LD-LD fusion events and hence clustering of small LDs as opposed to merging of droplets which was observed in control cells upon KSR treatment (Fig 3.5E).

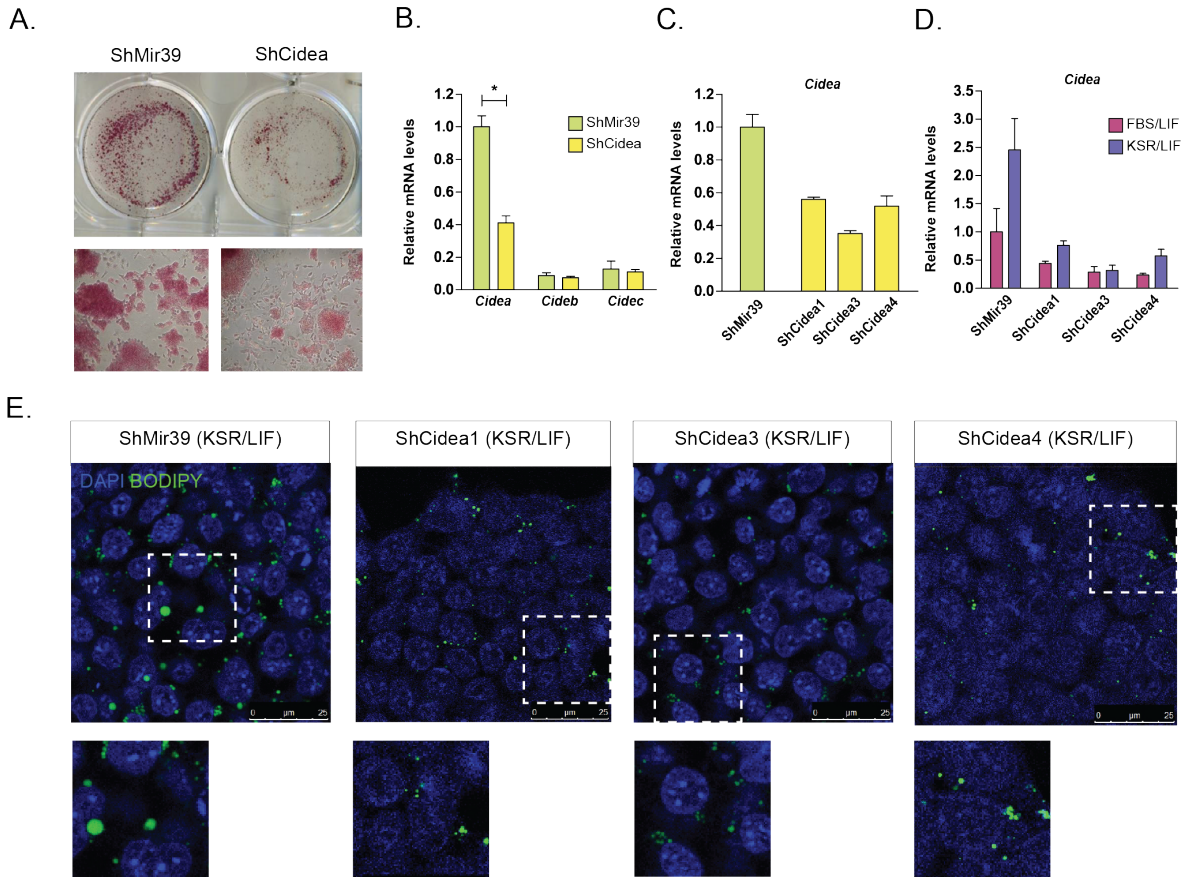


Figure 3.5: Generation and characterisation of Cidea knockdown ESCs.

(A) Alkaline phosphatase staining preformed 6 days after puromycin selection of Cidea shRNA-mediated knockdown ESCs (ShCidea) and control cells (ShMir39). Higher magnification pictures are shown below. **(B)** Relative mRNA levels of *Cidea*, *Cideb* and *Cidec* as assessed by RT-qPCR in a pool of ESCs transfected with Cidea-specific (shCidea) or control (shMir39) shRNAs 6 days post selection. Data were normalized to the housekeeping genes *S17* and *L19*, and expressed relative to ShMir39 Cidea. Error bars represent SEM of three biological replicates. $P<0.05$ (*), Student's t test. **(C)** Stable Cidea knockdown further confirmed in three independent shCidea-transfected ESC clones (ShCidea1, 3, 4) compared to control cells (ShMir39). Data were normalized to the housekeeping genes *S17* and *L19*, and expressed relative to ShMir39 *Cidea*. Error bars represent SEM of three biological replicates. **(D)** Relative mRNA levels of *Cidea* in Cidea-depleted (ShCidea1, 3, 4) and control (ShMir39) ESCs cultured in routine (FBS/LIF) and KSR media for 24 hours (KSR/LIF). Data were normalized to the housekeeping genes *S17* and *L19*, and expressed relative to ShMir39 in FBS. Error bars represent SEM of three biological replicates. **(E)** Confocal imaging in Cidea-depleted (ShCidea1, 3, 4) and control (ShMir39) ESCs cultured in KSR media for 24 hours (KSR/LIF), stained for neutral lipid dye BODIPY 493/503 (green). DAPI staining was used to visualise nuclei. Bar, 25μm. A zoom-in of the white dotted square is shown below. Images are representative of three independent experiments.

To further demonstrate the link between Cidea and LD dynamics, and exclude off-target effects of the shRNA knockdown, Cidea knockout cells were generated (by Tommy King Mau in our lab). Cidea knockout cells were generated using the CRISPR/Cas9 system, where the guide RNAs were designed to target and delete the whole *Cidea* locus (Fig 3.6A). Effective targeting would then result in a different (shorter) DNA fragment as detectable by PCR. Indeed, loss of *Cidea* was confirmed by genomic PCR in two clones (16 and 19), as indicated by the absence of the uncut band (575 bp), and appearance of the cut band (288 bp) (Fig 3.6B). The absence of *Cidea* gene expression was confirmed by RT-qPCR in three clones (16.1, 19.7 and 19.9) (Fig 3.6C). Phenotypic characterisation of the cells revealed that knockout of Cidea recapitulates the Cidea knockdown phenotype with clustering of small LDs, rendering them incapable of forming large LDs, even upon KSR treatment (Fig 3.6D).

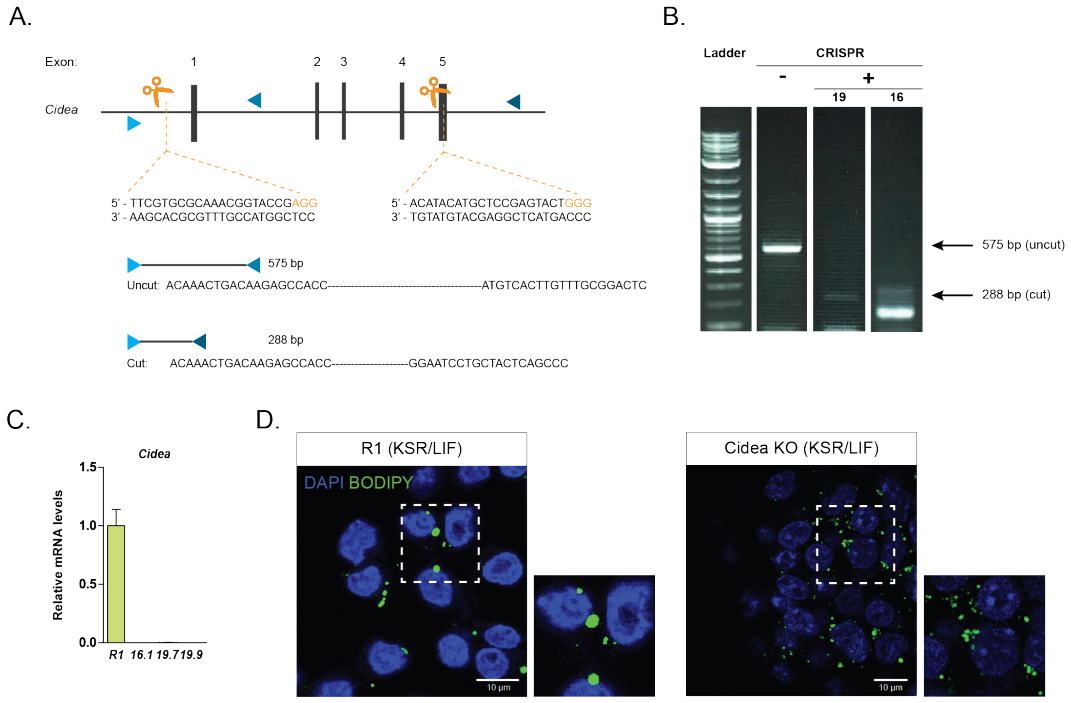


Figure 3.6: Generation and characterisation of Cidea knockout ESCs.

(A) Schematic diagram of CRISPR-mediated genomic deletion of *Cidea*, with full elimination of the targeted region through a pair of Cas9-gRNAs; upstream of exon 1 and within exon 5. The target sites are shown below in larger scale, with the protospacer-adjacent motif (PAM) sequence in orange. Genotyping primers are shown as blue arrowheads and indicated below, resulting in either a cut band (288 bp) upon successful deletion of the *Cidea* locus, or a uncut band (575 bp) if unsuccessful. **(B)** Enzymatic digestion analysis of Cas9-mediated cleavage via PCR. Lane 1, ladder; lane 2, control; lane 3 and 4, Cas9-gRNA treated (clone 19 and 16). Uncut (575 bp) and cut (288 bp) PCR bands are indicated. **(C)** Relative mRNA levels of *Cidea* in Cidea-depleted (16.1, 19.7, 19.9) and control (R1) ESCs cultured in routine (FBS/LIF) media. Data were normalized to the housekeeping genes *S17* and *L19*, and expressed relative to R1. Error bars represent SEM of three biological replicates.**(D)** Confocal imaging in Cidea knockout (16.1) and control (R1) ESCs cultured in KSR media for 24 hours (KSR/LIF), stained for neutral lipid dye BODIPY 493/503 (green). DAPI staining was used to visualise nuclei. Bar, 10μm. A zoom-in of the white dotted square is shown below. Images are representative of three independent experiments.

To gain greater mechanistic understanding of how Cidea functions in ESCs, we stably transfected Cidea KO cells with Cidea mutant forms where specific Cidea protein activities have been perturbed (by Tommy King Mau) (Fig 3.7). Previous studies of Cidea protein function in adipocyte tissue identified two point mutations, R47E and R171E, capable of retarding LD-LD docking and lipid transfer respectively, resulting in LD clustering rather than fusion [127]. Interestingly, the Cidea-depleted phenotype, i.e. clustering of small LDs, was conserved in Cidea KO ESCs when transfected with R47R and R171E mutated Cidea forms as tested upon KSR treatment and BODIPY staining (Fig 3.7). Taken together, these experiments establish Cidea as an essential regulator of LD dynamics and substrate storage in ESCs.

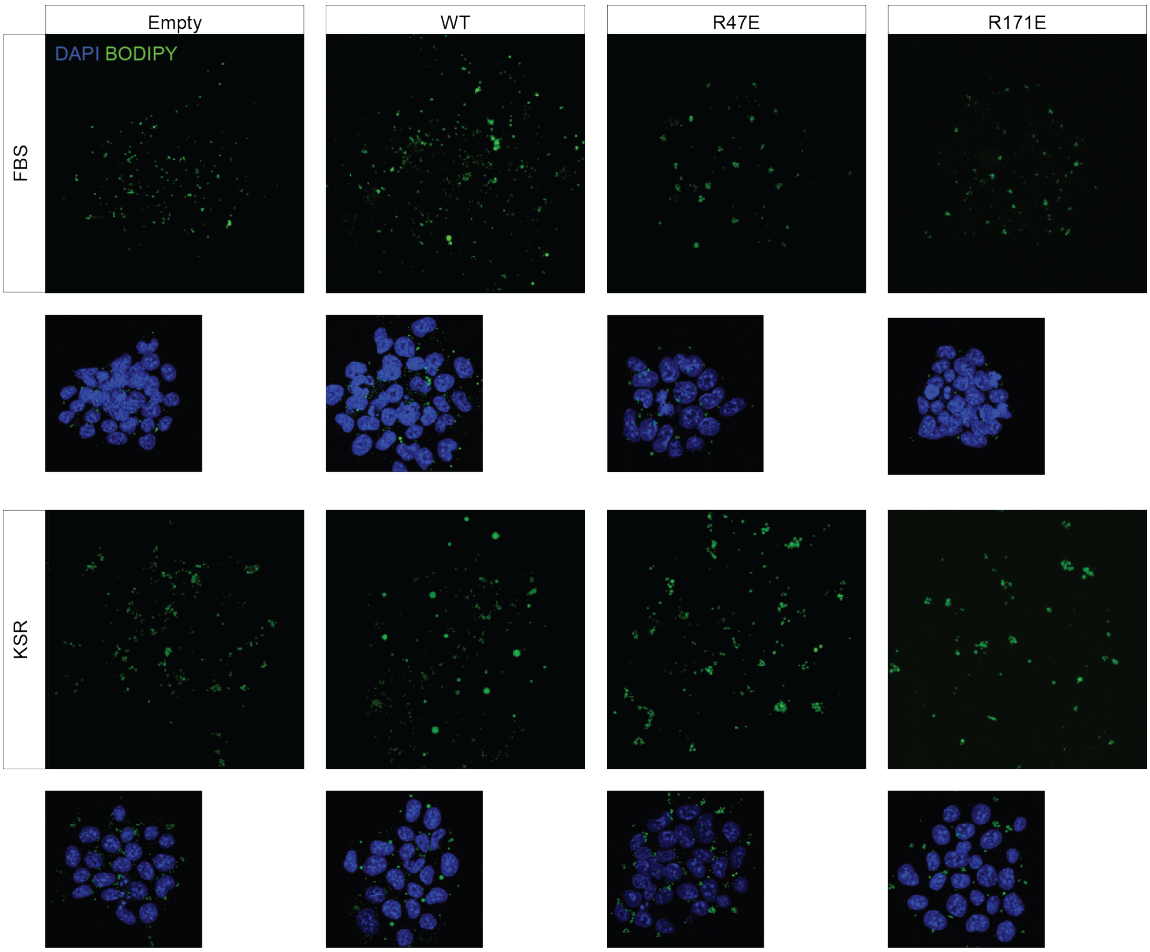


Figure 3.7: Lipid droplet morphology in Cidea knockout and rescue ESCs.

LDs staining with neutral lipid dye BODIPY 493/503 (green) in Cidea KO ESCs rescued by wild-type (WT) Cidea and two mutated forms R47E and R171E. DAPI staining was used to visualize nuclei (blue). Images are representative of three independent experiments.

3.2.6 *Cidea* expression is associated with an undifferentiated ESC state

We have shown that Cidea is highly expressed in ESCs as opposed to more differentiated MEFs, selectively promoting LD enlargement upon KSR treatment (Fig 3.1A). Furthermore, *Cidea* was previously identified as a putative gene target for *Esrrb* and *Ncoa3* in ESCs [185]; two factors that become rapidly down-regulated at the onset of ESC differentiation. This pointed to a possible link between *Cidea* expression and the undifferentiated ESC state. To further investigate this, we next thought to monitor *Cidea* expression profile along with the pluripotency-associated factors *Oct4* and *Esrrb* upon embryoid body (EB)-induced ESC differentiation. Here ESCs were cultured in suspension in the absence of LIF for 6 days to allow the formation of cell aggregates consisting of a PrE-like outer layer and an epiblast-like core. Collection of EB aggregates for gene expression analysis at the indicated time points showed a rapid downregulation of *Esrrb* expression. In contrast, we observed a gradual loss of *Cidea*, mirroring the gradual loss of *Oct4* in these cultures (Fig 3.8A). Next, the DNA motif scanning and enrichment analysis tool named PWM enrichment analysis was used to scan a sequence around the *Cidea* TSS (-500bp and +2000bp) for the presence of DNA words that are significantly more available in this sequence compared to the background. This motif sequence analysis furthermore revealed a significant enrichment for *Esrrb* DNA binding element (ERRE; $p<0.001$) in the vicinity of *Cidea* promoter region. Interestingly, other pluripotency factors like *Oct4* (*Pouf51*) DNA binding element ($p=0.07$) were also detected (Fig 3.8B and Appendix), suggesting that *Cidea* expression is, at least partly, under the control of some pluripotency transcription factors in ESCs.

To test whether *Esrrb* is indeed recruited to *Cidea* regulatory region in ESCs, chromatin immunoprecipitation (ChIP) coupled to qPCR analysis was performed. Locus-specific primers were designed to amplify ERRE-containing regions found in the vicinity of the *Cidea* gene promoter, as indicated by our previous motif sequence analysis. ChIP experiments carried out on chromatin prepared from ESCs confirmed that *Esrrb* was recruited to this locus, in contrast to a control intergenic region, which only showed background levels of enrichment similar to that immunoprecipitated by control IgGs (Fig 3.8C). To validate that *Cidea* promoter activity is dependent on *Esrrb* expression in ESCs, Cidea luciferase reporter assay in conjunction with Esrrb shRNA knockdown was performed. Here we utilized a previously-described luciferase reporter containing a Cidea promoter-Luc element cloned into a pGL3/basic vector. Cidea promoter activity was consequently tested upon 48 hours transient transfection with shRNA vectors against Esrrb or GFP used here as control [185]. As expected, we observed an enhanced luciferase activity over the control in cells transfected with GFP (Fig 3.8D). This increase was consequently partially lost upon depletion of *Esrrb*, confirming a direct role for *Esrrb*, amongst other factors, in regulating *Cidea* expression in ESCs (Fig 3.8D). These experiments demonstrate a role for *Esrrb* in regulating *Cidea* expression, prompting us to further explore a functional link between Esrrb and Cidea-mediated LD regulation.

For this analysis, Esrrb knockout cells kindly provided by Austin Smith and Hitoshi Niwa were used [202]. These Esrrb knockout cells carry a homozygous deletion of *Esrrb*, generated upon tamoxifen-induced deletion of the loxP flanked *Esrrb* second exon transgene (with Cre allele in the endogenous Sox2 locus). As expected, no *Esrrb* transcript was detected in $Esrrb^{-/-}$ in contrast to control cells, yet knockout cells

retained expression of its co-activator *Ncoa3* to similar extent as control cells. As previously described, *Esrrb* loss is accompanied by an attenuation of pluripotency-associated gene expression such as *Oct4* and others, nevertheless the cells retained their ability to self-renew (Fig 3.8E). The functional impact of *Esrrb* depletion on *Cidea* expression and LD morphology was tested upon 24 hours KSR treatment by RT-qPCR and confocal imaging, respectively. BODIPY staining of Esrrb-depleted cells revealed clustering of small droplets as opposed to large droplet formation, thus mimicking the phenotype of Cidea-depleted cells (Fig 3.8F). Interestingly, Erssb$^{-/-}$ cells show a more differentiated colony morphology compared to control cells in both FBS/LIF and KSR/LIF. Furthermore, we observed the emergence of numerous small lipid droplets in the Esrrb-depleted population in FBS/LIF, possibly indicative that the ability to form large lipid droplets is attenuated. These findings were consolidated by the fact that *Cidea* gene expression was slightly reduced in FBS/LIF conditions upon Esrrb knockdown, and by a loss of Cidea induction in Esrrb-depleted cells as opposed to control cells in KSR conditions (Fig 3.8E). Taken together, these findings point to a close association between Cidea expression and the undifferentiated ESC state.

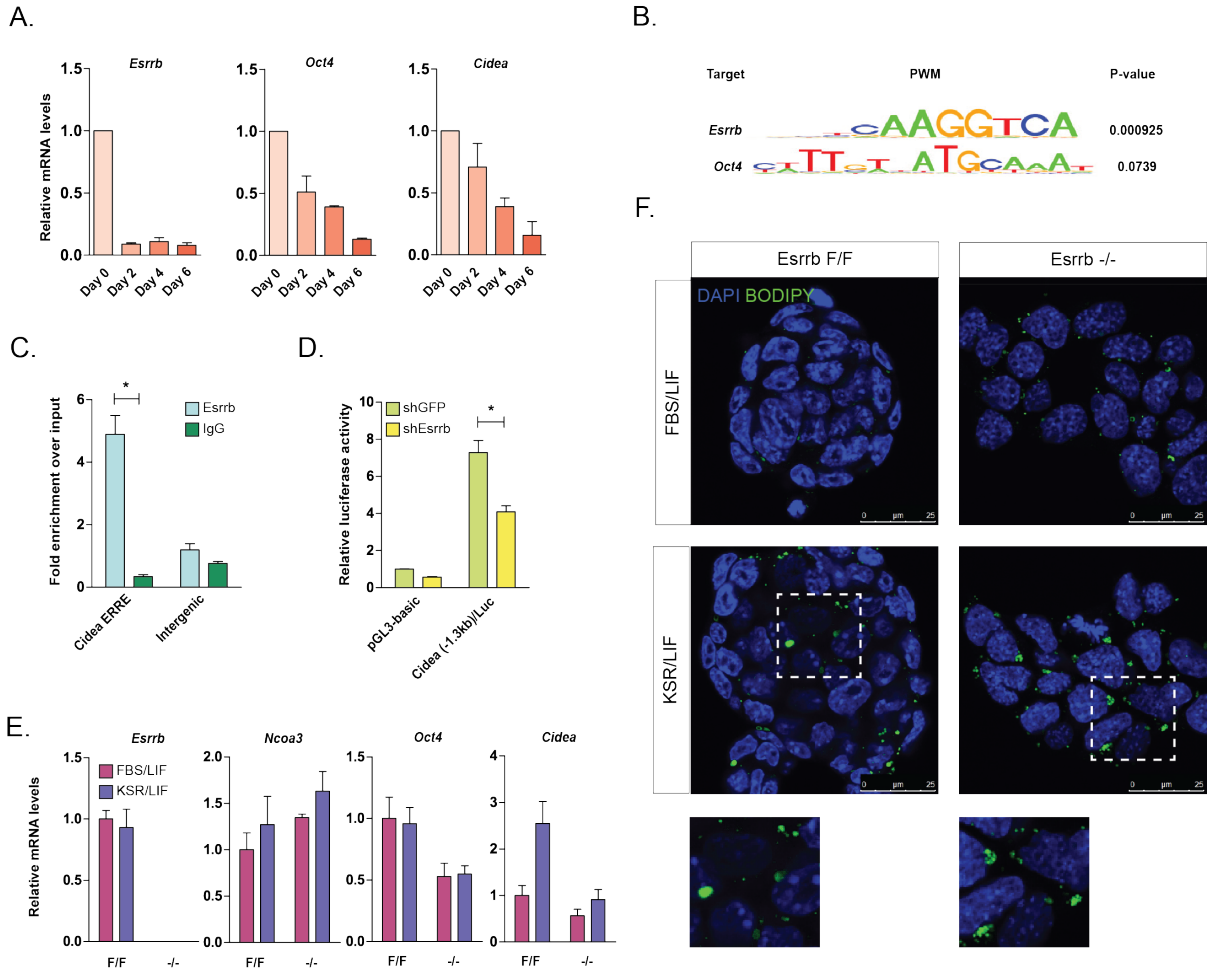


Figure 3.8: Cidea-mediated lipid droplet enlargement is partly regulated by key pluripotency transcription factors.

(A) *Esrrb*, *Oct4* and *Cidea* expression as assessed by RT-qPCR upon embryoid body (EB) formation over 6 days. Data were normalized to the housekeeping genes *S17* and *L19*, and expressed relative to day 0. Error bars represent SEM of 3 biological replicates. **(B)** Motif analysis at the *Cidea* promoter, showing the top hit *Esrrb* (ERRE; p< 0.001), and

Oct4 (*Pou5f1*) DNA binding element (p=0.07), as possible pluripotency-associated regulators of *Cidea* expression. **(C)** Chromatin-immunoprecipitation (ChIP) experiments assessing the recruitment of Esrrb to Cidea locus as examined at its ERRE-containing promoter region, expressed relative to input. Enrichment at an intergenic control region is shown as a negative control. Background enrichment is indicated by control IgGs. Error bars represent SEM of three biological replicates. P<0.05 (*), Student's t test. **(D)** Transient transfection of ESCs with reporter constructs pGL3-Basic or Cidea promoter (-1.3kb)/luc upon Esrrb knockdown (shEsrrb) and control (shGFP) measured 48 hours post transfection. Data were expressed relative to control (pGL3-Basic, shGFP). Error bars represent SEM of three biological replicates. P<0.05 (*), Student's t test. **(E)** *Esrrb*, *Ncoa3*, *Cidea* and *Oct4* expression by RT-qPCR in Esrrb knockout (-/-) and control (F/F) cells, cultured in routine FBS media (FBS/LIF) and upon 24 hour-KSR treatment (KSR/LIF). Data were normalized to the housekeeping genes *S17* and *L19*, and expressed relative to control (F/F) in FBS. Error bars represent SEM of three biological replicates. **(F)** Confocal imaging of Esrrb knockout (Esrrb -/-) and control (Esrrb F/F) ESCs stained for neutral lipid dye BODIPY 493/503 (green), cultured in routine FBS media (FBS/LIF) and upon 24 hour-KSR treatment (KSR/LIF). DAPI staining was used to visualise nuclei. Bar, 25μm. A zoom-in of the white dotted square is shown below. Images are representative of three independent experiments.

3.3 Summary and Conclusions

In summary, in this chapter we uncovered the dynamic presence of lipid droplets in ESCs, regulated by the lipid-droplet associated protein Cidea. Whereas our group previously observed that MEF-derived iPSC established under KSR conditions, a lipid rich media, contained a considerable number of large lipid droplets, we now conclude that the ability to form enlarged lipid droplets under KSR conditions is inherent to ESCs. Our findings demonstrate that ESCs have the capacity of dynamically forming enlarged lipid droplets upon KSR exposure in contrast to MEFs, indicating that enlarged LDs in iPSCs might indeed both reflect the acquisition of an ESC state and the ability of these cells to respond to lipid rich medium by increasing cellular neutral lipid storage.

In an attempt to uncover which intrinsic factors regulate LD dynamics in ESCs but not in MEFs, we screened for adipocyte-expressed molecules with known roles in modulating LD size. This revealed that culturing undifferentiated ESCs in lipid-enriched medium strongly and specifically induced expression of *Cidea*, a LD-associated factor that we know promotes LD enlargement in brown adipocytes via LD-LD fusion and transfer of stored lipid. Whereas KSR also induced the expression of *FFA* receptors, we closely examine the composition of KSR, leading us to uncover that the lipid-rich fraction of KSR can alone recapitulate KSR-induced *Cidea* expression and LD enlargement in ESCs. To directly test whether *Cidea* induction mediates LD enlargement in ESCs, we ectopically expressed Cidea in ESCs using a previously developed construct. These cells suggested that the Cidea protein might be stabilized under lipid-rich conditions, possibly involving post-transcriptional modifications, as previously mentioned but never fully investigated in brown adipocytes. Overall, Cidea overexpressing cells establish that Cidea expression alone is sufficient to promote LD enlargement in the absence of KSR induction. To further determine whether Cidea expression was strictly required for LD enlargement in ESCs, we knocked down Cidea using a previously validated puromycin-selectable shRNA vector. In addition, to exclude off-target effects of the shRNA knockdown, Cidea knockout were also generated (by Tommy King Mau in our lab). These experiments establish Cidea as an essential regulator of LD dynamics and substrate storage in ESCs.

Whereas previous data pointed to a possible link between Cidea expression and the undifferentiated ESC state, we further investigated this using amongst others ESC differentiation assay and Cidea promoter analysis. These experiments demonstrated a role for Esrrb in regulating Cidea expression, prompting us to further explore a functional link between Esrrb and Cidea-mediated LD regulation, using previously established Esrrb knockout cells kindly provide by Austin Smith and Hitoshi Niwa. Using these cells, we confirmed a close association between Cidea expression and the undifferentiated ESC state.

Chapter 4

Characterizing Cidea expression profile and lipid droplet dynamics in the developing embryo *in vivo*

4.1 Introduction

We uncovered that ESCs are capable of forming enlarged lipid droplets in the presence of lipid-rich media, and furthermore revealed that this process is strictly dependent on the LD-associated fusion factor Cidea. ESCs are originally derived from the ICM of pre-implantation blastocysts. Hence, we asked whether LD enlargement might also operate *in vivo* in association with Cidea expression, and whether this property is uniquely acquired by pluripotent cells prior to or after embryo implantation.

Here, we will firstly characterise the expression dynamics of *Cidea* and other lipid-associated gene transcripts at different time-points during early embryo development using publicly available RNA-sequencing datasets. We will examine Cidea protein expression and verify its specific LD location using immunofluorescence on freshly isolated embryos collected at pertinent time-points. The specific tissue-distribution of enlarged LDs will then be carefully investigated using BODIPY staining on peri-implantation embryos, coincident with the transition from naïve-to-primed pluripotency *in vivo*. Finally, we will test the requirement of Cidea for LD enlargement during pluripotency maturation using a newly designed 3 dimensional (3D) ESC differentiation protocol, which mimics the transition from pre-to-post implantation ICM/epiblast development *in vitro*.

4.2 Results

4.2.1 Cidea and lipid metabolism genes show dynamic expression patterns during early development

To examine *Cidea* expression profile *in vivo*, we here interrogated previously generated lineage-specific RNA sequencing datasets from the morula stage to post-implantation embryos - i.e. ICM and epiblast tissues were dissected from pre- and post-implantation embryos respectively and analysed along with morula embryos [203]. Sequencing reads were aligned to the GRCm38 assembly of the mouse genome (mm10), and FPKM (fragments per kilobase of transcript per million mapped reads) conversion was performed to represent levels of expression. We observed that *Cidea* is markedly induced in the ICM of pre-implantation embryos (E3.5) relative to the morula stage (E2.5) as opposed to *Cideb* and *Cidec* (Fig 4.1A), and in agreement with our previous results in ESCs. However, *Cidea* expression is promptly lost in the maturing epiblast right before implantation (E4.5); a critical point in mammalian development. This specific peak of *Cidea* expression coincides with maximal expression of *Esrrb* and its co-regulator *Ncoa3* shown to at least partly regulate the expression of *Cidea* transcript in ECSs. Maintenance of the pluripotency marker *Oct4* and induction of early differentiation markers *Fgf5* and *Otx2* in the post-implantation epiblast (E5.5) confirmed correct development of the investigated embryonic stages (Fig 4.1B). Along with members of the *Cide* gene family, we looked at the expression of the other adipocyte-expressed molecules with known roles in modulating LD size (*Plin 1-5*). Although *Plin1* and *4* were not expressed *in vivo*, *Plin2*, *3* and *5* were expressed and, like *Cidea*, showed maximal expression in the E3.5 ICM (Fig 4.1C). *Plin2* and *3*, however, remained expressed post-implantation, in contrast to *Cidea*. From these data we suggest that *Cidea* might work in cooperation with *Plins in vivo*. Indeed Cidea protein has previously been observed to interact with Plin5 *in vitro* in adipocytes [127]. Interestingly, we also note that the morula-blastocyst transition is marked by a noticeable increase in the transcript expression of enzymes involved in *de novo* lipid synthesis including *Acc1*, *Acly*, and especially *Fasn* (Fig 4.1D). While these genes remain expressed at higher levels up to E5.5, *Dgat1* and *Dgat2* show prevalent expression at E3.5 as seen for *Cidea* (Fig 4.1D). Of note, whereas Dgat1 enzyme functions in the re-esterification of triglyceride, Dgat2 determines the rate of *de novo* synthesis of triglyceride [204]. This suggests that enhanced lipid synthesis might be coupled to and/or inducing enhanced lipid storage in the early blastocyst. Strikingly, *Cidea*, *Plin5* and *Dgat1-2* are sharply and similarly downregulated at the onset of implantation and exit from naïve pluripotency (from E4.5 onwards). Altogether, these findings reveal dynamic expression profiles for *Cidea* and other lipid-associated genes in peri-implantation embryos, and provide the first indication that LD enlargement might operate *in vivo* in a timely manner.

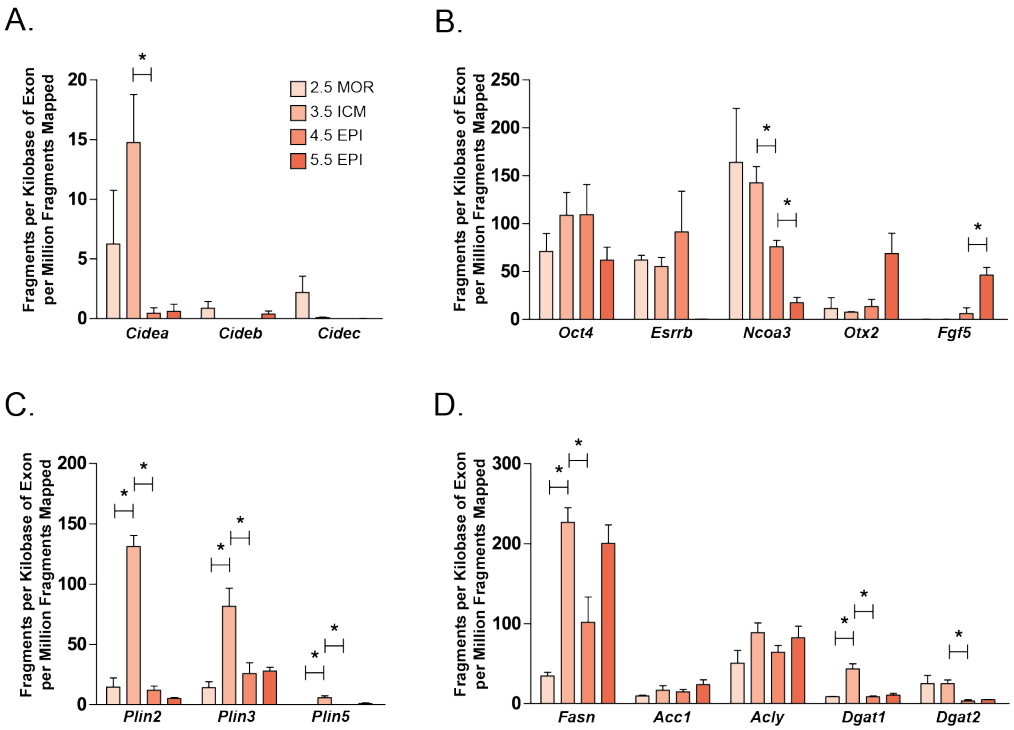


Figure 4.1: Lipid associated gene expression patterns in the early embryo.

(A) *Cidea-c*, **(B)** pluripotency markers (*Oct4*, *Esrrb* and *Ncoa3*) and differentiation (*Otx2* and *Fgf5*) markers, **(C)** *Plin2*, *Plin3* and *Plin5*, **(D)** *Fasn*, *Acc1*, *Acly*, and *Dgat1-2* expression profiles in E2.5 Morula (MOR), E3.5 inner cell mass (ICM), E4.5 and E5.5 epiblast (EPI). These histograms were plotted using previously published RNA sequencing datasets [203]. Sequencing reads were aligned to the GRCm38 assembly of the mouse genome (mm10), and FPKM (fragments per kilobase of transcript per million mapped reads) conversion was performed to represent levels of expression. Error bars represent SEM of three biological replicates. P<0.05 (*), Student's t test.

4.2.2 Cidea protein is coating lipid droplets in the *in vivo* early blastocyst

The prominent transcript expression of *Cidea* at E3.5 was next validated in our hands by RT-qPCR at the E3.5 developmental stage in contrast to E5.5. Embryos were flushed (E3.5) or dissected (E5.5) in M2 medium, followed by pooled RNA extraction of eight embryos, cDNA synthesis and RT-qPCR analysis. As seen in ESCs and by embryo RNA sequencing, we found that *Cidea* is highly expressed in pre-implantation E3.5 whole embryos as opposed to *Cideb* and *Cidec* (Fig 4.2A). In particular, we validated that *Cidea* is indeed selectively expressed at E3.5 in contrast to E5.5 embryos (Fig 4.2A). *Cidea* expression level in ESCs upon 24h KSR treatment (KSR/LIF) was used as a RT-qPCR control. To provide further evidence for LD enlargement in the early blastocyst and its association with Cidea protein expression, we thought to co-stain freshly isolated E3.5 embryos with the lipid droplet specific dye BODIPY, anti-E-CAD antibodies and DAPI. As shown in Fig 4.2B, large LDs could be readily detected in both ICM and TE tissues of pre-implantation embryos. This observation corroborates with previously published data by our collaborator Dr Shankar Srinivas using label-free imaging and harmonic generation microscopy [173]. In this study, LDs appeared larger in size, and their number and density lower in the blastocyst compared to earlier embryonic stages pointing to active LD-LD fusion events. To corroborate high *Cidea* transcript expression and its function as LD fusion factor, we consequently co-stained E3.5

whole-embryos with BODIPY, anti-Cidea and anti-CDX2 antibodies along with DAPI (Fig 4.2C). This confirmed Cidea protein expression *in vivo* appropriately surrounding the surface of large LDs as shown here in Cdx2-postive TE cells of blastocysts (Fig 4.2C). Overall, our findings demonstrate that LD enlargement operates *in vivo* and is associated with Cidea recruitment at the LD surface. The detection of LDs in both ICM and TE prompted us to investigate LD dynamics in a lineage-specific manner prior to and after implantation.

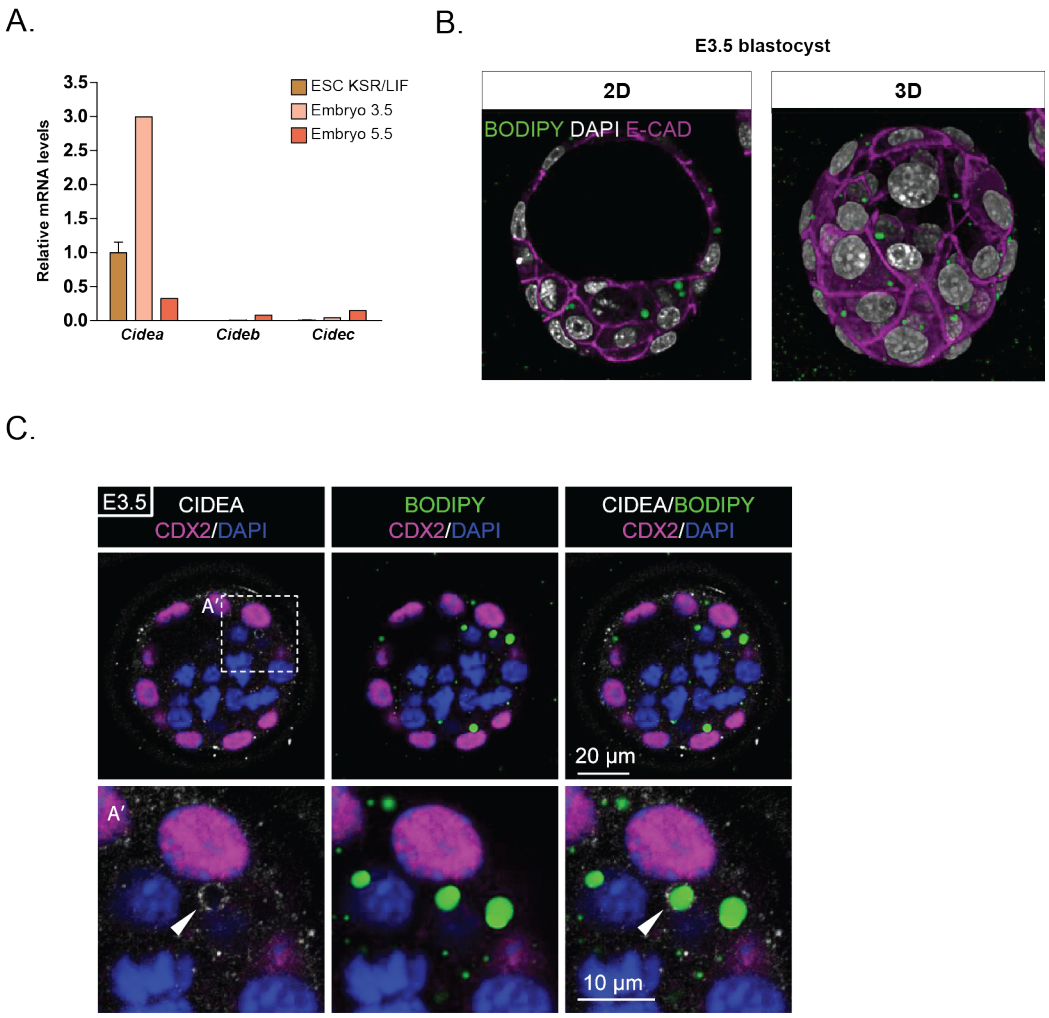


Figure 4.2: *In vivo* analysis of functional Cidea expression.

(A) *Cidea-c* transcript levels as assayed by RT-qPCR in pooled samples of E3.5 and E5.5 whole-embryos expressed relative to ESCs cultured in KSR/LIF. Data were normalized to the housekeeping genes *S17* and *L19*. Data were expressed relative to E14 24h KSR treatment (KSR/LIF). **(B)** E3.5 whole-embryos co-stained with BODIPY 493/503 (green), anti-E-CAD (purple) antibody and DAPI (white). SP5 confocal images are presented as a 2D section (left), and 3D convolution (right). **(C)** E3.5 whole-embryos co-stained with BODIPY 493/503 (green), anti-Cidea (white), anti-CDX2 (purple) antibody and DAPI (blue). A zoom-in of the white dotted square is shown in the lower panel. White arrow indicates Cidea protein ring on the surface of a large lipid droplet. Bar, 20μm in upper panel, 10μm in lower panel. Images are representative of at least three independent experiments.

4.2.3 Lipid droplet tissue-specificity and dynamics across peri-implantation *in vivo*

To investigate lineage-specific LD dynamics, we looked at developmental stages E3.5, E4.5 and E5.5, during which important extra-embryonic lineages are formed. By embryonic day 3.5 the blastocyst consists of the inner cell mass (ICM) located in the blastocyst interior, and the trophectoderm (TE) on the surface of the embryo. The polar TE overlays the ICM, whereas the mural TE encompasses the blastocoel cavity. By E4.5, the epiblast and primitive endoderm (PrE) layers have segregated in the ICM. After implantation (E5.5) the PrE gives rise, amongst other tissues, to the visceral endoderm (VE), which covers the epiblast and the extra-embryonic ectoderm (ExE) - a derivative of the polar TE [10, 205, 206]. To analyse and quantify LD sizes and numbers in the maturing ICM/epiblast and specific extra-embryonic tissues, peri-implantation embryos were co-stained with the neutral lipid dye BODIPY and anti-E-CAD (used as a cell surface marker) along with DAPI. Flushed or dissected embryos were mounted on glass slides customised with tape to create small chambers protecting the integrity of embryos during staining and washing steps. Embryos were then imaged using Zeiss LSM710 confocal microscope at an axial step-size of 0.5-1.0μm. A minimum of 3 embryos were stained at each developmental stage. Image analysis, 3D rendering, calculation of LD sizes and numbers were done using the Volocity software (see Fig 4.3A for an outline of data analysis process). In each 2D section, different embryonic tissues were manually outlined guided by the cell surface marker E-CAD, and to demonstrate embryo multi-lineages, by the transcription factor Esrrb as shown here on one example picture of E5.5 embryos analysed in this study (2D outline; Fig 4.3B, upper left). Using these 2D sections, Volocity software reconstitutes the 3D shapes of the stained embryos (Fig 4.3A; upper right); LDs (stained with BODIPY) falling within a selected 3D shape can then be exclusively visualized (Fig 4.3A; lower left). Using automatic segmentation, 3D projections are made of the LD signals (Fig 4.3A; lower right) followed by calculation of LD sizes and numbers in the specific tissue sections outlined. This process was repeated to detect all LDs in each embryonic tissue in individual embryos of the 3 different stages (E3.5, E4.5 and E5.5) (Fig 4.3C).

Here we observed a variety of LDs sizes, which were also abundant throughout the pre-implantation E3.5 embryos (ICM and trophectoderm), with a majority of the droplets observed being larger than 5μm^3 (93.5% and 87.4% in the ICM and TE respectively) up to supersized LDs (>50μm^3) most prevalently seen in the ICM (5.3% and 1.3% in the ICM and TE respectively) (Fig 4.3B; orange). Such heterogeneity in LD sizes are likely indicative of an active and cumulative process of LD formation and fusion in the pre-implantation embryos. By the late E4.5 stage, however, we observed a complete loss of supersized LDs and the prevalence of small (<5μm^3) LDs in the epiblast, as well as in the newly formed PrE - two lineages that arise from the E3.5 ICM. Interestingly, at this stage, polar and mural TE tissues set apart in terms of LD composition with the latter only retaining a substantial number of large LDs with a strong representation of supersized LDs (9.8% out of total). This might suggest a novel marker for the polarisation of the bilateral axis in late blastocysts [207]. At E5.5 all tissues examined contain small LDs, apart from the most distal VE overlying the epiblast, a group of cells that determine anterior-posterior polarity of post-implantation embryos [205]. Taken together, our findings suggest a building up of large

lipid storage in early blastocyst and mobilisation in a timely and tissue-specific manner in the pluripotent and trophoblast tissues. The appearance of supersized LDs in the polar TE and distal VE might represent an independent wave of LD generation and fusion coincident with establishment of embryo asymmetry.

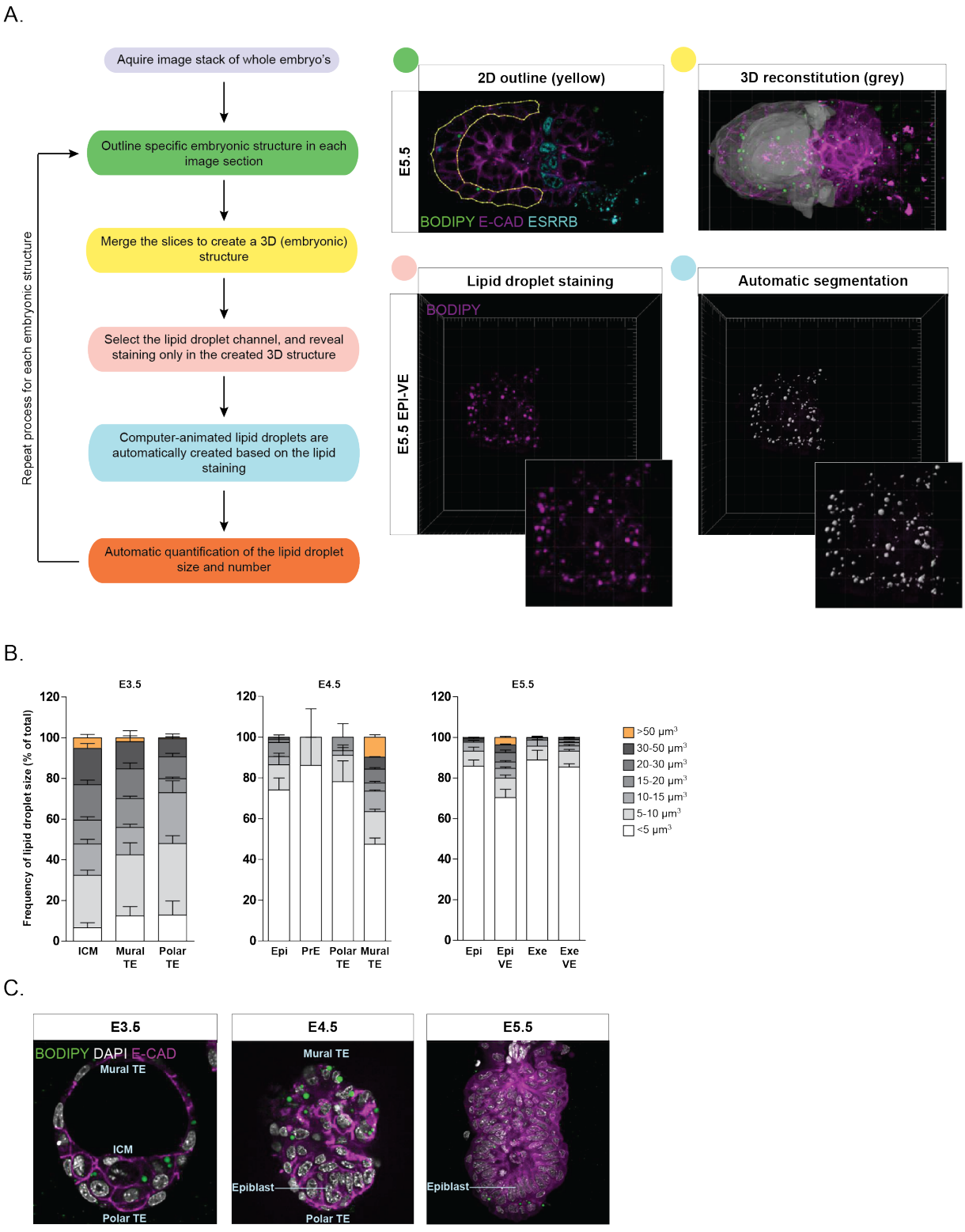


Figure 4.3: ***In vivo*** **analysis of lipid droplet size and distribution during early development.**

(A) Schematic of 3D reconstitution from 2D images. In each 2D image, specific embryonic tissues are outlined in yellow (here, the visceral endoderm overlying the epiblast (EPI-VE) from E5.5 embryo). Consequently, all outlines from each individual image section are merged together to reconstitute the 3D shape shown in grey. Lipid droplets, stained with

BODIPY, falling within a selected 3D shape can then be exclusively visualized, and their size and total number across the embryonic structures automatically quantify. **(B)** Quantification of all lipid droplets, size (μm^3) and number (percentage of total LDs) in various tissues throughout development (E3.5, E4.5, E5.5) performed on freshly isolated embryos **(C)** co-stained with BODIPY 493/503 (green), anti-E-CAD (used as a cell surface marker, purple), and DAPI (white). Embryos were imaged using Zeiss LSM710 confocal microscope at an axial step-size of 0.5-1.0μm. A minimum of 3 embryos were stained at each stage. Image analysis, 3D rendering, calculation of LD size and number were done using Volocity software. ICM, inner cell mass; TE, trophectoderm; Epi, epiblast; PrE, primitive endoderm; VE, visceral endoderm; Exe, extra-embryonic ectoderm.

4.2.4 ESC organoids in extracellular matrix recapitulate peri-implantation morphogenesis

LD dynamics in the pluripotent compartment across peri-implantation specifically caught our attention in the view of our studies in ESCs, and thus prompted us to more closely study LD dynamics using newly designed 3D differentiation of ESCs [206]. Indeed, while implantation events are most difficult to study *in vivo* due to the fact that they would take place within the maternal tissue and therefore hidden from view, interestingly, ESCs were recently shown capable of differentiating in a 3D protein matrix (e.g. Matrigel), where they can propagate, polarize and self-organize into rosette-like structures with the formation of a central lumen; a series of events thought to mirror the formation of the epiblast cylinder and pro-amniotic cavity *in vivo* (Fig 4.4A). In particular, we aimed here at precisely monitoring the kinetics of Cidea expression and LD enlargement and/or subsequent mobilisation upon 3D ESC differentiation, also in relation with remodelling of the transcriptional pluripotency network (from naïve to primed state) and morphogenesis events. For this, wild-type R1-ESCs cultured in serum/LIF were resuspended into matrigel as single cells and grown for 72 hours, with data collection time-points at the start (0h), 24h, 48h and 72h post induction. Confocal imaging of these organoids revealed a maximal LD enlargement by 24 hours (Figure B, upper panels), at which time *Cidea* transcript expression will start declining, and a primed pluripotency transcriptional network is established (Figure B, lower panels). By 48 hours, large LDs were not detectable, coincident with cell epithelisation and the formation of a nascent cavity (hollowing) as delineated by dense F-ACTIN staining at the apical sides of epithelised cells. This sequence of events thus closely recapitulates the gene expression dynamics we observed by interrogating *in vivo* RNA-seq datasets (Fig 4.1), and are consistent with the presence of supersized LDs in pre-implantation embryos and subsequent mobilization in the maturing epiblast of the late E4.5-E5.0 embryo (Fig 4.3). What is then the role of Cidea in LD enlargement during organoid development? For this we subsequently induced Cidea knockout ESCs to form organoids in a similar manner (Fig 4.4C). In contrast to control cells, these Cidea KO organoids failed to show any LD enlargement by 24 hours of differentiation. This agrees with the suggested role of Cidea as a LD fusion factor in both embryonic development and ESCs. No large LDs were detected at later differentiation times (48 and 72 hours) as similarly seen in wild-type and knockout organoids. Interestingly, we observed, however, that a lack of LD enlargement and/or timely mobilization was accompanied by morphological changes in terms of cavity formation, with the seemingly appearance

of multiple lumen in Cidea KO organoids instead of a single, expanding cavity in wild-type organoids (see Fig 4.4B-C; 72 hours). In contrast, no changes in the kinetics of exit from naïve ESC pluripotency was noticed in the absence of *Cidea* with the prompt downregulation of *Esrrb* by 24 hours and concomitant upregulation of primed pluripotency markers (*Otx2*, *Fgf5* and *Brachyury*) (Fig 4.4B-C; lower panels) as seen in wild-type organoids. This argues that the abnormal lumen formation we observed in the absence of Cidea might be directly linked to defective LD dynamics rather than changes in ESC differentiation kinetics upon organoid development. An in-depth exploration of this mutant phenotype together with attempts to rescue the observed defect by re-introducing a fully functional versus mutated Cidea forms (e.g. point-mutations abrogating Cideas ability to either promote LD-LD docking or LD-LDfusion [127]) will be required to formally establish a potentially important and novel role for LDs in orchestrating key cellular remodeling events upon embryo implantation.

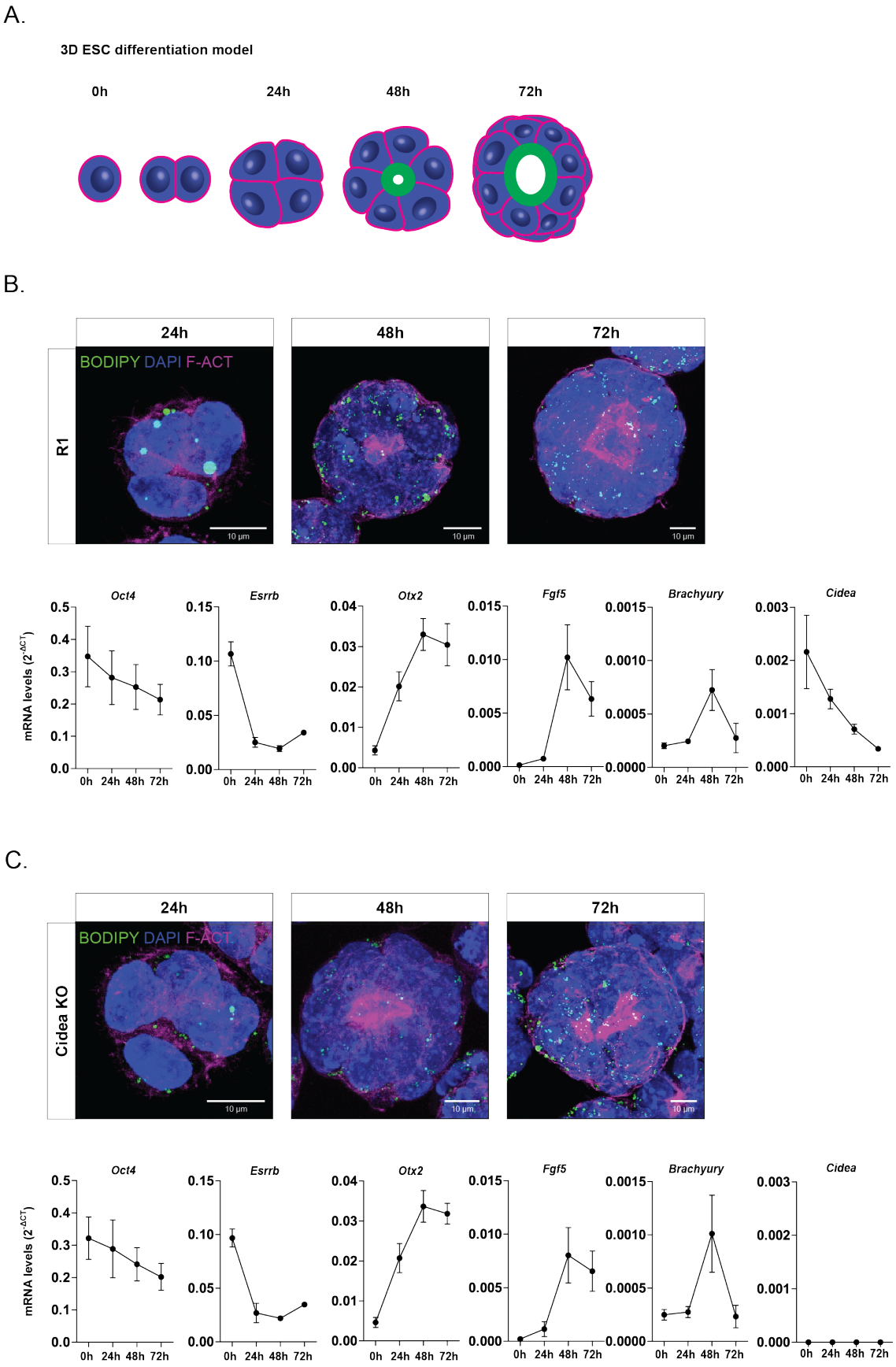


Figure 4.4: Cidea knockout ESC organoids display aberrant lumen formation.

(A) Schematic drawing of ESC organoid progression and lumen formation. Accumulation of F-ACTIN (F-ACT) at the apical domain is indicated in green. **(B, C upper panels)** Confocal imaging of lipid droplet staining with neutral lipid dye BODIPY 493/503 (green) in control (R1) and Cidea knockout (KO) ESCs in the course of 72 hour organoid

differentiation. Each picture represents a three-dimensional image of merged Z-stack images. DAPI staining was used to visualise nuclei (blue), and F-ACT was used as a cytoskeletal marker (purple). Images are representative of at least two independent experiments; at least twenty spheres were captured per experiment. **(B, C lower panels)** mRNA levels of key pluripotency (*Oct4*, *Esrrb*, *Otx2*), and differentiation (*Fgf5*, *Brachyury*) markers, and *Cidea* as assayed by RT-qPCR in ESC organoids 24, 48 and 72 hours post induction. Data were normalized to the housekeeping genes *S17* and *L19*. Error bars represent SEM of two biological replicates with at least twenty technical replicates. Bar, 10μm. Courtesy of King Hang (Tommy) Mau.

4.3 Summary and Conclusions

In summary, we established in this chapter that LD enlargement as described in Chapter 3 also operates *in vivo* in association with enhanced *Cidea* expression as seen upon the transition from morula to early blastocyst stages. Examining the expression profiles of lipid-associated genes *in vivo* furthermore suggested that enhanced lipid synthesis might be coupled to and/or inducing enhanced lipid storage in pre-implantation embryos. At the onset of implantation and exit from naïve pluripotency, a sharp down-regulation in the transcript levels of *Cidea* along with other genes encoding lipid-storing proteins (i.e. *Plin5* and *Dgat1-2*) was however observed. These data indicated that LD enlargement might operate *in vivo* as primed pluripotency establishes. An active role for Cidea in LD enlargement *in vivo* was further suggested by co-staining freshly isolated E3.5 embryo with anti-Cidea antibody and the lipid droplet marker BODIPY. As expected, we detected that Cidea protein surround large lipid droplets as seen in ESCs, however interestingly these large LDs were found throughout the embryo (i.e. in ICM and extra-embryonic TE cells). By investigating the number and size of BODIPY-stained LDs in peri-implantation embryos (late E4.5 and E5.5) alongside early blastocyst (E3.5), we interestingly uncovered that timely LD enlargement and mobilisation operate in a tissue-specific manner. In particular, we observed that enlarged LDs in the early blastocyst were selectively mobilised in the epiblast at the onset of implantation. With a particular focus on epiblast maturation we next investigated the requirement of Cidea expression for LD enlargement. As Cidea KO mice were not available at the time of this study, we made use of a 3D ESC differentiation model recapitulating *in vitro* the molecular and cellular remodelling events that occur upon embryo implantation *in vivo* [206]. Using this model, we were thus able to closely dissect the relation between LD dynamics and the naïve-to-primed pluripotency transition, but also morphogenesis events. Interestingly, we found that inhibiting LD enlargement by Cidea depletion does not impact on transcriptional rewiring from naïve-to-primed pluripotency. However, this system revealed morphological changes in Cidea-depleted organoids, an intriguing phenotype that will require further investigations.

Chapter 5

Assessing the impact of Cidea-modulation on embryonic stem cell biology

5.1 Introduction

Cidea is known to play an important role in adipocytes/oxidative tissues [128, 156], however a role for Cidea in embryonic stem cells and early development was not recognized before. We observed that ESCs and pluripotent cells *in vivo* have the ability to store lipids into LDs in a Cidea-dependent manner, in addition to timely LD mobilization and lipid usage upon implantation *in vivo*. However, the functional significance of these observations remains to be fully explored. Taking advantage of established Cidea overexpressing and depleted ESC models (see Chapter 3), we here examine the impact of modulating Cidea expression and hence LD enlargement on ESC biology and metabolism.

In this chapter the impact of Cidea-modulation on ESC self-renewal and differentiation potential was explored taking advantaged of previously mentioned Cidea overexpressing, knockdown and knockout cell lines. Characterization of the phenotype and functional abilities of Cidea-modulated ESCs was conducted using well-established methodologies such as self-renewal assays and embryoid body formation. A role for Cidea has been extensively studied in brown adipocyte tissues where Cidea plays a key role in regulating lipid storage as substrate for β-oxidation and heat production upon stimulation [127]. This prompted us to investigate whether the metabolic states of ESCs might be changed upon enforced or inhibited LD enlargement in self-renewing conditions. For this, we study the metabolic profiles of our Cidea-modulated ESCs combining GC-MS-based approaches and *in situ* measurements of metabolic status (e.g. oxidation and glycolysis) on a Seahorse Bioanalyzer.

5.2 Results

5.2.1 Modulating Cidea expression in ESCs does not impact on their self-renewing abilities

We here take advantage of established Cidea overexpressing and depleted ESC models from Chapter 3 (i.e. CAG-promoter driven plasmid Cidea over-expression, shRNA Cidea knockdown, CRISPR/Cas9 Cidea knockout). The three different ESC lines, Cidea-OE, KD and KO, were able to be routinely maintained in culture in the presence of leukemia inhibitory factor (LIF) and serum, suggesting that modulating the expression of this protein might not be detrimental to the maintenance of an undifferentiated ESC state. Although shCidea-transfected cells were initially destabilization, indicated by more differentiated colonies under normal culture conditions compared to control cells, three stable Cidea-KD ESC clones could be derived from this pool of transfected cells (see Chapter 3). To fully evaluate the undifferentiated state of the Cidea-modulated ESC lines, the expression of pluripotency-associated markers was investigated using real-time quantitative expression analysis (RT-qPCR). The transcript levels of the pluripotency-associated markers was overall unchanged upon ectopic expression of *Cidea* or its depletion in ESCs. *Oct4* transcript levels appeared slightly lower in Cidea-OE ESCs and variably expressed in Cidea-KD cells compared to their respective controls (Fig 5.1A). However, this was not accompanied by a loss of naïve pluripotency markers (*Esrrb*, *Klf4* and *Tbx3*) and/or noticeable increase in the expression of the early differentiation marker *Brachyury* (*T*) in any cell lines examined (Fig 5.1A). Consequently, growth rate was assessed by scoring the number of cells cumulating in routine culture conditions over seven consecutive passages, and found to be similar between control and Cidea-modulated ESC populations (Fig 5.1B). Next, Alkaline Phosphatase (AP) activity was used as an indicator of undifferentiated state in colony forming efficiency assays. For this, Cidea-modulated and control cells were plated at low density, cultured in the presence or in the absence of LIF for 7 passages, and then scored as undifferentiated, mixed or differentiated colonies based on the observed AP staining intensity and colony morphology (Fig 5.1C). In the presence of LIF, all cell lines studied (Cidea-OE, KD and KO and their respective controls) demonstrated similar self-renewing abilities regardless of Cidea expression level. In all cases, over 90% of colonies were scored as undifferentiated, showing a typical round and compact morphology and strong AP staining, whereas the remaining colonies were almost all scored as mixed with bright AP-positive centres surrounded by a ring of flattened differentiated cells. Very few (<1%) of the colonies were differentiated cells, displaying a sparse morphology and little or no AP staining. As expected, in the absence of LIF, the majority of colonies stained negative for AP, indicative of spontaneous differentiation, or mixed (>75%). In summary, these data demonstrate that Cidea-modulated ESC lines retain an undifferentiated state in culture, with similar growth rates and normal self-renewal abilities as compared to their controls.

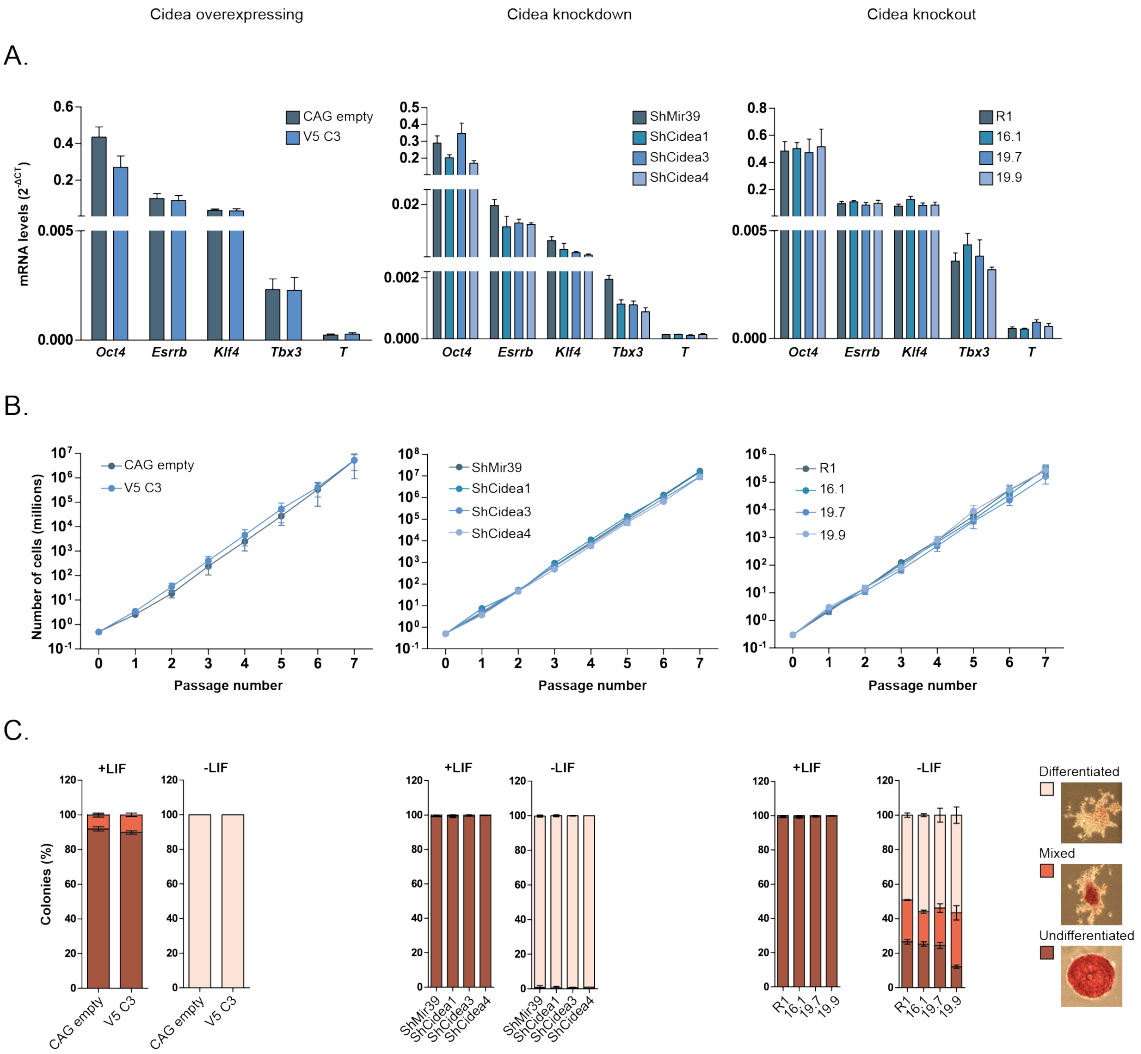


Figure 5.1: Cidea-modulated ESCs retain normal self-renewal ability.

(A) Transcript levels of pluripotency-associated markers *Oct4*, *Klf4*, *Esrrb*, *Tbx3* and early differentiation marker *Brachyury* (*T*) in Cidea-modulated cells and their corresponding control (Cidea-OE V5 C3 and control CAG-empty; Cidea-KD clones 1, 3 and 4, and control ShMir39; Cidea-KO clones 16.1, 19.7 and 19.9 and control R1). Data were normalized to the housekeeping genes *S17* and *L19*, and expressed relative to controls. Error bars represent SEM of three biological replicates. **(B)** Growth curve of cells mentioned above in self-renewing conditions over 7 passages (14 days). Plot represents an average of cell numbers scored in three independent experiments (with the exception of ShCidea1 and 4, which indicates a single experiment). Error bars indicate SEM. **(C)** Percentage of colony types scored in cells growing with (+) or without (-) LIF for 7 days. Colonies were counted and scored as undifferentiated, mixed or differentiated according to the intensity of alkaline phosphatase (AP) staining. Plots represent percentage of colonies counted in three biological replicates. Error bars indicate SEM.

5.2.2 Cidea knockdown impacts on embryoid body morphology

Pluripotent ESCs can be induced to differentiate into somatic derivatives when cultured under permissive conditions. To further assess whether Cidea modulation impacts on ESC differentiation abilities, Cidea knockdown and overexpressing cells were induced to form embryonic bodies. This involves culturing ESCs in suspension in the absence of LIF and in reduced serum level over 9 days, during which cell aggregates will form allowing the spontaneous emergence of cells derived from the three embryonic germ layers. EB morphology was recorded on a daily basis (Fig 5.2A-B; upper panels), and samples were collected at different time-points for subsequent mRNA expression analysis (Fig 5.2A-B; lower panels). Under these conditions Cidea-OE EB morphology was similar to their control counterparts with increasing size during the course of differentiation (Fig 5.2A). Both cell populations showed a progressive decline in the expression of pluripotency markers, *Nanog* and *Oct4*, indicative of successful differentiation. The expression of the early epiblast *(Fgf5)* and primitive streak (*Brachyury* and *Mixl1*) markers peaked at day 3 and day 6 respectively, resuming basal levels by day 9 of EB differentiation as expected (Fig 5.2A-B; lower panels). Both Cidea-KD and control EBs showed normal and similar morphology at early stages of differentiation (day 3) (Fig 5.2B). Interestingly, however, by day 6 of differentiation, differences between the two cultures became evident. Notably, Cidea-KD ESCs tend to form numerous EBs of variable sizes and irregular shapes. By day 9, knockdown cultures contained few relatively normal EBs, while the vast majority of them formed a cystic-like structure (Fig 5.2B). These cystic EBs are semi-transparent and of low cell density, which might be indicative of ongoing cell death events. This atypical morphology was uniquely seen in Cidea-KD EBs, but not in Cidea-OE EBs and control populations. At the same time, Cidea-KD EBs showed expected gene expression patterns during the course of differentiation (Fig 5.2B; lower panel). However, interestingly, we noticed that the expression of *Fgf5* was retained or lagging in Cidea-KD EBs, persisting up to day 6 of differentiation (Fig 5.2B; lower panel). This might suggest that not all Cidea-depleted cells were able to progress into differentiation beyond an early epiblast-like stage, or that the differentiation process itself was less synchronous in the absence of Cidea. No major differences were observed in the induction kinetics of late differentiation-associated markers *Brachyury* and *Mixl1*. *Cidea* showed the expected expression pattern of down-regulation alongside the pluripotency markers upon differentiation, however with different initial day zero expression levels according to manipulation (knockdown/overexpressing). Taken together, we conclude that while Cidea knockdown cells are able to normally exit the naïve ESC state, high incidence of apoptosis and/or abnormal morphogenesis events might be occuring in the absence of Cidea as indicated by the formation of cystic-structure.

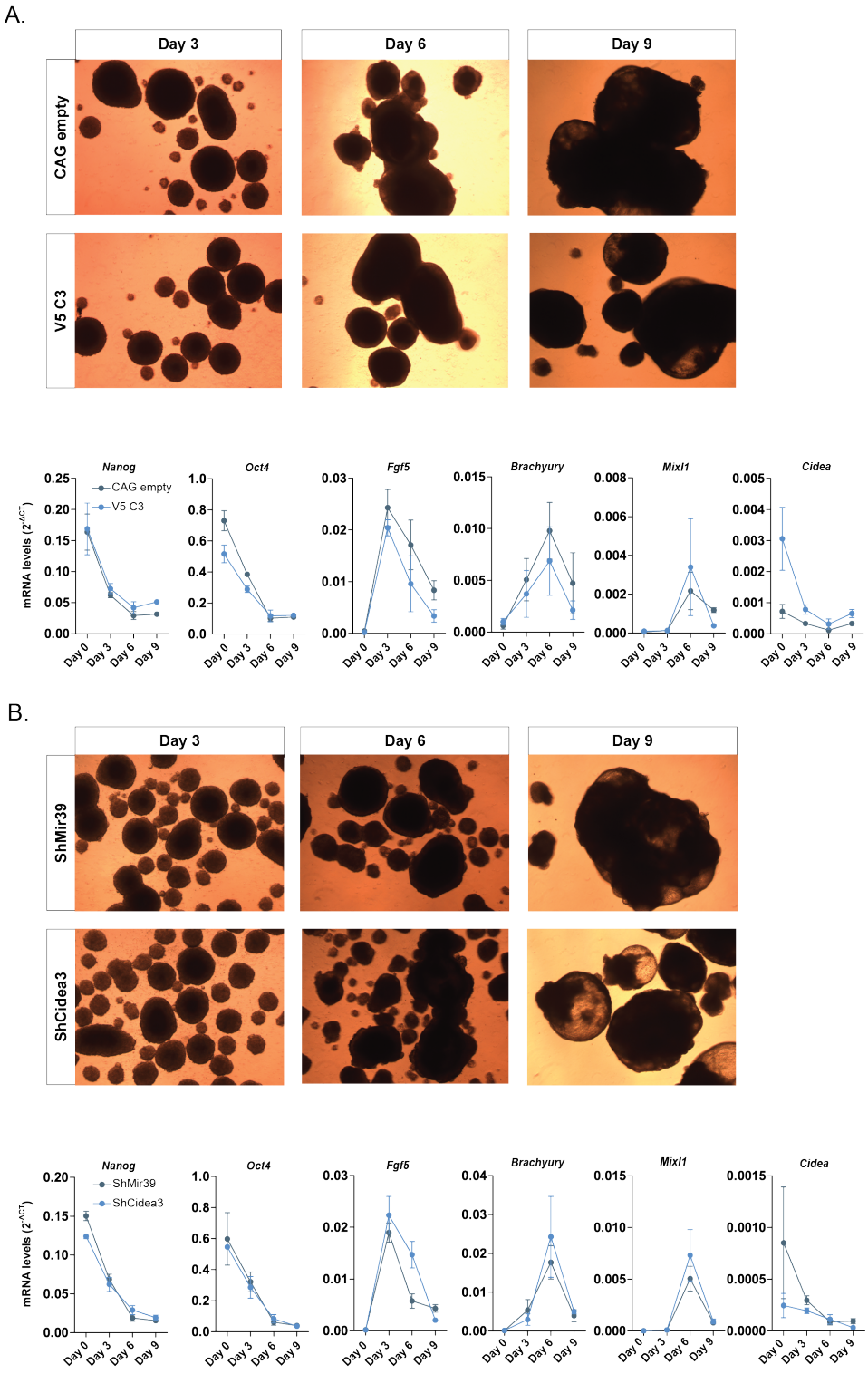


Figure 5.2: Embryoid body (EB) formation in Cidea overexpressing and knockdown ESCs.

(A) Cidea-OE (V5 C3) and control (CAG-empty) cells, and **(B)** Cidea-KD clone 3 (ShCidea3) and control ShMir39 cells. **(A, B upper panels)** ESCs were cultured in suspension and induced to differentiate upon EB formation in the absence of LIF and reduced serum level. Representative phase-contrast images of EBs at different time-points of differentiation are shown. **(A, B lower panels)** Transcript levels for pluripotency-associated (*Nanog*, *Oct4*), epiblast (*Fgf5*), mesoderm (*Brachyury*, *Mixl1*) markers, and *Cidea* itself in WT and Cidea-modulated derived EBs collected at day 0, 3, 6 and 9 of differentiation. Data were normalized to the housekeeping genes *S17* and *L19*. Error bars represent SEM of three biological replicates.

Cystic-structures in EB formation has been previously described in the literature as an indication of cavity formation (Fig 5.3A) [208]. In this model, apoptosis initially occurs in cells located around the middle of the EB appearing as split-like clefts, in which peripheral F-ACTIN replaces the apoptotic zone. During the course of differentiation apoptosis and cavitation then extend into the central portion of the surviving EB, eventually presenting the cystic structure. The partially polarized cells that form a rim around this cavity become pseudostratified, and F-ACTIN localizes at the apical zone of the polarizing epiblast [208]. Normally the cystic morphology is observed at later differentiation time-points (e.g. 12-15 days post EB induction), once again indicative of an advanced or unscheduled cavitation formation in Cidea-depleted cells. Therefore, we consequently investigated earlier time-points to examine the presence of an early cavity formation at the centre of Cidea-depleted EBs. Here, EBs were stained during differentiation at day 2, day 5 and day 8, for cytoskeleton marker F-ACTIN (purple) and adherent junction marker E-CAD (green). Z-stack confocal images were acquired from the entire embryoid body, and images in Fig 5.3 represent a 2D section through the middle of the newly formed EB. Control EBs show first the appearance of a central focal point of intense F-ACTIN/E-CAD staining at day 5 of differentiation, followed by the formation of lumen with borders intensively stained with F-ACTIN/E-CAD. In contrast, in KD EBs, a large cavity is already apparent by day 5 of differentiation consistent with the early formation of the cystic structure at day 9 of differentiation (Fig 5.3B). This advanced/unscheduled cavitation is indeed indicated by the cavity formation as early as day 2 post-EB induction which was not observed in control cells, where the cavity is only clearly visible at day 8. This morphological phenotype, i.e. the early detection of an internal lumen in Cidea-depleted EBs, was verified in the same experimental set-up with Cidea knockout ESCs (Fig 5.3C). Altogether, these data suggest an interesting potential link between Cidea expression and lumen formation in this ESC differentiation model. Yet, many questions still remain e.g. whether this in turn is linked with the function of Cidea in promoting LD enlargement? Whether advanced/unscheduled cavitation observed in this model is related to the timely release of lipids at the onset of implantation as seen *in vivo* (see Chapter 4), the time at which remodeling of cellular states is happening (i.e. epiblast epithelialization and lumen formation) [4].

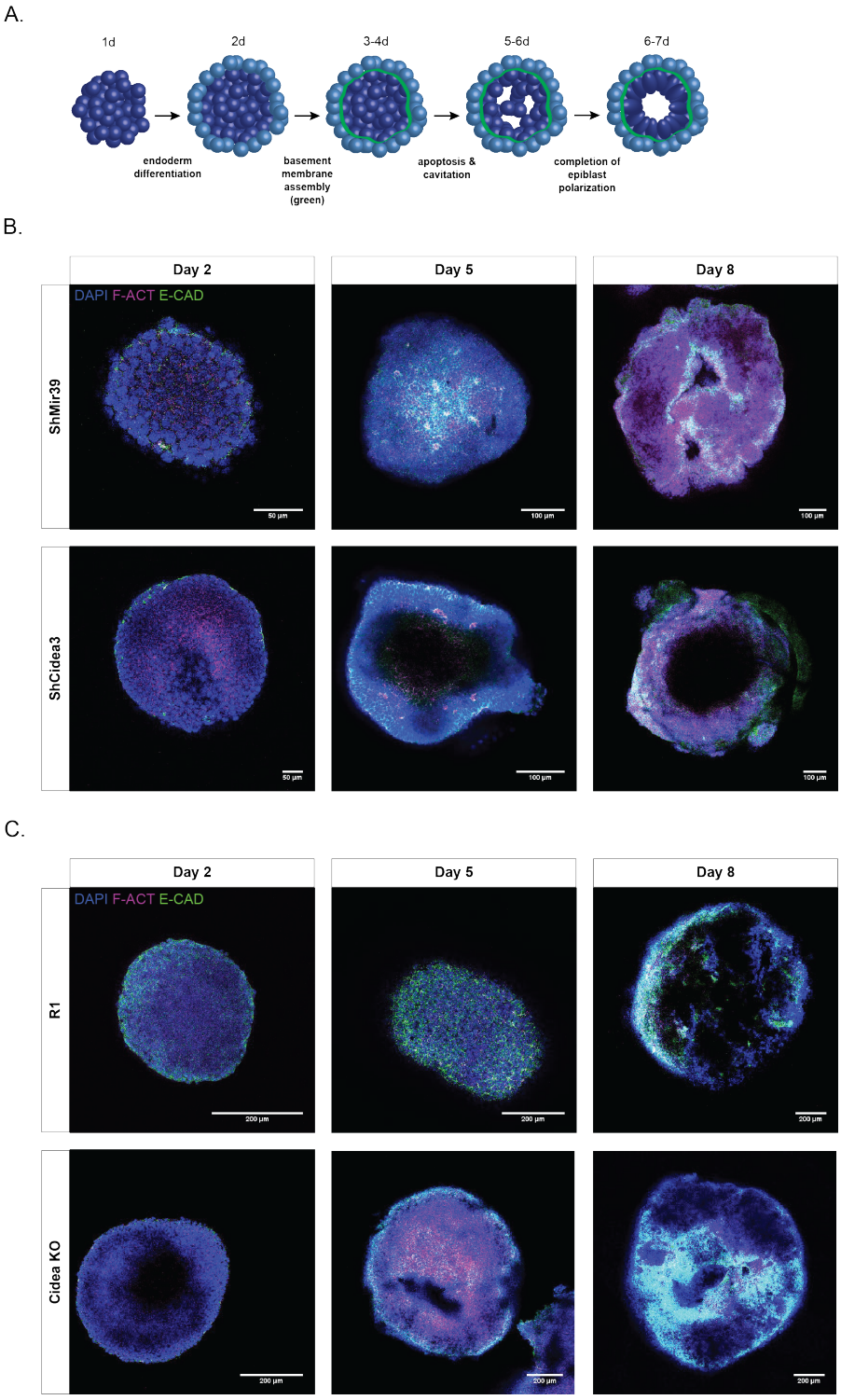


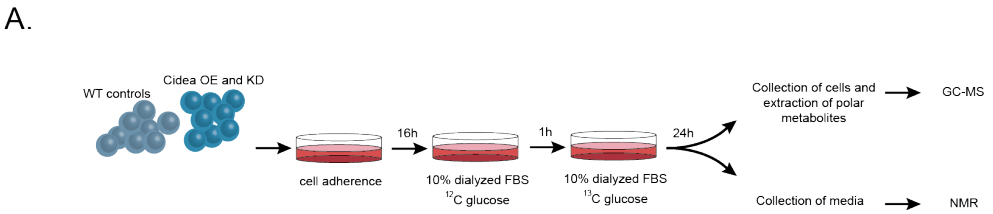
Figure 5.3: Cavity formation in embryoid bodies (EBs) from Cidea knockdown and knockout cells.

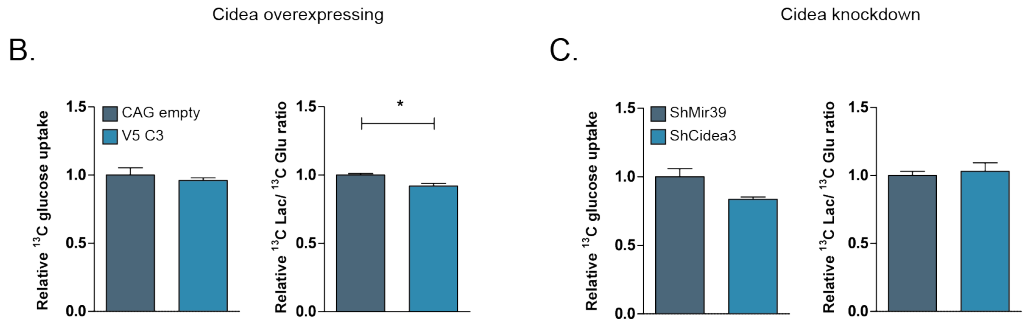
(A) Schematic drawing of embryoid body cavitation, an *in vitro* model commonly used for studying the formation of rosette-like structure and pro-amniotic cavity in post-implantation embryos [208]. **(B, C)** ESCs were cultured in suspension and induced to differentiate upon EBs formation in the absence of LIF and reduced serum level. Confocal imaging of EBs differentiation from **(B)** Cidea-KD and **(C)** Cidea-KO cells at day 2, day 5 and day 8, stained for cytoskeleton marker F-ACTIN (purple) and adherent junction marker E-CAD (green). DAPI staining was used to visualise cell nuclei (blue). Z-stack confocal images were acquired from the entire embryoid body; images represent a 2D section through the middle of the EB. Bars, 50, 100 and 200μm. Images are representative of three independent experiments. Courtesy of King Hang (Tommy) Mau.

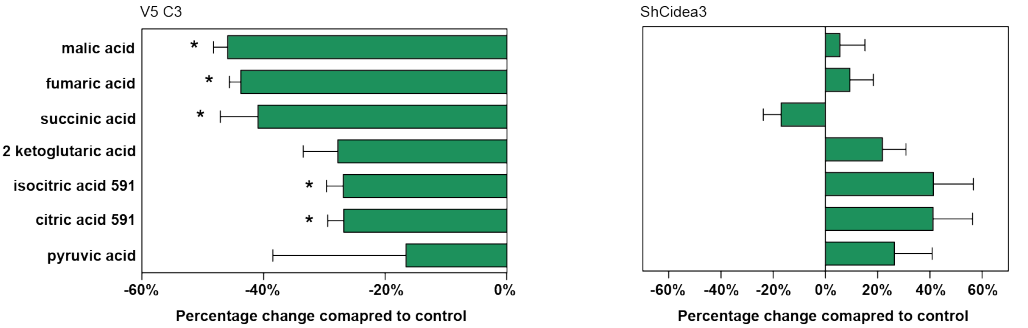
5.2.3 Characterising the impact of Cidea modulation on ESC metabolism

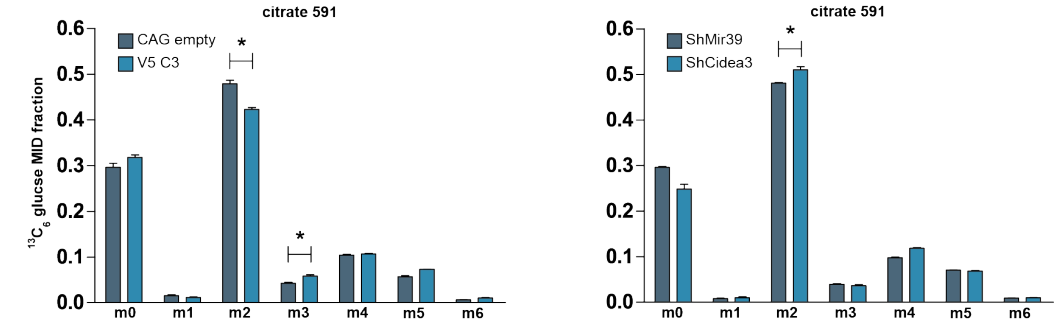
The role of Cidea-mediated LD enlargement in regulating the oxidative status of adipocytes is well known [127, 156]. How does this reflect in ESCs? ESCs are metabolically flexible, capable of both oxidative phosphorylation and anaerobic glycolysis to fulfil their energy demands [74]. However, the balance between the two fluxes, and the specific substrates used for oxidation is not fully explored. In this context, we were generally interested in exploring how enforcing or inhibiting Cidea function might impact on ESC metabolism. Therefore, to investigate the metabolic flux alterations that might result from modulating Cidea function, we here first study the utilisation of up-taken glucose. Stable isotope tracer experiments were performed on Cidea overexpressing and knockdown cells, whereby unlabelled glucose was substituted with uniformly ^{13}C-labelled glucose. Cell number at the beginning and end of each triplicate experiment was measured. As expected, no significant differences in cell growth between Cidea modulated and control cells were observed over the time-course of these experiments (24 hours) (data not shown)(see also Fig 5.1B). We first examined the consumption of labelled glucose from the culture media, and consequent production of labelled lactate, via ^{1}H NMR (Fig 5.4A). The net consumption or net release of the metabolites was calculated by subtracting metabolite concentrations in fresh/baseline medium from metabolite concentrations in spent medium from cultured cells. During the 24-hour period of ^{13}C glucose exposure, we noticed no significant differences in glucose uptake in Cidea overexpressing cells compared to their respective controls, however the glycolytic flux into ^{13}C lactate secretion was slightly reduced in Cidea overexpressing cells (p=0.03) (Fig 5.4B). In Cidea knockdown cells, ^{13}C glucose uptake and consequent ^{13}C lactate secretion in the culture media appeared unchanged compared to control cells (Fig 5.4C). This indicates that Cidea-OE ESCs possibly produce/secrete less ^{13}C glucose-derived ^{13}C lactate, or re-uptake more excreted ^{13}C lactate. Overall, the NMR results confirmed the efficient uptake and utilisation of labelled glucose by the cells and allowed further intracellular analysis of the cells. The intracellular metabolites of Cidea modulated cells cultured with ^{13}C glucose were analysed using GC-MS; the relative abundance of total metabolites and their ^{13}C mass isotopomer distributions were both examined. Global analysis of the total metabolite abundance profile indicated that the levels of TCA cycle intermediates detected in these experiments were almost all (malic acid, fumaric acid, succinic acid, isocitrate and citric acid, but not α-ketoglutaric acid) significantly reduced in Cidea overexpressing cells compared to control cells (Fig 5.4D; left). This could be indicative of increased *de novo* lipid synthesis or gluconeogenesis (generation of glucose), whereas TCA cycle intermediates are substrates for these pathways [209]. In addition, pyruvic acid (or pyruvate) levels are reduced or unchanged, known to fuel the TCA cycle (Fig 5.4D; left). On the other hand, results from the Cidea knockdown cells showed the opposite pattern, potentially pointing to a direct impact of modulating Cidea expression on TCA cycle flux (Fig 5.4D; right).

By closely inspecting the mass isotopomer distributions of individual metabolites we detected sizeable and significant shifts in the means by which ^{13}C glucose carbons were incorporated into citrate in Cidea overexpressing cells compared to controls (Fig 5.4E). In particular, the citrate M2 labelled from the $^{13}C_6$ glucose tracer was decreased in Cidea overexpressing cells. The synthesis of citrate is normally catalysed by citrate synthase, which utilises four-carbon oxaloacetate and two-carbon acetyl-CoA as substrates [210]. Mitochondrial acetyl-CoA is predominately derived from pyruvate via pyruvate dehydrogenase (PDH) activity whereas oxaloacetate can be formed by carboxylation of pyruvate or oxidation of malate. Importantly, PDH contributes to citrate M2 labels ($^{13}C_6$ glucose $\rightarrow$ $^{13}C_3$ pyruvate$\rightarrow$ $^{13}C_2$ acetyl-CoA $\rightarrow$ $^{13}C_2$ citrate) and pyruvate carboxylase (PC) contributes to citrate M3 labels ($^{13}C_6$ glucose $\rightarrow$ $^{13}C_3$ pyruvate $\rightarrow$ $^{13}C_3$ oxaloacetate $\rightarrow$ $^{13}C_3$ citrate) [210] (Fig 5.4F). The decrease in M2 citrate label, accompanied by a reciprocal increase in M3 citrate label might indicate that pyruvate entry into the TCA cycle via PC occurs more rapidly in the Cidea overexpressing cells compared to control cells. Again, this pattern seemed to be reversed in Cidea knockdown cells relative to control cells. Interestingly, PC is stimulated by acetyl-CoA, which in turn is predominantly derived from β-oxidation of acyl-CoAs and by decarboxylation of pyruvate [211]. This might suggest increased *de novo* lipid synthesis and increased β-oxidation in Cidea overexpressing cells, taking place simultaneously. Overall, our findings suggest that Cidea over-expression accelerates pyruvate usage into the TCA cycle, which might be accompanied by a change in the pyruvate entry point into the cycle.


A.
WT controls
Cidea OE and KD
cell adherence
16h
10% dialyzed FBS
12C glucose
1h
10% dialyzed FBS
13C glucose
24h
Collection of cells and extraction of polar metabolites
GC-MS
Collection of media
NMR


Cidea overexpressing
Cidea knockdown
B.
C.
CAG empty
V5 C3
ShMir39
ShCidea3
Relative 13C glucose uptake
Relative 13C Lac/ 13C Glu ratio
1.5
1.0
0.5
0.0
*


D.
V5 C3
ShCidea3
malic acid
fumaric acid
succinic acid
2 ketoglutaric acid
isocitric acid 591
citric acid 591
pyruvic acid
-60%
-40%
-20%
0%
20%
40%
60%
Percentage change comapred to control


E.
citrate 591
CAG empty
V5 C3
ShMir39
ShCidea3
13C6 glucse MID fraction
0.6
0.5
0.4
0.3
0.2
0.1
0.0
m0
m1
m2
m3
m4
m5
m6
*

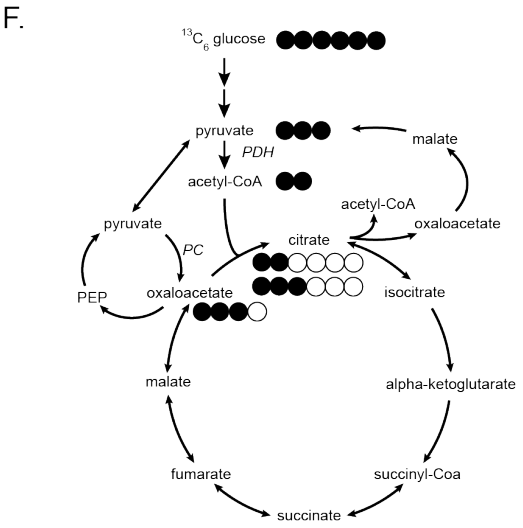

F.
13C6 glucose
pyruvate
PDH
acetyl-CoA
malate
acetyl-CoA
oxaloacetate
pyruvate
PC
citrate
PEP
oxaloacetate
isocitrate
malate
alpha-ketoglutarate
fumarate
succinyl-Coa
succinate

Figure 5.4: GC-MS analysis of Cidea-OE and Cidea-KD cells.

(A) Experimental setup of ^{13}C glucose tracing in Cidea-OE V5 C3 and Cidea-KD clone 3 (ShCidea3) cells and their controls (WT). Cells were seeded at 350,000 cells per well in 6-well plates. After an initial 16-hour period, which allowed the cells to adhere to the bottom of the wells, cells were equilibrated for 1 hour in DMEM supplemented media containing unlabelled ^{12}C glucose and dialyzed FBS in which unspecified small molecules are minimized. Hereafter cells were cultured for another 24 hours under similar culture conditions, however ^{12}C glucose was replaced by ^{13}C glucose. Cells were then collected, and parallel wells were counted to confirm similar growth rates amongst the clones. The polar metabolites were extracted from six independent cultures of each cell line to be analysed through GC-MS. Additionally, the culture media was collected for NMR analysis. **(B-C)** Relative ^{13}C glucose ^{13}C lactate changes in the culture media, compared to fresh media in **(B)** Cidea-OE V5 C3 and control (CAG empty) cells, and **(C)** Cidea-KD clone 3 (ShCidea3) and control (ShMir39) cells. **(D)** The intracellular relative abundance of total metabolites detected from the TCA-cycle intermediates (malic acid, fumaric acid, succinic acid, isocitrate and citric acid, α-ketoglutaric acid) and pyruvate, in Cidea-OE V5 C3 and Cidea-KD clone 3 (ShCidea3) cells expressed relative to their corresponding controls CAG-empty and ShMir39, respectively. **(E)** The mass isotopomer distribution of citrate from $^{13}C_6$ glucose tracer in Cidea-OE V5 C3, Cidea-KD clone 3 (ShCidea3) and control cells. **(F)** Schematic representation of isotope tracing experiment with $^{13}C_6$ glucose. Black-filled circles indicate ^{13}C-carbon, whereas the white filled circles represent the unlabelled carbon. The schematic shows the expected composition of labelled carbons of the indicated metabolites. Bar graphs represent mean SEM from three independent biological replicates. $P<0.05$ (*), Student's t test.

5.2.4 Cidea modulation impacts on ESC oxidative status

To complement our GC-MS approaches, we next thought to measure substrate usage and metabolic flux in Cidea-modulated ESCs using a Seahorse XFe24 Extracellular Flux Analyser. This instrument enables OCR (oxygen consumption rate) and ECAR (extracellular acidification) to be monitored in real time. OCR is an indicator of OXPHOS, and ECAR is predominantly the result of glycolytic capacity. Because measurements on Seahorse are non-destructive, the metabolic rate of the same cell population can be measured repeatedly over time with control and treatments. Here we use two different experimental setups referred as mitostress test and glycolytic stress test. Mitostress test provides information about mitochondrial respiration. Firstly, basal respiration (or basal OCR) is measured and by addition of oligomycin, a mitochondrial complex V inhibitor (see Fig 1.7D), it is possible to monitor the ATP-linked respiration capacity. Subsequently a mitochondrial uncoupler, carbonyl cyanide p-trifluoromethoxyphenylhydrazone (FCCP) is injected to measure the theoretical maximal mitochondrial respiration (or maximal OCR). Then antimycin A and rotenone are injected to eliminate all mitochondrial electron transfer and measure the non-mitochondrial portion of energy production (Fig 5.5A; left). Glycolytic activity is determined via the glycolytic stress test. The cells are initially starved of glucose as there is no glucose present in the Seahorse XF Base Medium. The non-glycolytic acidification rate therefore measures other sources of glycolytic flux that are not due to glycolysis. Anaerobic glycolysis can be calculated by the difference between the average of ECAR values prior to and after addition of glucose minus the non-glycolytic acidification rate. Glycolytic capacity is calculated by the difference between the average of ECAR values

prior to and after the addition of oligomycin minus the non-glycolytic acidification rate. Oligomycin suppresses mitochondrial respiration, therefore glycolytic capacity is an indication of the maximal rate of anaerobic glycolysis in the cell. The final injection is 2-deoxy-glucose (2-DG), a glucose analog, that inhibits glycolysis through competitive binding to glucose hexokinase, the first enzyme in the glycolytic pathway (Fig 5.5A; right). These experiments are designed to detect metabolic changes in cell cultures in real time. If Cidea modulation was to cause metabolic changes it would be likely to directly or indirectly affect oxygen consumption rates (OCR) and/or extracellular acidification rate (ECAR), and this system is a simple way of measuring several fundamental parameters simultaneously.

As recommended by the manufacturer, an initial FCCP titration experiment was conducted on wild-type ESCs testing two different cell numbers (50,000 and 100,000 cells). ESCs were seeded on gelatin-coated 24-well plates and incubated overnight. The following morning, cell media was replaced with Seahorse Assay culture media and cells were incubated for 1 hour at 37°C in the absence of carbon dioxide. The rate of oxygen consumption was measured in response to three different FCCP concentrations (0.2-0.4-0.8μM) in a Mitostress setting. Based on this experiment, it was decided that 50,000 cells will be plated in subsequent experiments, and a standard concentration of 0.4μM FCCP was selected (data not shown) [104]. As additional controls for the proposed experiments, we previously validated that no differences in the cell growth rates of Cidea-OE and Cidea-KD ESCs relative to their control populations were observed under self-renewing conditions (see also Fig 5.1B). As an additional control, DAPI staining and measurement of total fluorescence as a direct correlate for cell numbers was performed after each experiment. A test experiment was conducted in which increasing amount of cells were plated in the Seahorse plate, and DAPI staining and measurement of total fluorescence was performed (Fig 5.5B) after running a basic mitostress Seahorse experiment. This revealed that DAPI intensity could reliably be used as a normalization factor when plating the typical 50,000 cells per well (Fig 5.5B). However, we never observed any difference in total fluorescence intensity across wells after a Seahorse assay. Therefore, no cell number normalization factor is applied in our experiments.

We found that Cidea overexpressing ESCs showed both higher basal and maximal OCR in response to FCCP than control cells (Fig 5.5C), indicative of an enhanced oxidative state (Fig 5.5C; right). In contrast, glycolysis was not significantly different between Cidea overexpressing and control cells (Fig 5.5C; left). No major difference in mitochondrial respiration capacity and/or glycolysis rate was observed between Cidea-KD and control ESCs (Fig 5.5D). Interestingly, however, Cidea-KO cells did show a change in basal and maximal OCR, consistently showing lower scores than control cells (Fig 5.5E), and hence the opposite pattern of Cidea overexpressing cells. Glycolysis seems relatively unchanged in Cidea-KO cells, as observed in Cidea-OE and KD cells (Fig 5.5E). The discrepancy between the Cidea-KD and KO cells in mitochondrial respiration capacity compared to their respectively controls might reflect differences in Cidea depletion levels (partial versus complete depletion). From these data we concluded that modulating Cidea expression and/or function directly impacts on the oxidative state of ESCs, whereby increasing Cidea expression levels correlated with an increased in oxygen consumption while its complete depletion in ESCs led to the opposite effect.

We previously observed that Esrrb-depleted ESCs display a similar LD-phenotype as Cidea-depleted cells, that is, clustering of small LDs instead of LD enlargement in the presence of lipid rich media (see Chapter 3). Furthermore, Cidea expression was noticeably reduced in Esrrb-depleted cells under routine (FSB/LIF) conditions, and its induction compromised upon KSR treatment (see Fig 3.7). We were here interested to extend this analysis by also examining the impact of Esrrb depletion on ESC metabolism, as assayed by Seahorse measurement. We conducted both mitostress test and glycolysis stress test experiment on Esrrb-depleted (-/-) and control (F/F) cells. Interestingly Esrrb-depleted cells consistently showed a decreased in both basal and maximal respiration compared to control cells, as previously observed in Cidea-KO cells. As for Cidea-KO cells, the glycolytic capacity of ESCs remained unchanged regardless of Esrrb expression. These results therefore indicate that depleting Cideas transcriptional regulator seemingly leads to similar alterations in ESC metabolic flux, however we cannot exclude a broader role for ERR factors in regulating cellular oxidative pathways beyond regulating Cidea expression as previously described in other cell types [212].

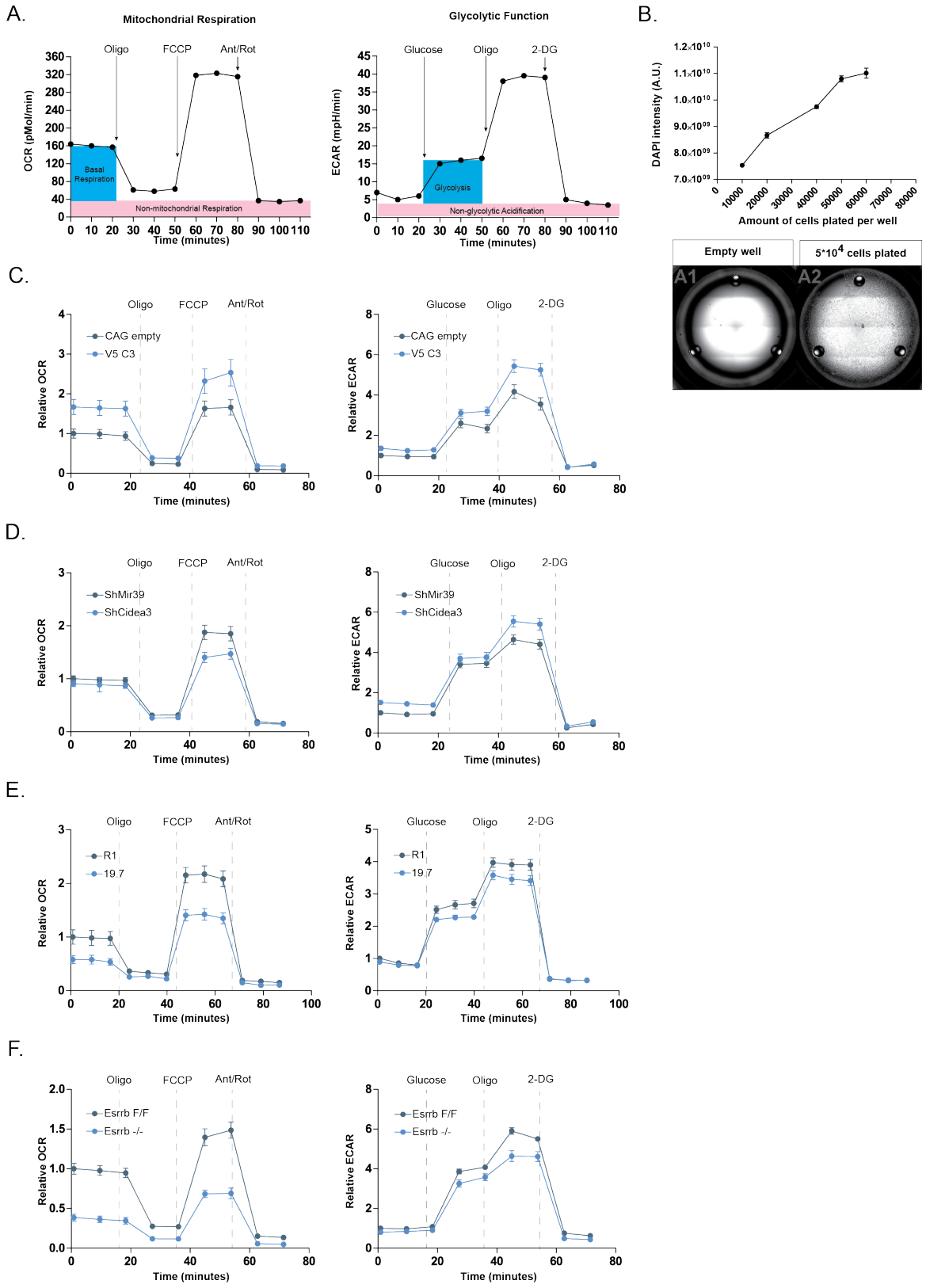


Figure 5.5: Seahorse analysis of Cidea-modulated cells and Esrrb-KO cells.

(A) Sample oxygen consumption rates (OCR) graph of Mitostress Test and sample extracellular acidification rate (ECAR) graph of Glycolytic Stress Test. Mitochondrial respiration is determined via the Mitostress Test. After measuring the basal oxygen consumption, the OCR is measured upon addition of oligomycin (a complex V inhibitor), carbonyl cyanide p-trifluoromethoxyphenylhydrazone (FCCP) (a mitochondrial uncoupler), and Antimycin A and Rotenone (to eliminate all mitochondrial electron transfer). Glycolytic activity is determined via the Glycolytic Stress Test. The cells are initially

starved of glucose, followed by the addition of glucose, oligomycin, and 2-deoxy-glucose (2-DG) (a glucose analogue that inhibits glycolysis). **(B)** Test experiment with increasing amount of cells plated in the Seahorse plate, followed by DAPI staining and measurement of total fluorescence as indicated by DAPI intensity in arbitrary units (A.U.). Below, an example picture of a Seahorse plate well, without (left) and with (right) cells, after DAPI staining. **(C,D,E,F)** Mitostress Test (left) and Glycolytic Stress Test (right) for **(C)** Cidea-OE V5 C3 and control CAG-empty, **(D)** Cidea-KD clone3 and control ShMir39, **(E)** Cidea-KO clone 19.7 and control R1, and **(F)** Esrrb-KO (-/-) and control (F/F) cells. Error bars represent SEM of three biological replicates (each containing 5 to 6 technical replicates). Data were expressed relative to the control at baseline.

5.2.5 Analysing substrate utilisation in Cidea overexpressing cells

To evaluate whether the enhanced oxygen consumption rate we observed in Cidea overexpressing ESCs reflects an increase in the usage of glucose versus lipids, we measured basal OCR levels in these cells under repeated treatments with specific chemical inhibitors. To prevent oxidation of fatty acids, the activity of Cpt1a, which is necessary for the transport of activated fatty acids into the mitochondria, was inhibited through use of Etomoxir [213]. To inhibit glucose usage, we used the previously mentioned 2-deoxy-glucose (2-DG) component. We first confirmed that Cidea-OE cells indeed showed higher basal respiration than the control populations at the beginning of the experiment (Fig 5.6A). Upon repeated addition of Etomoxir (40μM) we observed a gradual decrease of oxygen consumption in both Cidea-OE and control cells. When comparing oxygen consumption rate at basal level and after the first Etomoxir injection in both Cidea-OE and control cells, we observe a similar percentage change (40%) (Fig 5.6A). Addition of Etomoxir also affected the extracellular acidification rate of the cells (Fig 5.6B). Interestingly the percentage increase in acidification was significantly different between Cidea-OE and control cells. ECAR increased about 50% in Cidea-OE ESCs upon Etomoxir addition, compared to 30% in control cells. The main contributing factor to the extracellular acidification rate, which does not require oxygen consumption, is the formation of lactate, the final step of anaerobic glycolysis [214]. When consequently looking at the contribution of glucose oxidation to oxygen consumption via repeated addition of 2-DG, we observed no changes in basal respiration of either Cidea-OE or control cells. Therefore, the maximal capacity for glucose oxidation via the TCA-cycle is presumably the same for Cidea-OE and control cells (Fig 5.6C). As seen before, blocking the first step of glycolysis greatly impacts on the extracellular acidification rate of the cells. However, this impact was of similar extent in both Cidea-OE and control cells (Fig 5.6D). Overall, these data indicate that although Cidea-OE cells have increased capacity for oxygen consumption, the relative contribution of fatty acid oxidation to the overall oxygen consumption is the same in Cidea-OE and control cells. However, when the main contributor to oxygen consumption (fatty acid oxidation) is inhibited, Cidea-OE cells turn to fast anaerobic energy production (anaerobic glycolysis) in greater extent compared to control cells, possibly indicating a greater glycolytic reserve.
Mechanistically lipids are released from LDs by two pathways, known as lipolysis and lipophagy [119, 120]. Lipolysis is an enzymatic hydrolysis reaction of lipids, initiated by ATGL (Atglistatin) which resides on the surface of the lipid droplet. During lipophagy, on the other hand, LDs are sequestered in autophagosomes

and delivered to lysosomes for degradation by lysosomal acid lipases (LALs). Here we further investigated whether lipolysis, which precedes fatty acid oxidation, impacts on Cidea-OE OCR, by inhibiting ATGL with Atglistatin (10μM). In this preliminary experiment we observed no impact of repeated addition of Atglistatin on Cidea-OE OCR (Fig 5.6E). Overall, these experiments suggest that lipolysis linked to mitochondrial β-oxidation might not explain the increased oxygen consumption in Cidea overexpressing cells.

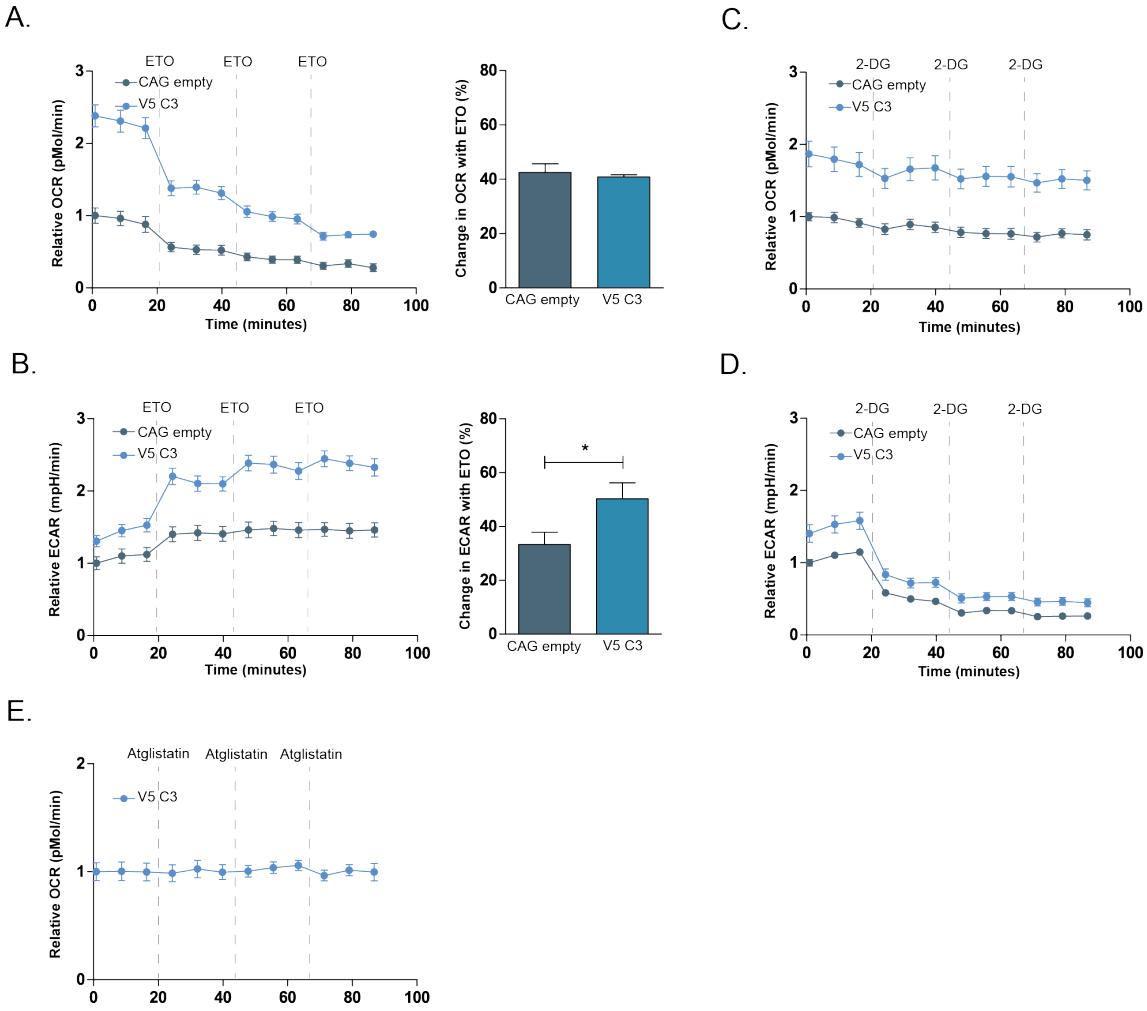


Figure 5.6: Analysis of increased oxygen consumption in Cidea-OE via Seahorse.

(A) Oxygen consumption rates (OCR) and **(B)** extracellular acidification rate (ECAR) upon repeated addition of Etomoxir (inhibitor of fatty acid oxidation), in Cidea-OE V5 C3 and control CAG-empty cells. **(A, B)** Bar graphs indicate the percentage change in OCR and ECAR from the mean of the three baseline values compared to the mean of the three values after the first addition of Etomoxir. **(C)** Oxygen consumption rates (OCR) and **(D)** extracellular acidification rate (ECAR) upon repeated addition of and 2-deoxy-glucose (2-DG) (a glucose analogue that inhibits glycolysis) in Cidea-OE V5 C3 and control CAG-empty cells. Error bars represent SEM of three biological replicates (each containing 5 to 6 technical replicates). Data were expressed relative to the control at baseline. P<0.05 (*), Student's t test. **(E)** Oxygen consumption rates (OCR) upon repeated addition of Atglistatin (inhibitor of lipid droplet lipolysis) in Cidea-OE V5 C3 cells. Error bars represent SEM of 5 to 6 technical replicates, and data is expressed relative to the first OCR measurement. This experiment does not contain any biological replicates or control CAG-empty cells

5.3 Summary and Conclusions

In summary, Cidea-modulated ESCs retain an undifferentiated state in culture with similar growth rate than their WT counterparts, and no obvious differences in the transcriptional activity of pluripotency-associated factors. Upon embryoid body formation we note that the differentiation ability of Cidea-OE and KD cells was not compromised. However, we observed a striking difference in the overall morphogenesis changes in these EBs in the absence of Cidea. Cidea-KD ESCs tend to form numerous EBs of variable sizes and irregular shapes, and by day 9 the vast majority of EBs formed a cystic-like structure. Upon further investigation of the 3D organisation of the EBs and cystic-like structures we observed that Cidea-depleted cells form an internal lumen at earlier-time points of differentiation than their normal counterparts, possibly indicative of advanced or unscheduled cavitation events. This potentially links for the first time a role for Cidea expression and/or Cidea-mediated LD enlargement in key cellular remodeling events.

The impact of modulating Cidea expression on ESC metabolism was further studied using different approaches. Here we first used ^{13}C-labelled glucose to investigate its utilisation via GC-MS. Studying the relative abundance of metabolites and their ^{13}C mass isotopomer distributions, highlights a potential important role for Cidea-mediated LD enlargement on overall ESC metabolism. In particular, Cidea over-expression seems to result in increased *de novo* lipid synthesis, indicated by reduced levels of levels of TCA cycle intermediates [209], accompanied by a change in the pyruvate entry point into the cycle - i.e. pyruvate entry into citrate via pyruvate carboxylase (PC) was favoured in the Cidea overexpressing cells compared to control cells. Interestingly, this reaction is important during anabolic processes to replenish the TCA cycle with oxaloacetate; for example, when TCA intermediates are shuttled into the cytoplasm to form triglycerides [215]. PC is also stimulated by acetyl-CoA, which in turn is predominantly derived from β-oxidation of acyl-CoAs and by decarboxylation of pyruvate [211]. This might suggestv that increased *de novo* lipid synthesis and increased β-oxidation in Cidea overexpressing cells take place simultaneously.

Substrate usage and metabolic flux were also explored *in situ* using Seahorse XFe24 Extracellular Flux Analyser. In particular, we analysed the oxygen consumption rates (OCR) and extracellular acidification rate (ECAR) of Cidea overexpressing and Cidea depleted cells relative to their respective controls. We observed increased oxygen consumption in Cidea-OE cells, and conversely decreased oxygen consumption in Cidea-KD, KO and Esrrb-KO cells. To consequently evaluate the contribution of β-oxidation and glycose oxidation in enhancing the oxygen consumption rate of Cidea overexpressing cells, we exposed the cells to specific chemical inhibitors. This indicated that Cidea-OE and control cells use the same sources of energy production in similar proportions to account for oxygen consumption. However, when the fatty acid oxidation is inhibited, Cidea-OE cells turn to fast anaerobic energy production (glycolysis) in greater extent compared to control cells, possibly indicating a greater glycolytic reserve in Cidea-OE cells.

Chapter 6

Investigating the functional importance of LDs and lipid metabolism at the onset of ESC differentiation and glycolytic switch

6.1 Introduction

We have so far demonstrated that ESCs have the ability to form large LDs, in a Cidea-dependent manner, under permissive lipid-rich conditions. In addition, lipid droplet formation and enlargement are dynamically regulated during blastocyst development *in vivo*, where we have observed the prevalence of large lipid droplets in the pre-implantation embryo (E3.5) and their timely mobilisation upon epiblast maturation at peri-implantation times. Interestingly, LD dynamics as observed *in vivo* could be recapitulated using 3D ESC differentiation with LD enlargement being observed as cells exit from naïve pluripotency and their timely mobilisation as primed pluripotency is established and morphogenesis events occur (formation of rosette-like structures). Altogether these findings suggest a link between neutral lipid accumulation at the onset of ESC differentiation and its associated remodelling of transcriptional and cellular states. ESCs grown under self-renewing conditions and more specifically serum/LIF conditions exhibit a high degree of transcriptional and epigenetic heterogeneity [27, 30, 24]. For example, cells expressing low and high levels of Nanog were previously found to delineate different ESC states, with cells expressing low levels being more prone to spontaneously differentiate [216].

In terms of lipid droplet dynamics, we also interestingly observed a degree of cell-to-cell heterogeneity in LD size and number under routine (FBS/LIF) self-renewing conditions. In general, the existence of LD heterogeneity is not uncommon and has even been reported in unicellular organisms such as the yeast Saccharomyces cerevisiae [217], but also in liver cells [218], and in adipocytes [219]. In hepatocytes, LD compartmentalization has been proposed to restrict the presence of potentially toxic metabolites in a limited number of cells, thus providing survival advantage for the whole population. In adipose tissues, subpopulations with higher numbers of large LDs appeared to be enriched towards the end of adipogenesis demarcating cells at later stages of differentiation. Thus far, LD heterogeneity has not been studied in embryonic stem cells, however high LD content has been used as a valuable marker to isolate cancer stem cells within heterogenic colorectal tumours [220].

In this chapter, we attempt to isolate and maintain *in vitro* ESC clonal populations harbouring different LD morphologies. The successful conservation of distinctive LD signatures over passaging allows us to explore in-depth the phenotype of the established clones using a variety of approaches. Notably, we aim to uncover inherent differences in the metabolic and functional abilities of these clones, possibly linking lipid droplet biology with fundamental developmental processes in pluripotent stem cells. First, alkaline phosphatase staining, embryoid body assays, and retinoic acid-induced differentiation are used to investigate the self-renewal and differentiation capacity of the distinct LD clones. This is further investigated by studying the gene expression patterns of the clones using RNA-sequencing and RT-qPCR analysis. Additionally, GC-MS and Seahorse analyses provide valuable insights into the metabolic profiles of the clones allowing us to propose possible mechanisms by which metabolic and/or lipid (droplet) heterogeneity might emerge within ESC cultures.

6.2 Results

6.2.1 Isolation of ESC clones that stably harbour different LD morphologies under self-renewing conditions.

When ESCs are cultured in routine FBS conditions, we observed cell-to-cell heterogeneity in LD size and number. To address whether this genuinely delineates distinct cell populations, we attempted to, under identical (FBS) culture conditions, isolate several ESC clones from parental (E14) ESCs that either harbour predominantly large or small LDs. Here ESCs were first plated at low density, after which several clones were picked based on their differential presence of granules (i.e. lipid droplets) as visualised under contrast-phase microscope, further confirmed with lipid droplet BODIPY staining (Fig 6.1A). Importantly, this confirmed the co-existence of ESCs with different LD morphologies hereafter referred to as large LD or LLD (orange), and small LD or sLD clones (blue) (Fig 6.1). As anticipated, preliminary characterization of the newly established clones (passage 2-4) highlighted that LLD clones tend to express the highest levels of *Cidea* transcript as determined by RT-qPCR (Fig 6.1B-C). Differential expression amongst selected clones was also evident for a limited set of metabolic genes including diacylglycerol acyl transferase 2 gene (*Dgat2*) and fatty acid binding protein 3 gene (*Fabp3*) with known roles in lipid storage and uptake respectively [221, 222]. Moreover, we identified enhanced expression of early differentiation markers (*Fgf5* and *T*), and conversely reduced expression of some self-renewal regulators (*Oct4* but not *Nanog*) in LLD as compared to sLD clones (Fig 6.1B), suggesting a possible link between the presence (or absence) of large LDs and the differentiation state of ESCs. Importantly, established clones were found to faithfully retain differential transcriptional signatures (*Cidea*, *Dgat2*, *Fabp3* and *Oct4*) as tested over 9 consecutive passages using clones initially selected based on highest and lowest Cidea expression levels (see Fig 6.1D).

In conclusion, we were able to, under FBS conditions, successfully isolated and maintain ESC clones that either harbour predominantly large or small LDs, in addition to differential gene expression patterns.

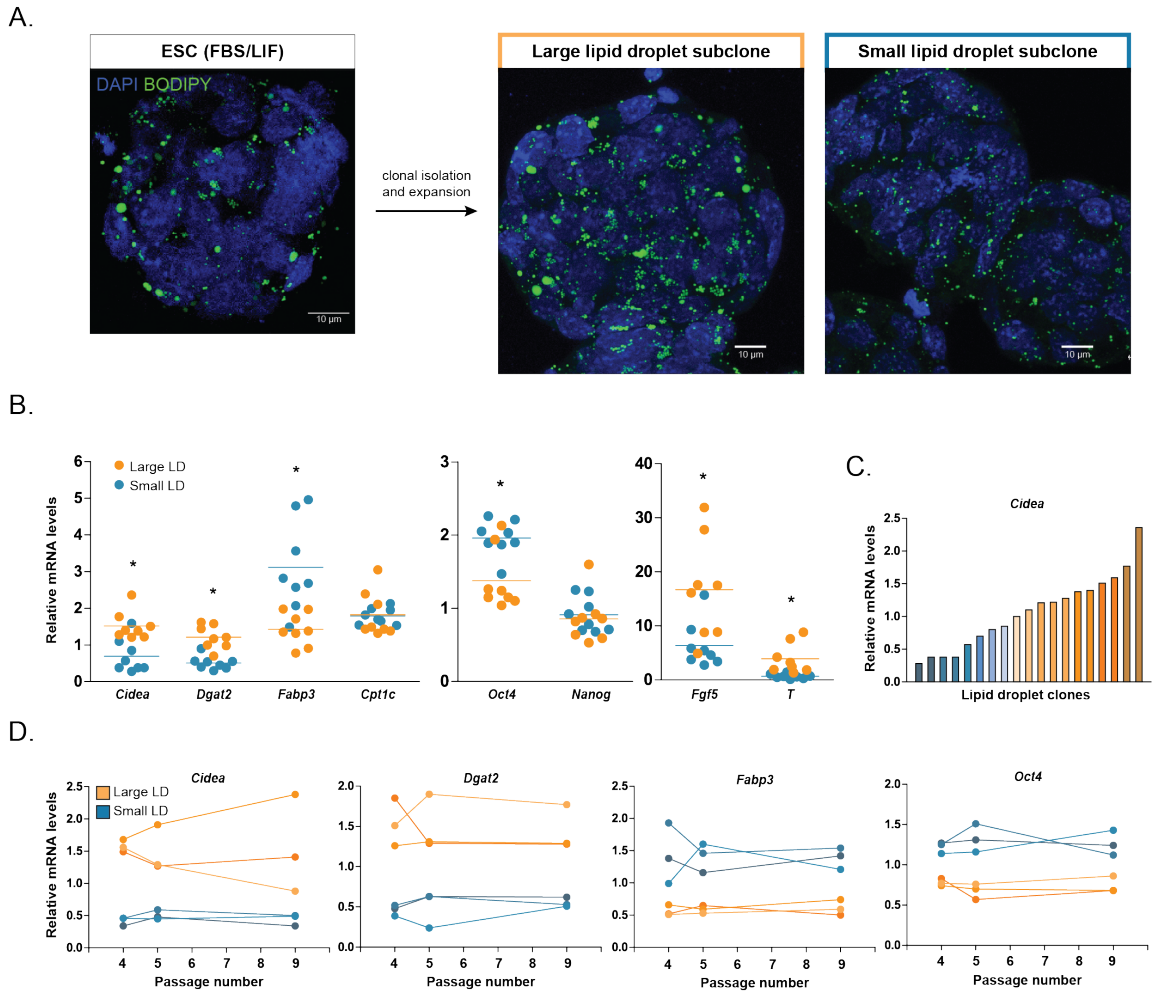


Figure 6.1: Generation of ESC clones with different LD morphologies.

(A) Confocal imaging of lipid droplet (LD) staining with neutral lipid dye BODIPY 493/503 (green) on ESCs cultured in routine media (FBS/LIF). Each picture represents a three-dimensional image of merged Z-stack images. DAPI staining was used to visualise nuclei (blue). Images represent several ESC clones harbouring either large or small LDs that were, under identical culture conditions, isolated from parental E14-ESCs. Bar, 10μm. **(B)** RT-qPCR analysis in newly isolated (passages 2-4) clones (clones 4, 10, 12, 11, 19, 6, 13, 16 (orange), and 5, 7, 9, 15, 18, 8, 14, 17 (blue)) of metabolic genes (*Cidea*, *Dgat2*, *Fabp3*, *Cpt1c*), self-renewal regulators (*Oct4* and *Nanog*), and early differentiation markers (*Fgf5* and *T*) in large LD (orange) and small LD (blue) clones. **(C)** RT-qPCR of *Cidea* in 18 newly isolated clones (passages 2-4). **(D)** RT-qPCR of *Cidea*, *Dgat2*, *Oct4* and *Fabp3* on later passage clones (clones 6, 11, 13 (orange), and 8, 14, 17 (blue)). RT-qPCR data were normalized to the housekeeping genes *S17* and *L19*, and expressed relative to clone 1 (not plotted in B and D). P<0.05 (*), Student's t test. Courtesy of David Barneda.

6.2.2 Functional characterization of selected small and large LD embryonic stem cell clones

Under self-renewal (FBS) conditions, no apparent difference was observed in the growth rate of the selected clones as assessed by scoring the number of cells cumulating over seven consecutive passages (Fig 6.2A). To further explore whether the different clones also possess similar plating efficiency, that is the ability to *de novo* form undifferentiated colonies from single cells, three sLD (8, 14 and 17) and six LLD (1, 4, 6, 10,11 and 13) clones were plated at low density (1,000 cells/ml in 6-well plates) in FBS-containing medium in the presence or absence of LIF in triplicate experiments. Following 7 days of cultures, cells were stained for alkaline phosphatase (AP) activity to score the number of undifferentiated, mixed and differentiated colonies formed under these conditions (Fig 6.2B). Strikingly, we could here identify clear differences in the self-renewal abilities of the clones analysed. Notably, we found that sLD clones consistently demonstrated the highest capacity to form undifferentiated colonies (96% out of total counted colonies per clone) compared to LLD clones (30-85%) (Fig 6.1B). Strikingly, large LD clones also exhibited a greater degree of heterogeneity, with clones 10 and 11 showing increased incidence of mixed/differentiated colonies formed (46-68%) as compared to clones 1, 4,6 and 13 (14-20%). LIF removal is here used as negative control, inducing differentiation in all cultures tested. Collectively, these data suggest that large and small LD clones possess differential functional abilities, with large LD clones being more prone for spontaneous differentiation at least as tested here under self-renewing culture conditions.

To address whether differential lipid storage capacities might also impact on ESC differentiation, three selected clones were induced to form embryoid bodies (EB). These clones represent the sLDs cluster (clone 8), LLDs cluster (clone 4), and LLDs with compromised plating efficiency cluster (clone 11) as described above (see Fig 6.2B). ESC clones and the parental E14-ESC line were cultured in suspension in the absence of LIF and reduced serum level (5%) to allow the generation of three-dimensional cellular aggregates where progenitors of the three germ layers form. All three selected clones efficiently formed EBs under the same conditions, showing morphologies comparable to those observed at the different time-points tested (0, 3, 6 and 9 days) in control cells (E14) (data not shown). Gene expression profiling in the course of differentiation similarly showed no major differences amongst clones, with self-renewal markers *Oct4* and *Nanog* being gradually down-regulated and key differentiation markers *Fgf5*, *Mixl1* and *Brachyury* (*T*) sequentially up-regulated, corroborating the *in vivo* developmental process (Fig 6.2C). Notably, clone 11, which is characterized by the presence of large LDs and relatively poor plating efficiency, showed a tendency of differentiating faster than the two other representative clones. This was evidenced by higher induction levels of both early (*Fgf5*) and late (*Brachyury* and *Mixl1*) differentiation markers (Fig 6.2C). This is also in agreement with lower expression levels of *Oct4* and *Nanog* at day 0 in clone 11 relative to clones 4 and 8 (Fig 6.1B). Interestingly, *Cidea* was transiently up-regulated at early stages of ESC differentiation alongside the early epiblast marker *Fgf5*, potentially suggesting that Cidea-mediated LD enlargement might be a hallmark of ESC priming for differentiation.

ESCs can also be preferentially converted into extra-embryonic primitive endoderm (PrE)-like cells upon LIF withdrawal and all trans retinoic acid (atRA) treatment [223, 224]. AtRA treatment on the three selected clones promptly resulted in a sharp downregulation of self-renewal markers *Oct4* and *Nanog*. As expected, this was furthermore accompanied by the up-regulation of the key PrE markers, *Gata6*, *Gata4* and *Dab2*, consistent with the preferential acquisition of a PrE-like identity under these differentiation conditions [223, 224] (Fig 6.2D). As seen upon EB formation, all three clones successfully differentiated into PrE-like cells with no clear differences in differentiation efficiency amongst them. We do note however, the advanced activation of the late PrE marker, *Dab2*, in clone 11 which peaks at day 2 relative to day 3 in clones 4 and 8. Besides, *Cidea* was further up-regulated at day 1 post treatment in both clones 4 and 11, which both exhibit large LDs under self-renewing conditions and to a less extent in clone 8 where *Cidea* remained expressed at lower levels throughout the course of differentiation (Fig 6.2D).

Taken together our findings demonstrate that LLD clones possess a large degree of heterogeneity in terms of their plating efficiency, whereby a subgroup of LLD clones were identified as being more prone to spontaneously differentiate than others. Regardless of this phenotype, all clones differentiate normally upon induction into either embryonic or extra-embryonic-like derivatives. However, we did observe differences in the level of induction of some differentiation markers amongst clones, with clone 11 (LLD) showing evidence of advanced differentiation. In both differentiation assays, we interestingly observed the further induction of *Cidea* at early differentiation time-points, possibly suggesting that LD enlargement might indeed be associated with the onset of differentiation.

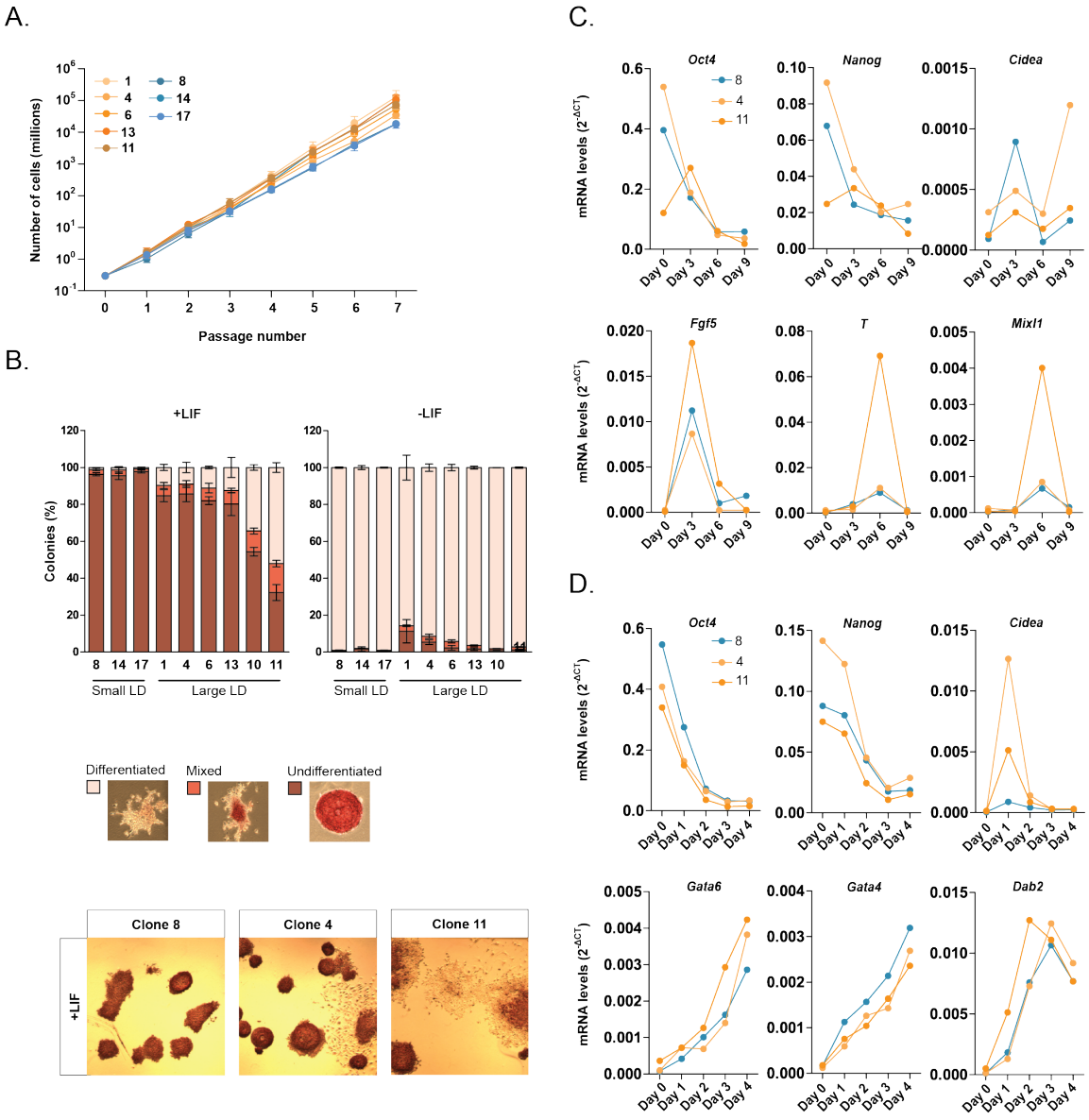


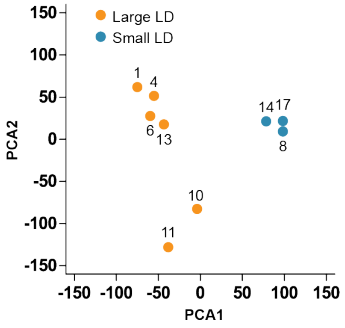
Figure 6.2: Functional characterization of ESC clones with different LD morphologies.

(A) Growth curve of selected large LD (orange) and small LD (blue) clones in self-renewing conditions over 7 passages (14 days). Plot represents an average of the cell numbers scored in three independent experiments. Error bars indicate SEM. **(B)** Percentage of colony types scored in cells growing with (+) or without (-) LIF for 7 days. Colonies were counted and scored as undifferentiated, mixed or differentiated according to the intensity of alkaline phosphatase (AP) staining. Plots represent percentage of colonies counted in three biological replicates. Error bars indicate SEM. AP staining of three clones (8, 4 and 11) are shown as example below. **(C)** Transcript levels for pluripotency-associated (*Oct4*, *Nanog*), epiblast (*Fgf5*), mesoderm (*Brachyury*, *Mixl1*), and lipid droplet associated *Cidea* markers in three distinct clone-derived embryoid body (EB) (clones 8, 4 and 11) cultures collected at day 0, 3, 6 and 9 of EB differentiation. Data were normalized to the housekeeping genes *S17* and *L19*. Data are representative of one of three independent experiments. **(D)** Transcript levels for pluripotency-associated (*Oct4*, *Nanog*) and primitive endoderm (*Gata6*, *Gata4*, *Dab2*), and lipid droplet associated *Cidea* markers in three distinct clone-derived all trans retinoic acid-induced cultures in the absence of LiF collected at day 0, 1, 2, 3 and 4 of differentiation. Data were normalized to the housekeeping genes *S17* and *L19*. Data are representative of one of three independent experiments.

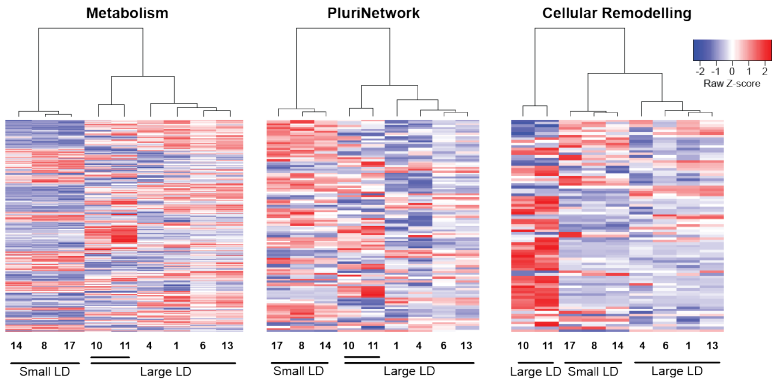
6.2.3 Clustering of small LD and large LD embryonic stem cell clones based on differential gene expression signatures

To further explore the suggested link between the presence (or absence) of large LDs and different ESC states we established the transcriptomes of several large and small LD clones using RNA-sequencing (RNA-seq). Unsupervised clustering via principal component analyses (PCA) was used, reliably discriminating LLD and sLD ESC clones based on differential gene expression profiles (Fig 6.3A) (in collaboration with Drs Mark Christian and Yi-Wah Chan). In PCA, the first principal component indicates the largest possible variance (i.e. it accounts for the majority of the variability in the data). In turn, each succeeding component has the highest variance possible while being uncorrelated with preceding component. Here we observed the emergence of three clusters; [a] sLD clones 8, 14 and 17, [b] LLD clones 1, 4, 6 and 13, [c] LLD clones 10 and 11. Interestingly these clusters correlate with the different plating efficiency phenotypes we previously identified amongst these clones. Hence, we will hereafter refer to the three identified cluster as small LD clones (sLD), large LD clones with good self-renewal ability (L_1LD), and large LD clones with reduced self-renewal ability (L_2LD). Further analysis of genes that are differentially expressed amongst clones using the meta-database ConsensusPathDB (CPDB), allowed us to identify significantly enriched pathways in pairwise comparison of clone clusters (see Appendix). From this exhaustive list of pathways, three of them initially retained our attention: Metabolism, PluriNetWork and Cellular Remodelling (including Cell-to-cell communication, Cell-to-ECM communication and ECM organisation) (Fig 6.3B). Using heat map analyses, we further confirmed that the clones could indeed be reliably discriminated in the same three clusters based on metabolic processes and pluripotency-associated gene networks. Interestingly, we found that L_2LD clones 10 and 11 could be further segregated from all other clones (as defined in our PCA analysis) based on differentiation-associated pathways (i.e. Cellular Remodelling). This strictly mirrored the increased incidence of spontaneous differentiation we have observed in these clones as assessed using self-renewal assays (Fig 6.2B). We then performed a closer inspection of differentially expressed pathways, in a pairs-wise comparison between the three clusters: sLD, L_1LD and L_2LD. Metabolism (including Glucose Metabolism, Lipid Metabolism or Adipogenesis, TCA cycle and Electron Transport Chain), PluriNetWork, Developmental Biology, Signalling Associated With Differentiation, and Cellular Remodelling were always discriminating between the three clusters (Fig6.3C). We interestingly observed a possible difference in oxidative status between the large LD clone clusters (Oxidative Stress Induced Senescence) (Fig 6.3C). We additionally noticed that the number of terms related to Cell Signalling Associated Differentiation, Differentiation Pathways and Cellular Remodelling were more abundant in any comparison involving the L_2LD cluster (Fig 6.3C). Collectively, these findings strongly suggest the co-existence of ESC sub-populations with distinct metabolic and/or differentiation status as delineated by the presence (or absence) of large LDs under self-renewing culture conditions.

A.



B.



C.

Pathway enrichment

L_1LD vs sLD		L_2LD vs sLD		L_1LD vs L_2LD	
Pathway	**P-value**	**Pathway**	**P-value**	**Pathway**	**P-value**
Metabolism	3.76E-04	Metabolism	5.90E-05	Metabolism	1.36E-04
Glucose metabolism	4.55E-04	Glucose metabolism	4.20E-04	Metabolism of RNA	6.41E-04
Metabolism of lipids and lipoproteins	7.23E-04	TCA cycle and respiratory ETC	4.23E-04	Metabolism of proteins	2.90E-04
Glutathione metabolism	4.55E-04	Metabolism of carbohydrates	3.15E-04	Adipogenesis	4.56E-04
PluriNetWork	3.76E-04	Adipogenesis	5.90E-05	Cellular responses to stress	3.61E-04
Focal adhesion	9.83E-04	PluriNetWork	5.90E-05	Oxidative Stress Induced Senescence	9.12E-04
Adherens junction	5.60E-04	ESC Pluripotency Pathways	5.90E-05	PluriNetWork	1.36E-04
p53 signaling pathway	4.55E-04	Developmental Biology	5.90E-05	ESC Pluripotency Pathways	2.21E-04
Senescence and Autophagy	4.55E-04	Dorso-ventral axis formation	8.86E-05	Developmental Biology	1.36E-04
Cell Cycle	3.76E-04	HIF-1 signaling pathway	5.90E-05	MAPK signaling pathway	1.36E-04
Immune System	4.55E-04	MAPK signaling pathway	5.90E-05	TGF Beta Signaling Pathway	1.36E-04
		Insulin Signaling	4.23E-04	PI3K-Akt signaling pathway	1.36E-04
		PI3K-Akt signaling pathway	5.90E-05	Wnt Signaling Pathway and	1.36E-04
		PIP3 activates AKT signaling	1.39E-04	Pluripotency	
		Wnt Signaling Pathway	2.21E-04	EGFR1 Signaling Pathway	5.11E-04
		TGF Beta Signaling Pathway	9.68E-04	Regulation of actin cytoskeleton	4.56E-04
		Signaling by EGFR	3.05E-04	Integrin-mediated Cell Adhesion	1.01E-03
		Id Signaling Pathway	3.80E-04	Focal Adhesion	1.36E-04
		Regulation of Actin Cytoskeleton	5.90E-05	Extracellular matrix organization	1.36E-04
		Integrin-mediated Cell Adhesion	5.90E-05	Cell-Cell communication	1.36E-04
		Non-integrin membrane-ECM	1.41E-04	Cell junction organization	4.18E-04
		interactions		p53 signaling pathway	1.36E-04
		Focal Adhesion	5.90E-05	Senescence and Autophagy	1.36E-04
		Extracellular matrix organization	5.90E-05	Cell Cycle	7.36E-04

Figure 6.3: RNA-sequencing data analysis of ESC clones with different LD morphology.

(A) Principal component analyses (PCA) of both large LD (orange) and small LD (blue) clones using RNA-sequencing data. The first principal component indicates the largest possible variance (i.e. it accounts for the majority of the variability in the data). In turn, each succeeding component has the highest variance possible while being uncorrelated with the preceding component. In collaboration with Mark Christian and Yi-Wah Chan. **(B)** Pathway analysis of the clones indicated above using the RNA-sequencing data. Heatmap analysis of differentially expressed genes associated with Metabolism, PluriNetWork, and Cellular Remodelling (in particular Cell-to-cell communication, Cell-to-ECM communication, and extracellular matrix (ECM) organisation). **(C)** In depth pathway analysis specifically comparing the three clones clusters; small LD clones (sLD), large LD clones with good self-renewal ability (L_1LD), and large LD clones with reduced self-renewal ability (L_2LD).

6.2.4 Preliminary evidence for different lipid trafficking and usage in sLD and LLD embryonic stem cell clones

Interestingly, a more in-depth analysis of the differentially regulated genes associated with the Metabolism pathway revealed that most of these genes relate to fatty-acid metabolism. Here we identified genes involved in *de novo* lipid synthesis (*Acly*, *Fasn* or *Dgat2*) [121] and degradation by lipolysis (*Atgl*) [121] versus fatty acid uptake/transport (*Fabp3*) [222] and oxidation (*Ascl1*, *Cpt1a* and *Cpt1b*) [121]. By RT-qPCR analysis, we confirmed on the same clones that large LD (L_1LDs and L_2LD) ESC populations exhibited enhanced expression of genes involved in lipid synthesis and storage compared to small LD clones (Fig 6.4A). Interestingly, lipid released from LDs (which is facilitated by *Atgl*) might be most incident in large LD clones that show poor self-renewing and enhanced spontaneous differentiation (L_2LD), also linked to increased expression of differentiation markers (*Fgf5* and *Brachyury/T*). This suggests that the timely release and/or degradation of stored lipids might coincide with a more advanced pluripotency state towards differentiation. Conversely, small LD clones showed higher expression of genes associated with the uptake/transport of free fatty acids (FFA) (*Fapb3*), and oxidation into mitochondria (*Ascl1*, *Cpt1a* and *b*) (Fig 6.4B). This seems to associate with a more naïve state as indicated by higher expression levels of the naïve (*Tbx3*) and general (*Oct4*) pluripotency transcription factors (Figure 6.4B) and potent self-renewal abilities (see Fig 6.2B).

Altogether, these data confirm that our established large and small LD clones not only differ in terms of LD morphologies, but are also characterized by distinct lipid signatures and pluripotency states (i.e. naïve versus primed state for differentiation). Whereas sLD clones might mainly oxidise exogenously scavenged lipids, LLD clones show evidence for enhanced *de novo* lipid synthesis and storage to be potentially released at the onset of differentiation (Fig 6.4C). This potential remodelling of ESC metabolic network, a proposed "lipid switch", as seen in sLD and LLD clones will be further explored in the next section.

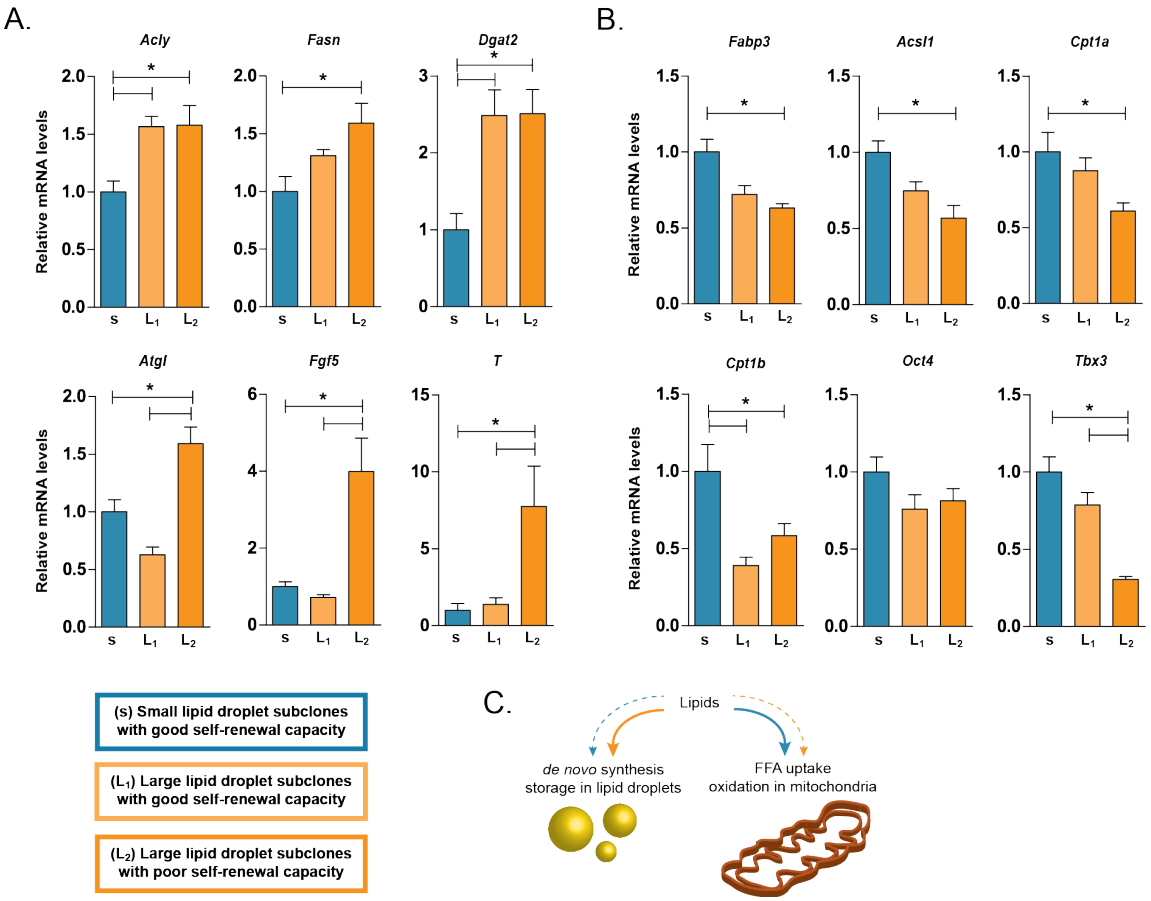


Figure 6.4: RT-qPCR validation of differential gene expression profiles in sLD and LLD clones.

(A) Gene expression signature of large LD clones, showing transcript levels of differentiation markers (*Fgf5* and *Brachyury*), and genes related to *de novo* fatty acid synthesis and lipid storage (*Acly*, *Fasn* and *Dgat2*, *Atgl*). **(B)** Gene expression signature of small LD clones showing expression of pluripotency markers (*Oct4* and *Tbx3*), and genes related to exogenous lipid uptake (*Fabp3*) and β-oxidation (*Acsl1*, *Cpt1a*, and *Cpt1b*). Data were normalized to the housekeeping genes *S17* and *L19*, and expressed relative to the small LD clones (sLD). Error bars represent SEM of three biological replicates. P<0.05 (*), Student's t test. Index recapitulates the three clone clusters: small LD clones (sLD), large LD clones with good self-renewal ability (L_1LD), and large LD clones with reduced self-renewal ability (L_2LD). **(C)** Proposed model of a "lipid switch" underlying the observed cell-to-cell heterogeneity in terms of LD size and numbers, where small LD clones might mainly oxidise exogenously scavenged lipids, and large LD clones enhancing *de novo* lipid synthesis and storage to be potentially released at the onset of differentiation.

6.2.5 Untargeted metabolic profiling of sLD and LLD embryonic stem cell clones.

The existence of distinct metabolic (lipid) signatures amongst ESCs prompted us to further assess the impact of LD sizes on ESC metabolism using GC-MS based untargeted metabolic profiling, in collaboration with Dr Hector Keun. Cells where seeded at equal density in regular culture media for 16 hours, followed by media swap to DMEM supplemented media containing dialyzed FBS in which unspecified small molecules are minimized (Fig 6.5A). After 24 hours cells were collected and total protein content confirmed similar growth rates amongst the clones (data not shown). Intracellular polar metabolites were extracted from five independent cultures of each clone analysed. The identity of metabolites was then assigned with the Automated Mass Spectral Deconvolution and Identification System (AMDIS) based on in-house databases and FiehnLib. Seventy-three metabolites could reliably be detected and identified across all clones analysed and thus used for data analysis (see Appendix). Here, we first focussed on metabolites involved in glycolysis, TCA-cycle as well as on essential and non-essential amino acids whose relative metabolite concentrations were compared in the three clone clusters as previously identified, namely small LD clones (sLD), large LD clones with good self-renewal ability (L_1LD), and large LD clones with reduced self-renewal ability (L_2LD).

We were able to reliably detect a number of metabolites associated with glycolysis including glucose-6-phosphate, pyruvate and lactate. Notably, our analysis highlighted an increase in the concentration of glucose-6-phosphate accompanied by a significant increase in pyruvate levels in large LD (L_1LD and L_2LD) compared to sLD clones (Fig 6.5B), suggesting a possible increased uptake of glucose and/or pyruvate in large LD clones. Alternative, glucose-derived production of pyruvate might be enhanced in these clones. Lactate-to-pyruvate ratio is slightly reduced in large LD clones compared to small LD clones, suggesting an increase in pyruvate generation from anaerobic glycolysis for metabolic branches other than lactate, or an increased pyruvate uptake (Fig 6.5C). Interestingly, the glycolytic intermediate that most significantly changed amongst the three clone clusters was glycerol-3-phosphate (G3P) with concentrations nearly 4-fold higher in L_1LD compared to sLD clones and intermediate levels detected in L_2LD (Fig 6.5D). It is worth noting that G3P is used to form triglycerides and on the converse be produced via breakdown of triglycerides [225] (Fig 6.5E). Our metabolomics study detected most TCA cycle intermediate with the exception of isocitrate, succinyl CoA and oxaloacetate (Fig 6.5F). We found that the concentration of citrate was significantly increased in large LD clones compared to sLD clones. The concentration of other TCA intermediate metabolites remained relatively unchanged, apart from a possible increase and decrease in α-ketoglutarate and succinate in large LD clones respectively. Interestingly, manipulation of the α-ketoglutarate:succinate ratio has been linked to regulation of pluripotency-associated gene in both mouse and human ESCs [226, 88]. The apparent discrepancy between significantly increased citrate levels not translating into increased levels of all other TCA cycle intermediates might potentially be explained by the fact that citrate can be broken down into acetyl-CoA for fatty acid synthesis, hence not entering the TCA cycle [227] (Fig 6.5G). Taken together, our results point to a possible shuffle of glycolysis intermediates into *de novo* lipid synthesis pathway in large LD clones.

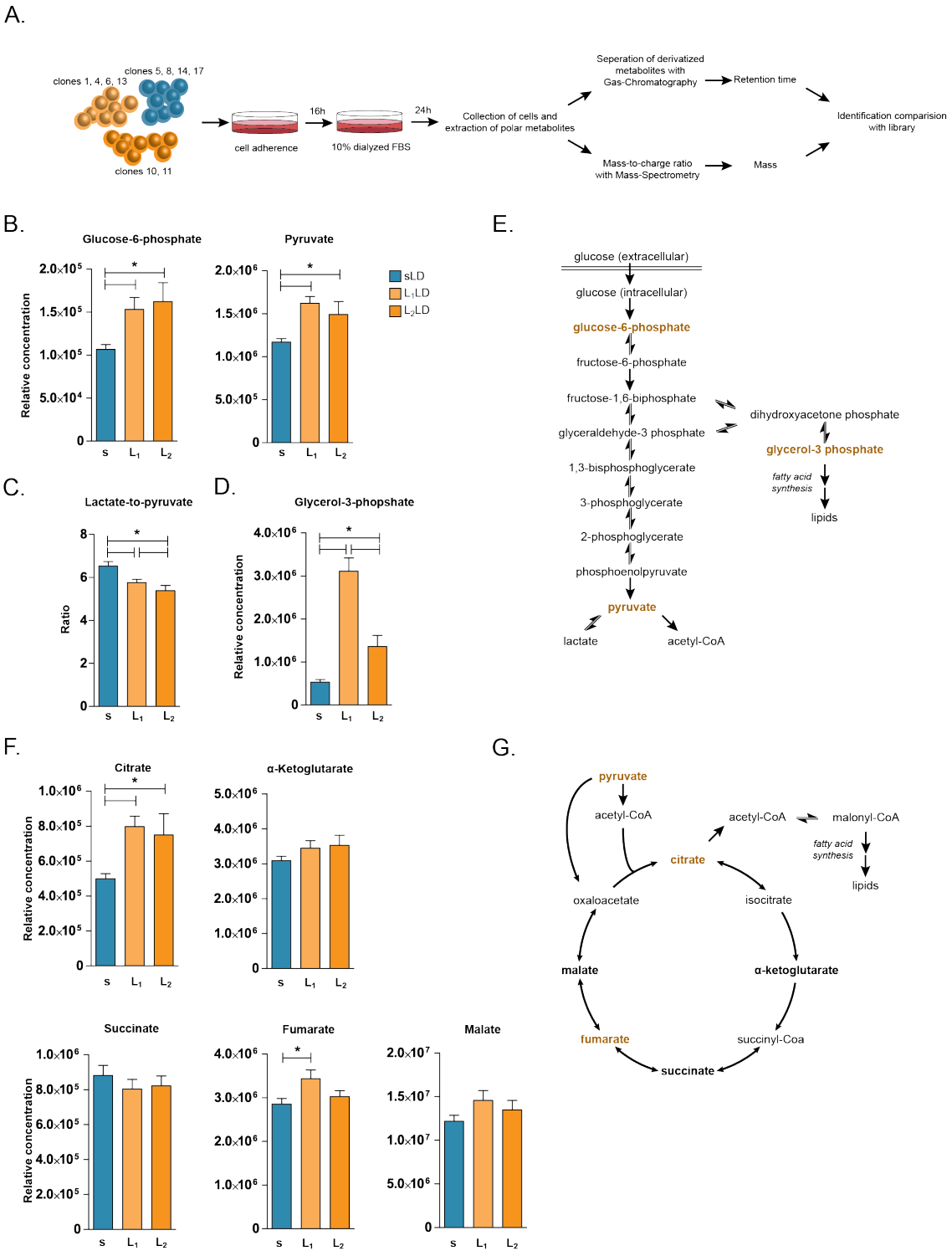


Figure 6.5: GC-MS based, glycolysis and TCA cycle-focused, metabolic profiling in the three LD clone clusters.

(A) Experimental setup of untargeted metabolic profile screening in the LD clones. Each clone was seeded at 500,000 cells per well in 6-wells plates (2 wells per clone); small LD clones 5, 8, 14 and 17, large LD clones with good self-renewal ability 1, 4, 6, 13, and large LD clones with reduced self-renewal ability 10 and 11. After an initial 16-hour period, which allowed the cells to adhere to the bottom of the wells, cells were cultured for another 24 hours under standard culture conditions in which GMEM was replaced by DMEM and 10% FBS was replaced by 10% dialyzed FBS in which unspecified small molecules are minimized. Cells were then collected and total protein content was used to confirm similar growth

rates amongst the clones. Intracellular polar metabolites were extracted from five independent wells of each clone analysed. The identity of metabolites was then assigned with the Automated Mass Spectral Deconvolution and Identification System (AMDIS) based on in-house databases and FiehnLib. **(B-D,F)** Relative concentration of metabolites involved in glycolysis and the citric acid cycle in the three clone clusters described in A. Error bars represent SEM of 2-3 technical replicates, and 2 biological replicates. $P<0.05$ (*), Student's t test. In collaboration with Hector Keun and James Ellis. **(E)** Schematic diagram of the glycolytic pathway with detected metabolites in bold and/or colour. **(G)** Schematic diagram of the citric acid cycle with detected metabolites in bold and/or colour.

Nineteen amino acids were also reliably detected across the three clone clusters of which some are shown here (Fig 6.6). There are at least five amino acid pools that showed pronounced changes. Aspartate levels are found increased in large LD clones as compared to small LD clones, concomitant with lower levels of asparagine specifically in L_1LD clones (Fig 6.6A). This might indicate differences in fuelling of the citric acid cycle at the oxaloacetate entry (Fig 6.5E). Interestingly, glutamine, which is linked to the previously mentioned α-ketoglutarate:succinate ratio, was significantly higher in large LD clones possibly linking again to a difference in pluripotency status between the large and small LD clones (Fig 6.6B). Methionine (reduced) displayed a greater than 2-fold decreased concentration in large LD clusters (Fig 6.6C). Note that methionine can be oxidized to methionine sulfoxide, conferring protection from oxidative stress (Fig 6.6D). This coincided with a decrease in the concentration of reduced glutathione (Fig 6.6C), further suggesting that large and small LD clones might have a different redox status. Other amino acids detected which were able to fuel the citric acid cycle generally showed a trend towards lowered concentration in large LD versus small LD clones, such as leucine and isoleucine (Fig 6.6F). In contrast, the levels of threonine, an essential amino acid for ESC proliferation and maintenance [86], remained steady across all clone clusters.

Overall, our untargeted metabolic profiling of the distinct LD clone clusters revealed profound differences in glucose metabolism. This potentially includes enhanced pyruvate and citrate production in LLD clones along with compensation mechanisms in fuelling the citric acid cycle by amino acids. As citrate is an important intermediate in *de novo* lipid synthesis pathway, this data reinforces our working hypothesis of a possible "lipid switch" in LLD clones, associated with different pluripotency and redox status. This prompted us to further investigate and compare the fate of glucose in sLD and LLD clones using stable isotope tracer experimental setting where unlabelled glucose is substituted with uniformly ^{13}C-labelled glucose.

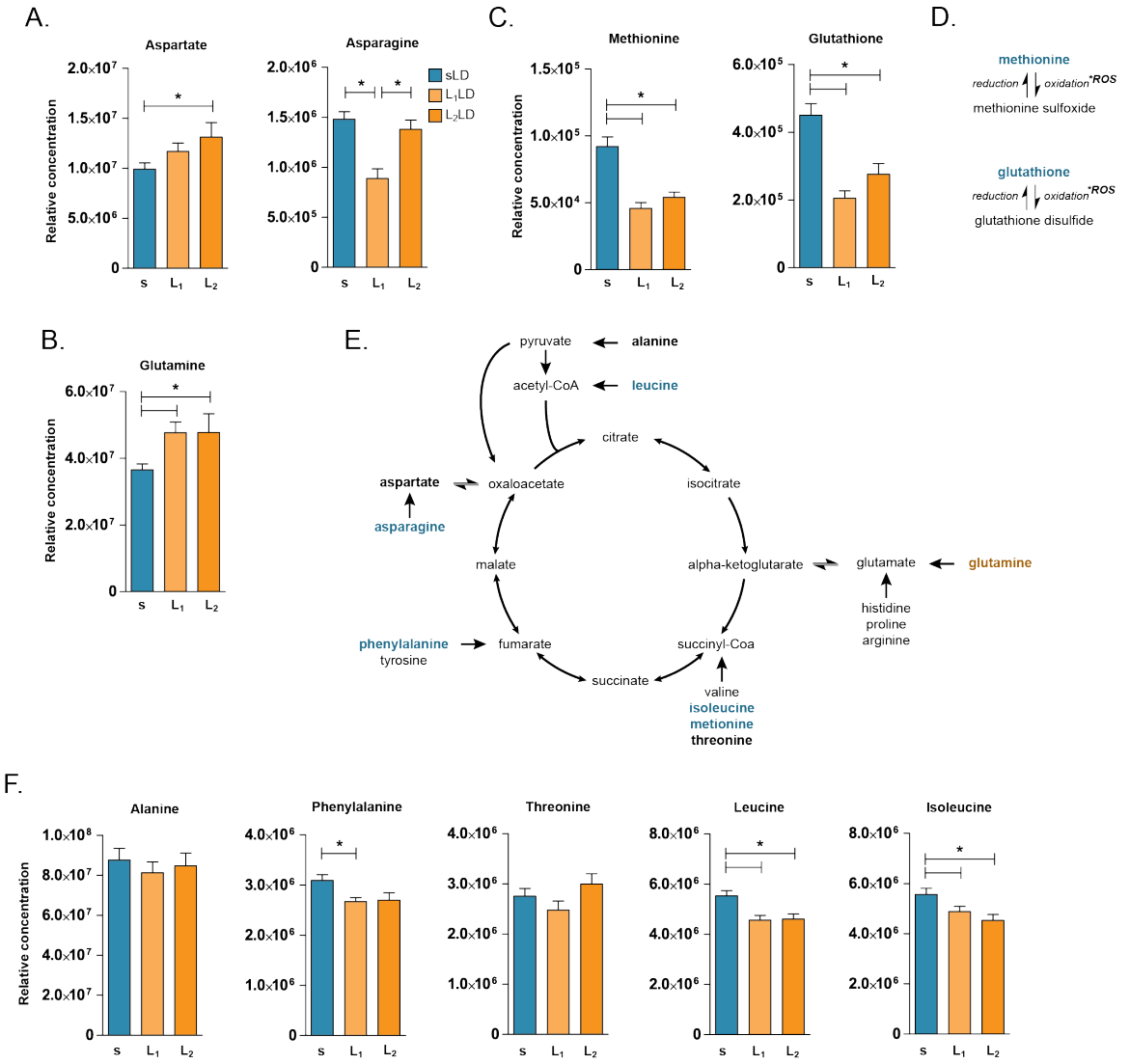


Figure 6.6: GC-MS based protein-focused metabolic profiling in the three LD clone clusters.

(A-C,F) Relative concentration of essential and non-essential amino acids, and anti-oxidant proteins in the three clone clusters described in Fig 6.5A. For experimental setup, also see Fig 6.5A. Error bars represent SEM of 2-3 technical replicates, and 2 biological replicates. P<0.05 (*), Student's t test. In collaboration with Hector Keun and James Ellis. **(D)** Schematic diagram of the citric acid cycle with detected amino acids in bold and/or colour. **(F)** Redox reaction of two detected antioxidants methionine and glutathione.

6.2.6 Glucose tracing in sLD and LLD embryonic stem cell clones.

For stable isotope tracer experiments, cell numbers at the beginning and end of each experiment were counted confirming no significant difference in growth rate amongst clones over the time-course of ^{13}C glucose labelling. As depicted in Fig 6.7A, cells were plated overnight, followed by a 1 hour equilibration period in DMEM supplemented media containing unlabelled ^{12}C glucose and dialyzed FBS in which unspecified small molecules are minimized. Hereafter media was swapped, where unlabelled ^{12}C glucose was substituted by ^{13}C glucose, and the cells were collected after an additional 72-hour culture period. Intracellular lipid species (apolar fraction) were analysed by GC-MS using an extraction and derivatisation method that enabled the detection of fatty acid esters, so called bound fatty acids (Fig 6.7B). Of note, the origins of the fatty acid methyl esters detected were not restricted to a specific class of lipid molecules. These trans-esterified fatty acids could come from membrane phospholipids, or signalling and functional lipids such as diacylglycerol and triacylglycerol. Global analysis of the lipid abundance profile indicated that the levels of bound palmitate (16:0) and oleate (18:1) were the same amongst all clones (Fig 6.7C-D). However, an increase in methyl stearate (18:0) levels was found in the L_1LD clones compared to sLD and L_2LD clones. Interestingly, the availability of stearate has previously been reported as a valuable distinctive marker between naïve and primed ESCs [104]. Therefore, this data furthermore highlights the distinct pluripotency status of our clone clusters. Although characterising the full lipidomic profiles of clones would be interesting in this respect, we here focussed on examining the relative ability of clones to *de novo* synthesise and elongate lipids via inspection of their mass isotopomer distributions. In particular, we closely examined the mass isotopomer distributions of methyl palmitate and stearate to determine if uptaken ^{13}C glucose carbons were incorporated into newly synthesised fatty acids (Fig 6.7E). Labelled carbon groups are incorporated into fatty acids via synthesis by incorporation of carbon labelled acetyl-CoA units (Fig 6.7E-F)). This is indicated as the normal/unlabelled fatty acid mass (M) plus the amount of labelled carbons incorporated into fatty acid chains. As shown Fig E, we found increased incorporation of glucose derived two-carbon acetyl-CoA units into both the methyl palmitate and stearate in large LD clones compared to small LD clones. More precisely, large LD clones showed a bias towards methyl palmitate with 12 labelled carbons (M+12), and methyl stearate with 12 or 14 labelled carbons (M+12 and M+14) in contrast to small LD clones. This indicates that *de novo* fatty acid synthesis of palmitate and stearate from exogenous uptaken glucose is enhanced in both L_1LD and L_2LD clones.

Overall, our profiling of apolar metabolites reveals distinctive lipid profiles amongst sLD and LLD clone clusters. In particular, we here provide direct evidence for enhanced *de novo* fatty acid synthesis in the large LD clones as a possible novel hallmark of primed ESCs.

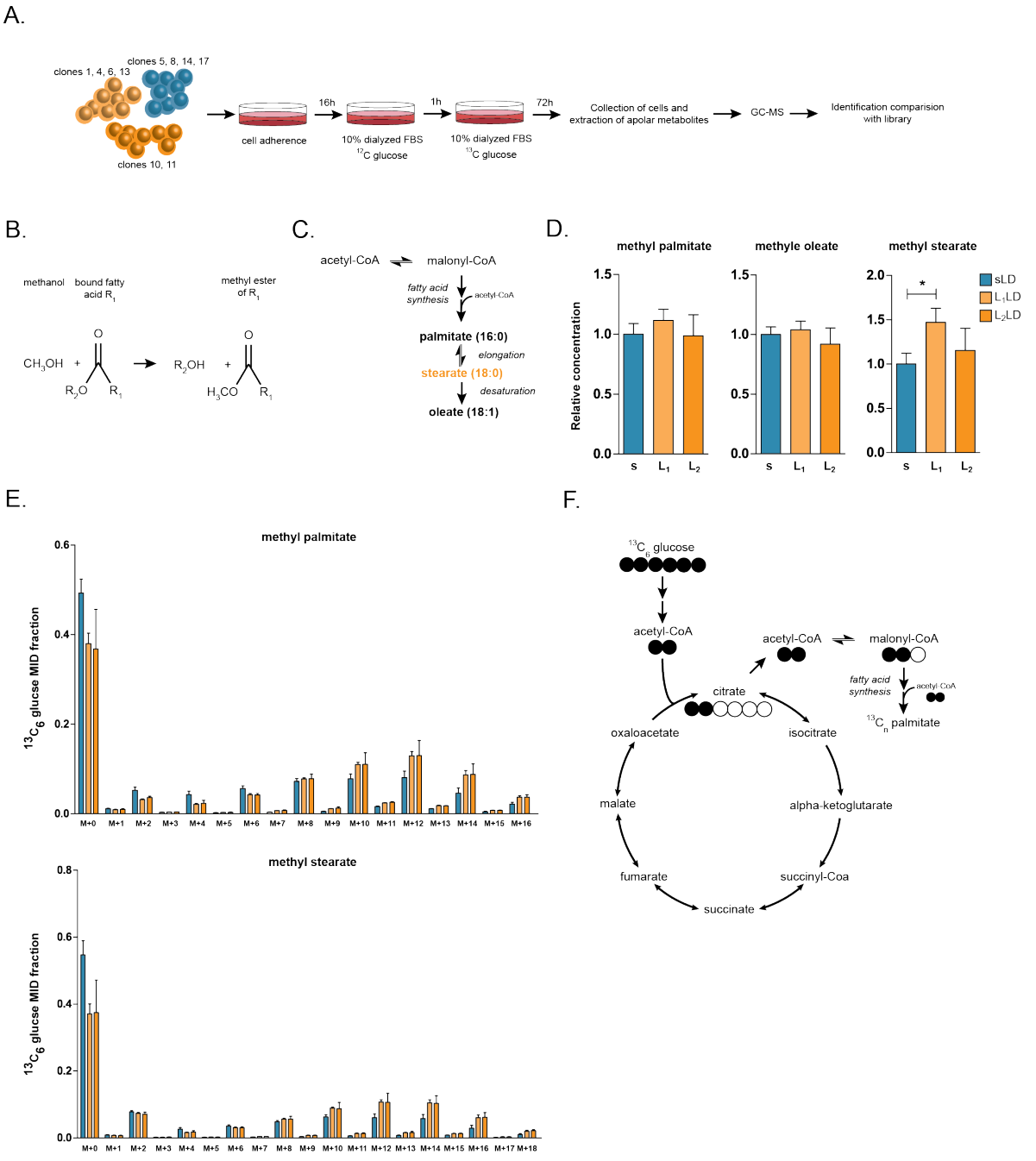


Figure 6.7: GC-MS lipid-focused metabolic analysis of ^{13}C glucose tracing in the three LD clone clusters. **(A)** Experimental setup of ^{13}C glucose tracing in the LD clones. Each clone was seeded at 250,000 cells per well in 6-well plates; small LD clones 5, 8, 14 and 17, large LD clones with good self-renewal ability 1, 4, 6, 13, and large LD clones with reduced self-renewal ability 10 and 11. After an initial 16-hour period, which allowed the cells to adhere to the bottom of the wells, cells were equilibrated for 1 hour in DMEM supplemented media containing unlabelled ^{12}C glucose and dialyzed FBS in which unspecified small molecules are minimized. Hereafter cells were cultured for another 72 hours under similar culture conditions, however ^{12}C glucose was replaced by ^{13}C glucose. Cells were then collected, and parallel wells were counted to confirm similar growth rates amongst the clones. Intracellular apolar metabolites (i.e. lipids) were extracted from six independent cultures of each clone analysed. The identity of metabolites was then assigned with the Automated Mass Spectral Deconvolution and Identification System (AMDIS) based on in-house databases and FiehnLib. **(B)** Bound fatty acid transesterification in preparation of GC-MS. Adapted from Chung Ho Lau. **(C)** Schematic diagram of fatty acid synthesis and elongation with detected metabolites in bold and/or colour. **(D)** The intracellular relative concentration of

methyl palmitate, methyl oleate, methyl stearate in the three clone clusters, expressed relative to the small LD clones (sLD). **(E)** Labelling of methyl palmitate and methyl stearate after incubation with labelled $^{13}C_6$ glucose. Data are represented as the mass isotopomer distribution (MID); the fraction of the indicated isotopologue to the total pool size of each metabolite. **(F)** Schematic representation of isotope tracing experiment with $^{13}C_6$ glucose. Black-filled circles indicate ^{13}C-carbon, whereas the white filled circles represent the unlabelled carbon. The schematic shows the expected composition of labelled carbons of the indicated metabolites. Bar graphs represent mean SEM from 3 independent biological replicates. $P<0.05$ (*), Student's t test.

6.2.7 LLD and sLD embryonic stem cell clones display different oxidative status and glycolytic rate

Following our observation that LD clones display a variety of metabolic differences, we here further investigate metabolic flux using a complementary approach. As previously discussed (see Chapter 5), Seahorse Extracellular Flux Analyser allows us to determine the mitochondrial respiration and glycolytic function of cells in real time (Fig 6.8A-B; upper panels). Seahorse-based measurements of oxygen consumption rate (OCR) and extracellular acidification rate (ECAR) provide, in comparison with GC-MS-based approaches, a direct and simple way of evaluating fundamental metabolic parameters simultaneously upon drug treatments. In these experiments, we observed that basal and maximal mitochondrial respiration of clones varies greatly, as expressed relative to the E14 parental cell line (Fig 6.8A; bottom panel). Interestingly, large LD clones overall exhibited the highest OCR values relative to small LD clones. This presents an interesting paradox with our previous analyses suggesting reduced lipid oxidation and conversely enhanced lipid storage in these cells. We thus reckoned that the increased oxygen consumption we observed in large LD clones might result from other oxidative pathways and more specifically glucose via the citric acid cycle rather than lipid oxidation. This also corroborates well with LD enlargement providing an effective mechanism to regulate lipid consumption upon demands as extensively studied in brown adipocytes [124]. Anaerobic glycolytic function is measured as the extracellular acidification rate (ECAR) during the subsequent addition of a series of chemicals targeting mitochondria activity and anaerobic glycolysis (Fig 6.8B, upper panel). Of note, in this test, cells are initially starved of extracellular glucose, so that glycolysis can be calculated upon acute addition of glucose. We thus observed that large LD clones have increased glycolytic capacity compared to small LD clones (Fig 6.8B; bottom panel). Increased ECAR was reportedly associated with the primed pluripotency state [74]. Interestingly, a burst of oxidation might precede the so-called glycolytic switch normally observed upon exit of naïve ESC pluripotency as indicated by a peak of basal respiration in L_1LD relative to sLD clones; an effect attenuated in L_2LD clones concomitant with enhanced glycolytic function (Fig 6.8C). Taken together, our findings reiterate the existence of metabolic heterogeneity amongst ESC populations and furthermore indicate that small LD clones might represent a more steady metabolic state when compared to large LD clones, being less responsive to metabolic disruptions.

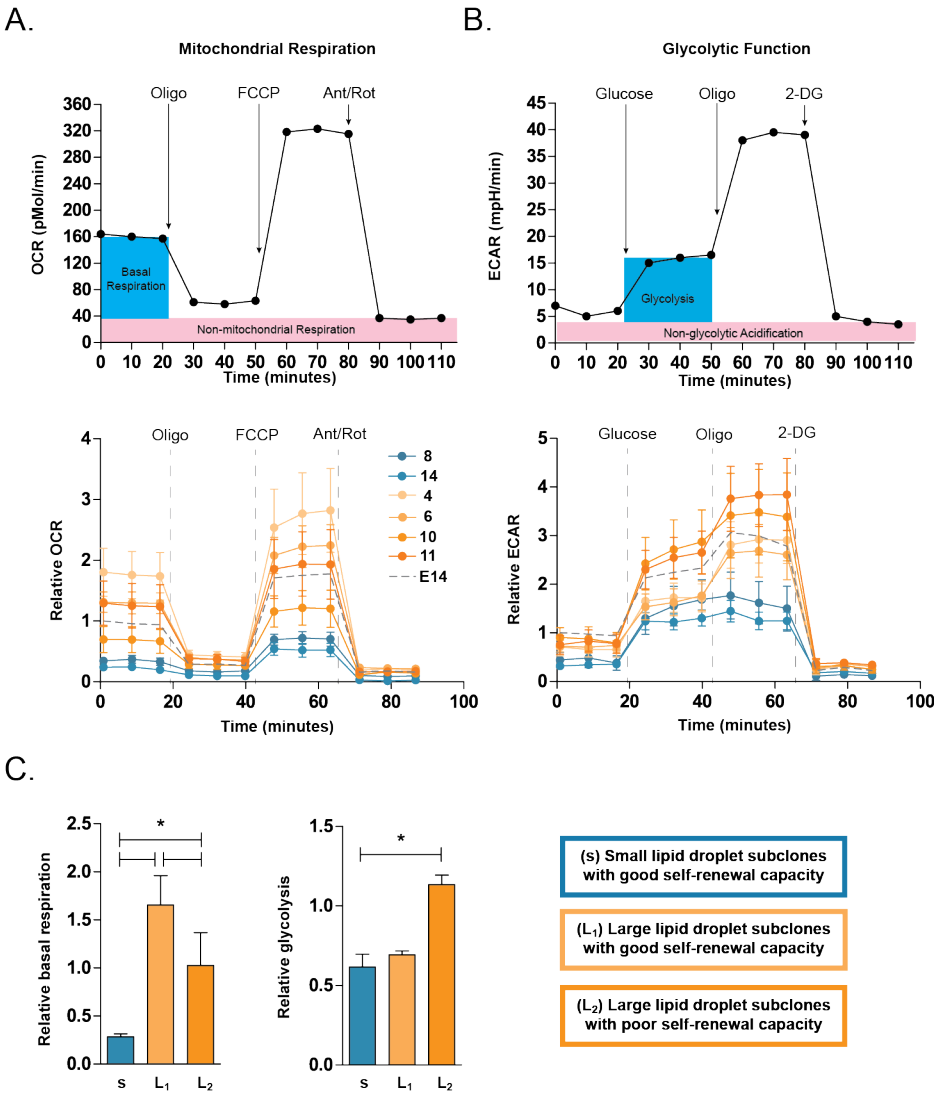


Figure 6.8: Seahorse-based analysis of the sLD and LLD clones.

(A) Oxygen consumption rates (OCR) and **(B)** extracellular acidification rate (ECAR) upon Mitostress test and Glycolytic Stress Test respectively, in selected LD clones; small LD clones 8 and 14, large LD clones with good self-renewal ability 4 and 6, and large LD clones with reduced self-renewal ability 10 and 11. Top panels indicate **(A)** sample OCR graph of Mitostress Test and **(B)** sample ECAR graph of Glycolytic Stress Test. **(C)** Relative basal respiration and glycolytic rates from the plots in A and B respectively, when combining the individual clones in each cluster. Error bars represent SEM of 3 biological replicates with 5 to 6 technical replicates. Data were expressed relative to parental E14-ESCs. $P<0.05$ (*), Student's t test.

6.3 Summary and Conclusions

In summary, following our initial observation of cell-to-cell heterogeneity in LD size and number we were here able to successfully isolate and maintain ESC clones that harbour, under the same (FBS/LIF) culture conditions, different lipid signatures. These clones not only present differences in LD morphologies (i.e. small and large LDs), but also display differential gene expression patterns, functional and metabolic capacities. Importantly, despite the metastable expression of self-renewal and differentiation markers in ESCs cultured in the presence of FBS and LIF [228], the distinct characteristics of the clones were faithfully retained upon propagation. The reason beyond this unexpected stability remain to be fully investigated. Here, we found that small LD clones consistently demonstrate the highest capacity to form undifferentiated colonies. This is in line with their enhanced expression of self-renewal regulators, and conversely reduced expression of early differentiation markers as we initially noticed during the establishment of LD clones. In contrast, large LD clones portray more spontaneous differentiation, of variable extent, concomitant with reduced and increased expression of self-renewal and differentiation markers, respectively. Upon differentiation assays, we confirmed that all clones retain the capacity to differentiate normally into either embryonic or extra-embryonic-like lineages. However, we did observe differences in the induction kinetics of some differentiation markers especially amongst large LD clones. Of note, in both differentiation assays, we observed the consistent induction of *Cidea* at early differentiation time-points, suggesting that LD enlargement might indeed be associated with the onset of differentiation.

To further explore the suggested link between the presence (or absence) of large LDs and different ESC states, we established the transcriptomes of large and small LD clones using RNA-sequencing. This, in conjunction with the differential self-renewal capacities of these clones, led us to establish three main clusters of small LD clones (sLD), large LD clones with good self-renewal ability (L_1LD), and large LD clones with reduced self-renewal ability (L_2LD). Metabolism (including Glucose Metabolism, Lipid Metabolism or Adipogenesis, TCA cycle and Electron Transport Chain), PluriNetWork, Developmental Biology, Signalling associated with differentiation, and Cellular Remodelling were always discriminating between the three clusters. Interestingly, a more in-depth analysis of our RNA-seq data indicated that, in particular, the large LD clusters differ in their oxidative status, and that the L_2LD cluster further segregated from the two other clone clusters based on Cell Signalling Associated Differentiation, Differentiation Pathways and Cellular Remodelling. Amongst the metabolic pathways, fatty-acid metabolism was of our particular interest, in relation to the difference in LD size and number we uncovered amongst the clones. RT-qPCR confirmation prompted us to propose the following "lipid switch" working hypothesis whereby small LD clones might mainly oxidise exogenously scavenged lipids, whereas large LD clones show evidence for enhanced *de novo* lipid synthesis and storage.

This hypothesis was further substantiated using GC-MS based untargeted metabolic profiling. Our data revealed striking differences in metabolic flux amongst the clone clusters, with profound differences in glucose metabolism pointing to a possible "shuffle" of anaerobic glycolysis intermediates towards increased *de novo* lipid synthesis activity in large LD clones. This was further investigated using ^{13}C glucose tracing

experiments where unlabelled glucose was substituted with uniformly ^{13}C-labelled glucose. Analysis of apolar metabolites (i.e. lipids) revealed increased levels of total methyl stearate in L_1LD clones. Interestingly, the availability of stearate has previously been reported to discriminate between the naïve and primed pluripotent state [104], suggesting that L_1LD clones might represent a distinc metabolic state as compared to sLD (naïve) and L_2LD (relatively primed) clones. In this report, analysis of untargeted LC-MS profiles of naïve and primed ESCs interestingly revealed that these subpopulations could be best discriminated based on stearic acid and cholesterol levels. Hence, it would also be of interest to further evaluate the relative composition of enlarged LDs in terms of neutral lipids (i.e. triglycerides versus cholesterol esters). Importantly, inspection of lipid mass isotopomer distributions reinforced our conclusion of increased *de novo* fatty acid synthesis in both L_1LD and L_2LD clones.

We therefore further investigated the metabolic state of the clones via Seahorse extracellular flux analyser, which in comparison to GC-MS provides a direct and simple way of measuring several fundamental metabolic parameters in real-time. This confirmed the prevalence of different metabolic fluxes in large and small LD clones, and most particularly, between L_1LD and L_2LD clones. In general, large LD clones were found to be more oxidative, despite compelling evidence for increased lipid synthesis and storage in these clones. It seems therefore unlikely that fatty acids are the primary substrates for oxidation in large LD clones. In agreement, we observed that *Cpt1* expression is down-regulated in large LD clones relative to small LD clones. What oxidative pathway(s) might therefore account for the observed increased oxygen consumption in large LD clones? From our GC-MS analysis, we reckon that this is, at least partly, related to the enhanced citric acid cycle activity we observed in large LD clones, with increased citrate production to be used for *de novo* lipid synthesis. How is then the citric acid cycle sustained in large LD clones, if citrate is shunted out of the cycle for this purpose? This can be potentially explained by fuelling of the cycle with other metabolites, most likely glutamine, with increased intracellular concentration being observed in large LD clones indicative of enhanced uptake from the culture medium. Further Seahorse experiments in the presence or absence of glutamine as well as ^{13}C glutamine tracing experiments would be useful to further establish this pathway. Interestingly, our Seahorse data corroborate with our suggestion that L_1LD clones might present a "transitional" metabolic state from the "steady" state of sLD clones and the glycolytic profile of L_2LD clones, which is characterised by an enhanced oxidative status to potentially sustain the energy-demanding process of lipid synthesis occurring at the exit of naïve ESC pluripotency and glycolytic switch [57, 104].

Chapter 7

Discussion

Dynamic metabolism remodeling occurs throughout embryogenesis. In the early mouse embryo this is typified by a gradual shift from the capacity to use both oxidative and anaerobic glycolytic metabolism, towards almost exclusively anaerobic glycolysis upon embryo implantation [78, 229, 74]. However, the importance of lipid metabolism, and how alternative energy substrates are used in a coordinated manner at key developmental steps remain to be fully investigated both *in vivo* and in stem cells. Concomitant with reduced metabolic flexibility, we have observed that substantial amounts of lipids accumulate in the pre-implantation blastocyst and ICM-derived (naïve) ESCs. In this study, we aimed at determining the molecular mechanism(s) underlying LD dynamics in pluripotent cells both *in vivo* and *in vitro*, as well as understanding the functional importance of LD heterogeneity in ESCs possibly linking lipid droplet biology with fundamental developmental processes in pluripotent stem cells.

7.1 Investigating the molecular mechanism(s) underlying LD dynamics in ESCs and in the early embryo.

7.1.1 Does Cidea expression control the formation of supersized LDs in ESCs?

We observed that ESCs dynamically form large LDs in contrast to MEFs upon stimulation. This is mirrored by an ESC-specific induction of the LD-associated protein Cidea; a factor extensively studied in brown adipocytes where it promotes LD enlargement via LD-LD fusion and transfer of stored lipids [127, 128]. Interestingly, similar LD-LD fusion events were found to operate in ESCs as captured by live cell imaging, further pointing to Cidea as an important regulator of LD dynamics in ESCs. To infer an essential role for Cidea in this process, we ectopically overexpressed v5-tagged Cidea forms in ESCs. By modulating Cidea expression and assessing its impact on LD morphology we thus determined that Cidea alone is sufficient to support LD enlargement in ESCs. Notably, we found that abrogating Cidea induction interferes with LD-fusion ability of ESCs upon treatment with KSR. LD mobility and enlargement by coalescence was previously reported to dependent on microtubules and actin [173, 230]. This process remains unaffected in Cidea knockdown and knockout ESCs where clustering of small LDs is evident. Our results, however, confirmed previous findings in adipocytes that Cidea essentially promotes LD enlargement via fusion of pre-existing LDs [128], rather than controlling their motility. Conversely, we found that overexpressing Cidea in ESCs results in LD enlargement regardless of tissue-culture conditions (i.e. with or without KSR). When stably transfecting Cidea KO cells with Cidea mutant forms where specific Cidea protein activities have been perturbed, the Cidea-depleted phenotype, i.e. clustering of small LDs, was conserved in Cidea KO ESCs as tested upon KSR treatment and BODIPY staining. These experiments thus established that the expression of a fully functional Cidea protein is strictly required for LD enlargement in ESCs.

7.1.2 What regulates Cidea expression in pluripotent stem cells?

We have observed that Cidea expression declines upon embryoid body (EB)-induced ESC differentiation, pointing to a close association with the undifferentiated ESC state. The Cidea promoter was previously studied in adipocytes where it is regulated by oestrogen-related receptors, Nrf-1 and co-factors [231]. Similarly, Cidea was identified amongst putative targets of the nuclear receptor Esrrb and its essential co-activator Ncoa3 in ESCs [185]; two pluripotency-associated factors that are promptly down regulated upon EB formation. Here we confirmed via motif sequence enrichment analysis, ChIP-qPCR and luciferase reporter assay that Cidea is indeed regulated by Esrrb and possibly other pluripotency factors, like Oct4, in ESCs. It will be interesting to examine whether Ncoa3 recruitment at Esrrb-bound Cidea promoter might be enhanced in KSR-treated cells using ChIP-qPCR assays. Furthermore, it has been previously reported that insulin suppresses Cidea expression in bovine mammary epithelial cells [232]. In addition, insulin treatment decreased the levels of Cidea mRNA and protein in human-differentiated adipocytes [233]. Although insulin is also typically present in FBS, its impact on Cidea in stem cells (as opposed to somatic cells) remains to be investigated. Insulin is likewise present in KSR media, in which we consistently observe marked increase in Cidea expression in ESCs. It is therefore expected that other media components are more important in regulating Cidea expression in ESCs. Here we propose a role for free fatty acids (FFAs), whereas we observed all G-protein coupled FFA receptors to be induced upon KSR treatment. Indeed, Cidea expression has been reportedly induced by saturated fatty acids in hepatocytes [234]. Such induction was then reduced when sterol response elementbinding protein (Srebp)1c was knocked down [234]. In contrast, the overexpression of Srebp1c restored the saturated fatty acidinduced expression of Cidea [234]. Moreover, Cidea expression was shown to be induced by Srebp-1 via a direct effect of Srebp-1 occupying the Cidea promoter [235]. Cidea expression in ESCs is therefore most likely regulated by interplay of pluripotent (i.e. Esrrb and Ncoa3) as well as metabolic (Nrf-1 and Srebp) factors. ChIP-qPCR and luciferase reporter assays can provide further confirmation about which specific factors regulate Cidea expression in pluripotent stem cells. The stability of Cidea protein was found significantly increased in response to treatment with fatty acids in hepatocytes [234]. Post-translational modifications of the Cidea protein have not been investigated in this thesis, however they are likely to take place and could explain why we unexpectedly observed increased levels of ectopic Cidea protein upon KSR treatment, without any noticeable change at the transcriptional level. Moreover, in adipocytes, the ubiquitin-proteasome system confers an important post-translational modification that controls the protein stability of Cidea [236]. In this published report, Cidea was uncovered as a short-lived protein, which can only be accumulated in the presence of the specific proteasome inhibitors ALLN and MG132. It would be interesting to know whether this also plays a role in ESC Cidea regulation, and whether ESC treatment with the cysteine protease/proteasome inhibitor ALLN or the specific proteasome inhibitor MG132, would lead to Cidea protein accumulation and consequently LD enlargement, recapitulating the Cidea-OE phenotype.

7.1.3 Does Cidea-mediated LD enlargement operate in the developing embryo *in vivo*?

Our collaborator Dr Shankar Srinivas previously reported that the distribution, size and numbers of LDs dynamically change in the developing embryo, showing numerous, small LDs at the morula stage with an increase in size and decrease in numbers of LDs upon blastocyst formation (Fig 7.1). This indicates that LD enlargement also operates in the pre-implantation embryo [173]. What about Cidea expression profile *in vivo*, especially during the transition from morula-to-blastocyst stage? Taking advantage of previously generated lineage-specific RNA sequencing datasets from the morula stage to post-implantation embryos, we observed the induction of Cidea expression at the blastocyst relative to morula stage. This corroborates with maximal LD enlargement at the blastocyst stage as confirmed in this study using BODIPY staining. Strikingly, however, we observed a sharp and concomitant down regulation of *Cidea*, *Plin5* and *Dgat1-2* at the onset of implantation and exit from naïve pluripotency (from E4.5 onwards) (Fig 7.1). These findings revealed a dynamic expression profiles for Cidea and other lipid-associated genes in peri-implantation embryos, and provide first indication that LD enlargement might operate *in vivo* in a timely manner.

As seen in blastocyst-derived ESCs, we have now confirmed by RT-qPCR on a pool of freshly isolated E3.5 and E5.5 embryos that Cidea transcript is indeed highly and selectively expressed in pre-implantation blastocyst relative to post-implantation embryos. Co-staining for BODIPY and Cidea protein *in vivo* at different developmental stages (i.e. prior and upon blastocyst implantation) further allowed us to test whether *Cidea* expression correlates with LD enlargement in a tissue-specific manner as well as determining where and when large LDs might be consumed (or mobilised) in the implanting embryo. Here we carefully monitored that supersized LD pre-dominantly form in the pluripotent compartment of blastocysts and are mobilization at peri-implantation. LD enlargement is thus not resumed at post-implantation stage where Cidea is normally not expressed. Interestingly, LD enlargement is retained in extra-embryonic tissues, i.e. the mural TE at E4.5, and the VE at E5.5. As for Cidea protein dynamics, we have so far demonstrated that Cidea protein resides on the surface of LDs in E3.5 embryos as seen both in ICM and TE cells. At E4.5, Cidea signals were also selectively detected in mural TE, however strong background expression remained despite extensive effort by our collaborator Christopher Royer to optimize this staining.

These results indicate that Cidea-mediated LD enlargement likely operates *in vivo* in the developing embryo. To further explore a role for Cidea-mediated LD enlargement in the embryo we are currently investigating in detail the phenotype of the Cidea KO in ESC organoids *in vitro*, and additionally, collaborating with Dr Alice Jouneau for generating chimera embryos. By injecting labelled ESCs (WT and Cidea KO) into 4 cells-embryos, we are hoping to achieve a high percentage of colonization in the ICM of blastocysts. This could provide a valuable phenotypic validation of the cell autonomous action of Cidea-mediated LD enlargement in the ICM as compared to host TE cells that are expected to retain normal LD enlargement and Cidea protein expression. Notably a chimera embryo, with only epiblast

Cidea depleted, is a good model for validating the role of Cidea-mediated LD fusion in epiblast lineage specifically. These experiments could also possibly provide validation for the morphogenetic defect we observed upon organoids *in vitro* in the absence of Cidea expression; Cidea KO organoids were here found by Tommy King Mau to show pronounced defect in lumen formation and the maintenance of epiblast cell polarity (see Chapter 4 and data not shown). Additionally, a direct link with effective LD enlargement was inferred upon rescued experiments, in which Cidea KO ESCs transfected with WT Cidea displayed a WT organoid phenotype in contrast to Cidea KO ESCs transfected with mutant Cidea (data not shown).

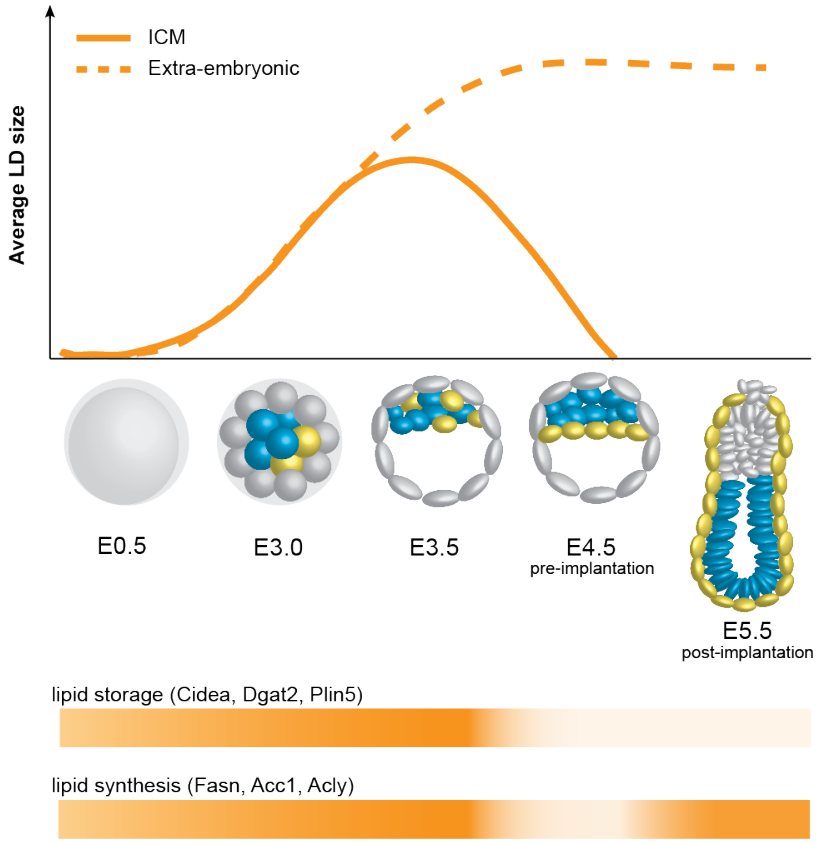


Figure 7.1: Lipid droplet dynamics throughout peri-implantation development.

Schematic representation of large lipid droplet accumulation in early mouse embryonic development from zygote (E0.5) to post-implantation stage (E5.5), in the inner cell mass (ICM) and extra-embryonic structures. Highlighting the expression pattern of key lipid storage (*Cidea*, *Dgat2* and *Plin5*) and lipid synthesis (*Fasn*, *Acc1* and *Acly*) genes at these developmental stages.

7.1.4 What is the role of Cidea in ESC self-renewal and differentiation ability?

Cidea promoter regulation by the pluripotency factor Esrrb provides a possible link between Cidea and the ESC pluripotent state, which was here further investigated in Cidea-depleted ESCs. In this ESC model, we confirmed that Cidea depletion interferes with the LD-forming ability of ESCs upon treatment with KSR, evident by clustering of small LDs. Interestingly, we demonstrated that Cidea-depleted ESCs display a particular phenotype embryoid body formation. Although the early stages of differentiation were similarly characterized by the swift down-regulation of pluripotency-associated genes and concomitant up-regulation of early differentiation markers in both Cidea-depleted and control EBs, unexpectedly late EBs formed from Cidea-depleted cells exhibited abnormal morphology with the emergence of cystic-like structures that were not observed in control EB cultures. The formation of cystic EBs is reminiscent of what is normally observed during further development of EBs undergoing amniotic cavitation [237]. The process is known to be a developmental event involving high incidence of cell death, which might strike a possible link with the known role of Cidea as apoptotic factor [237, 196]. However, while Cidea was proposed to be a pro-apoptotic protein, our observations would rather suggest an anti-apoptotic action in this context. Cavitation, as observed in our Cidea-depleted EBs, is merely one mechanism of lumen formation, the other being hollowing with the establishment of cell polarity and gradual expansion of a central lumen [237]. Interestingly, it has been demonstrated that MDCK cells, a well-studied epithelial cell model, can switch from hollowing to cavitation when cell polarity is disrupted [238]. In our system, the formation of multiple cavities could also suggest a similar switch towards cavitation and enhanced apoptosis in Cidea KO EBs and organoids. To address this, we are planning to further investigate apoptotic events during differentiation of Cidea KO by TUNEL assay or apoptotic factor (cleaved caspase-3) staining. A switch of lumen formation mechanisms could act as a compensation mechanism, which might potentially explain the non-lethality of Cidea KO embryos [156].

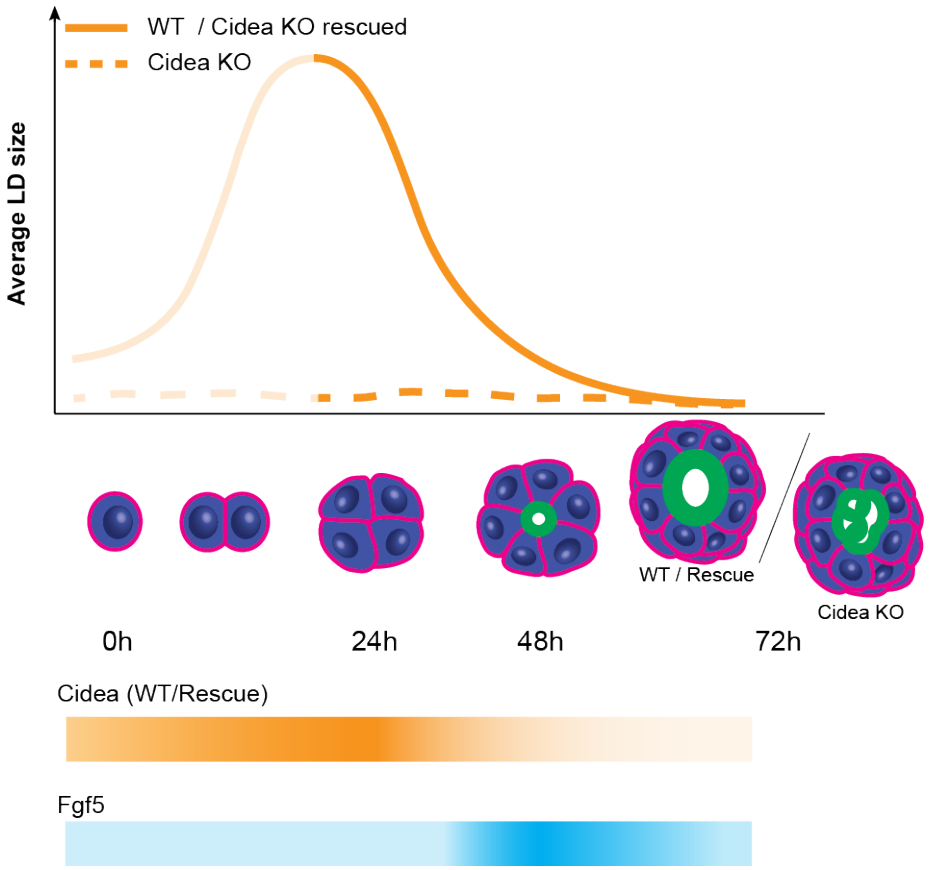


Figure 7.2: Lipid droplet dynamics throughout 3D ESC organoid differentiation.

Schematic representation of large lipid droplet accumulation in 3D ESC organoid differentiation, up untill 72 hours after differentiation initiation of Wildtype (WT) ESCs, Cidea knockout (KO) ESCs, and Cidea KO ESCs rescued with WT Cidea. Defective (multiple) lumen formation at 72h is indicated in Cidea KO organoids. Highlighted below is the expression pattern of *Cidea* in WT and Cidea KO rescued ESCs organoids, and differentiation marker *Fgf5*.

7.1.5 Characterising the impact of Cidea expression modulation on ESC metabolism

The role of Cidea-mediated LD enlargement in regulating the oxidative status of brown adipocytes is well established [127, 156]. We were here interested to examine whether a similar role for Cidea exists in ESCs. ESCs are known to be metabolically flexible, capable of both oxidative phosphorylation (OXPHOS) and anaerobic glycolysis to fulfil their energy and biomass production requirements [74]. However, the balance between these two metabolic fluxes (OXPHOS versus anaerobic glycolysis), and the specific substrates used for oxidation is not fully explored. In this context, we explored how enforcing or inhibiting Cidea function might impact on ESC metabolism via two main approaches.

To investigate metabolic flux alterations that might result from modulating Cidea function, we firstly studied the utilization of up-taken glucose via GC-MS based technologies. Stable isotope tracer experiments were performed on Cidea overexpressing and knockdown ESCs, whereby unlabelled glucose was substituted with uniformly ^{13}C-labelled glucose. While the uptake of ^{13}C glucose was relatively similar between the Cidea-OE and control cells, we found that the glycolytic flux of uptaken ^{13}C glucose into ^{13}C lactate secretion was slightly attenuated in Cidea over-expressing cells. This could be explained by either a net reduction in the production of ^{13}C glucose-derived ^{13}C lactate, or increased re-uptake of excreted ^{13}C lactate in Cidea-OE cells. The former explanation might suggest increased shunting of ^{13}C glucose into other metabolites (e.g. acetyl-CoA for OXPHOS/lipid synthesis, or glycerol-3-phosphate for lipid synthesis). The latter, lactate re-uptake, would possibly be accomplished by monocarboxylate transporter (MCT), which transports lactate, and other monocarboxylates, across the plasma membrane in a proton-linked bidirectional manner [239, 240]. Various studies have been carried out to investigate the effect of lactate on ESCs, although there are contradictions in the available data. Extracellular lactate possibly affects the growth and pluripotency of ESCs [241]. MCT1 levels are reportedly modestly elevated in naïve versus primed human ESCs [242], however MCT expression is relatively unknown in mouse ESCs. To further investigate the significance of MCT expression for lactate re-uptake in Cidea-OE versus WT ESCs, its expression profile in mouse ESCs should first be established via RT-qPCR, possibly followed by cell treatment with MCT1 inhibitor α-cyano-4-hydroxycinnamate (α-CHC) [243] under glucose-free and lactate-rich conditions. Upon LD staining, these experiments can eventually elucidate the importance of lactate as a substrate for LD enlargement in Cidea-OE cells.

Looking at the total metabolite abundance profile, we noticed that TCA cycle intermediates detected were generally reduced in Cidea overexpressing cells compared to control cells, whereas Cidea knockdown cells showed an opposite trend. This data indicates a direct impact of modulating Cidea expression on TCA cycle flux, possibly indicative of increased *de novo* lipid synthesis in Cidea overexpressing cells [209]. By closely inspecting the mass isotopomer distributions of citrate, we concluded that Cidea overexpression might change the entry point of pyruvate into the cycle, in which pyruvate entry via pyruvate carboxylase (PC) (compared to pyruvate dehydrogenase) seems to be increased (or favoured) in the Cidea

overexpressing cells compared to control cells. Interestingly, PC is stimulated by acetyl-CoA, which in turn is predominantly derived from β-oxidation of acyl-CoAs and by decarboxylation of pyruvate [211]. This might suggest that increased β-oxidation and increased *de novo* lipid synthesis are taking place simultaneously in Cidea overexpressing cells. Furthermore, PC knockdown reportedly severely inhibits lipid production by blocking the biosynthesis of fatty acyl components [244], linking increased PC activity to both β-oxidation and *de novo* lipid synthesis.

In line with these observations, Cidea expression has previously been reported to coincide with *de novo* fatty acid (FA) synthesis and storage associated with elevated lipolysis in adipose tissue [127]. Therefore, we hypothesized that Cidea might also have a central role in coupling these processes to package newly synthesized TAG into LDs for subsequent lipolysis in ESCs [127]. Here, we observed in Cidea overexpressing ESCs, increased basal and maximal oxygen consumption compared to control cells via Seahorse-based analyses. To further address the contribution of β-oxidation to the observed enhanced oxidative state in ESCs, we repeated our Seahorse experiments with pre-treatment of the cells with the β-oxidation inhibitor Etomoxir. To our surprise, these experiments revealed that the relative contribution of FA oxidation to the overall oxygen consumption was the same in Cidea-OE and control cells. Moreover, we observed that, when fatty acid oxidation is inhibited, Cidea-OE cells turn to fast anaerobic energy production (glycolysis) in greater extent compared to control cells. This may suggest that the Cideo OE cells have a greater glycolytic reserve compared to control cells.

Taken together, our findings obtained from GC-MS and Seahorse studies suggest that Cidea-mediated LD enlargement might be linked to an increase in *de novo* lipid synthesis derived from glucose, where TCA cycle intermediates serve as substrates. Whereas glucose uptake seems to be similar in Cidea-OE versus control cells, uptake of other metabolites like pyruvate and glutamine might be increased in Cidea-OE cells to support an enhanced TCA cycle activity in these cells. Labelled pyruvate and glutamine tracing coupled to NMR and GC-MS analyses could provide more insights into the specific uptake differences in substrate preference between Cidea-OE and control cells. In addition, investigating the organic (as opposed to here described aqueous) fraction of ^{13}C glucose tracing experiments could provide direct evidence for the proposed increased lipid synthesis in Cidea-OE cells. We observed a net increase in cellular oxygen consumption in Cidea-OE cells, suggesting that the TCA cycle can also be fueled by acetyl-CoA derived from β-oxidation. This would contrast the results of our experiments using the β-oxidation inhibitor Etomoxir, which should therefore be verified in a different setting (e.g. lower concentration/single injection of Etomoxir to control for toxicity).

7.2 Investigating the functional importance of LD biology and heterogeneity in ESCs.

7.2.1 Lipid accumulation in an ESC differentiation trajectory.

Under routine (FBS/LIF) culture conditions, we have observed that a small subset of ESCs contain supersized LDs. To further investigate whether this might delineate distinct metabolic states in ESCs, we thought to clonally derive ESC sub-populations that harbour either large or small LDs, hereafter also referred to as LLD and sLD clones respectively. Importantly, these clones stably retain, under the same culture conditions, distinctive LD morphologies and expression patterns as assayed for *Cidea*, *Dgat2*, *Oct4* and *Fabp3* over serial passages, suggesting intrinsic regulatory differences. This was also confirmed when using different FBS batches to supplement routine ESC media (data not shown). Interestingly, we identified a trend for enhanced spontaneous differentiation in LLD relative to sLD clones, as monitored upon ESC self-renewal assays. This was further evidenced by a decrease in pluripotency-associated *Oct4* and *Nanog* transcript levels concomitant with an increase in *Fgf5* and *T* expression in large LD clones. To address whether LD size impacts on differentiation, three selected clones were induced to form embryoid bodies (EB). Notably, clone 11, which is characterized by the abundant presence of large LDs and relatively poor plating efficiency, showed a tendency of differentiating faster than the two other (clones 8 and 4) representative clones. Interestingly, *Cidea* expression was transiently upregulated at early stages of ESC differentiation alongside the early epiblast marker *Fgf5*. ESCs can also be converted into extra-embryonic PrE-like cells upon LIF withdrawal and all trans retinoic acid (atRA) treatment. Here we observed that all three representative clones successfully differentiated into PrE-like cells with no clear differences in differentiation efficiency amongst them. We did note however, the advanced activation of the late PrE marker, *Dab2*, which peaks at day 2 in clone 11 relative to day 3 in clones 4 and 8. Besides, *Cidea* was further up-regulated at day 1 post treatment in both clones 4 and 11, which both exhibit large LDs under self-renewing conditions but not in clone 8 where *Cidea* remained expressed at low levels throughout the course of differentiation. The induction of *Cidea* at early differentiation time-points in both differentiation assays possibly suggests that LD enlargement might be associated with the onset of ESC differentiation. This also suggested a link between the presence (or absence) of large LDs and different ESC states (i.e. self-renewal versus priming for differentiation) that was further explored by establishing the transcriptional profiles of sLD and LLD clones using RNA-sequencing, in collaboration with Dr Mark Christian and Yi-Wah Chan. Unsupervised clustering via principal component analyses (PCA) could reliably discriminate large and small LD clones primarily based on differential enrichment for various metabolic processes, in particular lipid metabolism as further revealed by CPDB pathway analysis. Interestingly, large LD clones could be further segregated into two sub-groups (L_1LD and L_2LD - see Chapter 6) also characterized by differential self-renewal abilities with increasing spontaneous differentiation incidence in the L_2LD clone cluster. This was also highlighted by differential enrichment of biological pathways involved in cell-to-cell communication, cell-to-extra-cellular matrix (ECM) communication, and ECM organisation indicative of cellular remodelling. Indeed, 3D ESC differentiation

indicated that LD enlargement coincides with the establishment of primed pluripotency and associated morphogenetic changes in preparation for differentiation. Collectively, these observations suggest that the LD-forming ability of ESCs might correlate with the onset of differentiation. It would be furthermore interesting to establish RNA-seq profiling upon 3D cell differentiation to confirm whether differences between sLD and LLD clones in terms of transcriptional signatures can also be recapitulated in a differentiation trajectory. This will potentially confirm that the LD clone clusters correspond to sequential stages of pluripotency and lipid metabolic remodelling from naïve to primed states.

An important finding arising from our clone transcriptional profiling is the discovery of distinct lipid metabolic signatures in sLD and LLD clones that we further validated by RT-qPCR examining the relative expression status of identified pathway-associated genes. Here, we interestingly observed increased expression of fatty acid uptake/transport (*Fabp3*) and oxidation (*Ascl1*, *Cpt1a* and *Cpt1b*) concomitant with higher expression levels of the naïve (*Tbx3*) and general (*Oct4*) pluripotency transcription factors in small LD clones. Conversely, genes involved in *de novo* lipid synthesis (*Acly*, *Fasn* or *Dgat2*) and degradation by lipolysis (*Atgl*) where increased in expression in LLD clones concomitant with increased expression of differentiation markers (*Fgf5* and *Brachyury/T*). Therefore, whereas sLD clones might mainly oxidize lipids either exogenously scavenged or endogenously recycled via organelle autophagy [120], large LD clones might enhance their *de novo* lipid synthesis and storage ability to potentially release lipids from LDs at the onset of differentiation via a mechanism to be yet uncovered. Here, we thus propose that a "lipid switch" might operate possibly underscoring the transition between naïve-to-primed pluripotency. Although *Cpt1a* and *Cpt1b* expression is lower in LLD clones, these cells display a higher oxygen consumption rate (OCR) compared to the sLD clones. Further verification of *Cpt1* expression, for instance at the protein level, would therefore be important to clarify this discrepancy. Furthermore, although we have evidence for increased fatty acid uptake in sLD clones, through high expression of *Fabp3*, confirmation of active FFA uptake remains to be explored upon FFA treatment in conjunction with OCR measurements through Seahorse. Additionally, lipids can also be internally "recycled", it will therefore be interesting to investigate whether the lipid buildup in the LLD clones is lost upon treatment with autophagy inhibitors (chloroquin). Mechanistically lipids are released from LDs by two pathways, known as lipolysis and lipophagy [119, 120]. Lipolysis is an enzymatic hydrolysis reaction of lipids, initiated by ATGL which resides on the surface of the lipid droplet. During lipophagy, on the other hand, LDs are sequestered in autophagosomes and delivered to lysosomes for degradation by lysosomal acid lipases (LALs). By using LysoTracker, a fluorescent probe specifically targeting lysosomes based on their acidity, combined with BODIPY staining in live cells, we can image cellular lipophagy in real time. Coupling our 3D differentiation assay with drug treatments targeting specific enzymes either involved in lipophagy (Lalistat) or lipolysis (Atglistatin), we are curious to test whether large LDs can be retained, possibly recapitulating in wild-type organoids the morphological defects we have observed in the absence of Cidea-mediated LD enlargement. Preliminary data using Atglistatin during OCR measurements in Seahorse suggests that lipolysis might be less important than lipophagy in releasing lipids from lipid

droplets in self-renewing ESCs, whereas addition of Atglistatin did not impact on OCR, however this needs to be verified (See Fig 5.6E) .

A follow-up and intriguing question is whether *de novo* lipid synthesis and further utilization would then be required per se for the exit from naïve pluripotent state enabling differentiation. To further investigate this, we could take advantage of previously established Rex1-GFP knock-in ESCs where naïve (Rex1-high) and primed (Rex1-low) ESCs for differentiation can be identified and visualised based on differential GFP fluorescence intensity [245]. A previously reported whole genome siRNA-based screening conducted in this Rex1-GFP reporter line, identified 400 genes that are important for the onset of differentiation [246]. The established list of hits was re-visited in the context of this project and interestingly, *Fasn*, the gene encoding fatty acid synthase was identified. While this screening was specifically designed to primarily identified early factors in regulating ERK and GSK3 pathways, we find that the identification of *Fasn* as potential facilitator or driver of differentiation is a promising observation and thus we propose to exploit a similar setting in the future to further test the roles of other enzymes involved in fatty acid synthesis/desaturation (e.g. *Acly*, *Scd1* and *Dgat2*) and/or degradation (e.g. *Atgl* and *LAL*) using transient siRNA and/or drug treatment in regulating the transition from naïve-to-primed state for differentiation. GC-MS based metabolomics approaches aimed at tracing the utilization of ^{13}C labelled glucose would then also be instrumental to further assess the dynamics of metabolic fluxes in these different ESC states (see also section below). Of note, the Rex1-GFP system provides a valuable but rather late marker for the exit of naïve pluripotency. What if lipid switch is a very early event, or a driving mechanism, and therefore precede Rex1 downregulation? In that sense, an early reporter, like Esrrb-GFP would be preferable - this reporter is available via Nicola Festuccia (unpublished work). Additionally, the 3D ESC differentiation assay could also provide a good alternative system, in which we have already accumulated some information in terms of kinetics of LD enlargement/mobilisation and transition from naïve-to-primed pluripotency network.

7.2.2 The lipid switch in self-renewing ESCs prior to the exit of the naïve pluripotent state.

We observed a build-up of pyruvate and citrate levels in both large LD (L_1LD and L_2LD) clusters relative to small LD clones through untargeted GC-MS. Coinciding, however, we did not find increased lactate levels in our large LD clones, in addition to the absence of a general increase of TCA cycle intermediates. We are therefore interested in investigating where the increased in citrate is coming from. Is the observed increased in citrate in large LD clones coming from enhanced glucose or pyruvate uptake? This can be studied via ^{13}C-glucose and ^{13}C-pyruvate labelling studies, linked to NMR and GC-MS analysis. Consequently, we question the meaning of this enhanced citrate production. Our C13-glucose tracing study showed the enhanced usage of ^{13}C-glucose in lipid synthesis in large LD clones. We therefore suspect, in these large LD clones, a change in metabolic flux of citrate into lipid synthesis. However, seahorse data showed that the large LD clones cells are actually more oxidative (OCR). Supposedly, increased OCR

could be due to enhanced fatty acid oxidation, or increased TCA cycle flux (which is indirectly dependent on oxygen). The contribution of fatty acid oxidation can be tested through OCR measurements upon Etomoxir treatment, although we have already observed decreased levels of *Cpt1* in large LD clones. Increased TCA cycle flux, and therefore fuelling of the cycle via glutamine and other amino acids seems therefore likely. Indeed, we found a build-up of glutamine in our large LD clones, compared to sLD clones, suggestive of increased glutamine uptake (to be tested via ^{13}C glutamine and NMR analysis). Interestingly, we also found an increased α-ketoglutarate to succinate ratio, suggesting that glutamine is entering the TCA cycle at this point. We additionally, found the same dynamics between asparagine and aspartate (higher aspartate and lower asparagine in the large LD clones), which enter the TCA cycle through conversion into oxaloacetate (which itself was unfortunately not detectable). Generally, amino acid levels were decreased in large LD clones, suggesting that they might be more utilized to fuel the TCA cycle, as the citrate is going towards lipid synthesis. To test the contributions of pyruvate, glutamine and amino acids we could modulate the ESC media composition, coupled to OCR measurements upon Seahorse.

Interestingly, while we do see an enhanced OCR - i.e. decreased levels of reduced glutathione and methionine - especially in L_1LD, there is also increased anti-oxidant activity in these cells. This could provide protection against oxidative stress and consequently opposed oxidative stress- induced differentiation. Additionally, methionine is required for the production of S-Adenosyl methionine (SAM), which in turn acts as the primary methyl donor for DNA and histone methylation [247]. Possibly indicating discrepancies in DNA methylation status between the lipid clones, which is generally linked to the pluripotent state of the cells (i.e. naïve versus primed). PRC2-mediated H3K27me3 is enhanced when the cells are primed for differentiation [53, 54, 248]. In addition, global *de novo* DNA methylation is a hallmark of primed pluripotency both *in vitro* and *in vivo* [249]. Hence, it would be interesting to explore epigenetic differences of clone clusters in relation to their distinct metabolic states.

Another hallmark of the naïve-to-primed transition is anaerobic glycolysis. Interestingly, our seahorse has highlighted a difference in the glycolytic profile between the clones clusters; [a] the small LD clones seems to be more quiescent than LLD, [b] L_1LD show a burst of oxidation, [c] the L_2LD OCR is already attenuated and there is a shift towards anaerobic glycolysis. This suggests that the cells could already transit through a burst of oxidation before the glycolytic switch. This in turn may reflect, as discussed above, tightly regulated substrate usage. Glucose might be mainly used in sLD for glycolysis mediated acetyl-CoA production which is not going towards lipid synthesis. This would provide the cell with proficient levels of ATP to sustain a highly proliferative profile, but also to support histone acetylation in these more naïve cells. Glycolysis-mediated changes in acetyl-CoA production and histone acetylation control of early differentiation has been linked in ESCs [85]. It would be interesting to examine whether usage of citrate/acetyl-CoA towards lipid synthesis is at the expense of histone acetylation, coordinating changes of epigenetic state and metabolic state of cells at the onset of differentiation. Global analysis

of bulk histone acetylation levels in clones could be examined as a starting point to potentially draw a functional link there.
We learned via our Etomoxir experiment that ESCs are highly oxidative in terms of fatty acids oxidation. Therefore, we suspect that the sLD are also more FAO, using more free fatty acids compared to the LLDs. We need to validate this more directly be looking at the OCR response upon FFA treatment in sLD and LLDs. Here we expect to see a bigger increase in OCR in sLD (as compared to LLDs), also supported by high levels of *Cpt1a* in sLDs. In contrast, we then expect LLDs to uptake and use more other metabolites (pyruvate and/or glutamine), to really support the energy demands of *de novo* lipid synthesis.
Finally, it will be interesting to come back to our 3D differentiation assay, and set-up seahorse and GC-MS in this system to determine if the different timepoints present different metabolic states. We could then correlate Seahose and GC-MS data with the accumulation of lipids and timely mobilization, starting to dissect which trigger is involved in this metabolic switch.

In conclusion, all of this work highlighted the existence of ESC-heterogeneity in a self-renewing state, suggesting that the lipid switch might be happening in these conditions prior to the exit of the naïve pluripotent state (Fig 7.3). In turn, the glycolytic switch will then be the hallmark of the establishment of primed pluripotency.

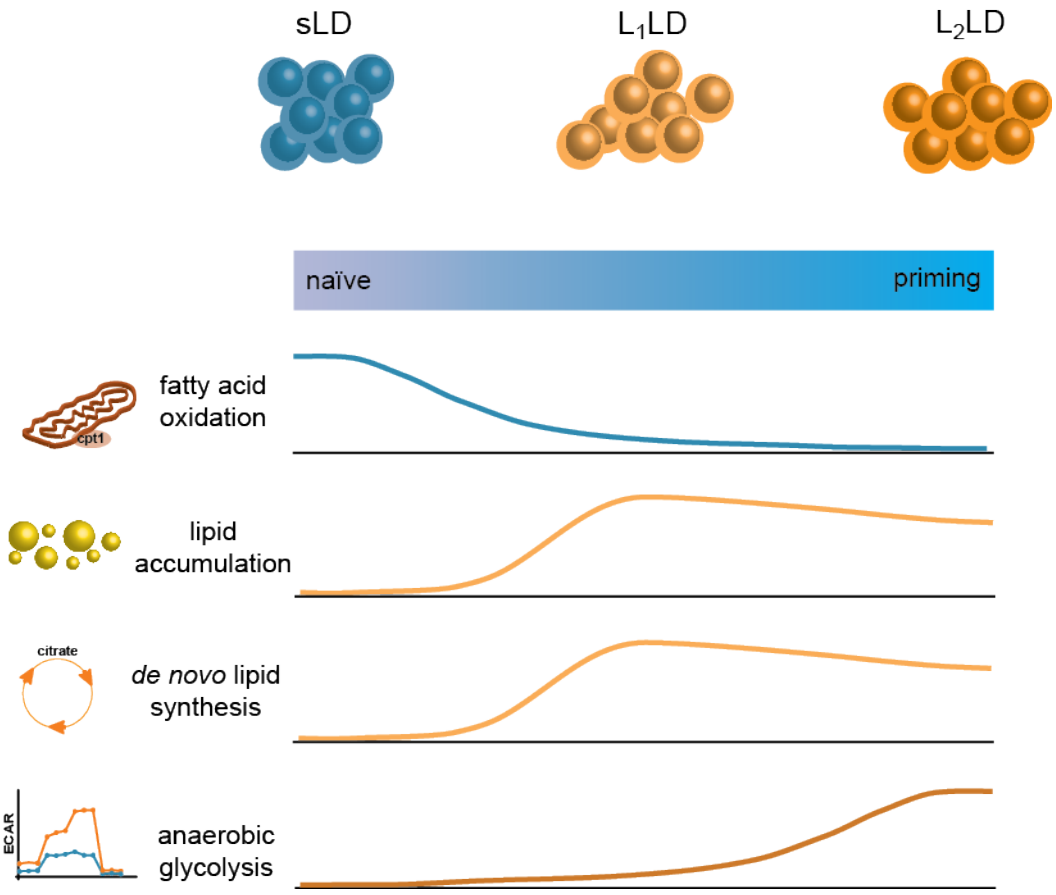


Figure 7.3: Model of the lipid switch in a heterogeneous self-renewing ESC population.

Proposed model for the lipid switch in a heterogeneous self-renewing ESC population taking place before the glycolytic switch - the hallmark of the establishment of primed pluripotency. The lipid switch being reduced fatty acid oxidation, and increased lipid accumulation in the form of lipid droplets supported by increased *de novo* lipid synthesis fuelled by TCA cycle intermediates.

7.2.3 What is the functional importance of the lipid switch for enabling differentiation in ESCs?

LDs can act as reservoir for lipid precursors or fuels for mitochondria. However, our Seahorse analyses suggest that LD enlargement might not be functionally linked with enhanced fatty acid oxidation as tested upon ectopic expression of Cidea in ESCs. We are currently elucidating the functional importance of LD accumulation in ESC differentiation. Tommy King Mau in our lab has indeed confirmed that both LD enlargement and subsequent mobilisation is strictly required for normal morphogenesis events during the transition from naïve-to-primed pluripotency. This involves the establishment of cell polarity and formation of a central lumen. Inhibiting LD enlargement via depletion of Cidea leads to the loss of cell polarity and abnormal formation of multiple cavities. A similar defect is observed upon inhibition of lipophagy - the main mechanism identified by Tommy King Mau for LD mobilisation at the onset of lumen formation.We therefore hypothesize that lipid droplets act as reservoir for lipid precursors, critical factors for cellular remodelling during the onset of differentiation. Among lipid species, phosphatidylinositol lipid (PI) has a strong implication for proper cell polarization. Phosphorylated PIP2/PIP3 segregation, with PIP2 localizing on apical and PIP3 on baso-lateral membranes, is essential for cell polarity maintenance [250, 251]. These lipids are biochemically made up of a diacylglycerol backbone esterified to inositol head groups, with different degrees of phosphorylation [252]. This implies that a continuous supply of diacylglycerol would be needed for replenishing membrane phosphatidylinositol lipids during cell divisions. Diacylglycerol is one of the major products derived from mobilized LD triacylglycerol, hence we speculate an interplay between LDs and PIP3/PIP2 distribution. To further investigate this hypothesis, our lab is now establishing ESCs expressing GFP labelled probes with high specificity for PIP3 and/or PIP2 binding in different cellular compartments [253]. We hypothesize a potential disrupted localization of PIP2/PIP3 in Cidea KO compared to the control. Furthermore, we will also be interested in investigating the metabolic pathway in PI conversion from lipid precursors from LDs, striking a link between LDs acting as regulators for PI lipid synthesis.

Bibliography

[1] B. Lo and L. Parham, "Ethical issues in stem cell research," *Endocrine Reviews*, vol. 30, no. 3, pp. 204–213, 2009.

[2] M. J. Evans and M. H. Kaufman, "Establishment in culture of pluripotential cells from mouse embryos," *Nature*, vol. 292, no. 5819, pp. 154–6, 1981.

[3] K. R. Thomas and M. R. Capecchi, "Site-directed mutagenesis by gene targeting in mouse embryo-derived stem cells," *Cell*, vol. 51, no. 3, pp. 503–12, 1987.

[4] I. Bedzhov and M. Zernicka-Goetz, "Self-organizing properties of mouse pluripotent cells initiate morphogenesis upon implantation," *Cell*, vol. 156, no. 5, pp. 1032–1044, 2014.

[5] S. a. Morris, R. T. Y. Teo, H. Li, P. Robson, D. M. Glover, and M. Zernicka-Goetz, "Origin and formation of the first two distinct cell types of the inner cell mass in the mouse embryo.," *Proceedings of the National Academy of Sciences of the United States of America*, vol. 107, no. 14, pp. 6364–9, 2010.

[6] C. Chazaud, Y. Yamanaka, T. Pawson, and J. Rossant, "Early Lineage Segregation between Epiblast and Primitive Endoderm in Mouse Blastocysts through the Grb2-MAPK Pathway," *Developmental Cell*, vol. 10, no. 5, pp. 615–24, 2006.

[7] J. Rossant, C. Chazaud, Y. Yamanaka, M. Jones, E. J. Robertson, A. Smith, and R. G. Edwards, "Lineage allocation and asymmetries in the early mouse embryo," *Philosophical Transactions of the Royal Society B: Biological Sciences*, vol. 358, no. 1436, pp. 1341–8, 2003.

[8] E. Coucouvanis and G. R. Martin, "Signals for death and survival: A two-step mechanism for cavitation in the vertebrate embryo," *Cell*, vol. 83, no. 2, pp. 279–87, 1995.

[9] L. Wolpert, *Principles of Development*. New York: Oxford University Press, 2011.

[10] M. J. Stower and S. Srinivas, "Heading forwards: Anterior visceral endoderm migration in patterning the mouse embryo," *Philosophical Transactions of the Royal Society B: Biological Sciences*, vol. 369, no. 1657, p. 20130546, 2014.

[11] P. P. L. Tam and D. A. F. Loebel, "Gene function in mouse embryogenesis: get set for gastrulation," *Nature Reviews Genetics*, vol. 8, no. 5, pp. 368–81, 2007.

[12] S. Nowotschin and A.-K. Hadjantonakis, "Cellular dynamics in the early mouse embryo: from axis formation to gastrulation," *Current Opinion in Genetics & Development*, vol. 20, no. 4, pp. 420–7, 2010.

[13] N. Perrimon, C. Pitsouli, and B.-Z. Shilo, "Signaling mechanisms controlling cell fate and embryonic patterning.," *Cold Spring Harbor perspectives in biology*, vol. 4, p. a005975, aug 2012.

[14] J. Gerhart, "1998 Warkany Lecture: Signaling pathways in development," *Teratology*, vol. 60, no. 4, pp. 226–239, 1999.

[15] S. Barolo and J. W. Posakony, "Three habits of highly effective signaling pathways: Principles of transcriptional control by developmental cell signaling," *Genes and Development*, vol. 16, no. 10, pp. 1167–1181, 2002.

[16] S. Bessonnard, L. De Mot, D. Gonze, M. Barriol, C. Dennis, A. Goldbeter, G. Dupont, and C. Chazaud, "Gata6, Nanog and Erk signaling control cell fate in the inner cell mass through a tristable regulatory network," *Development*, vol. 141, no. 19, pp. 3637–3648, 2014.

[17] J. Rossant, "Stem cells and early lineage development," *Cell*, vol. 132, pp. 527–531, 2008.

[18] B. W. Kahan and B. Ephrussi, "Developmental potentialities of clonal in vitro cultures of mouse testicular teratoma," *Journal of the National Cancer Institute*, vol. 44, no. 5, pp. 1015–36, 1970.

[19] G. R. Martin and M. J. Evans, "Differentiation of clonal lines of teratocarcinoma cells: formation of embryoid bodies in vitro.," *Proceedings of the National Academy of Sciences*, vol. 72, no. 4, pp. 1441–5, 1975.

[20] G. R. Martin, "Isolation of a pluripotent cell line from early mouse embryos cultured in medium conditioned by teratocarcinoma stem cells.," *Proceedings of the National Academy of Sciences*, vol. 78, no. 12, pp. 7634–8, 1981.

[21] H. Niwa, T. Burdon, I. Chambers, and A. Smith, "Self-renewal of pluripotent embryonic stem cells is mediated via activation of STAT3.," *Genes & development*, vol. 12, no. 13, pp. 2048–60, 1998.

[22] Q. L. Ying, J. Nichols, I. Chambers, and A. Smith, "BMP induction of Id proteins suppresses differentiation and sustains embryonic stem cell self-renewal in collaboration with STAT3," *Cell*, vol. 115, no. 3, pp. 281–92, 2003.

[23] J. Nichols and A. Smith, "Naive and Primed Pluripotent States," *Cell Stem Cell*, vol. 4, no. 6, pp. 487–92, 2009.

[24] Q.-L. Ying, J. Wray, J. Nichols, L. Batlle-Morera, B. Doble, J. Woodgett, P. Cohen, and A. Smith, "The ground state of embryonic stem cell self-renewal," *Nature*, vol. 453, no. 7194, pp. 519–523, 2008.

[25] J. A. Hackett and M. Azim Surani, "Regulatory principles of pluripotency: From the ground state up," *Cell Stem Cell*, vol. 15, no. 4, pp. 416–430, 2014.

[26] I. Chambers, J. Silva, D. Colby, J. Nichols, B. Nijmeijer, M. Robertson, J. Vrana, K. Jones, L. Grotewold, and A. Smith, "Nanog safeguards pluripotency and mediates germline development," *Nature*, vol. 450, no. 7173, pp. 1230–4, 2007.

[27] M.-E. Torres-Padilla and I. Chambers, "Transcription factor heterogeneity in pluripotent stem cells: a stochastic advantage," *Development*, vol. 141, no. 11, pp. 2173–81, 2014.

[28] Y. Chung, I. Klimanskaya, S. Becker, J. Marh, S. J. Lu, J. Johnson, L. Meisner, and R. Lanza, "Embryonic and extraembryonic stem cell lines derived from single mouse blastomeres," *Nature*, vol. 439, no. 7073, pp. 216–9, 2006.

[29] P. J. Tesar, "Derivation of germ-line-competent embryonic stem cell lines from preblastocyst mouse embryos," *Proceedings of the National Academy of Sciences*, vol. 102, no. 23, pp. 8239–44, 2005.

[30] Y. Toyooka, D. Shimosato, K. Murakami, K. Takahashi, and H. Niwa, "Identification and characterization of subpopulations in undifferentiated ES cell culture," *Development*, vol. 135, no. 5, pp. 909–18, 2008.

[31] S. M. Morgani, M. A. Canham, J. Nichols, A. A. Sharov, R. P. Migueles, M. S. Ko, and J. M. Brickman, "Totipotent Embryonic Stem Cells Arise in Ground-State Culture Conditions," *Cell Reports*, vol. 3, no. 6, pp. 1945–57, 2013.

[32] I. G. Brons, L. E. Smithers, M. W. Trotter, P. Rugg-Gunn, B. Sun, S. M. Chuva de Sousa Lopes, S. K. Howlett, A. Clarkson, L. Ahrlund-Richter, R. A. Pedersen, and L. Vallier, "Derivation of pluripotent epiblast stem cells from mammalian embryos," *Nature*, vol. 448, pp. 191–195, 2007.

[33] P. J. Tesar, J. G. Chenoweth, F. A. Brook, T. J. Davies, E. P. Evans, D. L. Mack, R. L. Gardner, and R. D. McKay, "New cell lines from mouse epiblast share defining features with human embryonic stem cells," *Nature*, vol. 448, pp. 196–199, 2007.

[34] G. Guo, J. Yang, J. Nichols, J. S. Hall, I. Eyres, W. Mansfield, and A. Smith, "Klf4 reverts developmentally programmed restriction of ground state pluripotency," *Development*, vol. 136, no. 7, pp. 1063–9, 2009.

[35] Y. Huang, R. Osorno, A. Tsakiridis, and V. Wilson, "In Vivo Differentiation Potential of Epiblast Stem Cells Revealed by Chimeric Embryo Formation," *Cell Reports*, vol. 2, no. 6, pp. 1571–8, 2012.

[36] M. M. Shen, "Nodal signaling: developmental roles and regulation," *Development*, vol. 134, no. 6, pp. 1023–34, 2007.

[37] D. W. Han, N. Tapia, J. Y. Joo, B. Greber, M. J. Araúzo-Bravo, C. Bernemann, K. Ko, G. Wu, M. Stehling, J. T. Do, and H. R. Schöler, "Epiblast stem cell subpopulations represent mouse embryos of distinct pregastrulation stages," *Cell*, vol. 143, no. 4, pp. 617–27, 2010.

[38] Y. Kojima, K. Kaufman-Francis, J. B. Studdert, K. A. Steiner, M. D. Power, D. A. Loebel, V. Jones, A. Hor, G. De Alencastro, G. J. Logan, E. T. Teber, O. H. Tam, M. D. Stutz, I. E. Alexander, H. A.

Pickett, and P. P. Tam, "The transcriptional and functional properties of mouse epiblast stem cells resemble the anterior primitive streak," *Cell Stem Cell*, vol. 14, no. 1, pp. 107–20, 2014.

[39] D. C. Factor, O. Corradin, G. E. Zentner, A. Saiakhova, L. Song, J. G. Chenoweth, R. D. McKay, G. E. Crawford, P. C. Scacheri, and P. J. Tesar, "Epigenomic comparison reveals activation of "seed" enhancers during transition from naive to primed pluripotency," *Cell Stem Cell*, vol. 14, no. 6, pp. 854–63, 2014.

[40] H. K. Long, S. L. Prescott, and J. Wysocka, "Ever-Changing Landscapes: Transcriptional Enhancers in Development and Evolution," *Cell*, vol. 167, no. 5, pp. 1170–1187, 2016.

[41] S. H. Yang, T. Kalkan, C. Morissroe, H. Marks, H. Stunnenberg, A. Smith, and A. D. Sharrocks, "Otx2 and Oct4 Drive Early Enhancer Activation during Embryonic Stem Cell Transition from Naive Pluripotency," *Cell Reports*, vol. 7, no. 6, pp. 1968–81, 2014.

[42] C. L. Novo, B. M. Javierre, J. Cairns, A. Segonds-Pichon, S. W. Wingett, P. Freire-Pritchett, M. Furlan-Magaril, S. Schoenfelder, P. Fraser, and P. J. Rugg-Gunn, "Long-Range Enhancer Interactions Are Prevalent in Mouse Embryonic Stem Cells and Are Reorganized upon Pluripotent State Transition," *Cell Reports*, vol. 22, no. 10, pp. 2615–2627, 2018.

[43] R. Hirasawa and H. Sasaki, "Dynamic transition of Dnmt3b expression in mouse pre- and early post-implantation embryos," *Gene Expression Patterns*, vol. 9, no. 1, pp. 27–30, 2009.

[44] W. Reik, "Stability and flexibility of epigenetic gene regulation in mammalian development," *Nature*, vol. 447, no. 7143, pp. 425–32, 2007.

[45] A. Jouneau, C. Ciaudo, O. Sismeiro, V. Brochard, L. Jouneau, S. Vandormael-Pournin, J.-Y. Coppée, Q. Zhou, E. Heard, C. Antoniewski, and M. Cohen-Tannoudji, "Naive and primed murine pluripotent stem cells have distinct miRNA expression profiles.," *RNA (New York, N.Y.)*, vol. 18, no. 2, pp. 253–64, 2012.

[46] N. Festuccia, R. Osorno, F. Halbritter, V. Karwacki-Neisius, P. Navarro, D. Colby, F. Wong, A. Yates, S. R. Tomlinson, and I. Chambers, "Esrrb is a direct Nanog target gene that can substitute for Nanog function in pluripotent cells," *Cell Stem Cell*, vol. 11, no. 4, pp. 477–90, 2012.

[47] A. Smith, "Formative pluripotency: the executive phase in a developmental continuum," *Development*, vol. 44, no. 3, pp. 365–373, 2017.

[48] P. Du, M. Pirouz, J. Choi, A. J. Huebner, K. Clement, A. Meissner, K. Hochedlinger, and R. I. Gregory, "An Intermediate Pluripotent State Controlled by MicroRNAs Is Required for the Naive-to-Primed Stem Cell Transition," *Cell Stem Cell*, vol. 22, no. 6, pp. 851–864, 2018.

[49] S. A. Fonseca, R. M. Costas, and L. V. Pereira, "Searching for naïve human pluripotent stem cells.," *World journal of stem cells*, vol. 7, no. 3, pp. 649–56, 2015.

[50] B. Di Stefano, M. Ueda, S. Sabri, J. Brumbaugh, A. J. Huebner, A. Sahakyan, K. Clement, K. J. Clowers, A. R. Erickson, K. Shioda, S. P. Gygi, H. Gu, T. Shioda, A. Meissner, Y. Takashima, K. Plath, and K. Hochedlinger, "Reduced MEK inhibition preserves genomic stability in naive human embryonic stem cells," *Nature Methods*, vol. 15, no. 9, pp. 732–740, 2018.

[51] L. Weinberger, M. Ayyash, N. Novershtern, and J. H. Hanna, "Dynamic stem cell states: Naive to primed pluripotency in rodents and humans," *Nature Reviews Molecular Cell Biology*, vol. 17, no. 3, pp. 155–69, 2016.

[52] C. E. Weidgang, T. Seufferlein, A. Kleger, and M. Mueller, "Pluripotency factors on their lineage move," *Stem Cells International*, p. 6838253, 2016.

[53] B. E. Bernstein, T. S. Mikkelsen, X. Xie, M. Kamal, D. J. Huebert, J. Cuff, B. Fry, A. Meissner, M. Wernig, K. Plath, R. Jaenisch, A. Wagschal, R. Feil, S. L. Schreiber, and E. S. Lander, "A Bivalent Chromatin Structure Marks Key Developmental Genes in Embryonic Stem Cells," *Cell*, vol. 125, no. 2, pp. 315–26, 2006.

[54] V. Azuara, P. Perry, S. Sauer, M. Spivakov, H. F. Jørgensen, R. M. John, M. Gouti, M. Casanova, G. Warnes, M. Merkenschlager, and A. G. Fisher, "Chromatin signatures of pluripotent cell lines," *Nature Cell Biology*, vol. 8, no. 5, pp. 532–8, 2006.

[55] S. Chandrasekaran, J. Zhang, Z. Sun, L. Zhang, C. A. Ross, Y. C. Huang, J. M. Asara, H. Li, G. Q. Daley, and J. J. Collins, "Comprehensive Mapping of Pluripotent Stem Cell Metabolism Using Dynamic Genome-Scale Network Modeling," *Cell Reports*, vol. 21, no. 10, pp. 2965–2977, 2017.

[56] J. M. Berg, J. L. Tymoczko, and S. Lubert, *Biochemistry, 5th edn.* New York: W H Freeman, 2002.

[57] P. Dahan, V. Lu, R. M. Nguyen, S. A. Kennedy, and M. A. Teitell, "Metabolism in pluripotency: Both driver and passenger?," *Journal of Biological Chemistry*, p. 000832, 2018.

[58] A. D. Panopoulos, O. Yanes, S. Ruiz, Y. S. Kida, D. Diep, R. Tautenhahn, A. Herrerias, E. M. Batchelder, N. Plongthongkum, M. Lutz, W. T. Berggren, K. Zhang, R. M. Evans, G. Siuzdak, and J. C. Izpisua Belmonte, "The metabolome of induced pluripotent stem cells reveals metabolic changes occurring in somatic cell reprogramming," *Cell Research*, vol. 22, no. 1, pp. 168–77, 2012.

[59] F. L. Crespo, V. R. Sobrado, L. Gomez, A. M. Cervera, and K. J. McCreath, "Mitochondrial reactive oxygen species mediate cardiomyocyte formation from embryonic stem cells in high glucose," *Stem Cells*, vol. 28, no. 7, pp. 1132–42, 2010.

[60] Y. M. Cho, S. Kwon, Y. K. Pak, H. W. Seol, Y. M. Choi, J. Park do, K. S. Park, H. K. Lee, D. J. Park, K. S. Park, H. K. Lee, J. Park do, K. S. Park, and H. K. Lee, "Dynamic changes in mitochondrial biogenesis and antioxidant enzymes during the spontaneous differentiation of human embryonic stem cells," *Biochem Biophys Res Commun*, vol. 348, no. 4, pp. 1472–8, 2006.

[61] J. Zhang, I. Khvorostov, J. S. Hong, Y. Oktay, L. Vergnes, E. Nuebel, P. N. Wahjudi, K. Setoguchi, G. Wang, A. Do, H.-J. Jung, J. M. McCaffery, I. J. Kurland, K. Reue, W.-N. P. Lee, C. M. Koehler, and M. A. Teitell, "UCP2 regulates energy metabolism and differentiation potential of human pluripotent stem cells," *The EMBO Journal*, vol. 30, no. 24, pp. 4860–73, 2011.

[62] D. T. Madden, D. Davila-Kruger, S. Melov, and D. E. Bredesen, "Human embryonic stem cells express elevated levels of multiple Pro-Apoptotic BCL-2 family members," *PLoS ONE*, vol. 6, no. 12, p. e28530, 2011.

[63] A. Prigione, B. Fauler, R. Lurz, H. Lehrach, and J. Adjaye, "The senescence-related mitochondrial/oxidative stress pathway is repressed in human induced pluripotent stem cells," *Stem Cells*, vol. 28, no. 4, pp. 721–33, 2010.

[64] J. Zhang, J. Zhao, P. Dahan, V. Lu, C. Zhang, H. Li, and M. A. Teitell, "Metabolism in Pluripotent Stem Cells and Early Mammalian Development," *Cell Metabolism*, vol. 27, no. 2, pp. 332–338, 2018.

[65] D. Jukam, S. A. M. Shariati, and J. M. Skotheim, "Zygotic Genome Activation in Vertebrates," *Developmental Cell*, vol. 42, no. 4, pp. 316–332, 2017.

[66] J. D. West, J. H. Flockhart, J. Peters, and S. T. Ball, "Death of mouse embryos that lack a functional gene for glucose phosphate isomerase," *Genetical Research*, vol. 56, no. 2-3, pp. 223–36, 1990.

[67] W. Pretsch, "Enzyme-activity mutants in Mus musculus. I. Phenotypic description and genetic characterization of ethylnitrosourea- induced mutations," *Mammalian Genome*, vol. 11, no. 7, pp. 537–42, 2000.

[68] S. Merkle and W. Pretsch, "Characterization of triosephosphate isomerase mutants with reduced enzyme activity in Mus musculus," *Genetics*, vol. 123, no. 4, pp. 837–44, 1989.

[69] S. Merkle, J. Favor, J. Graw, S. Hornhardt, and W. Pretsch, "Hereditary lactate dehydrogenase A-subunit deficiency as cause of early postimplantation death of homozygotes in Mus musculus," *Genetics*, vol. 131, no. 2, pp. 413–21, 1992.

[70] L. Yan, M. Yang, H. Guo, L. Yang, J. Wu, R. Li, P. Liu, Y. Lian, X. Zheng, J. Yan, J. Huang, M. Li, X. Wu, L. Wen, K. Lao, R. Li, J. Qiao, and F. Tang, "Single-cell RNA-Seq profiling of human preimplantation embryos and embryonic stem cells," *Nature Structural & Molecular Biology*, vol. 20, no. 9, pp. 1131–9, 2013.

[71] Z. Xue, K. Huang, C. Cai, L. Cai, C. Y. Jiang, Y. Feng, Z. Liu, Q. Zeng, L. Cheng, Y. E. Sun, J. Y. Liu, S. Horvath, and G. Fan, "Genetic programs in human and mouse early embryos revealed by single-cell RNA sequencing," *Nature*, vol. 500, no. 7464, pp. 593–7, 2013.

[72] F. D. Houghton, J. G. Thompson, C. J. Kennedy, and Henry J. Leese, "Oxygen consumption and energy metabolism of the early mouse embryo.," *Molecular reproduction and development*, vol. 44, no. 4, pp. 476–85, 1996.

[73] H. J. Leese, "Metabolism of the preimplantation embryo: 40 Years on," *Reproduction*, vol. 143, no. 4, pp. 417–27, 2012.

[74] W. Zhou, M. Choi, D. Margineantu, L. Margaretha, J. Hesson, C. Cavanaugh, C. A. Blau, M. S. Horwitz, D. Hockenbery, C. Ware, and H. Ruohola-Baker, "HIF1alpha induced switch from bivalent to exclusively glycolytic metabolism during ESC-to-EpiSC/hESC transition," *EMBO J*, vol. 31, pp. 2103–2116, 2012.

[75] C. D. Folmes, P. P. Dzeja, T. J. Nelson, and A. Terzic, "Metabolic plasticity in stem cell homeostasis and differentiation," *Cell Stem Cell*, vol. 11, pp. 596–606, 2012.

[76] M. T. Johnson, S. Mahmood, and M. S. Patel, "Intermediary metabolism and energetics during murine early embryogenesis," *J Biol Chem*, vol. 278, pp. 31457–31460, 2003.

[77] N. G. Larsson, J. Wang, H. Wilhelmsson, A. Oldfors, P. Rustin, M. Lewandoski, G. S. Barsh, and D. A. Clayton, "Mitochondrial transcription factor A is necessary for mtDNA maintenance and embryogenesis in mice," *Nature Genetics*, vol. 18, no. 3, pp. 231–6, 1998.

[78] A. Lima, J. Burgstaller, J. M. Sanchez-Nieto, and T. A. Rodríguez, "The Mitochondria and the Regulation of Cell Fitness During Early Mammalian Development," in *Current topics in developmental biology*, vol. 128, pp. 339–363, 2018.

[79] K. Huang, T. Maruyama, and G. Fan, "The naive state of human pluripotent stem cells: A synthesis of stem cell and preimplantation embryo transcriptome analyses," *Cell Stem Cell*, vol. 15, no. 4, pp. 410–415, 2014.

[80] T. Y., "Resetting Transcription Factor Control Circuitry toward Ground-State Pluripotency in Human.," *Resetting Transcription Factor Control Circuitry toward Ground-State Pluripotency in Human.*, vol. 158, no. 6, pp. 1254–1269, 2014.

[81] S. Varum, A. S. Rodrigues, M. B. Moura, O. Momcilovic, C. A. Easley IV, J. Ramalho-Santos, B. van Houten, and G. Schatten, "Energy metabolism in human pluripotent stem cells and their differentiated counterparts," *PLoS ONE*, vol. 6, no. 6, p. e20914, 2011.

[82] H. Zhang, M. G. Badur, A. S. Divakaruni, S. J. Parker, C. Jäger, K. Hiller, A. N. Murphy, and C. M. Metallo, "Distinct Metabolic States Can Support Self-Renewal and Lipogenesis in Human Pluripotent Stem Cells under Different Culture Conditions," *Cell Reports*, vol. 16, no. 6, pp. 1536–1547, 2016.

[83] S. Taleahmad, S. N. Hassani, G. Hosseini Salekdeh, and H. Baharvand, "Metabolic Signature of Pluripotent Stem Cells.," *Cell journal*, vol. 20, pp. 388–395, oct 2018.

[84] F. Santos, B. Hendrich, W. Reik, and W. Dean, "Dynamic reprogramming of DNA methylation in the early mouse embryo," *Developmental Biology*, vol. 241, no. 1, pp. 172–82, 2002.

[85] A. Moussaieff, M. Rouleau, D. Kitsberg, M. Cohen, G. Levy, D. Barasch, A. Nemirovski, S. Shen-Orr, I. Laevsky, M. Amit, D. Bomze, B. Elena-Herrmann, T. Scherf, M. Nissim-Rafinia, S. Kempa, J. Itskovitz-Eldor, E. Meshorer, D. Aberdam, and Y. Nahmias, "Glycolysis-mediated changes in acetyl-CoA and histone acetylation control the early differentiation of embryonic stem cells," *Cell Metabolism*, vol. 21, no. 3, pp. 392–402, 2015.

[86] J. Wang, P. Alexander, L. Wu, R. Hammer, O. Cleaver, and S. L. McKnight, "Dependence of Mouse Embryonic Stem Cells on Threonine Catabolism," *Science*, vol. 325, no. 5939, pp. 435–9, 2009.

[87] N. Shyh-Chang, J. W. Locasale, C. A. Lyssiotis, Y. Zheng, R. Y. Teo, S. Ratanasirintrawoot, J. Zhang, T. Onder, J. J. Unternaehrer, H. Zhu, J. M. Asara, G. Q. Daley, and L. C. Cantley, "Influence of threonine metabolism on S-adenosylmethionine and histone methylation," *Science*, vol. 339, no. 6116, pp. 22–6, 2013.

[88] T. TeSlaa, A. C. Chaikovsky, I. Lipchina, S. L. Escobar, K. Hochedlinger, J. Huang, T. G. Graeber, D. Braas, and M. A. Teitell, "α-Ketoglutarate Accelerates the Initial Differentiation of Primed Human Pluripotent Stem Cells," *Cell Metabolism*, vol. 24, no. 3, pp. 485–493, 2016.

[89] M. Sone, N. Morone, T. Nakamura, A. Tanaka, K. Okita, K. Woltjen, M. Nakagawa, J. E. Heuser, Y. Yamada, S. Yamanaka, and T. Yamamoto, "Hybrid Cellular Metabolism Coordinated by Zic3 and Esrrb Synergistically Enhances Induction of Naive Pluripotency," *Cell Metabolism*, vol. 25, no. 5, pp. 1103–1117, 2017.

[90] J. Zhang, S. Ratanasirintrawoot, S. Chandrasekaran, Z. Wu, S. B. Ficarro, C. Yu, C. A. Ross, D. Cacchiarelli, Q. Xia, M. Seligson, G. Shinoda, W. Xie, P. Cahan, L. Wang, S. C. Ng, S. Tintara, C. Trapnell, T. Onder, Y. H. Loh, T. Mikkelsen, P. Sliz, M. A. Teitell, J. M. Asara, J. A. Marto, H. Li, J. J. Collins, and G. Q. Daley, "LIN28 Regulates Stem Cell Metabolism and Conversion to Primed Pluripotency," *Cell Stem Cell*, vol. 19, no. 1, pp. 66–80, 2016.

[91] E. Carbognin, R. M. Betto, M. E. Soriano, A. G. Smith, and G. Martello, "Stat3 promotes mitochondrial transcription and oxidative respiration during maintenance and induction of naive pluripotency," *The EMBO Journal*, vol. 35, no. 6, pp. 618–34, 2016.

[92] X. Ma, C. Li, L. Sun, D. Huang, T. Li, X. He, G. Wu, Z. Yang, X. Zhong, L. Song, P. Gao, and H. Zhang, "Lin28/let-7 axis regulates aerobic glycolysis and cancer progression via PDK1," *Nature Communications*, vol. 5, p. 5212, 2014.

[93] C. D. L. Folmes, A. Martinez-Fernandez, R. S. Faustino, S. Yamada, C. Perez-Terzic, T. J. Nelson, and A. Terzic, "Nuclear reprogramming with c-Myc potentiates glycolytic capacity of derived induced pluripotent stem cells," *Journal of Cardiovascular Translational Research*, vol. 6, no. 1, pp. 10–21, 2013.

[94] Y. Cao, W.-T. Guo, S. Tian, X. He, X.-W. Wang, X. Liu, K.-L. Gu, X. Ma, D. Huang, L. Hu, Y. Cai, H. Zhang, Y. Wang, and P. Gao, "miR-290/371-Mbd2-Myc circuit regulates glycolytic metabolism to promote pluripotency," *The EMBO Journal*, vol. 34, no. 5, pp. 609–23, 2015.

[95] J. A. Hanover, M. W. Krause, and D. C. Love, "Bittersweet memories: Linking metabolism to epigenetics through O-GlcNAcylation," *Nature Reviews Molecular Cell Biology*, vol. 13, no. 5, pp. 312–21, 2012.

[96] H. Jang, T. W. Kim, S. Yoon, S. Y. Choi, T. W. Kang, S. Y. Kim, Y. W. Kwon, E. J. Cho, and H. D. Youn, "O-GlcNAc regulates pluripotency and reprogramming by directly acting on core components of the pluripotency network," *Cell Stem Cell*, vol. 11, no. 1, pp. 62–74, 2012.

[97] H. Jasper and D. L. Jones, "Metabolic regulation of stem cell behavior and implications for aging," *Cell Metabolism*, vol. 12, no. 6, pp. 561–5, 2010.

[98] V. M. Renault, V. A. Rafalski, A. A. Morgan, D. A. M. Salih, J. O. Brett, A. E. Webb, S. A. Villeda, P. U. Thekkat, C. Guillerey, N. C. Denko, T. D. Palmer, A. J. Butte, and A. Brunet, "FoxO3 Regulates Neural Stem Cell Homeostasis," *Cell Stem Cell*, vol. 5, no. 5, pp. 527–39, 2009.

[99] J. Shim, T. Mukherjee, and U. Banerjee, "Direct sensing of systemic and nutritional signals by haematopoietic progenitors in Drosophila," *Nature Cell Biology*, vol. 14, no. 4, pp. 394–400, 2012.

[100] M. Murakami, T. Ichisaka, M. Maeda, N. Oshiro, K. Hara, F. Edenhofer, H. Kiyama, K. Yonezawa, and S. Yamanaka, "mTOR is essential for growth and proliferation in early mouse embryos and embryonic stem cells.," *Molecular and cellular biology*, vol. 24, no. 15, pp. 6710–8, 2004.

[101] O. Yanes, J. Clark, D. M. Wong, G. J. Patti, A. Sánchez-Ruiz, H. P. Benton, S. A. Trauger, C. Desponts, S. Ding, and G. Siuzdak, "Metabolic oxidation regulates embryonic stem cell differentiation," *Nature Chemical Biology*, vol. 6, no. 6, pp. 411–7, 2010.

[102] M. Knobloch, G. A. Pilz, B. Ghesquière, W. J. Kovacs, T. Wegleiter, D. L. Moore, M. Hruzova, N. Zamboni, P. Carmeliet, and S. Jessberger, "A Fatty Acid Oxidation-Dependent Metabolic Shift Regulates Adult Neural Stem Cell Activity," *Cell Reports*, vol. 20, no. 9, pp. 2144–2155, 2017.

[103] K. Ito, A. Carracedo, D. Weiss, F. Arai, U. Ala, D. E. Avigan, Z. T. Schafer, R. M. Evans, T. Suda, C. H. Lee, and P. P. Pandolfi, "A PML-PPAR-δ pathway for fatty acid oxidation regulates hematopoietic stem cell maintenance," *Nature Medicine*, vol. 18, no. 9, pp. 1350–8, 2012.

[104] H. Sperber, J. Mathieu, Y. Wang, A. Ferreccio, J. Hesson, Z. Xu, K. A. Fischer, A. Devi, D. Detraux, H. Gu, S. L. Battle, M. Showalter, C. Valensisi, J. H. Bielas, N. G. Ericson, L. Margaretha, A. M. Robitaille, D. Margineantu, O. Fiehn, D. Hockenbery, C. A. Blau, D. Raftery, A. A. Margolin, R. D. Hawkins, R. T. Moon, C. B. Ware, and H. Ruohola-Baker, "The metabolome regulates the epigenetic landscape during naive-to-primed human embryonic stem cell transition.," *Nature cell biology*, vol. 17, pp. 1523–35, dec 2015.

[105] D. J. Murphy, "The biogenesis and functions of lipid bodies in animals, plants and microorganisms," *Progress in Lipid Research*, vol. 40, no. 5, pp. 325–438, 2001.

[106] T. C. Walther and R. V. Farese Jr., "Lipid droplets and cellular lipid metabolism," *Annu Rev Biochem*, vol. 81, pp. 687–714, 2012.

[107] R. Bartz, W. H. Li, B. Venables, J. K. Zehmer, M. R. Roth, R. Welti, R. G. Anderson, P. Liu, and K. D. Chapman, "Lipidomics reveals that adiposomes store ether lipids and mediate phospholipid traffic," *J Lipid Res*, vol. 48, pp. 837–847, 2007.

[108] M. Suzuki, Y. Shinohara, Y. Ohsaki, and T. Fujimoto, "Lipid droplets: Size matters," *Journal of Electron Microscopy*, vol. 60, no. Suppl 1, pp. S101–16, 2011.

[109] N. Jacquier, V. Choudhary, M. Mari, A. Toulmay, F. Reggiori, and R. Schneiter, "Lipid droplets are functionally connected to the endoplasmic reticulum in Saccharomyces cerevisiae," *Journal of Cell Science*, vol. 124, no. Pt 14, pp. 2424–37, 2011.

[110] D. J. Murphy and J. Vance, "Mechanisms of lipid-body formation," *Trends in Biochemical Sciences*, vol. 24, no. 3, pp. 109–15, 1999.

[111] K. Tauchi-Sato, S. Ozeki, T. Houjou, R. Taguchi, and T. Fujimoto, "The surface of lipid droplets is a phospholipid monolayer with a unique fatty acid composition," *Journal of Biological Chemistry*, vol. 277, no. 46, pp. 44507–12, 2002.

[112] L. Kuerschner, C. Moessinger, and C. Thiele, "Imaging of lipid biosynthesis: How a neutral lipid enters lipid droplets," *Traffic*, vol. 9, no. 3, pp. 338–52, 2008.

[113] L. L. Listenberger, X. Han, S. E. Lewis, S. Cases, R. V. Farese, D. S. Ory, and J. E. Schaffer, "Triglyceride accumulation protects against fatty acid-induced lipotoxicity," *Proceedings of the National Academy of Sciences*, vol. 100, no. 6, pp. 3077–82, 2003.

[114] G. Frühbeck, J. Gómez-Ambrosi, F. J. Muruzábal, and M. A. Burrell, "The adipocyte: a model for integration of endocrine and metabolic signaling in energy metabolism regulation," *American Journal of Physiology-Endocrinology and Metabolism*, vol. 309, no. 8, pp. E691–714, 2001.

[115] A. P. Bailey, G. Koster, C. Guillermier, C. P. Lechene, A. D. Postle, A. P. Gould Correspondence, E. M. A. Hirst, J. I. Macrae, and A. P. Gould, "Antioxidant Role for Lipid Droplets in a Stem Cell Niche of Drosophila," *Cell*, vol. 163, no. 2, pp. 340–53, 2015.

[116] C.-L. E. Yen, S. J. Stone, S. Koliwad, C. Harris, and R. V. Farese, "Thematic review series: glycerolipids. DGAT enzymes and triacylglycerol biosynthesis.," *Journal of lipid research*, vol. 49, no. 11, pp. 2283–301, 2008.

[117] T.-Y. Chang, B.-L. Li, C. C. Y. Chang, and Y. Urano, "Acyl-coenzyme A:cholesterol acyltransferases," *AJP: Endocrinology and Metabolism*, vol. 297, no. 1, pp. E1–9, 2009.

[118] K. Takeuchi and K. Reue, "Biochemistry, physiology, and genetics of GPAT, AGPAT, and lipin enzymes in triglyceride synthesis," *AJP: Endocrinology and Metabolism*, vol. 296, no. 6, pp. E1195–209, 2009.

[119] M. A. Welte and A. P. Gould, "Lipid droplet functions beyond energy storage," *Biochimica et Biophysica Acta - Molecular and Cell Biology of Lipids*, vol. 1862, no. 10 Pt B, pp. 1260–1272, 2017.

[120] R. Zechner, F. Madeo, and D. Kratky, "Cytosolic lipolysis and lipophagy: Two sides of the same coin," *Nature Reviews Molecular Cell Biology*, vol. 18, no. 11, pp. 671–684, 2017.

[121] E. Currie, A. Schulze, R. Zechner, T. C. Walther, and R. V. Farese, "Cellular fatty acid metabolism and cancer," *Cell Metabolism*, vol. 18, no. 2, pp. 153–61, 2013.

[122] S. Murphy, S. Martin, and R. G. Parton, "Lipid droplet-organelle interactions; sharing the fats," *Biochimica et Biophysica Acta - Molecular and Cell Biology of Lipids*, vol. 1791, no. 6, pp. 441–7, 2009.

[123] R. Singh, S. Kaushik, Y. Wang, Y. Xiang, I. Novak, M. Komatsu, K. Tanaka, A. M. Cuervo, and M. J. Czaja, "Autophagy regulates lipid metabolism," *Nature*, vol. 458, no. 7242, pp. 1131–5, 2009.

[124] A. S. Rambold, S. Cohen, and J. Lippincott-Schwartz, "Fatty acid trafficking in starved cells: Regulation by lipid droplet lipolysis, autophagy, and mitochondrial fusion dynamics," *Developmental Cell*, vol. 32, no. 6, pp. 678–92, 2015.

[125] B. Jaishy and E. D. Abel, "Lipids, lysosomes, and autophagy.," *Journal of lipid research*, vol. 57, no. 9, pp. 1619–35, 2016.

[126] M. Beller, K. Thiel, P. J. Thul, and H. Jäckle, "Lipid droplets: A dynamic organelle moves into focus," *FEBS Letters*, vol. 584, no. 11, pp. 2176–82, 2010.

[127] D. Barneda, J. Planas-Iglesias, M. L. Gaspar, D. Mohammadyani, S. Prasannan, D. Dormann, G.-S. Han, S. A. Jesch, G. M. Carman, V. Kagan, M. G. Parker, N. T. Ktistakis, J. Klein-Seetharaman, A. M. Dixon, S. A. Henry, and M. Christian, "The brown adipocyte protein CIDEA promotes lipid droplet fusion via a phosphatidic acid-binding amphipathic helix.," *eLife*, vol. 4, p. e07485, nov 2015.

[128] L. Wu, L. Zhou, C. Chen, J. Gong, L. Xu, J. Ye, D. Li, and P. Li, "Cidea controls lipid droplet fusion and lipid storage in brown and white adipose tissue," *Science China Life Sciences*, vol. 57, pp. 107–116, jan 2014.

[129] N. Kory, R. V. Farese, and T. C. Walther, "Targeting Fat: Mechanisms of Protein Localization to Lipid Droplets," *Trends in Cell Biology*, vol. 26, no. 7, pp. 535–546, 2016.

[130] A. S. Greenberg, J. J. Egan, S. A. Wek, N. B. Garty, E. J. Blanchette-Mackie, and C. Londos, "Perilipin, a major hormonally regulated adipocyte-specific phosphoprotein associated with the

periphery of lipid storage droplets," *Journal of Biological Chemistry*, vol. 266, no. 17, pp. 11341–6, 1991.

[131] D. L. Brasaemle, T. Barber, A. R. Kimmel, and C. Londos, "Post-translational regulation of perilipin expression: Stabilization by stored intracellular neutral lipids," *Journal of Biological Chemistry*, vol. 272, no. 14, pp. 9378–87, 1997.

[132] N. E. Wolins, B. Rubin, and D. L. Brasaemle, "TIP47 Associates with Lipid Droplets," *Journal of Biological Chemistry*, vol. 276, no. 7, pp. 5101–8, 2001.

[133] N. E. Wolins, J. R. Skinner, M. J. Schoenfish, A. Tzekov, K. G. Bensch, and P. E. Bickel, "Adipocyte protein S3-12 coats nascent lipid droplets," *Journal of Biological Chemistry*, vol. 278, no. 39, pp. 37713–21, 2003.

[134] T. Yamaguchi, S. Matsushita, K. Motojima, F. Hirose, and T. Osumi, "MLDP, a novel PAT family protein localized to lipid droplets and enriched in the heart, is regulated by peroxisome proliferator-activated receptorα," *Journal of Biological Chemistry*, vol. 281, no. 20, pp. 14232–40, 2006.

[135] S. Miura, J. W. Gan, J. Brzostowski, M. J. Parisi, C. J. Schultz, C. Londos, B. Oliver, and A. R. Kimmel, "Functional conservation for lipid storage droplet association among perilipin, ADRP, and TIP47 (PAT)-related proteins in mammals, Drosophila, and Dictyostelium," *Journal of Biological Chemistry*, vol. 277, no. 35, pp. 32253–7, 2002.

[136] S. Grönke, M. Beller, S. Fellert, H. Ramakrishnan, H. Jäckle, and R. P. Kühnlein, "Control of fat storage by a Drosophila PAT domain protein," *Current Biology*, vol. 13, no. 7, pp. 603–6, 2003.

[137] R. T. Patel, J. L. Soulages, B. Hariharasundaram, and E. L. Arrese, "Activation of the lipid droplet controls the rate of lipolysis of triglycerides in the insect fat body," *Journal of Biological Chemistry*, vol. 280, no. 24, pp. 22624–31, 2005.

[138] S. Ozeki, "Rab18 localizes to lipid droplets and induces their close apposition to the endoplasmic reticulum-derived membrane," *Journal of Cell Science*, vol. 118, no. Pt 12, pp. 2601–11, 2005.

[139] S. Martin, K. Driessen, S. J. Nixon, M. Zerial, and R. G. Parton, "Regulated localization of Rab18 to lipid droplets: Effects of lipolytic stimulation and inhibition of lipid droplet catabolism," *Journal of Biological Chemistry*, vol. 280, no. 51, pp. 42325–35, 2005.

[140] D. L. Brasaemle, G. Dolios, L. Shapiro, and R. Wang, "Proteomic analysis of proteins associated with lipid droplets of basal and lipolytically stimulated 3T3-L1 adipocytes.," *The Journal of biological chemistry*, vol. 279, no. 45, pp. 46835–42, 2004.

[141] J. Bouchoux, F. Beilstein, T. Pauquai, I. C. Guerrera, D. Chateau, N. Ly, M. Alqub, C. Klein, J. Chambaz, M. Rousset, J.-M. Lacorte, E. Morel, and S. Demignot, "The proteome of cytosolic lipid droplets isolated from differentiated Caco-2/TC7 enterocytes reveals cell-specific characteristics," *Biology of the Cell*, vol. 103, no. 11, pp. 499–517, 2011.

[142] S. Cermelli, Y. Guo, S. P. Gross, and M. A. Welte, "The Lipid-Droplet Proteome Reveals that Droplets Are a Protein-Storage Depot," *Current Biology*, vol. 16, no. 18, pp. 1783–95, 2006.

[143] T. D'Aquila, D. Sirohi, J. M. Grabowski, V. E. Hedrick, L. N. Paul, A. S. Greenberg, R. J. Kuhn, and K. K. Buhman, "Characterization of the proteome of cytoplasmic lipid droplets in mouse enterocytes after a dietary fat challenge," *PLoS ONE*, vol. 10, no. 5, p. e0126823, 2015.

[144] Y. Ding, L. Yang, S. Zhang, Y. Wang, Y. Du, J. Pu, G. Peng, Y. Chen, H. Zhang, J. Yu, H. Hang, P. Wu, F. Yang, H. Yang, A. Steinbüchel, and P. Liu, "Identification of the major functional proteins of prokaryotic lipid droplets," *Journal of Lipid Research*, vol. 53, no. 3, pp. 399–411, 2012.

[145] N. Krahmer, M. Hilger, N. Kory, F. Wilfling, G. Stoehr, M. Mann, R. V. Farese, and T. C. Walther, "Protein Correlation Profiles Identify Lipid Droplet Proteins with High Confidence," *Molecular & Cellular Proteomics*, vol. 12, no. 5, pp. 1115–26, 2013.

[146] P. Zhang, H. Na, Z. Liu, S. Zhang, P. Xue, Y. Chen, J. Pu, G. Peng, X. Huang, F. Yang, Z. Xie, T. Xu, P. Xu, G. Ou, S. O. Zhang, and P. Liu, "Proteomic study and marker protein identification of Caenorhabditis elegans lipid droplets.," *Molecular & cellular proteomics : MCP*, vol. 11, no. 8, pp. 317–28, 2012.

[147] E. Currie, X. Guo, R. Christiano, C. Chitraju, N. Kory, K. Harrison, J. Haas, T. C. Walther, and R. V. Farese, "High confidence proteomic analysis of yeast LDs identifies additional droplet proteins and reveals connections to dolichol synthesis and sterol acetylation," *Journal of Lipid Research*, vol. 55, no. 7, pp. 1465–77, 2014.

[148] J. G. Granneman, H. P. H. Moore, R. Krishnamoorthy, and M. Rathod, "Perilipin controls lipolysis by regulating the interactions of AB-hydrolase containing 5 (Abhd5) and adipose triglyceride lipase (Atgl)," *Journal of Biological Chemistry*, vol. 284, no. 50, pp. 34538–44, 2009.

[149] J. G. Granneman, H. P. H. Moore, E. P. Mottillo, Z. Zhu, and L. Zhou, "Interactions of Perilipin-5 (Plin5) with adipose triglyceride lipase," *Journal of Biological Chemistry*, vol. 286, no. 7, pp. 5126–35, 2011.

[150] C. Sztalryd, G. Xu, H. Dorward, J. T. Tansey, J. A. Contreras, A. R. Kimmel, and C. Londos, "Perilipin A is essential for the translocation of hormone-sensitive lipase during lipolytic activation," *Journal of Cell Biology*, vol. 161, no. 6, pp. 1093–103, 2003.

[151] N. M. Pollak, D. Jaeger, S. Kolleritsch, R. Zimmermann, R. Zechner, A. Lass, and G. Haemmerle, "The interplay of protein kinase a and Perilipin 5 regulates cardiac lipolysis," *Journal of Biological Chemistry*, vol. 290, no. 3, pp. 1295–306, 2015.

[152] N. Inohara, T. Koseki, S. Chen, X. Wu, and G. Núñez, "CIDE, a novel family of cell death activators with homology to the 45 kDa subunit of the DNA fragmentation factor.," *The EMBO journal*, vol. 17, pp. 2526–33, may 1998.

[153] A. B. Chapman, D. M. Knight, B. S. Dieckmann, and G. M. Ringold, "Analysis of gene expression during differentiation of adipogenic cells in culture and hormonal control of the developmental program.," *The Journal of biological chemistry*, vol. 259, pp. 15548–55, dec 1984.

[154] L. Liang, M. Zhao, Z. Xu, K. K. Yokoyama, and T. Li, "Molecular cloning and characterization of CIDE-3, a novel member of the cell-death-inducing DNA-fragmentation-factor (DFF45)-like effector family.," *The Biochemical journal*, vol. 370, no. Pt 1, pp. 195–203, 2003.

[155] C. Wu, Y. Zhang, Z. Sun, and P. Li, "Molecular evolution of Cide family proteins: novel domain formation in early vertebrates and the subsequent divergence.," *BMC evolutionary biology*, vol. 8, p. 159, may 2008.

[156] Z. Zhou, S. Y. Toh, Z. Chen, K. Guo, C. P. Ng, S. Ponniah, S. C. Lin, W. Hong, and P. Li, "Cidea-deficient mice have lean phenotype and are resistant to obesity," *Nature Genetics*, vol. 35, no. 1, pp. 49–56, 2003.

[157] S. Y. Toh, J. Gong, G. Du, J. Z. Li, S. Yang, J. Ye, H. Yao, Y. Zhang, B. Xue, Q. Li, H. Yang, Z. Wen, and P. Li, "Up-regulation of mitochondrial activity and acquirement of brown adipose tissue-like property in the white adipose tissue of Fsp27 deficient mice," *PLoS ONE*, vol. 3, no. 8, p. e2890, 2008.

[158] N. Nishino, Y. Tamori, S. Tateya, T. Kawaguchi, T. Shibakusa, W. Mizunoya, K. Inoue, R. Kitazawa, S. Kitazawa, Y. Matsuki, R. Hiramatsu, S. Masubuchi, A. Omachi, K. Kimura, M. Saito, T. Amo, S. Ohta, T. Yamaguchi, T. Osumi, J. Cheng, T. Fujimoto, H. Nakao, K. Nakao, A. Aiba, H. Okamura, T. Fushiki, and M. Kasuga, "FSP27 contributes to efficient energy storage in murine white adipocytes by promoting the formation of unilocular lipid droplets," *Journal of Clinical Investigation*, vol. 118, no. 8, pp. 2808–21, 2008.

[159] L. Erdtmann, N. Franck, H. Lerat, J. Le Seyec, D. Gilot, I. Cannie, P. Gripon, U. Hibner, and C. Guguen-Guillouzo, "The hepatitis C virus NS2 protein is an inhibitor of CIDE-B-induced apoptosis," *Journal of Biological Chemistry*, vol. 278, no. 20, pp. 18256–64, 2003.

[160] A. Chatterjee, P. Mondal, S. Ghosh, V. S. Mehta, and E. Sen, "PPARγ regulated CIDEA affects pro-apoptotic responses in glioblastoma.," *Cell death discovery*, vol. 1, p. 15038, 2015.

[161] K. Liu, S. Zhou, J.-Y. Kim, K. Tillison, D. Majors, D. Rearick, J. H. Lee, R. F. Fernandez-Boyanapalli, K. Barricklow, M. S. Houston, and C. M. Smas, "Functional analysis of FSP27 protein regions for lipid droplet localization, caspase-dependent apoptosis, and dimerization with CIDEA.," *American journal of physiology. Endocrinology and metabolism*, vol. 297, no. 6, pp. E1395–413, 2009.

[162] J. Z. Li, J. Ye, B. Xue, J. Qi, J. Zhang, Z. Zhou, Q. Li, Z. Wen, and P. Li, "Cideb regulates diet-induced obesity, liver steatosis, and insulin sensitivity by controlling lipogenesis and fatty acid oxidation," *Diabetes*, vol. 56, no. 10, pp. 2523–32, 2007.

[163] V. Puri, S. Konda, S. Ranjit, M. Aouadi, A. Chawla, M. Chouinard, A. Chakladar, and M. P. Czech, "Fat-specific protein 27, a novel lipid droplet protein that enhances triglyceride storage," *Journal of Biological Chemistry*, vol. 282, no. 47, pp. 34213–8, 2007.

[164] V. Puri, S. Ranjit, S. Konda, S. M. C. Nicoloro, J. Straubhaar, A. Chawla, M. Chouinard, C. Lin, A. Burkart, S. Corvera, R. A. Perugini, and M. P. Czech, "Cidea is associated with lipid droplets and insulin sensitivity in humans," *Proceedings of the National Academy of Sciences*, vol. 105, no. 22, pp. 7833–8, 2008.

[165] M. Feldo, J. Kocki, S. Łukasik, and J. Bogucki, "CIDEA gene expresion in patients with abdominal obesity and LDL hyperlipoproteinemia qualified for surgical revascularization in chronic limb ischemia," *Polski Przeglad Chirurgiczny/ Polish Journal of Surgery*, vol. 85, no. 11, pp. 644–8, 2013.

[166] J. Laurencikiene, B. M. Stenson, E. A. Nordström, T. Agustsson, D. Langin, B. Isaksson, J. Permert, M. Rydén, and P. Arner, "Evidence for an important role of CIDEA in human cancer cachexia," *Cancer Research*, vol. 68, no. 22, pp. 9247–54, 2008.

[167] L. F. B. Bortolotto, F. R. Barbosa, G. Silva, T. A. Bitencourt, R. O. Beleboni, S. J. Baek, M. Marins, and A. L. Fachin, "Cytotoxicity of trans-chalcone and licochalcone A against breast cancer cells is due to apoptosis induction and cell cycle arrest," *Biomedicine & Pharmacotherapy*, vol. 85, pp. 425–433, 2017.

[168] J. Yu, S. Zhang, L. Cui, W. Wang, H. Na, X. Zhu, L. Li, G. Xu, F. Yang, M. Christian, and P. Liu, "Lipid droplet remodeling and interaction with mitochondria in mouse brown adipose tissue during cold treatment," *Biochimica et Biophysica Acta - Molecular Cell Research*, vol. 1853, no. 5, pp. 918–28, 2015.

[169] E. P. Mottillo, P. Balasubramanian, Y.-H. Lee, C. Weng, E. E. Kershaw, and J. G. Granneman, "Coupling of lipolysis and de novo lipogenesis in brown, beige, and white adipose tissues during chronic β3-adrenergic receptor activation," *Journal of Lipid Research*, vol. 55, no. 11, pp. 2276–86, 2014.

[170] F. F. Martins, T. C. L. Bargut, M. B. Aguila, and C. A. Mandarim-de Lacerda, "Thermogenesis, fatty acid synthesis with oxidation, and inflammation in the brown adipose tissue of ob/ob (/) mice," *Annals of Anatomy - Anatomischer Anzeiger*, vol. 210, pp. 44–51, mar 2017.

[171] M. H. Oosterveer, A. Grefhorst, T. H. van Dijk, R. Havinga, B. Staels, F. Kuipers, A. K. Groen, and D.-J. Reijngoud, "Fenofibrate Simultaneously Induces Hepatic Fatty Acid Oxidation, Synthesis, and Elongation in Mice," *Journal of Biological Chemistry*, vol. 284, pp. 34036–34044, dec 2009.

[172] G. Callaini, "Cleavage and membrane formation in the blastoderm of the dipteranCeratitis capitata wied," *Journal of Morphology*, vol. 193, pp. 305–315, sep 1987.

[173] T. Watanabe, A. Thayil, A. Jesacher, K. Grieve, D. Debarre, T. Wilson, M. Booth, and S. Srinivas, "Characterisation of the dynamic behaviour of lipid droplets in the early mouse embryo using adaptive harmonic generation microscopy," *BMC Cell Biol*, vol. 11, p. 38, 2010.

[174] R. Kan, M. Jin, V. Subramanian, C. P. Causey, P. R. Thompson, and S. A. Coonrod, "Potential role for PADI-mediated histone citrullination in preimplantation development," *BMC Developmental Biology*, vol. 12, no. 19, 2012.

[175] T. A. Webb, W. J. Kowalski, and R. A. Fluck, "Microtubule-Based Movements During Ooplasmic Segregation in the Medaka Fish Egg (Oryzias latipes)," *The Biological Bulletin*, vol. 188, pp. 146–156, apr 1995.

[176] V. C. Abraham, S. Gupta, and R. A. Fluck, "Ooplasmic Segregation in the Medaka (Oryzias latipes) Egg," *The Biological Bulletin*, vol. 184, no. 2, pp. 115–124, 1993.

[177] I. Jeogonekdrzejowska and J. Kubrakiewicz, "Yolk nucleus - The complex assemblage of cytoskeleton and ER is a site of lipid droplet formation in spider oocytes," *Arthropod Structure and Development*, vol. 39, no. 5, pp. 350–9, 2010.

[178] Y. Yamahama, K. Seno, and T. Hariyama, "Changes in Lipid Droplet Localization During Embryogenesis of the Silkworm, Bombyx mori," *Zoological Science*, vol. 25, pp. 580–586, jun 2008.

[179] T. Shimizu, "Cytoskeletal mechanisms of ooplasmic segregation in annelid eggs," *International Journal of Developmental Biology*, vol. 43, no. 1, pp. 11–8, 1999.

[180] P. C. K. Au, L. Selwood, and M. Familari, "Cloning and characterization of a new gene from the PAT protein family, in a marsupial, the stripe-faced dunnart (Sminthopsis macroura)," *Molecular Reproduction and Development*, vol. 77, pp. 373–83, apr 2010.

[181] H. Yost, "The early development of Xenopus laevis: An Atlas of the histology," *Trends in Genetics*, vol. 8, p. 186, may 1992.

[182] Z. Li, M. R. Johnson, Z. Ke, L. Chen, and M. A. Welte, "Drosophila lipid droplets buffer the h2av supply to protect early embryonic development," *Current Biology*, vol. 24, no. 13, pp. 1485–91, 2014.

[183] Z. Li, K. Thiel, P. J. Thul, M. Beller, R. P. Kühnlein, and M. A. Welte, "Lipid droplets control the maternal histone supply of Drosophila embryos," *Current Biology*, vol. 22, no. 22, pp. 2104–13, 2012.

[184] L. Tirinato, F. Pagliari, T. Limongi, M. Marini, A. Falqui, J. Seco, P. Candeloro, C. Liberale, and E. Di Fabrizio, "An Overview of Lipid Droplets in Cancer and Cancer Stem Cells," *Stem Cells International*, p. 1656053, 2017.

[185] M. Percharde, F. Lavial, J. H. Ng, V. Kumar, R. A. Tomaz, N. Martin, J. C. Yeo, J. Gil, S. Prabhakar, H. H. Ng, M. G. Parker, and V. Azuara, "Ncoa3 functions as an essential Esrrb coactivator to

sustain embryonic stem cell self-renewal and reprogramming," *Genes Dev*, vol. 26, pp. 2286–2298, 2012.

[186] S. Morita, T. Kojima, and T. Kitamura, "Plat-E: An efficient and stable system for transient packaging of retroviruses," *Gene Therapy*, vol. 7, no. 12, pp. 1063–1066, 2000.

[187] Y. Gluzman, "SV40-transformed simian cells support the replication of early SV40 mutants," *Cell*, vol. 23, no. 1, pp. 175–182, 1981.

[188] I. Chambers, D. Colby, M. Robertson, J. Nichols, S. Lee, S. Tweedie, and A. Smith, "Functional expression cloning of Nanog, a pluripotency sustaining factor in embryonic stem cells," *Cell*, vol. 113, pp. 643–655, 2003.

[189] M. E. Ritchie, B. Phipson, D. Wu, Y. Hu, C. W. Law, W. Shi, and G. K. Smyth, "Limma powers differential expression analyses for RNA-sequencing and microarray studies," *Nucleic Acids Research*, vol. 43, no. 7, p. e47, 2015.

[190] R. Fisher, "Statistical methods for research workers," 1925.

[191] M. Vinken, M. Maes, R. Cavill, D. Valkenborg, J. K. Ellis, E. Decrock, L. Leybaert, A. Staes, K. Gevaert, A. G. Oliveira, G. B. Menezes, B. Cogliati, M. L. Z. Dagli, T. M. Ebbels, E. Witters, H. C. Keun, T. Vanhaecke, and V. Rogiers, "Proteomic and metabolomic responses to connexin43 silencing in primary hepatocyte cultures," *Archives of Toxicology*, vol. 87, no. 5, pp. 883–894, 2013.

[192] K. J. Livak and T. D. Schmittgen, "Analysis of relative gene expression data using real-time quantitative PCR and the 2(-Delta Delta C(T)) Method.," *Methods (San Diego, Calif.)*, vol. 25, no. 4, pp. 402–408, 2001.

[193] M. W. Pfaffl, "A new mathematical model for relative quantification in real-time RT-PCR," *Nucleic Acids Research*, vol. 29, no. 9, p. e45, 2001.

[194] Y. Pei, L. Yue, W. Zhang, Y. Wang, B. Wen, L. Zhong, J. Xiang, J. Li, S. Zhang, H. Wang, H. Mu, Q. Wei, and J. Han, "Improvement in Mouse iPSC Induction by Rab32 Reveals the Importance of Lipid Metabolism during Reprogramming," *Scientific Reports*, vol. 5, p. 16539, 2015.

[195] D. Barneda, A. Frontini, S. Cinti, and M. Christian, "Dynamic changes in lipid droplet-associated proteins in the "browning" of white adipose tissues," *Biochim Biophys Acta*, vol. 1831, pp. 924–933, 2013.

[196] T. Yonezawa, R. Kurata, M. Kimura, and H. Inoko, "Which CIDE are you on? Apoptosis and energy metabolism," *Mol. BioSyst.*, vol. 7, pp. 91–100, jan 2011.

[197] D. Barneda and M. Christian, "Lipid droplet growth: regulation of a dynamic organelle," *Current Opinion in Cell Biology*, vol. 47, pp. 9–15, 2017.

[198] J. Miyamoto, S. Hasegawa, M. Kasubuchi, A. Ichimura, A. Nakajima, and I. Kimura, "Nutritional signaling via free fatty acid receptors," *International Journal of Molecular Sciences*, vol. 17, no. 4, p. 450, 2016.

[199] Do Hyun Nam, "Stem cell culture medium and method for culturing stem cells using same."

[200] Garcia-Gonzalo Francesc R. and J. C. I. Belmonte, "Composition of Knockout Serum Replacement," 2013.

[201] H. Abe, M. Nakazawa, K. Kasuga, I. Kojima, and M. Kobayashi, "The CAG promoter is more active than the CEF promoter for the expression of transgenes in a mouse ES cell line E14-derived EB3 cells," *Biotechnology and Biotechnological Equipment*, vol. 25, no. 1, pp. 2301–2304, 2011.

[202] G. Martello, T. Sugimoto, E. Diamanti, A. Joshi, R. Hannah, S. Ohtsuka, B. Göttgens, H. Niwa, and A. Smith, "Esrrb is a pivotal target of the Gsk3/Tcf3 axis regulating embryonic stem cell self-renewal," *Cell Stem Cell*, vol. 11, no. 4, pp. 491–504, 2012.

[203] T. Boroviak, R. Loos, P. Lombard, J. Okahara, R. Behr, E. Sasaki, J. Nichols, A. Smith, and P. Bertone, "Lineage-Specific Profiling Delineates the Emergence and Progression of Naive Pluripotency in Mammalian Embryogenesis," *Developmental Cell*, vol. 35, no. 3, pp. 366–382, 2015.

[204] H. R. Wurie, L. Buckett, and V. A. Zammit, "Diacylglycerol acyltransferase 2 acts upstream of diacylglycerol acyltransferase 1 and utilizes nascent diglycerides and de novo synthesized fatty acids in HepG2 cells," *FEBS Journal*, vol. 279, no. 17, pp. 3033–3047, 2012.

[205] K. Takaoka, M. Yamamoto, and H. Hamada, "Origin and role of distal visceral endoderm, a group of cells that determines anterior-posterior polarity of the mouse embryo," *Nature Cell Biology*, vol. 13, no. 7, pp. 743–752, 2011.

[206] I. Bedzhov, S. J. L. Graham, C. Y. Leung, and M. Zernicka-Goetz, "Developmental plasticity, cell fate specification and morphogenesis in the early mouse embryo," *Philosophical Transactions of the Royal Society B: Biological Sciences*, vol. 369, no. 1657, pp. 20130538–20130538, 2014.

[207] R. L. Gardner and T. J. Davies, "Trophectoderm growth and bilateral symmetry of the blastocyst in the mouse," *Human Reproduction*, vol. 17, no. 7, pp. 1839–1845, 2002.

[208] S. Li, D. Edgar, R. Fässler, W. Wadsworth, and P. D. Yurchenco, "The role of laminin in embryonic cell polarization and tissue organization," *Developmental Cell*, vol. 4, no. 5, pp. 613–624, 2003.

[209] S. J. Han, S.-E. Choi, S.-A. Yi, J. G. Jung, I.-R. Jung, M. Shin, S. Kang, H. Oh, H. J. Kim, D. J. Kim, J. E. Kwon, C. S. Choi, K. W. Lee, and Y. Kang, "Glutamate dehydrogenase activator BCH stimulating reductive amination prevents high fat/high fructose diet-induced steatohepatitis and hyperglycemia in C57BL/6J mice.," *Scientific reports*, vol. 5, p. 37468, 2016.

[210] C. H. E. Lau, G. D. Tredwell, J. K. Ellis, E. W. Lam, and H. C. Keun, "Metabolomic characterisation of the effects of oncogenic PIK3CA transformation in a breast epithelial cell line," *Scientific Reports*, vol. 7, p. 46079, 2017.

[211] S. Jitrapakdee and J. C. Wallace, "Structure, function and regulation of pyruvate carboxylase.," *The Biochemical journal*, vol. 340, pp. 1–16, may 1999.

[212] L. J. Eichner and V. Giguère, "Estrogen related receptors (ERRs): A new dawn in transcriptional control of mitochondrial gene networks," *Mitochondrion*, vol. 11, no. 4, pp. 544–552, 2011.

[213] P. E. Declercq, J. R. Falck, M. Kuwajima, H. Tyminski, D. W. Foster, and J. D. McGarry, "Characterization of the mitochondrial carnitine palmitoyltransferase enzyme system. I. Use of inhibitors.," *Journal of Biological Chemistry*, vol. 262, no. 20, pp. 9812–9821, 1987.

[214] S. A. Mookerjee and M. D. Brand, "Measurement and Analysis of Extracellular Acid Production to Determine Glycolytic Rate," *Journal of Visualized Experiments*, no. 106, p. e53464, 2015.

[215] T. Palm, S. Bolognin, J. Meiser, S. Nickels, C. Träger, R. L. Meilenbrock, J. Brockhaus, M. Schreitmüller, M. Missler, and J. C. Schwamborn, "Rapid and robust generation of long-term self-renewing human neural stem cells with the ability to generate mature astroglia," *Scientific Reports*, vol. 5, p. 16321, 2015.

[216] J. Silva, J. Nichols, T. W. Theunissen, G. Guo, A. L. van Oosten, O. Barrandon, J. Wray, S. Yamanaka, I. Chambers, and A. Smith, "Nanog Is the Gateway to the Pluripotent Ground State," *Cell*, vol. 138, no. 4, pp. 722–37, 2009.

[217] K. M. Szymanski, D. Binns, R. Bartz, N. V. Grishin, W.-P. Li, A. K. Agarwal, A. Garg, R. G. W. Anderson, and J. M. Goodman, "The lipodystrophy protein seipin is found at endoplasmic reticulum lipid droplet junctions and is important for droplet morphology," *Proceedings of the National Academy of Sciences*, vol. 104, no. 52, pp. 20890–5, 2007.

[218] A. Herms, M. Bosch, N. Ariotti, B. J. Reddy, A. Fajardo, A. Fernández-Vidal, A. Alvarez-Guaita, M. A. Fernández-Rojo, C. Rentero, F. Tebar, C. Enrich, M. I. Geli, R. G. Parton, S. P. Gross, and A. Pol, "Cell-to-cell heterogeneity in lipid droplets suggests a mechanism to reduce lipotoxicity," *Current Biology*, vol. 23, no. 15, pp. 1489–96, 2013.

[219] L. H. Loo, H. J. Lin, D. K. Singh, K. M. Lyons, S. J. Altschuler, and L. F. Wu, "Heterogeneity in the physiological states and pharmacological responses of differentiating 3T3-L1 preadipocytes," *Journal of Cell Biology*, vol. 187, no. 3, pp. 375–84, 2009.

[220] L. Tirinato, C. Liberale, S. Di Franco, P. Candeloro, A. Benfante, R. La Rocca, L. Potze, R. Marotta, R. Ruffilli, V. P. Rajamanickam, M. Malerba, F. De Angelis, A. Falqui, E. Carbone, M. Todaro, J. P. Medema, G. Stassi, and E. Di Fabrizio, "Lipid droplets: a new player in colorectal cancer stem cells unveiled by spectroscopic imaging.," *Stem cells (Dayton, Ohio)*, vol. 33, pp. 35–44, jan 2015.

[221] S. J. Stone, H. M. Myers, S. M. Watkins, B. E. Brown, K. R. Feingold, P. M. Elias, and R. V. Farese, "Lipopenia and Skin Barrier Abnormalities in DGAT2-deficient Mice," *Journal of Biological Chemistry*, vol. 279, pp. 11767–11776, mar 2004.

[222] F. G. Schaap, B. Binas, H. Danneberg, G. J. van der Vusse, and J. F. Glatz, "Impaired long-chain fatty acid utilization by cardiac myocytes isolated from mice lacking the heart-type fatty acid binding protein gene.," *Circulation research*, vol. 85, pp. 329–37, aug 1999.

[223] C. D. Capo-Chichi, M. E. Rula, J. L. Smedberg, L. Vanderveer, M. S. Parmacek, E. E. Morrisey, A. K. Godwin, and X. X. Xu, "Perception of differentiation cues by GATA factors in primitive endoderm lineage determination of mouse embryonic stem cells," *Developmental Biology*, vol. 286, no. 2, pp. 574–86, 2005.

[224] J. Artus, J.-J. Panthier, and A.-K. Hadjantonakis, "A role for PDGF signaling in expansion of the extra-embryonic endoderm lineage of the mouse blastocyst," *Development*, vol. 137, no. 20, pp. 3361–72, 2010.

[225] Y. Mugabo, S. Zhao, A. Seifried, S. Gezzar, A. Al-Mass, D. Zhang, J. Lamontagne, C. Attane, P. Poursharifi, J. Iglesias, E. Joly, M.-L. Peyot, A. Gohla, S. R. M. Madiraju, and M. Prentki, "Identification of a mammalian glycerol-3-phosphate phosphatase: Role in metabolism and signaling in pancreatic β-cells and hepatocytes," *Proceedings of the National Academy of Sciences*, vol. 113, no. 4, pp. E430–9, 2016.

[226] B. W. Carey, L. W. Finley, J. R. Cross, C. D. Allis, and C. B. Thompson, "Intracellular α-ketoglutarate maintains the pluripotency of embryonic stem cells," *Nature*, vol. 518, no. 7539, pp. 413–6, 2015.

[227] F. P. Kuhajda, "Fatty-acid synthase and human cancer: new perspectives on its role in tumor biology.," *Nutrition (Burbank, Los Angeles County, Calif.)*, vol. 16, no. 3, pp. 202–8, 2000.

[228] M. Tosolini and A. Jouneau, "Acquiring Ground State Pluripotency: Switching Mouse Embryonic Stem Cells from Serum/LIF Medium to 2i/LIF Medium.," in *Turksen K. (eds) Embryonic Stem Cell Protocols.*, vol. 1341, pp. 41–8, Humana Press, New York, NY, 2015.

[229] C. D. L. Folmes, P. P. Dzeja, T. J. Nelson, and A. Terzic, "Metabolic plasticity in stem cell homeostasis and differentiation," *Cell Stem Cell*, vol. 11, no. 5, pp. 596–606, 2012.

[230] P. Boström, M. Rutberg, J. Ericsson, P. Holmdahl, L. Andersson, M. A. Frohman, J. Borén, and S. O. Olofsson, "Cytosolic lipid droplets increase in size by microtubule-dependent complex formation," *Arteriosclerosis, Thrombosis, and Vascular Biology*, vol. 25, no. 9, pp. 1945–51, 2005.

[231] M. Hallberg, D. L. Morganstein, E. Kiskinis, K. Shah, A. Kralli, S. M. Dilworth, R. White, M. G. Parker, and M. Christian, "A functional interaction between RIP140 and PGC-1alpha regulates the expression of the lipid droplet protein CIDEA," *Mol Cell Biol*, vol. 28, pp. 6785–6795, 2008.

[232] T. Yonezawa, S. Haga, Y. Kobayashi, K. Katoh, and Y. Obara, "Saturated fatty acids stimulate and insulin suppresses CIDE-A expression in bovine mammary epithelial cells," *Biochemical and Biophysical Research Communications*, vol. 384, pp. 535–539, jul 2009.

[233] M. Ito, M. Nagasawa, T. Hara, T. Ide, and K. Murakami, "Differential roles of CIDEA and CIDEC in insulin-induced anti-apoptosis and lipid droplet formation in human adipocytes.," *Journal of lipid research*, vol. 51, no. 7, pp. 1676–84, 2010.

[234] L. Zhou, L. Xu, J. Ye, D. Li, W. Wang, X. Li, L. Wu, H. Wang, F. Guan, and P. Li, "Cidea promotes hepatic steatosis by sensing dietary fatty acids," *Hepatology*, vol. 56, no. 1, pp. 95–107, 2012.

[235] A. M. Hall, E. M. Brunt, Z. Chen, N. Viswakarma, J. K. Reddy, N. E. Wolins, and B. N. Finck, "Dynamic and differential regulation of proteins that coat lipid droplets in fatty liver dystrophic mice.," *Journal of lipid research*, vol. 51, no. 3, pp. 554–63, 2010.

[236] S. C. Chan, S.-C. Lin, and P. Li, "Regulation of Cidea protein stability by the ubiquitin-mediated proteasomal degradation pathway.," *The Biochemical journal*, vol. 408, pp. 259–66, dec 2007.

[237] D. Hernández-García, S. Castro-Obregón, S. Gómez-López, C. Valencia, and L. Covarrubias, "Cell death activation during cavitation of embryoid bodies is mediated by hydrogen peroxide," *Experimental Cell Research*, vol. 314, no. 10, pp. 2090–9, 2008.

[238] F. Martín-Belmonte, W. Yu, A. E. Rodríguez-Fraticelli, A. Ewald, Z. Werb, M. A. Alonso, and K. Mostov, "Cell-Polarity Dynamics Controls the Mechanism of Lumen Formation in Epithelial Morphogenesis," *Current Biology*, vol. 18, no. 7, pp. 507–13, 2008.

[239] J. R. Doherty and C. Yang, "Blocking lactate export by inhibiting the Myc target MCT1 Disables glycolysis and glutathione synthesis.," *Cancer research*, vol. 74, no. 3, pp. 908–20, 2014.

[240] J. Adijanto and N. J. Philp, "The SLC16A family of monocarboxylate transporters (MCTs)-physiology and function in cellular metabolism, pH homeostasis, and fluid transport," *Current Topics in Membranes*, vol. 70, pp. 275–311, 2012.

[241] P. Gupta, K. Hourigan, S. Jadhav, J. Bellare, and P. Verma, "Effect of lactate and pH on mouse pluripotent stem cells: Importance of media analysis," *Biochemical Engineering Journal*, vol. 118, pp. 25–33, 2017.

[242] W. Gu, X. Gaeta, A. Sahakyan, A. B. Chan, C. S. Hong, R. Kim, D. Braas, K. Plath, W. E. Lowry, and H. R. Christofk, "Glycolytic Metabolism Plays a Functional Role in Regulating Human Pluripotent Stem Cell State," *Cell Stem Cell*, vol. 19, no. 4, pp. 476–490, 2016.

[243] P. Sonveaux, F. Végran, T. Schroeder, M. C. Wergin, J. Verrax, Z. N. Rabbani, C. J. De Saedeleer, K. M. Kennedy, C. Diepart, B. F. Jordan, M. J. Kelley, B. Gallez, M. L. Wahl, O. Feron, and M. W. Dewhirst, "Targeting lactate-fueled respiration selectively kills hypoxic tumor cells in mice," *Journal of Clinical Investigation*, vol. 118, no. 12, pp. 3930–42, 2008.

[244] K. Sellers, M. P. Fox, M. B. Ii, S. P. Slone, R. M. Higashi, D. M. Miller, Y. Wang, J. Yan, M. O. Yuneva, R. Deshpande, A. N. Lane, and T. W. Fan, "Pyruvate carboxylase is critical for non small-

cell lung cancer proliferation," *The Journal of Clinical Investigation*, vol. 125, no. 2, pp. 687–98, 2015.

[245] J. Wray, T. Kalkan, S. Gomez-Lopez, D. Eckardt, A. Cook, R. Kemler, and A. Smith, "Inhibition of glycogen synthase kinase-3 alleviates Tcf3 repression of the pluripotency network and increases embryonic stem cell resistance to differentiation," *Nature Cell Biology*, vol. 13, no. 7, pp. 838–45, 2011.

[246] R. Yang, R. G. Lacson, G. Castriota, X. D. Zhang, Y. Liu, W. Zhao, M. Einstein, L. M. Camargo, S. Qureshi, K. K. Wong, B. B. Zhang, M. Ferrer, and J. P. Berger, "A genome-wide siRNA screen to identify modulators of insulin sensitivity and gluconeogenesis," *PLoS ONE*, vol. 7, no. 5, p. e36384, 2012.

[247] N. Shiraki, Y. Shiraki, T. Tsuyama, F. Obata, M. Miura, G. Nagae, H. Aburatani, K. Kume, F. Endo, and S. Kume, "Methionine metabolism regulates maintenance and differentiation of human pluripotent stem cells," *Cell Metabolism*, vol. 19, no. 5, pp. 780–94, 2014.

[248] H. Marks, T. Kalkan, R. Menafra, S. Denissov, K. Jones, H. Hofemeister, J. Nichols, A. Kranz, A. Francis Stewart, A. Smith, and H. G. Stunnenberg, "The transcriptional and epigenomic foundations of ground state pluripotency," *Cell*, vol. 149, no. 3, pp. 590–604, 2012.

[249] M. Tosolini, V. Brochard, P. Adenot, M. Chebrout, G. Grillo, V. Navia, N. Beaujean, C. Francastel, A. Bonnet-Garnier, and A. Jouneau, "Contrasting epigenetic states of heterochromatin in the different types of mouse pluripotent stem cells," *Scientific Reports*, vol. 8, p. 5776, dec 2018.

[250] A. Gassama-Diagne, W. Yu, M. ter Beest, F. Martin-Belmonte, A. Kierbel, J. Engel, and K. Mostov, "Phosphatidylinositol-3,4,5-trisphosphate regulates the formation of the basolateral plasma membrane in epithelial cells," *Nature Cell Biology*, vol. 8, no. 9, pp. 963–70, 2006.

[251] F. Martin-Belmonte, A. Gassama, A. Datta, W. Yu, U. Rescher, V. Gerke, and K. Mostov, "PTEN-Mediated Apical Segregation of Phosphoinositides Controls Epithelial Morphogenesis through Cdc42," *Cell*, vol. 128, no. 2, pp. 383–97, 2007.

[252] L. C. Skwarek and G. L. Boulianne, "Great Expectations for PIP: Phosphoinositides as Regulators of Signaling During Development and Disease," *Developmental Cell*, vol. 16, no. 1, pp. 12–20, 2009.

[253] D. J. Gillooly, "Localization of phosphatidylinositol 3-phosphate in yeast and mammalian cells," *The EMBO Journal*, vol. 19, no. 17, pp. 4577–88, 2000.

Chapter 8

Appendix

Table 8.1: Sequences of primers used for RT-qPCR.

Gene	Forward (5'-3')	Reverse (5'-3')
Acc1	GGCCTTTCACATGAGATCCAG	GATCGCATGCATTTCACTGCT
Acly	TTCCTCCTTAATGCCAGCGG	TTGGGACTGAATCTTGGGGC
Acsl1	TGGGGTGGAAATCATCAGCC	CCTTTGGGGTTGCCTGTAGT
Atgl	CCTTAGGAGGAATGCCCTGC	CTCCAACAAGCGGATGGTGA
Brachyury	CCGGTGCTGAAGGTAAATGT	CCTCCATTGAGCTTGTTGGT
Cdx2	TCAACCTCGCCACAACCTTCCC	TGGCTCAGCCTGGGATTGCT
*Cidea**	CACGCATTTCATGATCTTGGA	GTTGCTTGCAGACTGGGACAT
*Cidea***	AAGCTTCAAGGCCGTGTTA	CTGTAGCTGTGCCCTGGTTA
*Cidea****	TACAGAAGAGCAGCCATCCC	GCCACTGTGCTGGATATCTG
Cideb	GCTGGAGCCCCAAGAGTGGGA	GGTGATGCGGGCGATGTCCT
Cidec	GCCCCCATCAGAACAGCGCA	AGGTTACCCGGGCCACATCG
Cox7a1	CCACTTAGAAAACCGTGTGG	AGTCTGTACAGGACGTTGTC
Cpt1a	CTCAGTGGGAGCGACTCTTCA	GGCCTCTGTGGTACACGACAA
Cpt1b	CAAGTTCAGAGACGAACGCC	CCACCCCTTATGCCTGTGAG
Cpt1c	GCAGCTGCTGACCTCTGAC	AAGTCATTCCAGACACGCCA
Dab2	GGCAACAGGCTGAACCATTAGT	TTGGTGTCGATTTCAGAGTTTAGAT
Dgat1	GTTTCCGTCCAGGGTGGTAG	GACGATGGCACCTCAGATCC
Dgat2	AGTGGCAATGCTATCATCATCGT	TCTTCTGGACCCATCGGCCCCAGGA
Esrrb	GCACCTGGGCTCTAGTTGC	TACAGTCCTCGTAGCTCTTGC
Fabp3	CTGGAAGCTAGTGGACAGCAA	TCCCAGCTGAAAGTTGATCTCT
Fasn	TGCGGAAACTTCAGGAAATGT	AGAGACGTGTCACTCCTGGACTT
Fgf5	TGTGTCTCAGGGGATTGTAGG	AGCTGTTTTCTTGGAATCTCTC
Gata4	GAACACCCTGAGCAGGCCTC	TTTCTGGGAAACTGGAGCTGG
Gata6	GAGCTGGTGCTACCAAGAGG	TGCAAAAGCCCATCTCTTCT
Klf4	GTGCCCCGACTAACCGTTG	GTCGTTGAACTCCTCGGTCT
L19	TGATCTGCTGACGGAGTTG	GGAAAAGAAGGTCTGGTTGGA
Mixl1	GACAGACCATGTACCCAGAC	GCTTCAAACACCTAGCTTCAG
Nanog	CTTACAAGGGTCTGCTACTGA	TCTGCTTCCTGGCAAGGACC
Ncoa3	TCTCAGCGACATCGACAACTT	GCCTGTAGTAAAAGCGGTCCTA
Oct4	CGTGGAGACTTTGCAGCCTG	GCTTGGAAACTGTTCTAGCTCCT
Otx2	TATCTAAAGCAACCGCCTTACG	AAGTCCATACCCGAAGTGGTC
Pdk1	TCTGCGACAAGAGTTGCCTG	CTTTGGATATACCAACTTTGCACC
Plin1	TGGCAGCAGCAGTAGTGGAT	AGCTCACCAAGGGCAGGTT
Plin2	GGCTCTGGGAAGCATCGA	GGCCTTGGGAGCCTTCTG
Plin3	AAACAGGGTGTGGACCAGAG	GGCTTAGCTGGGTCCTTTTC
Plin4	GCTGACACCAAAACCCTTGT	ACCACACTCCTCCACTGACC
Rex1	CTCCTAGCCGCCTAGATTTCCA	CGTGTCCCAGCTCTTAGTCCATT
S17	ATGACTTCCACACCAACAAGC	GCCAACTGTAGGCTGAGTGAC
Sox17	GGAATCCAACCAGCCCACTG	GGACACCACGGAGGAAATGG
Sox2	AAAACCACCAATCCCATCCA	CGAAGCGCCTAACGTACCAC
Sox7	CAAGGATGAGAGGAAACGTCTG	TCATCCACATAGGGTCTCTTCTG
Tbx3	GAACCTACCTGTTCCCGGAAA	CAATGCCCAATGTCTCGAAAAC

*genomic and plasmid, **genomic, ***plasmid

Table 8.2: Cidea promoter motif enrichment.

Rank	Target	P-value
1	Esrrb	0.000925
2	Evx1	0.00143
3	Emx2	0.00172
4	Esrra	0.00355
5	Pou2f2	0.0111
6	Cphx	0.0136
7	Jundm2	0.0136
8	Nkx1-1	0.0183
9	Pou2f3	0.0189
10	Evx2	0.0214
11	Hoxb3	0.0256
12	Sox15	0.03
13	Vax1	0.0303
14	Atf1	0.0388
15	Hand1::Tcfe2a	0.039
16	Hbp1	0.0401
17	Lhx6	0.0421
18	Mtf1	0.0432
19	Ipf1	0.0473
20	Gsh2	0.0539
21	Myf6	0.0568
22	Eomes	0.0678
23	Pou5f1	0.0739
24	Klf7	0.0751
25	Gcm1	0.0792
26	Pax2	0.0853
27	Six4	0.0858
28	Hoxa1	0.0878
29	Gmeb1	0.092
30	Hoxa2	0.103

Table 8.3: All metabolites reliably detected in untargetted GC-MS analysis of lipid droplet clones

Metabolite	Metabolite (continued)
L-(+) lactic acid	glyceric acid
pyruvic acid	Beta- alanine 1
glycerol 1-phosphate	L-mimosine 2
D-glucose-6-phosphate 1	D-threitol
citric acid	4-guanidinobutyric acid 2
alpha ketoglutaric acid	hypotaurine
succinic acid	5-aminovaleric acid 1
fumaric acid	N-acetyl-L-aspartic acid 1
D-malic acid	D-lyxose 2
oxalic acid	D-lyxosylamine 2
Phenylalanine 1	arabitol
L-valine 2	trans-aconitic acid
L-threonine 1	DL-4-hydroxymandelic acid
L-tryptophan 2	alpha-D-glucosamine phosphate
L-methionine 1	alpha-glucosamine 1-phosphate
L-leucine 1	tagatose 1
DL-isoleucine 1	fructose 1
L-lysine 2	D-allose 1
glycine	methyl-beta-D-galactopyranoside
L-glutamine 1	D-glucose 1
L-proline 1	talose 1
L-proline 2	D-sorbitol
L-tyrosine 1	D-mannitol
L-ornithine 2	sedoheptulose anhydride monohydrate
L-serine 1	pantothenic acid 2
L-alanine 1	myo-inositol
aspartic acid 1	N-acetyl-D-glucosamine 2
L-asparagine 2	L-glutathione reduced
L-glutamic acid 1	2”-deoxyadenosine
L-glutamic acid 2	xanthosine
xylitol	5”-deoxy-5”-(methylthio)adenosine 1
D-ribose-5-phosphate 1	lactobionic acid 2
sedoheptulose anhydride monohydrate	D-(+) trehalose
2-ketoisocaproic acid 2	5”-deoxy-5”-(methylthio)adenosine 2
benzoic acid	isomaltose 1
caprylic acid	daidzein
glycerol	

Table 8.4: Pathway enrichment analysis in large LD and small LD clones.

Pathway enrichment analysis using limmas geneSetTest() function in conjunction with the meta-database Consensus-PathDB in large (LLD) and small (sLD) clones. The presented combined P-values represent the probability of finding the specific subset of genes from a certain pathway in a random set of genes drawn from the complete gene list, an arbitrary cut-off of P=0.001 was used. Pathways are ordered based on similarities.

Pathway	**P-value**
PluriNetWork	5.18E-04
TGF-beta Receptor Signalling Pathway	5.18E-04
Wnt Signalling Pathway NetPath	8.13E-04
XPodNet - protein-protein interactions in the podocyte expanded by STRING	8.13E-04
Senescence and Autophagy	5.18E-04
p53 signalling pathway - Mus musculus (mouse)	6.61E-04
HTLV-I infection - Mus musculus (mouse)	5.18E-04
MAPK signalling pathway	9.22E-04
MAPK signalling pathway - Mus musculus (mouse)	1.19E-03
Insulin Signalling	9.81E-04
Cellular Senescence	6.61E-04
Cellular responses to stress	6.61E-04
Oxidative Stress Induced Senescence	9.81E-04
Cell Cycle, Mitotic	5.18E-04
Cell Cycle	5.18E-04
Mitotic M-M/G1 phases	6.61E-04
Mitotic G1-G1/S phases	8.27E-04
Cell cycle - Mus musculus (mouse)	9.81E-04
Class I MHC mediated antigen processing & presentation	6.61E-04
Ubiquitin mediated proteolysis - Mus musculus (mouse)	9.81E-04
Adaptive Immune System	9.88E-04
Membrane Trafficking	5.18E-04
Endocytosis - Mus musculus (mouse)	9.88E-04
TNF-alpha NF-kB Signalling Pathway	8.13E-04
Proteasome Degradation	5.18E-04
mRNA processing	5.18E-04
Metabolism of RNA	5.18E-04
Gene Expression	5.18E-04
RNA transport - Mus musculus (mouse)	8.27E-04
Metabolism	5.18E-04
Metabolism of proteins	5.18E-04
Protein processing in endoplasmic reticulum - Mus musculus (mouse)	9.88E-04

Table 8.5: Pathway enrichment analysis in large LD (L_1LD only) and small LD clones.

Pathway enrichment analysis using limmas geneSetTest() function in conjunction with the meta-database Consensus-PathDB in large (L_1LD only) and small (sLD) clones. The presented combined P-values represent the probability of finding the specific subset of genes from a certain pathway in a random set of genes drawn from the complete gene list, an arbitrary cut-off of P=0.001 was used. Pathways are ordered based on similarities.

Pathway	**P-value**
PodNet- protein-protein interactions in the podocyte	3.76E-04
XPodNet - protein-protein interactions in the podocyte expanded by STRING	3.76E-04
Focal adhesion - Mus musculus (mouse)	9.83E-04
PluriNetWork	3.76E-04
p53 signalling pathway - Mus musculus (mouse)	4.55E-04
Senescence and Autophagy	4.55E-04
Insulin Signalling	3.76E-04
Endocytosis - Mus musculus (mouse)	4.55E-04
Adherens junction - Mus musculus (mouse)	5.60E-04
EGFR1 Signalling Pathway	5.60E-04
Disease	7.98E-04
MAPK signalling pathway - Mus musculus (mouse)	3.76E-04
TNF-alpha NF-kB Signalling Pathway	3.76E-04
TGF-beta Receptor Signalling Pathway	3.76E-04
MAPK signalling pathway	4.55E-04
HTLV-I infection - Mus musculus (mouse)	5.60E-04
Wnt Signalling Pathway NetPath	6.35E-04
Adaptive Immune System	3.76E-04
Immune System	4.55E-04
Class I MHC mediated antigen processing & presentation	1.04E-03
Glycolysis / Gluconeogenesis - Mus musculus (mouse)	4.55E-04
Glucose metabolism	4.55E-04
Metabolism	3.76E-04
Lipoprotein metabolism	7.17E-04
Metabolism of lipids and lipoproteins	7.23E-04
Glutathione metabolism - Mus musculus (mouse)	4.55E-04
Membrane Trafficking	4.55E-04
trans-Golgi Network Vesicle Budding	9.00E-04
mRNA processing	3.76E-04
Proteasome Degradation	5.43E-04
Protein processing in endoplasmic reticulum - Mus musculus (mouse)	6.35E-04
Metabolism of proteins	6.35E-04
Regulation of PLK1 Activity at G2/M Transition	3.76E-04
Cell Cycle, Mitotic	3.76E-04
Cell Cycle	3.76E-04
Mitotic G1-G1/S phases	4.55E-04
Mitotic M-M/G1 phases	5.60E-04
G2/M Transition	7.23E-04
Cell cycle - Mus musculus (mouse)	7.98E-04

Table 8.6: Pathway enrichment analysis in large LD (L_2LD only) and small LD clones.

Pathway enrichment analysis using limmas geneSetTest() function in conjunction with the meta-database Consensus-PathDB in large (L_2LD only) and small (sLD) clones. The presented combined P-values represent the probability of finding the specific subset of genes from a certain pathway in a random set of genes drawn from the complete gene list, an arbitrary cut-off of P=0.001 was used. Pathways are ordered based on similarities.

Pathway	P-value
HIF-1 signalling pathway - Mus musculus (mouse)	5.90E-05
Renal cell carcinoma - Mus musculus (mouse)	5.90E-05
MAPK signalling pathway - Mus musculus (mouse)	5.90E-05
IL-3 Signalling Pathway	5.90E-05
IL-6 signalling Pathway	8.86E-05
Acute myeloid leukemia - Mus musculus (mouse)	3.40E-04
Insulin Signalling	4.23E-04
ErbB signalling pathway - Mus musculus (mouse)	8.60E-04
Neurotrophin signalling pathway - Mus musculus (mouse)	8.82E-04
MAPK signalling pathway	5.90E-05
MicroRNAs in cancer - Mus musculus (mouse)	5.90E-05
Proteoglycans in cancer - Mus musculus (mouse)	5.90E-05
Pathways in cancer - Mus musculus (mouse)	5.90E-05
HTLV-I infection - Mus musculus (mouse)	5.90E-05
Ras signalling pathway - Mus musculus (mouse)	5.90E-05
ESC Pluripotency Pathways	5.90E-05
Prostate cancer - Mus musculus (mouse)	4.23E-04
Glioma - Mus musculus (mouse)	7.14E-04
Regulation of actin cytoskeleton - Mus musculus (mouse)	5.90E-05
Regulation of Actin Cytoskeleton	5.90E-05
Integrin-mediated Cell Adhesion	5.90E-05
Response to elevated platelet cytosolic Ca2+	5.90E-05
Hemostasis	5.90E-05
Platelet degranulation	1.19E-04
Platelet activation, signalling and aggregation	1.41E-04
PI3K-Akt signalling pathway - Mus musculus (mouse)	5.90E-05
Focal adhesion - Mus musculus (mouse)	5.90E-05
Focal Adhesion	5.90E-05
Non-integrin membrane-ECM interactions	1.41E-04
Growth hormone receptor signalling	5.90E-05
Signalling by Leptin	1.39E-04
Signalling by Leptin1	2.27E-04
IRS activation	8.97E-04
IL-2 Signalling Pathway	5.90E-05
Alpha6-Beta4 Integrin Signalling Pathway	5.90E-05
IL-4 signalling Pathway	5.90E-05
EPO Receptor Signalling	4.10E-04
Disease	5.90E-05
Signalling by NGF	5.90E-05
Immune System	2.48E-04
Innate Immune System	2.55E-04
Adaptive Immune System	1.08E-03
PluriNetWork	5.90E-05
Androgen Receptor Signalling Pathway	5.90E-05
Apoptosis	1.19E-04
Delta-Notch Signalling Pathway	1.85E-04
Senescence and Autophagy	5.90E-05
Bladder cancer - Mus musculus (mouse)	2.02E-04
p53 signalling pathway - Mus musculus (mouse)	2.45E-04

Pathway	P-value
Adherens junction - Mus musculus (mouse)	5.90E-05
PodNet- protein-protein interactions in the podocyte	5.90E-05
Primary Focal Segmental Glomerulosclerosis FSGS	5.90E-05
XPodNet - protein-protein interactions in the podocyte expanded by STRING	5.90E-05
Transcriptional misregulation in cancer - Mus musculus (mouse)	5.90E-05
Endochondral Ossification	8.86E-05
Endocytosis - Mus musculus (mouse)	1.19E-04
TGF-beta signalling pathway - Mus musculus (mouse)	5.90E-05
TGF-beta Receptor Signalling Pathway	5.90E-05
TGF Beta Signalling Pathway	9.68E-04
Adipogenesis	5.90E-05
Id Signalling Pathway	3.80E-04
Bacterial invasion of epithelial cells - Mus musculus (mouse)	5.90E-05
EGFR1 Signalling Pathway	8.86E-05
B Cell Receptor Signalling Pathway	8.86E-05
Kit Receptor Signalling Pathway	1.41E-04
Fc gamma R-mediated phagocytosis - Mus musculus (mouse)	9.14E-04
Osteoclast differentiation - Mus musculus (mouse)	5.90E-05
Cytokine Signalling in Immune system	4.47E-04
Arrhythmogenic right ventricular cardiomyopathy (ARVC) - Mus musculus (mouse)	5.90E-05
Molecules associated with elastic fibres	8.86E-05
Elastic fibre formation	9.27E-05
Dilated cardiomyopathy - Mus musculus (mouse)	1.24E-04
Hypertrophic cardiomyopathy (HCM) - Mus musculus (mouse)	2.27E-04
Syndecan interactions	3.20E-04
ECM proteoglycans	2.44E-04
Signal transduction by L1	3.40E-04
L1CAM interactions	8.17E-04
Axon guidance	5.90E-05
Developmental Biology	5.90E-05
Semaphorin interactions	1.41E-04
Sema4D in semaphorin signalling	8.76E-04
Tight junction - Mus musculus (mouse)	5.90E-05
Leukocyte transendothelial migration - Mus musculus (mouse)	5.90E-05
Striated Muscle Contraction	5.90E-05
Smooth Muscle Contraction	5.90E-05
Axon guidance - Mus musculus (mouse)	5.90E-05
Myometrial Relaxation and Contraction Pathways	5.90E-05
Dorso-ventral axis formation - Mus musculus (mouse)	8.86E-05
Spinal Cord Injury	8.86E-05
Signalling by Hippo	8.86E-05
Neural Crest Differentiation	1.19E-04
Prostaglandin Synthesis and Regulation	2.21E-04
Hypertrophy Model	6.17E-04
Cell junction organization	5.90E-05
Cell-Cell communication	5.90E-05

Pathway	**P-value**
Cell-extracellular matrix interactions	8.86E-05
Localization of the PINCH-ILK-PARVIN complex to focal adhesions	2.27E-04
Signalling by Rho GTPases	5.90E-05
Rho GTPase cycle	8.86E-05
G alpha (12/13) signalling events	4.10E-04
Metabolism	5.90E-05
Metabolism of carbohydrates	3.15E-04
Glucose metabolism	4.20E-04
O2/CO2 exchange in erythrocytes	2.44E-04
Uptake of Carbon Dioxide and Release of Oxygen by Erythrocytes	3.09E-04
Uptake of Oxygen and Release of Carbon Dioxide by Erythrocytes	4.72E-04
Reversible Hydration of Carbon Dioxide	6.38E-04
Nitrogen metabolism - Mus musculus (mouse)	8.14E-04
Wnt Signalling Pathway and Pluripotency	8.86E-05
Wnt Signalling Pathway	2.21E-04
Wnt Signalling Pathway NetPath	3.05E-04
Wnt signalling pathway - Mus musculus (mouse)	5.88E-04
Hippo signalling pathway - Mus musculus (mouse)	5.90E-05
Basal cell carcinoma - Mus musculus (mouse)	5.90E-05
Hedgehog signalling pathway - Mus musculus (mouse)	5.90E-05
Melanogenesis - Mus musculus (mouse)	5.90E-05
WNT ligand biogenesis and trafficking	1.80E-04
Signalling by Wnt	4.18E-04
Non-alcoholic fatty liver disease (NAFLD) - Mus musculus (mouse)	9.27E-05
Alzheimer,s disease - Mus musculus (mouse)	1.19E-04
Huntington,s disease - Mus musculus (mouse)	1.41E-04
Parkinson,s disease - Mus musculus (mouse)	1.41E-04
Respiratory electron transport, ATP synthesis by chemiosmotic coupling, and heat production by uncoupling proteins.	2.89E-04
The citric acid (TCA) cycle and respiratory electron transport	4.23E-04
Respiratory electron transport	7.37E-04
Amoebiasis - Mus musculus (mouse)	5.90E-05
Scavenging by Class A Receptors	5.90E-05
Collagen biosynthesis and modifying enzymes	5.90E-05
Collagen formation	5.90E-05
Binding and Uptake of Ligands by Scavenger Receptors	1.63E-04
Protein digestion and absorption - Mus musculus (mouse)	9.33E-04
ECM-receptor interaction - Mus musculus (mouse)	5.90E-05
Integrin cell surface interactions	5.90E-05
Extracellular matrix organization	5.90E-05
Inflammatory Response Pathway	6.60E-04
Small cell lung cancer - Mus musculus (mouse)	5.90E-05
Laminin interactions	8.86E-05
Anchoring fibril formation	2.26E-04

Pathway	**P-value**
Assembly of collagen fibrils and other multimeric structures	4.10E-04
Degradation of the extracellular matrix	4.23E-04
Fc epsilon receptor (FCERI) signalling	5.90E-05
Downstream signal transduction	5.90E-05
Role of LAT2/NTAL/LAB on calcium mobilization	8.86E-05
PIP3 activates AKT signalling	1.39E-04
DAP12 signalling	1.39E-04
Downstream signalling of activated FGFR	1.41E-04
PI3K/AKT Signalling in Cancer	1.63E-04
PI-3K cascade	1.85E-04
PI3K/AKT activation	1.85E-04
PI3K events in ERBB4 signalling	1.86E-04
Signalling by ERBB4	1.86E-04
Signalling by SCF-KIT	2.02E-04
Constitutive PI3K/AKT Signalling in Cancer	2.21E-04
GAB1 signalosome	2.45E-04
PI3K events in ERBB2 signalling	2.89E-04
Downstream Signalling Events Of B Cell Receptor (BCR)	3.50E-04
DAP12 interactions	5.70E-04
Signalling by PDGF	5.90E-05
NGF signalling via TRKA from the plasma membrane	1.19E-04
Signalling by FGFR in disease	1.41E-04
Signalling by FGFR	2.02E-04
Signalling by EGFR in Cancer	2.24E-04
Signalling by EGFR	3.05E-04
Signalling by ERBB2	3.20E-04

Table 8.7: Pathway enrichment analysis in L_1LD and L_2LD clones.

Pathway enrichment analysis using limmas geneSetTest() function in conjunction with the meta-database Consensus-PathDB in L_1LD and L_2LD clones. The presented combined P-values represent the probability of finding the specific subset of genes from a certain pathway in a random set of genes drawn from the complete gene list, an arbitrary cut-off of P=0.001 was used. Pathways are ordered based on similarities.

Pathway	**P-value**
Arrhythmogenic right ventricular cardiomyopathy (ARVC) - Mus musculus (mouse)	1.36E-04
Non-integrin membrane-ECM interactions	1.36E-04
Integrin cell surface interactions	1.36E-04
ECM proteoglycans	2.10E-04
Regulation of actin cytoskeleton - Mus musculus (mouse)	4.56E-04
Integrin-mediated Cell Adhesion	1.01E-03
Elastic fibre formation	8.44E-04
Molecules associated with elastic fibres	8.78E-04
Amoebiasis - Mus musculus (mouse)	1.36E-04
Alpha6-Beta4 Integrin Signalling Pathway	1.36E-04
Small cell lung cancer - Mus musculus (mouse)	8.44E-04
Cell-extracellular matrix interactions	1.36E-04
Cell-Cell communication	1.36E-04
Cell junction organization	4.18E-04
MAPK signalling pathway - Mus musculus (mouse)	1.36E-04
MAPK signalling pathway	1.36E-04
Platelet degranulation	1.36E-04
Response to elevated platelet cytosolic Ca2+	1.36E-04
Hemostasis	1.36E-04
EGFR1 Signalling Pathway	5.11E-04
Platelet activation, signalling and aggregation	8.47E-04
Endocytosis - Mus musculus (mouse)	5.72E-04
Endochondral Ossification	6.99E-04
Disease	7.36E-04
Axon guidance	1.36E-04
Developmental Biology	1.36E-04
Spinal Cord Injury	2.21E-04
Axon guidance - Mus musculus (mouse)	8.31E-04
p53 signalling pathway - Mus musculus (mouse)	1.36E-04
Senescence and Autophagy	1.36E-04
PluriNetWork	1.36E-04
TGF-beta signalling pathway - Mus musculus (mouse)	1.36E-04
TGF Beta Signalling Pathway	1.36E-04
PodNet- protein-protein interactions in the podocyte	1.36E-04
Primary Focal Segmental Glomerulosclerosis FSGS	1.36E-04
XPodNet - protein-protein interactions in the podocyte expanded by STRING	1.36E-04
Tight junction - Mus musculus (mouse)	2.21E-04
Myometrial Relaxation and Contraction Pathways	1.36E-04

Pathway	**P-value**
TGF-beta Receptor Signalling Pathway	2.21E-04
Proteoglycans in cancer - Mus musculus (mouse)	1.36E-04
Pathways in cancer - Mus musculus (mouse)	1.36E-04
ESC Pluripotency Pathways	2.21E-04
MicroRNAs in cancer - Mus musculus (mouse)	2.10E-04
Signalling by PDGF	4.56E-04
PI3K-Akt signalling pathway - Mus musculus (mouse)	1.36E-04
ECM-receptor interaction - Mus musculus (mouse)	1.36E-04
Focal adhesion - Mus musculus (mouse)	1.36E-04
Focal Adhesion	1.36E-04
Extracellular matrix organization	1.36E-04
Inflammatory Response Pathway	1.36E-04
Scavenging by Class A Receptors	1.36E-04
Collagen biosynthesis and modifying enzymes	1.36E-04
Collagen formation	1.36E-04
Binding and Uptake of Ligands by Scavenger Receptors	5.89E-04
HTLV-I infection - Mus musculus (mouse)	1.36E-04
Wnt Signalling Pathway NetPath	1.36E-04
Wnt Signalling Pathway and Pluripotency	1.36E-04
Wnt signalling pathway - Mus musculus (mouse)	7.05E-04
Hippo signalling pathway - Mus musculus (mouse)	1.36E-04
Basal cell carcinoma - Mus musculus (mouse)	1.36E-04
Hedgehog signalling pathway - Mus musculus (mouse)	3.61E-04
Signalling by Wnt	5.50E-04
Cellular Senescence	1.36E-04
Cellular responses to stress	3.61E-04
Cell Cycle	7.36E-04
Oxidative Stress Induced Senescence	9.12E-04
Metabolism of mRNA	4.18E-04
Metabolism of RNA	6.41E-04
Gene Expression	7.57E-04
Metabolism of proteins	2.90E-04
Nonsense Mediated Decay Enhanced by the Exon Junction Complex	5.46E-04
Nonsense-Mediated Decay	9.09E-04
Metabolism	1.36E-04
HDL-mediated lipid transport	3.40E-04
Adipogenesis	4.56E-04